SafeG

(Project Number: 945 041)

D3.10 CFD study of core cooling in LOFAs

Authors:	Pavel Zácha, Václav Železný	
For the Lead Beneficiary	**Reviewed by Work package Leader**	**Approved by Coordinator**
Pavel Zácha	**Boris Kvizda**	**Branislav Hatala**

Start date of project: **01/10/2020** Duration:**48 Months**
Project Coordinator: **Branislav Hatala**
Project Coordinator Organisation: **VUJE, a. s.** VERSION: 1.1

Version control table

Version number	Date of issue	Author(s)	Brief description of changes made
1.0	10/10/2023	Pavel Zácha, Václav Železný	1st draft
1.1	23/10/2023	Boris Kvizda, Slavomir Bebjak, Michaela Velckova	Reviewed by consortium, WP leader and MST Final version

Project information

Project full title:	Safety of GFR through innovative materials, technologies and processes
Acronym:	SafeG
Funding scheme:	Research and innovation action
ECGA number:	945041
Programme and call	Horizon 2020 Framework Programme for Research and Innovation (2014-2020) NFRP-2019-2020 (Nuclear Fission and Radiation Protection Research)
Coordinator:	Dr. Branislav Hatala
EC Project Officer:	Cristina Fernandez Ramos
Start date – End date:	01/10/20 – 30/09/2024 i.e. 48 months
Coordinator contact:	+421 905 567 985, Branislav.hatala@vuje.sk
Administrative contact:	+420 602 771 784, jakub.heller@evalion.cz
Online contacts (website):	www.safeg.eu

Copyright

1 CONTENT

2 INTRODUCTION

The detailed study of flow patterns inside the core during a loss-of-flow type of transient using the CFD approach aims at discovering complex flow behavior in the core during decreasing induced flow rate and gradual transition to natural convection. Such flow patterns cannot be predicted by system TH computer codes on their own. Lack of understanding and estimation of magnitude of these effects can lead to misinterpretation of experimental data coming from integral thermal-hydraulic experiments.

A similar study on sodium cooled fast reactor (SFR) found out that not all coolant follows pathways between the core and the decay heat removal heat exchanger has been predicted [1]. This effect can be caused by a multitude of physical phenomena:

- Dissymmetry in the reactor/primary circuit geometry
- Different rate of heat production/dissipation in various parts of the core – the inner fuel assemblies, outer fuel assemblies, reflector, etc.
- The geometry of the upper plenum

In the most extreme case, it was observed, that a non-neglectable portion of the coolant flows in a closed loop between the hot and the cold part of the core (the fuel assemblies and the reflector/shielding assemblies), never reaching the decay heat exchanger. This behavior in SFR is described in Fig.1 coming from [1].

Identification and evaluation of the magnitude of these effects helped to reach much better agreement between the Phénix natural convection experimental data and the computational results.

In GFRs, it is expected, that those effects will be even more pronounced, due to generally higher temperature gradients in the core, and between the core and the heat exchangers, than in SFRs. Moreover, helium, unlike sodium, possess much lower thermal inertia, and its viscosity increase with rising temperature. Last, the largely dissymmetrical loop geometry of the ALLEGRO reactor again contributes to enhancement in the effects described above.

The main objective of Deliverable D3.10 („CFD study of core cooling in LOFAs") is to create a CFD model of the flow section in the reactor core area and perform calculations of the selected LOFA scenario. The computational analyses are solved using the CFD code ANSYS Fluent and are divided into two parts. In the first part, the pressure losses of different types of core assemblies are analyzed in detail. The second part deals with the study of the coolant behavior in a simplified model of the whole core during a defined scenario. The scenario was taken from the Apros program (from BME) and includes the assumption of a simple DHR loop failure.

An integral part of the achieved results are the calculations performed on the CFD model of the PIROUETE facility, which allowed the successful implementation of new correlations of heat transfer coefficients in Apros. The results are summarized in the appendix.
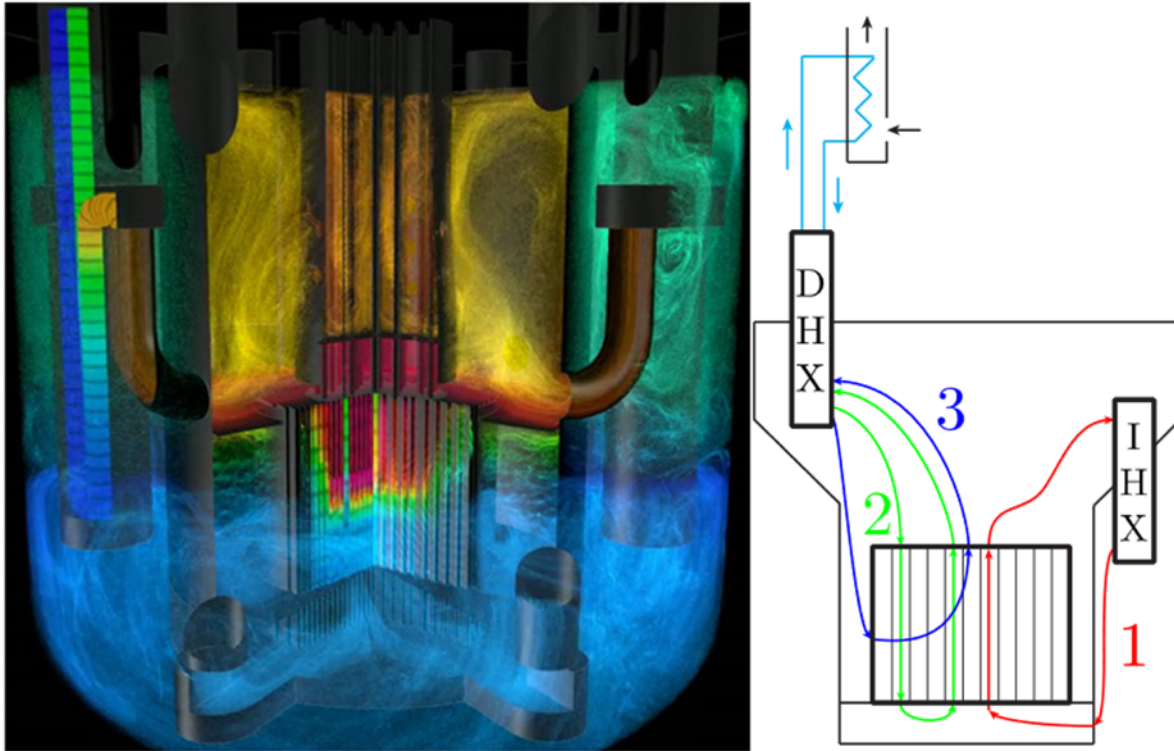
Figure 1: Complex local phenomena with global effects in liquid-metal reactors: jet behavior in large plena (left) and decay heat removal paths by dipped heat exchanger (right)

The work presented in this deliverable lays a foundation for a full-scale analysis done with coupled codes, that could help explain experimental data from complex thermal-hydraulics experiments done with helium in the near future, using the S-ALLEGRO integral facility, and, later, the ALLEGRO reactor itself.

3 DETAILED CALCULATIONS OF FUEL ASSEMBLY

The following chapter describes the creation of detailed CFD models and calculations of the basic fuel assembly types, which are reflector, shielding, control, shutdown and fuel assembly. The arrangement of the assemblies in the reactor core can be seen in Figure 2, where a cross section through the core is shown. It should also be mentioned here that the design of, for example, the reflector and shielding assemblies has been unified over time. Thus, one detailed model will be created and used for both types of assemblies. The same is also true for the control and shutdown assemblies [2].
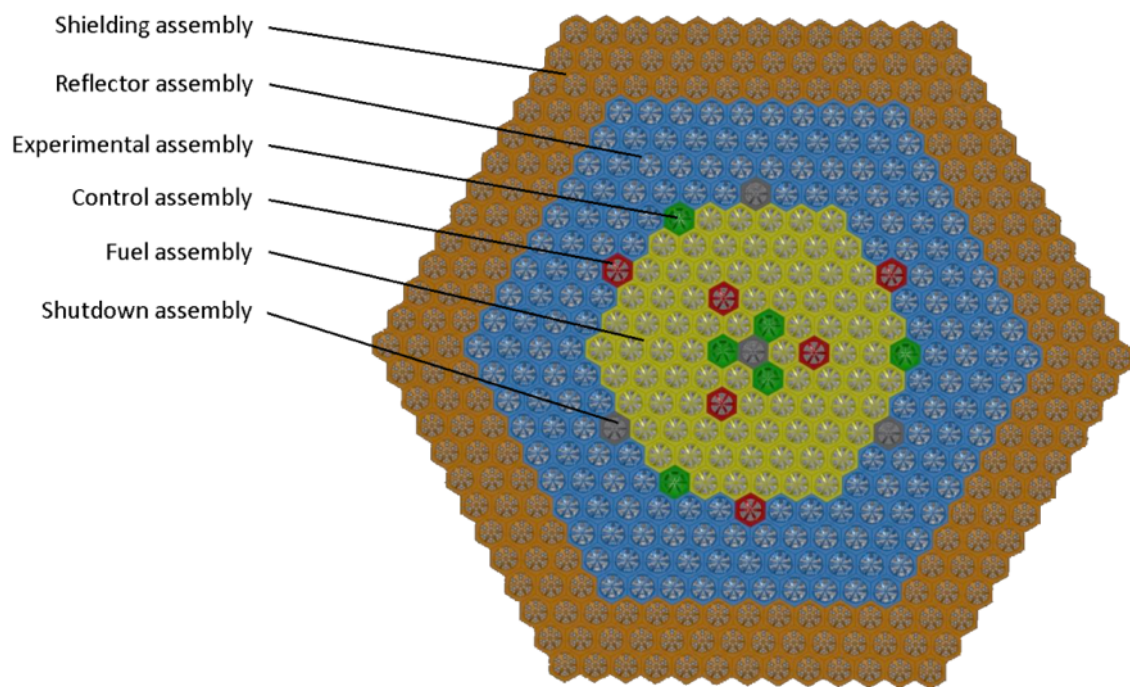
Figure 2: Cross section of the core assemblies

3.1 REFLECTOR/SHIELDING ASSEMBLY

3.1.1 GEOMETRY AND MESH

Figure 3, which presents the construction of the reflector and shield assembly, shows that this type of assembly consists of two main parts. The lower part, which goes through the lower support plate, and the upper part with the reflector itself.

In the detailed picture on the right, you can see that the bottom of the assembly is equipped with a perforated inlet flow restrictor. Its purpose is to reduce the flow through this type of assembly due to the increased flow resistance, as there is virtually none or very little heat to be drawn from it compared to the actual fuel assemblies.

It also acts as a protection against the possible ingress of larger debris into the interior of the assembly where it could cause buckling, particularly at the lower distribution chamber where the 56 mm diameter feed pipe divides into eight 17.5 mm diameter

channels. These channels then pass through the top of the assembly. This consists of four hexagonal blocks in a row, which forms the reflector itself. The upper part of the assembly ends with a collector chamber where the individual assemblies are rejoined, followed by a discharge pipe.

Figure 3: Design of reflector/shielding assembly [3]

During the geometry analyses, it was further shown that this assembly exhibits semi-symmetry. Therefore, to reduce the computational effort, only half of the assembly was modelled with the symmetric boundary condition set on the symmetry plane.

The following figure shows the surface computational mesh in the flow restrictor at the inlet of the reflector/shielding assembly. Highlighted here is the surface of the external fixer, which forms a kind of funnel around the inlet to direct the flow. The actual inlet is modelled at the end of the extended section, the diameter of which corresponds to the outer diameter of the fixer. The wall of this section is modelled for calculation purposes only.

In the real geometry, there is a continuous space under the support plate, which is limited by the walls of the reactor shaft and the perforated bottom. To achieve a steady flow at the inlet of the flow restrictor, a sufficiently long area upstream of the restrictor has been added to the model.

In terms of the creation of the computational mesh, it was necessary to use an unstructured computational mesh of tetrahedral cells due to the complexity of this part of the geometry. The surface computational mesh and the mesh in the holes were created from triangular cells.

This type of mesh can better fill the complex surface of the sieve, which is perforated by several hundred holes. It also provides a smoother connection to the internal volumetric mesh of tetrahedral cells. Only at the outlet of the restrictor was a surface mesh of tetrahedral cells used, as can be seen in Figure 5.
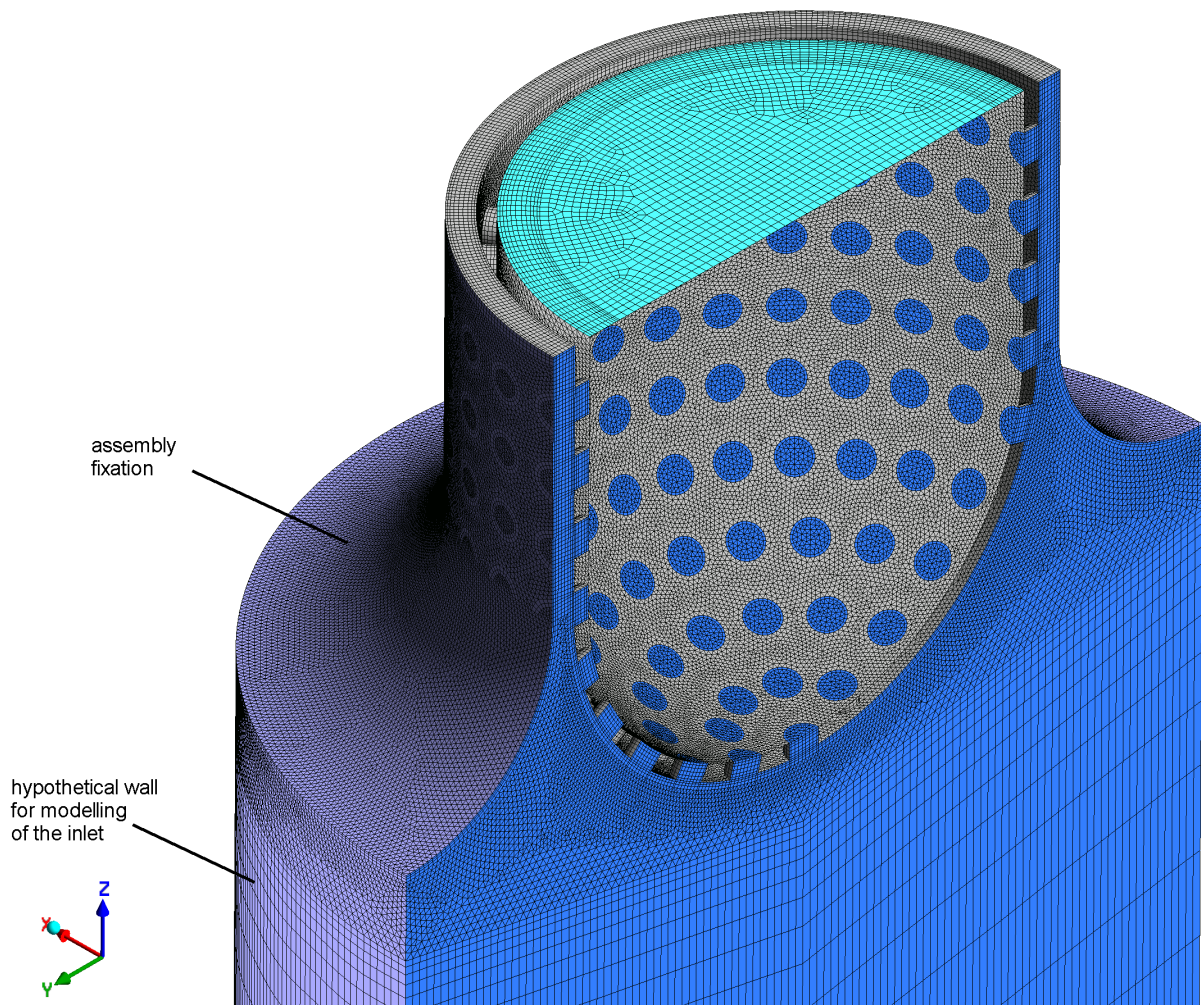
Figure 4: Surface mesh in the area of inlet flow restrictor
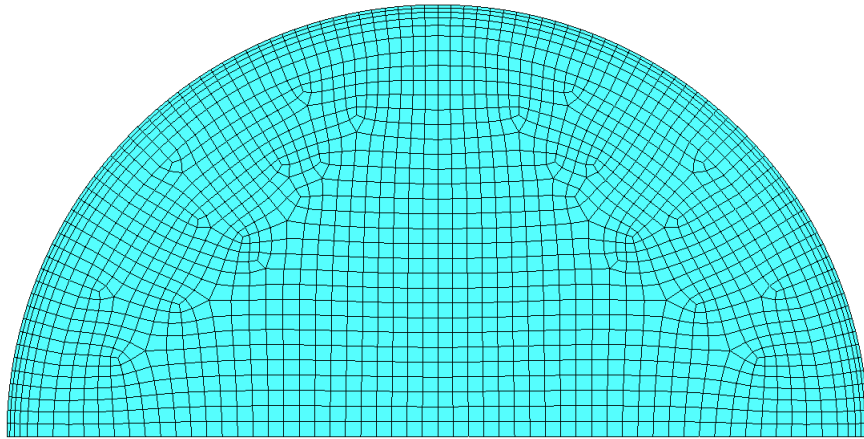
Figure 5: Cross-sectional mesh in the inlet tube

Figure 6 shows the surface mesh in the lower distribution chamber where the flow is distributed from a 56 mm diameter inlet pipe into eight 17.5 mm diameter channels. In this chamber it was also necessary to use a volumetric mesh of tetrahedral cells, as the arrangement of the meshes at the two ends of the chamber is quite different.
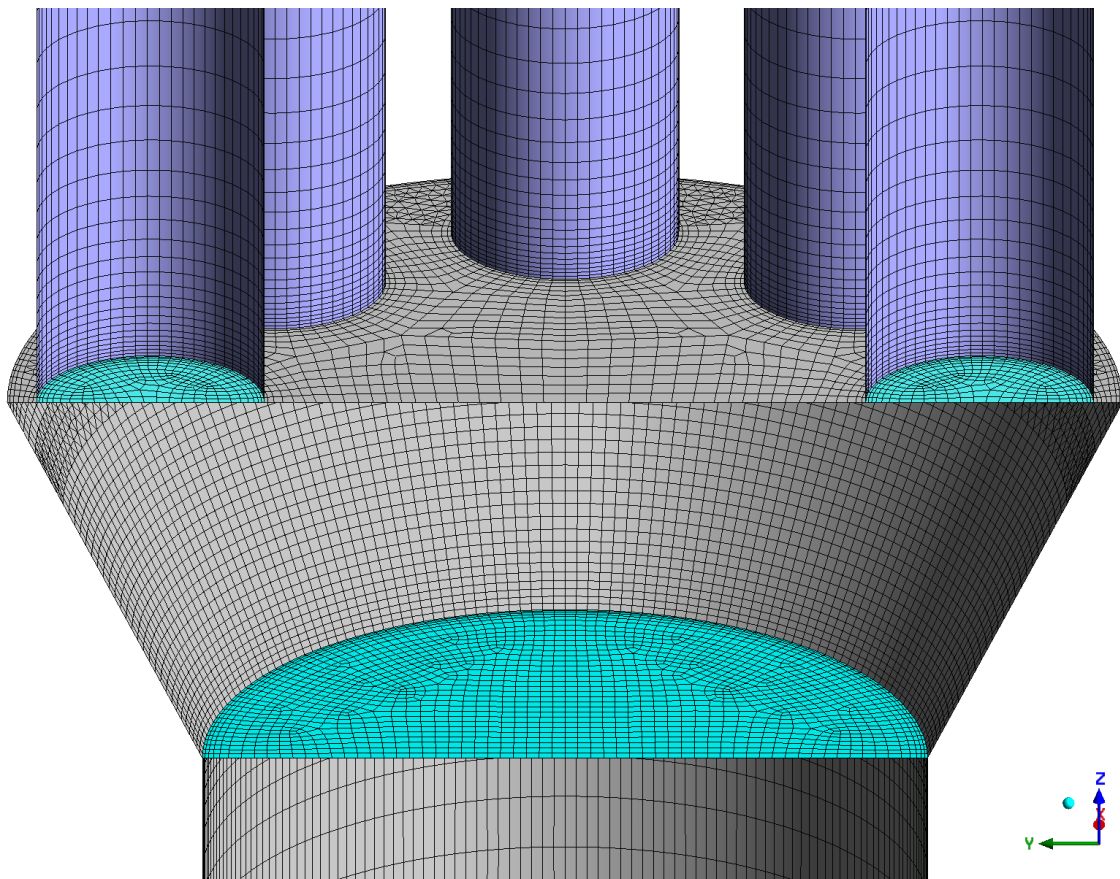
Figure 6: Surface mesh in the area of bottom distribution chamber

Figure 7 shows the surface mesh in the upper collection chamber, where the flow reconnects from eight channels to a discharge pipe with a diameter of approximately 80

mm. The gradual narrowing of the pipe to a smaller diameter allowed the formation of a volume mesh by stretching the surface mesh from the bottom of the chamber into the outlet pipe.
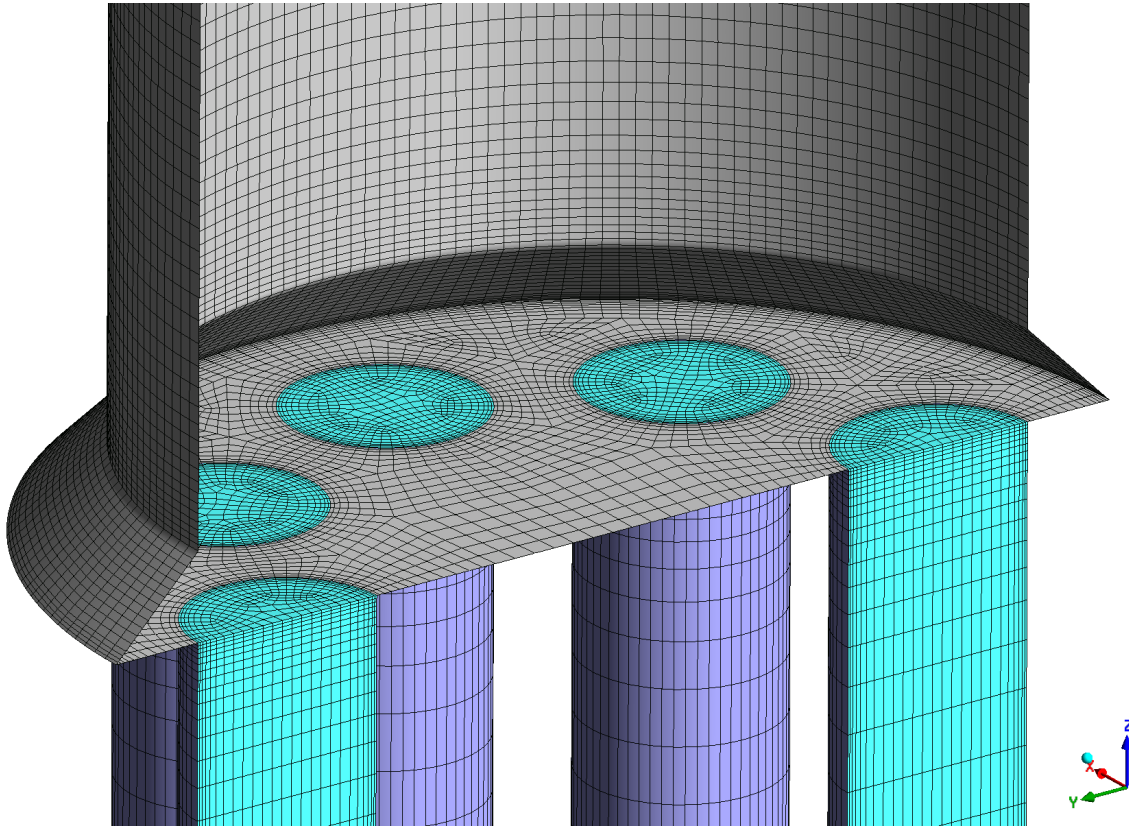
Figure 7: Surface mesh in the area of top collection chamber

3.1.2 COMPUTATIONAL MESH QUALITY

The graph in Figure 8 shows the frequency distribution of cells as a function of the cell skewness parameter. In general, cells with skewness greater than 0.9 should preferably not be present in the computational grid, and the number of cells with skewness greater than 0.75 should be minimized. [4]

Both requirements are met in this case. The highest level of skew is approximately 0.86. Furthermore, we can observe a break at 0.75 and the subsequent significant decrease in cell frequency is very evident in the graph. Approximately 130 cells out of a total of 5.67 million have a skew exceeding this value.
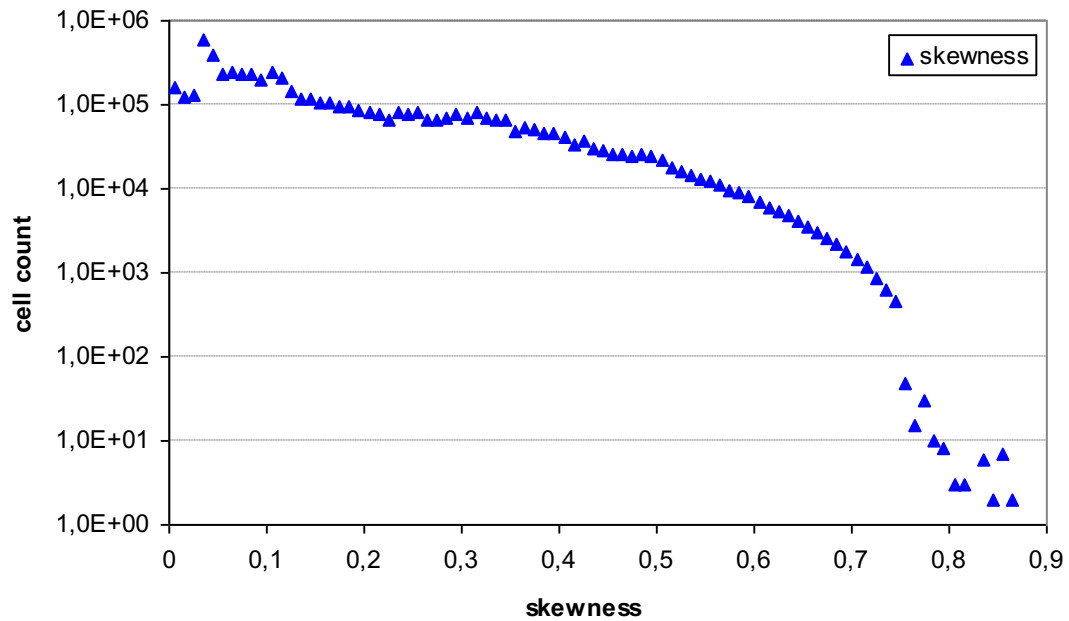
Figure 8: Skewness cells distribution in computational mesh
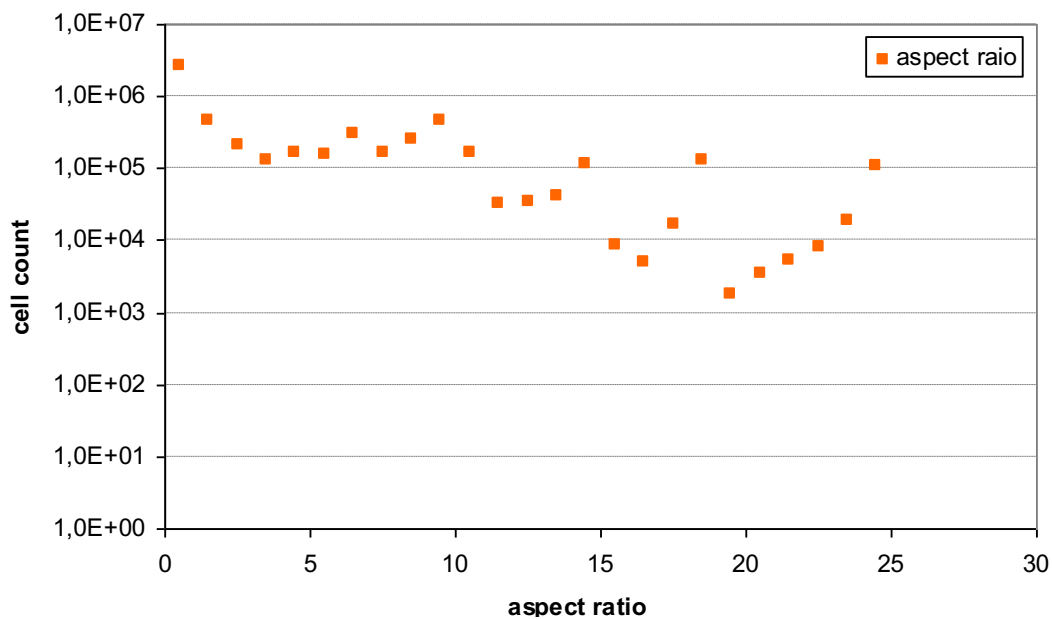
Figure 9: Aspect ratio cells distribution in computational mesh

Another important parameter in terms of the quality of the computational mesh is the Aspect Ratio. This parameter expresses how much the cell is stretched and its value is equal to the ratio of the lengths of the longest and shortest sides of the cell. In general, in the case of directionally disordered flow, this ratio should not be greater than 5. Conversely, in the case where the flow is close to the 1D case, this parameter may be in the lower order of magnitude. Even higher values are permissible for cells located in the boundary layer at the wall surface.

The graph in Figure 9 shows that the maximum Aspect Ratio values are around 25. Closer analysis confirmed that these are cells located in the boundary layer near the walls in the

channels passing through the reflector. Controlled cell stretching can significantly reduce the total number of cells and thus the overall computational complexity of the task.

3.1.3 NUMERICAL MODEL DEFINITIONS

3.1.3.1 Solver settings

Table 1 summarizes the settings of the basic parameters of the model used. The used definitions of the individual parameters of the numerical model are based on generally valid recommendations and on the experience gained from previously solved and numerically similar problems [4] [5].

Table 1 Setting of the basic numerical parameters of the calculation

Parameter	Setting	Note
Time dependence	Stationary simulation, transient simulation	The case is solved as a steady state. The transient solution is used only when the steady state solution proves to be unattainable due to the nature of the flow.
Solver	Pressure-based	The flow of both media is simulated as insufficient, and the thermal-physical properties are dependent only on temperature.
Pressure-velocity coupling	SIMPLE, PISO	The scheme used depends on whether the steady state or transient case was simulated and also on the behavior of the calculation.
Discretization schemes	Gradient – least squares cell based	
	Pressure – body force weighted or second order	
	Others – second order upwind	
Turbulence model	k-ω sst (low Reynolds)	The k-ω sst model has a good ability to approximate a steady state, which can then be used as an initial state for a defined scenario.

3.1.3.2 Settings of thermo-physical properties of helium

This subsection deals with the definition of the basic thermos-physical properties (density, heat capacity, thermal conductivity and dynamic viscosity) for helium. A method referred to as piecewise linear is usually used to define the properties of materials as a function of temperature, based on experience from previous calculations. In this method, the material properties are calculated by linear interpolation between two adjacent defined values.

However, the problem is solved only as a hydraulic problem, i.e. without considering thermal energy. The helium properties, in this case only density and dynamic viscosity, are therefore defined as constant for the conditions corresponding to time t=0 s, i.e., for the steady state before the start of the simulated scenario.

Table 2 Helium properties

Density	6.35 kg/m^3

Viscosity	$2.975 \cdot 10^{-5}$ Pa·s

3.1.4 CALCULATION

3.1.4.1 Boundary conditions

Table 3 summarizes the settings of the main boundary conditions of the nominal operating state. The setting of the boundary conditions corresponds to the real conditions in the assembly of this type at time t=0 s. The mass flux is determined as the corresponding fraction of the known bypass outside the fuel assembly Pressure and temperature are only used to determine helium density and viscosity.

Table 3 Setting of boundary conditions

Location	Condition	Note
Helium inlet	Velocity inlet	Velocity magnitude was set to 0.1143 m/s The inlet velocity condition was chosen for better numerical stability. The velocity was determined based on the mass flux, density and inlet flow cross section.
Helium outlet	Pressure outlet	Static pressure was set at 0 Pa.
The outer walls of the model	Wall	Standard stationary wall
Plane of symmetry	Symmetry	

3.1.4.2 Solution and results

The aim of the solved task was to verify the possibility of simulation of individual types of assemblies by means of substitute porous bodies. This allows to dramatically reduce the total number of cells in the computational grid for the creation of the entire reactor core CFD model.

The graphs in Figure 10 and Figure 11 provide information on the progress of the calculation in terms of stability and convergence capability. From both graphs it is well evident that a steady state solution of the problem was achieved without any problems. The graph in Figure 10 shows the weighted residuals for key solved equations such as the continuity equation, the equations for the individual velocity components and the equations for the quantities describing turbulence.

A sufficient level of convergence is required to achieve values of 10^{-3} and below for all residues monitored. This requirement has been met, and by a considerable margin. Except for turbulence kinetic energy, all other monitored residuals have dropped to the 10^{-5} or 10^{-6} order.
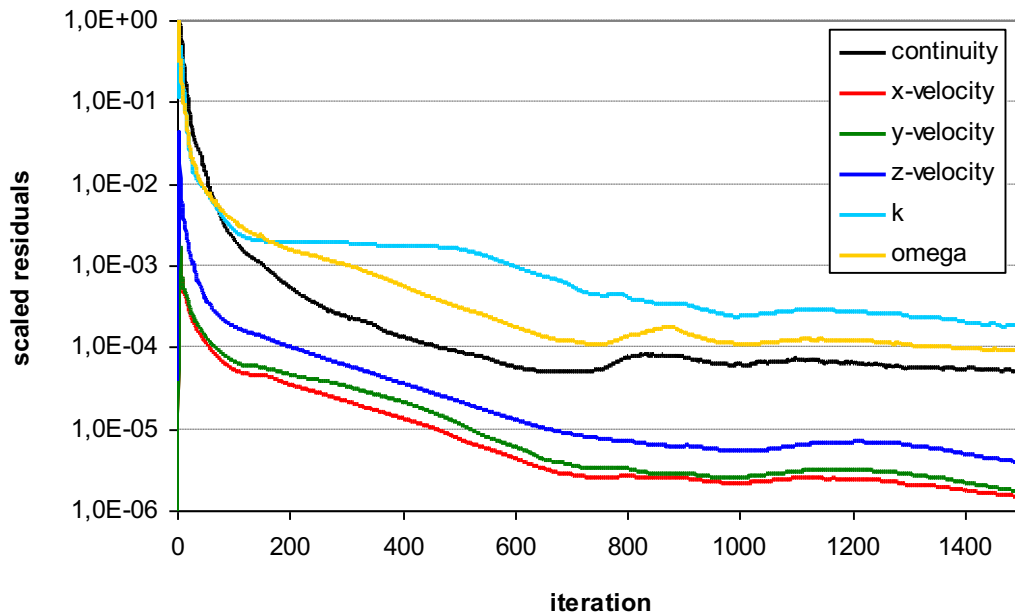
Figure 10: Scaled residuals

The convergence is also confirmed by the graph in Figure 11, which shows the gradual stabilization of other variables. These are the mass flux at the outlet of the simulated domain and the centered value of the static pressure at the inlet of the simulated domain.
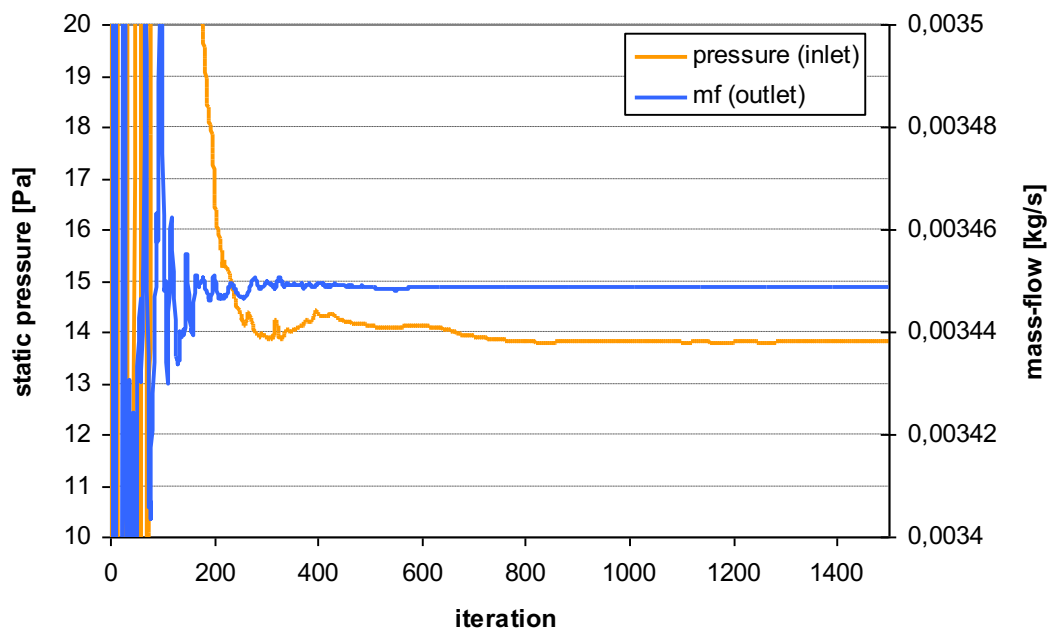
Figure 11: Time profile of inlet static pressure and outlet mass-flow

Figure 12 shows the velocity-z and velocity-magnitude distribution in the flow restrictor area and at the inlet of the reflector/shielding assembly. It can be seen from the velocity distribution in front of the restrictor that the inlet has been simulated at a sufficient distance and the flow here is no longer affected by the set boundary conditions.

Furthermore, the helium flow through the restrictor itself and the subsequent formation of the velocity field in the inlet area can be seen.
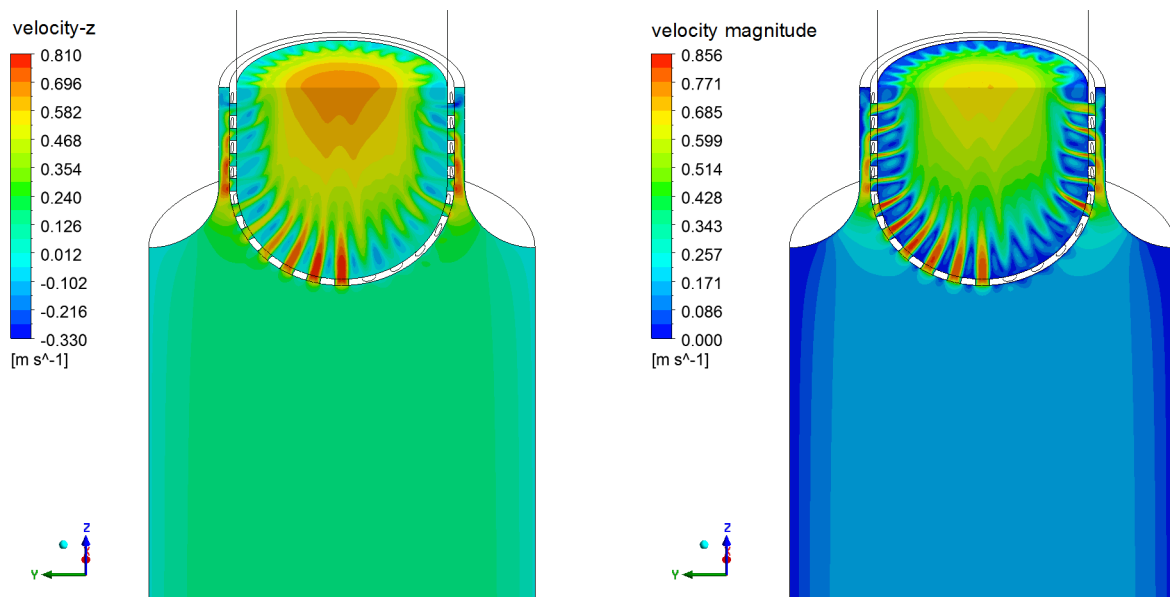
Figure 12: Velocity-z and velocity magnitude distribution in the inlet part of assembly
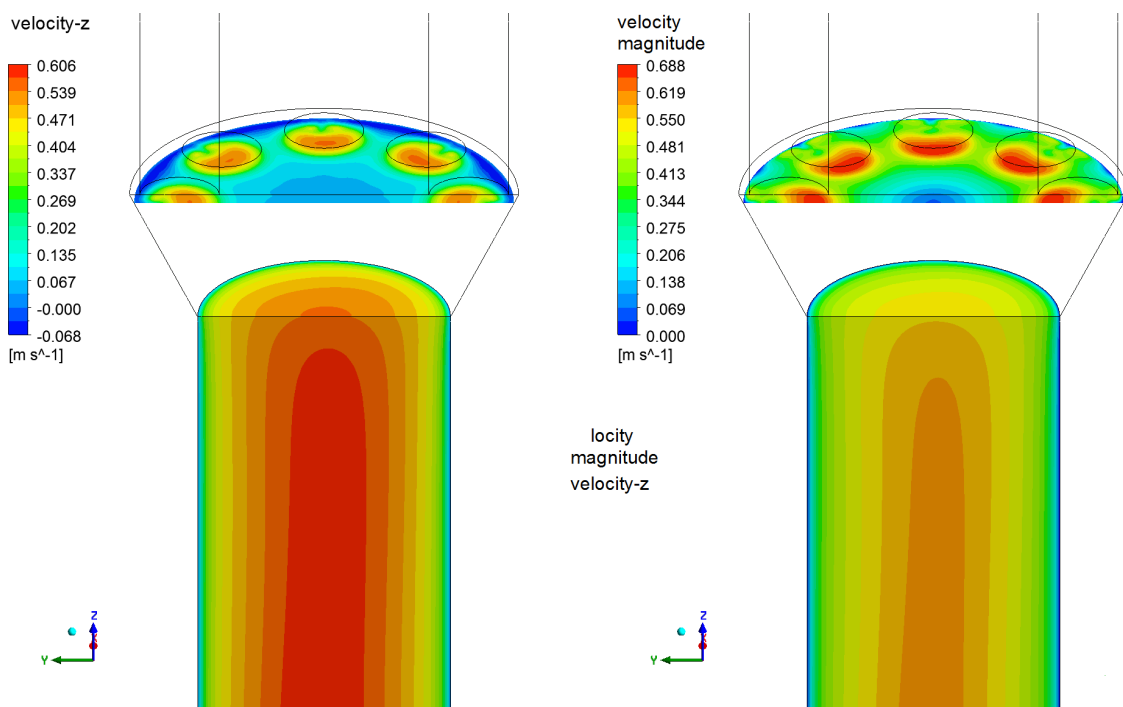
Figure 13: Velocity-z and velocity magnitude distribution in the bottom distribution chamber

Figure 13 shows the velocity-z and velocity-magnitude distribution in the lower distribution chamber, where the helium flow from the inflow channel is split into eight smaller channels that pass through the reflector itself. In particular, the velocity-z distribution shows that a standard velocity profile has been formed during the flow

through the inflow channel and the velocity distribution here is no longer affected by the flow through the restrictor, see Figure 12.

Furthermore, the direction of the helium flow to the inlets of the individual channels can be observed. On the plane of the section just below the top of the distribution chamber, the locations of the highest velocity below the inlets to the individual channels can be seen. In the middle part of the distribution chamber, on the other hand, the flow gradually stagnates. In the peripheral parts of the chamber, there is a slight backflow, which shows that eddies are forming at these locations.

The velocity-z and velocity-magnitude distributions at approximately half the length of the reflector can be seen in Figure 14. The nearly identical velocity-z and velocity-magnitude distributions show that the velocity profile in each channel is already fully formed in the z-axis direction.
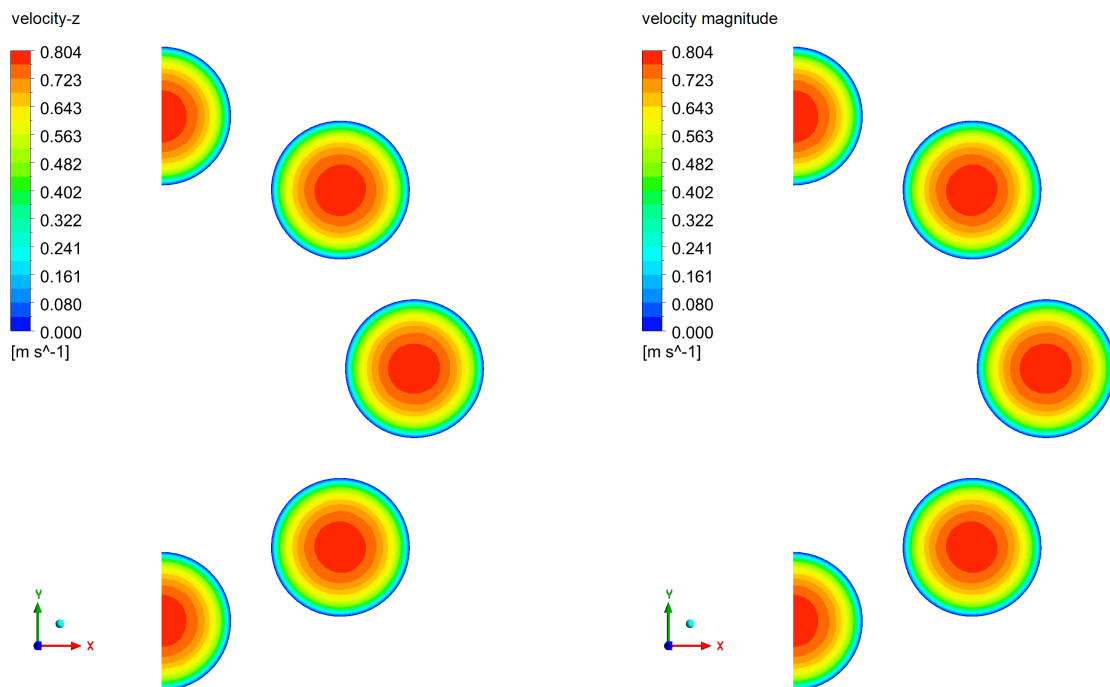
Figure 14: Velocity-z and velocity magnitude distribution in the reflector channels

Figure 15 shows the distribution of velocity-z and velocity-magnitude in the space of the upper collection chamber and the outlet pipe. In this case, the plane of symmetry and a section at the end of the discharge pipe approximately 100 mm away from the duct outlets that pass through the reflector were chosen for display.
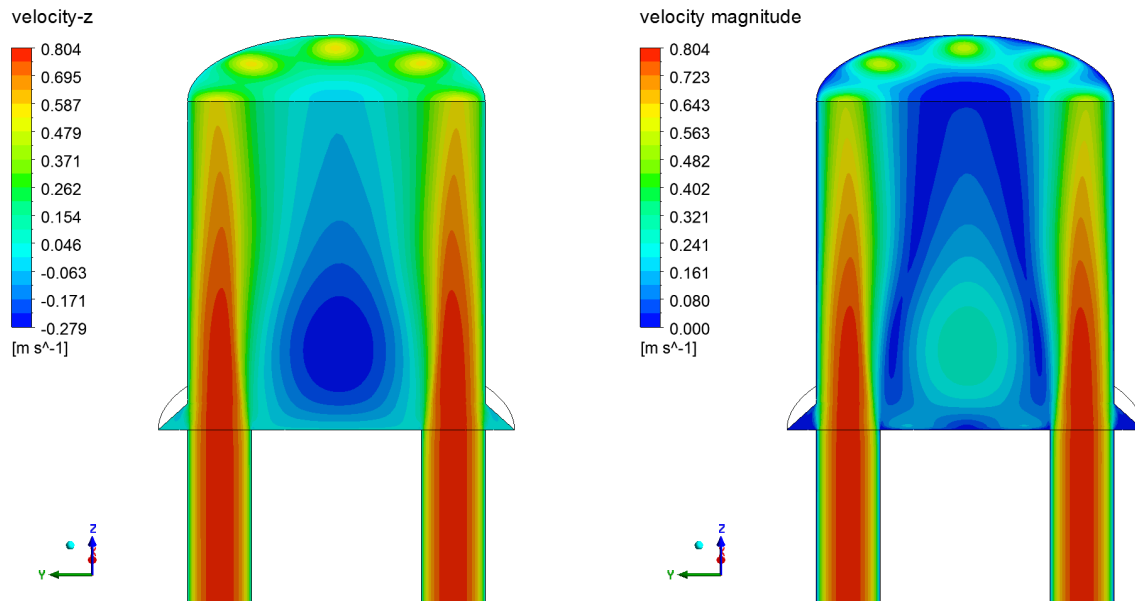
Figure 15: Velocity-z and velocity magnitude distribution in the outlet part of assembly

It can be observed that the flow in the outlet of the assembly is significantly affected due to the helium discharge from these channels. On the other hand, a rather massive outflow can be observed in the middle part, where the backflow occurs.
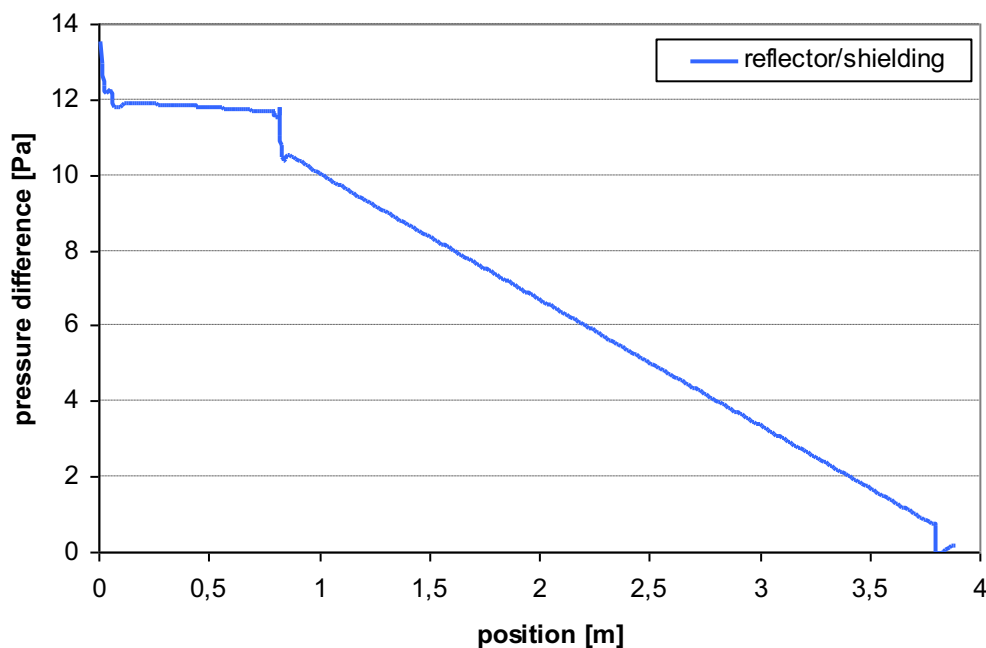
Figure 16: Total pressure profile along of reflector/shielding assembly

The graph in Figure 16 shows the variation of the total pressure (static + dynamic component) of helium over the height of the reflector/shielding assembly. This change is related to the value of the static pressure defined at the exit of the domain, therefore the value at the exit differs slightly from zero. The use of total pressure here is dictated by

changes in the flow cross section, and as a result the ratios of the two components (static and dynamic) change.

The influence of the individual parts of the assembly and their pressure losses can be identified in the graph. At the inlet, the first pressure loss caused by the flow restrictor can be seen. The pressure loss in the inlet channel is relatively small due to its large diameter. The next pressure loss due to the flow through the lower distribution chamber. By far the most significant contribution is the frictional pressure loss due to the flow through the channels in the reflector itself.

3.2   CONTROL ASSEMBLY

3.2.1   GEOMETRY AND MESH

Figure 17 shows the design of the control assembly. Like the reflector/shade assembly, there is an inlet section that passes through the bottom support plate. In the next section there are 3 layers of shielding blocks designed to prevent neutrons from escaping the reactor core. Each layer consists of 3 symmetrical parts separated by a slit through which the helium passes.
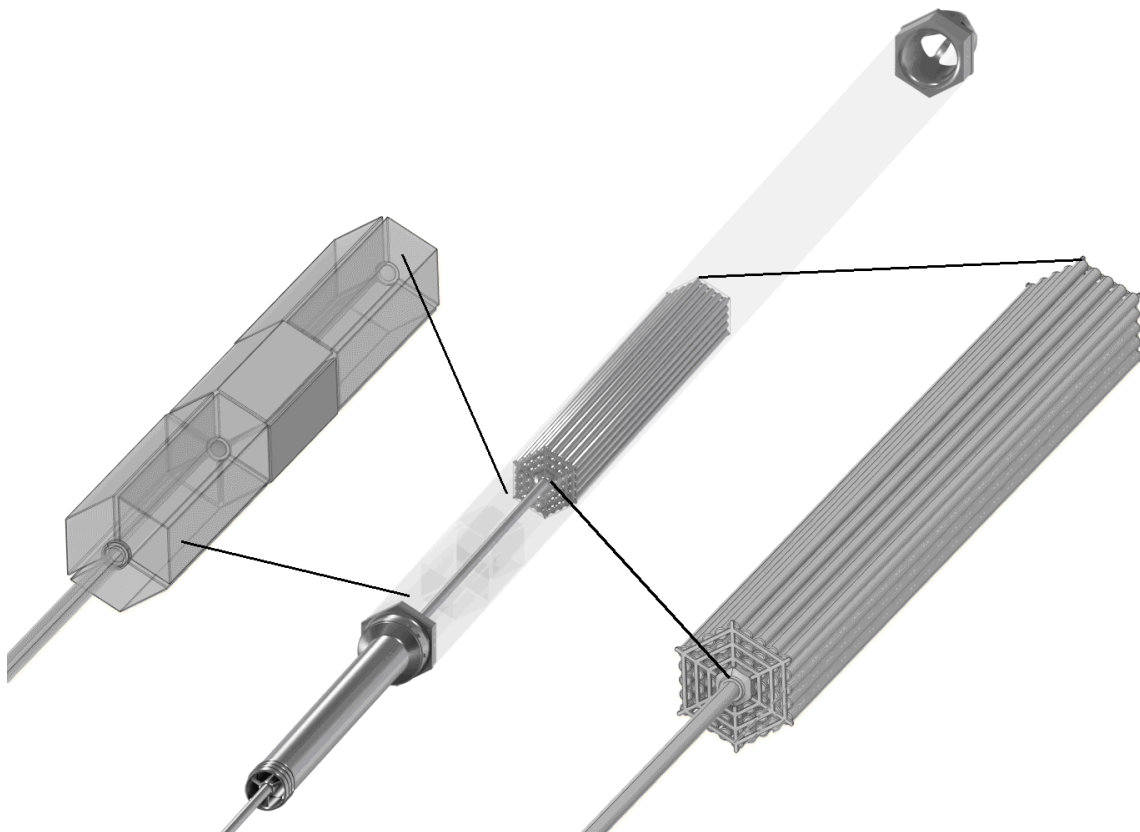
Figure 17: Design of control/shutdown assembly [3]

A bundle of boron carbide control rods is connected to the shielding section. The end of the assembly is an empty space into which the control rod bundle can be inserted if

necessary. Unlike the reflector/shielding assembly, the inlet section does not have a flow restrictor.

An actuator passes through both the inlet and the shielding part of the assembly to provide the movement of the control bundle, see Figure 17. The geometry of the assembly exhibits a periodicity of 120°. Therefore, to reduce the computational complexity, this symmetry will be utilized together with the use of a symmetric boundary condition on the dividing planes.

The guiding tube, through which the actuator of the control bundle passes, is anchored in the inlet part of the assembly by three spacers fixed in the outer wall of the inlet tube. Figure 18 shows the surface computational mesh in the inlet portion of the assembly. From the figure, it can be seen that a hexahedral cell mesh has been suitably applied.
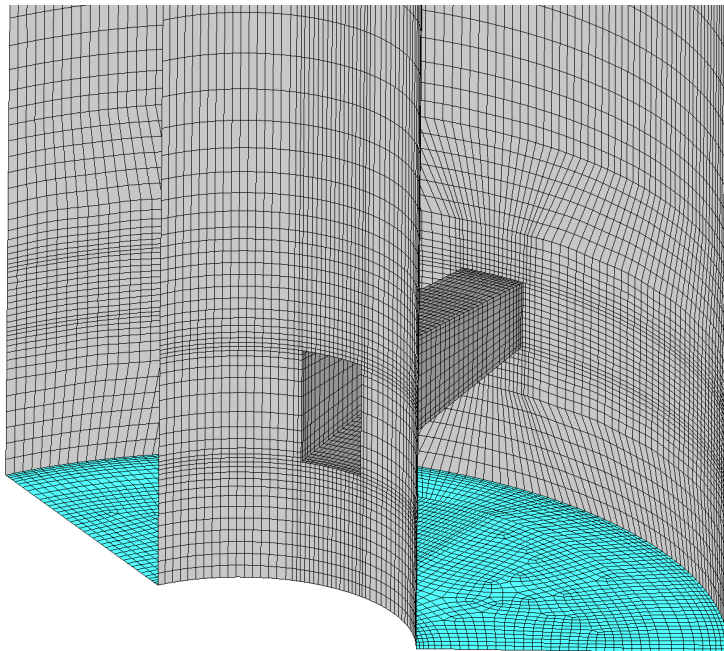
Figure 18: Surface mesh at the inlet part of control/shutdown assembly

Figure 19 shows the surface computational mesh design in the area where the inlet section of the inlet tube assembly transitions into the shielding block section. The figure indicates the areas that are key in terms of helium flow, the outlet of the feed tube and the entrance to the very narrow slots between the shielding blocks.

The solution of the surface mesh at the interface of the different layers of shielding blocks can be seen in Figure 20.

inlet to the gap
in the shielding

the end of
inlet tube
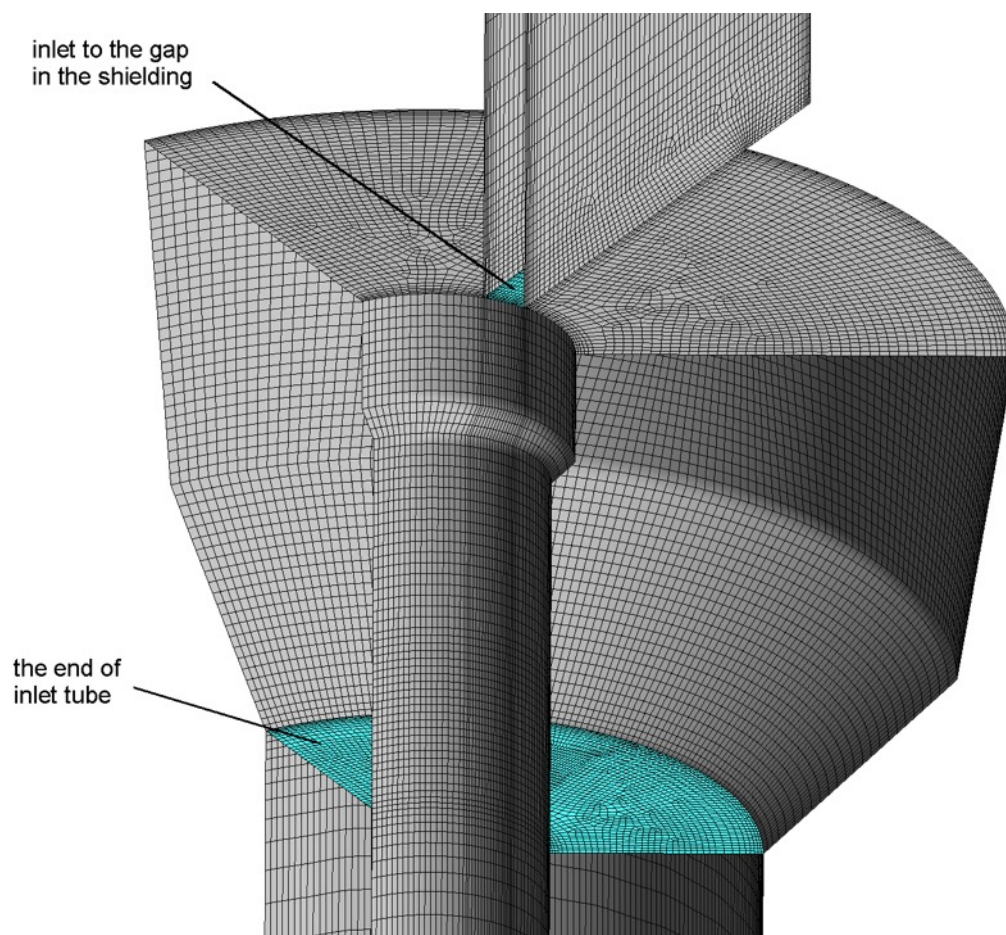
Figure 19: Surface mesh at the inlet part of shielding part
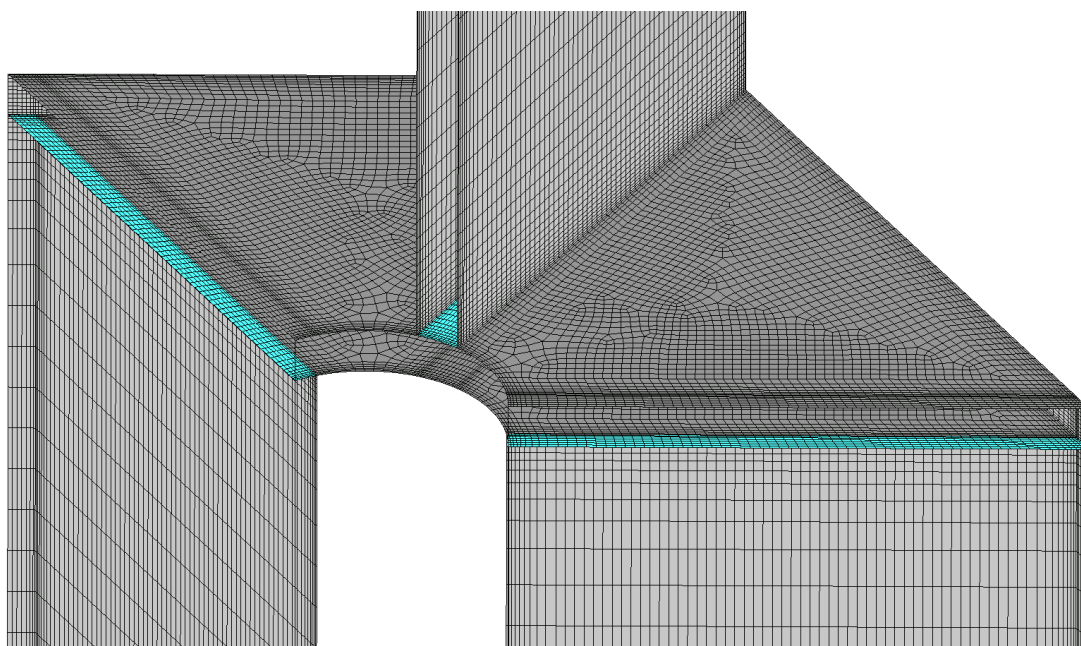
Figure 20: Surface mesh at the border of two parts of shielding
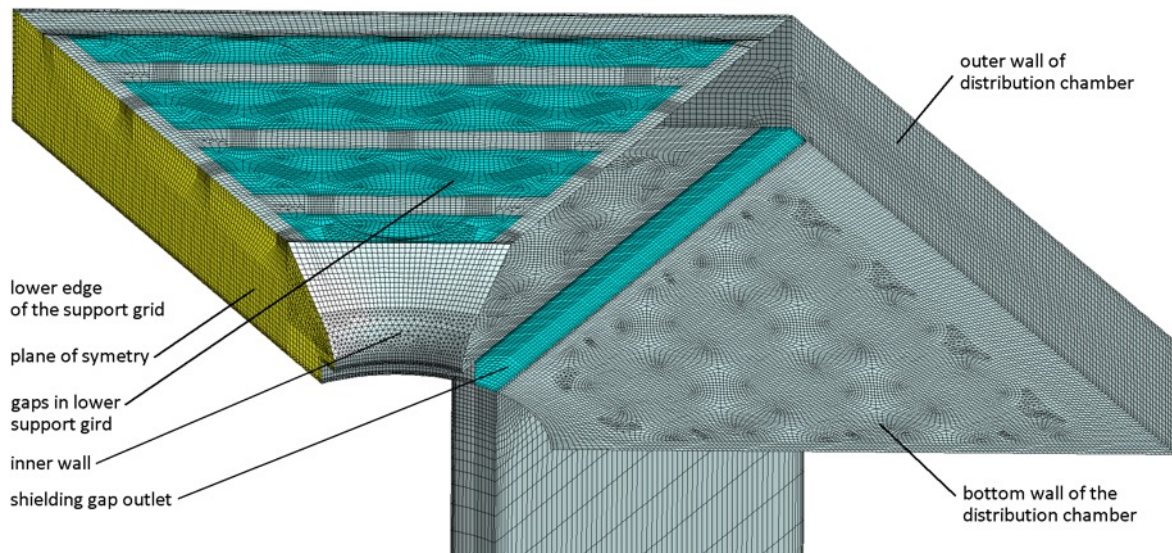
Figure 21: Surface mesh in the lower distribution chamber

Figure 21 shows the layout of the computational mesh in the lower distribution chamber. Here the helium leaves the gap between the shielding blocks and flows into the gaps between the grid sections, which are supported by the lower ends of the control rods. In spite of the relatively high complexity of the geometry of this space, it has been possible to re-create a grid of hexahedral cells. The only exception is a small part of the space near the inner wall of the chamber. As a result of this procedure, very favourable parameters in terms of the quality of the computational mesh have been achieved.
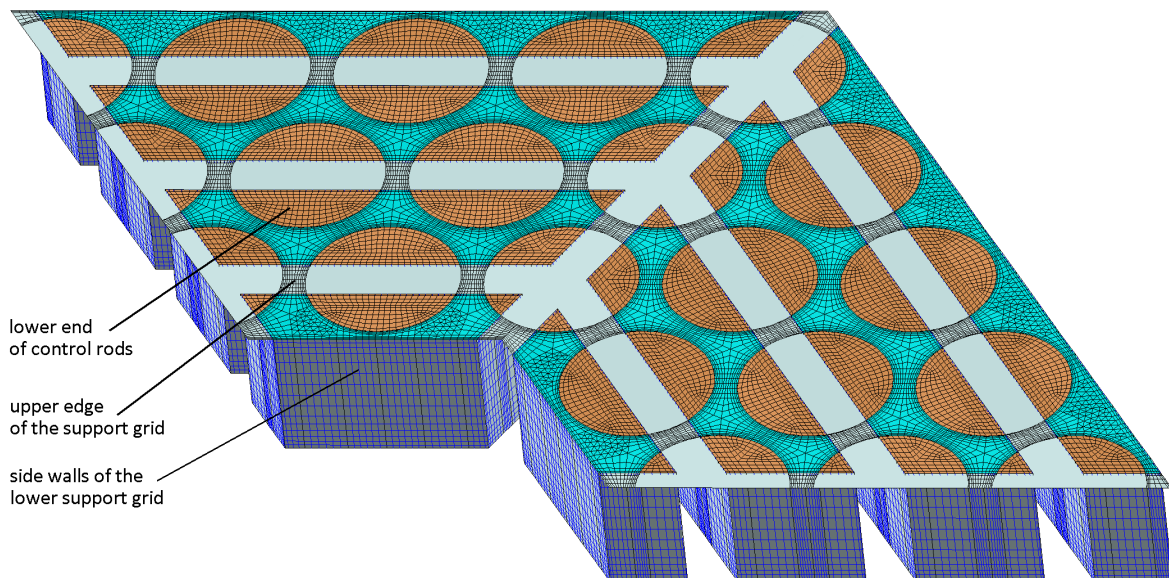
Figure 22: Surface mesh in the area of lower support grid

Figure 22 shows the arrangement of the computational mesh on the surface of the lower support plate and also on the lower ends of the control rods that are supported by the

grid. Here again, the use of a mesh with tetrahedral cells has been avoided due to the partitioning of the space into smaller volumes.

The cross-sectional arrangement of the computational mesh in the control rod space is shown in Figure 23. Only in the peripheral parts, five-walled cells in the shape of a triangular prism were used to maintain sufficient grid quality.
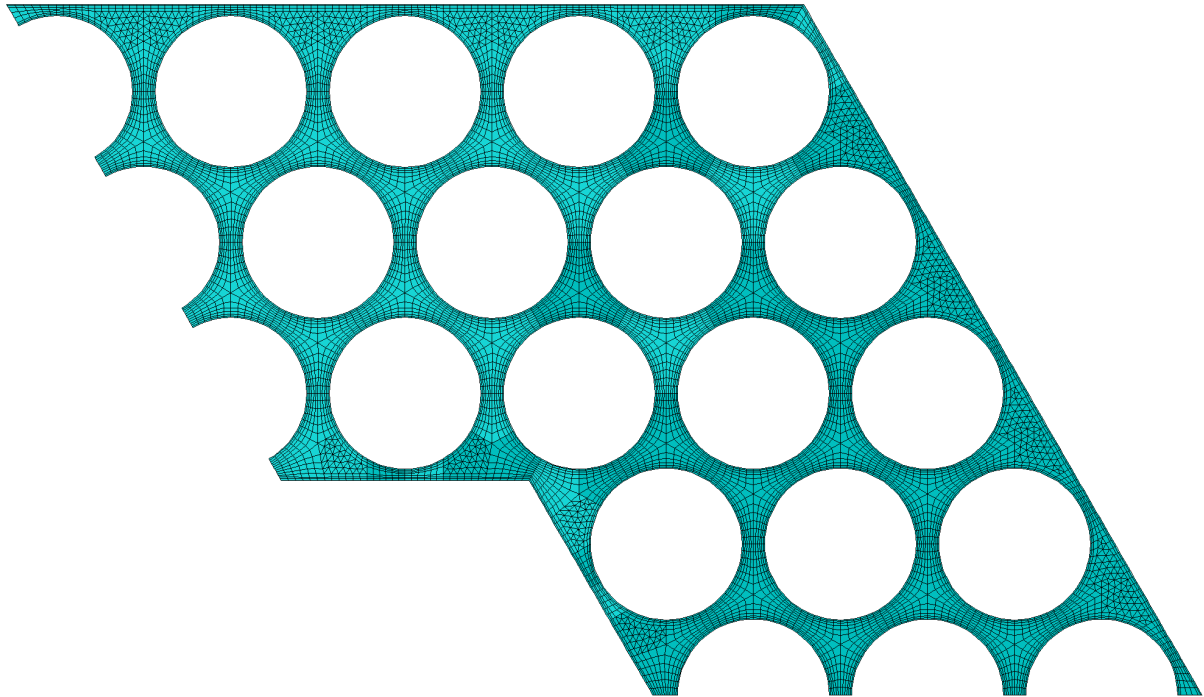
Figure 23: Cross-sectional mesh in the regulation part

Figure 24 shows the arrangement of the surface mesh in the area of the upper collector chamber, where the helium flows out of the gaps between the different parts of the upper support plate, which supports the upper ends of the control rods. A tetrahedral cell mesh was used in this area. The reason for this was the need to reduce the density of the mesh, which would be disproportionately high for the needs of the empty space in the upper part of the assembly.
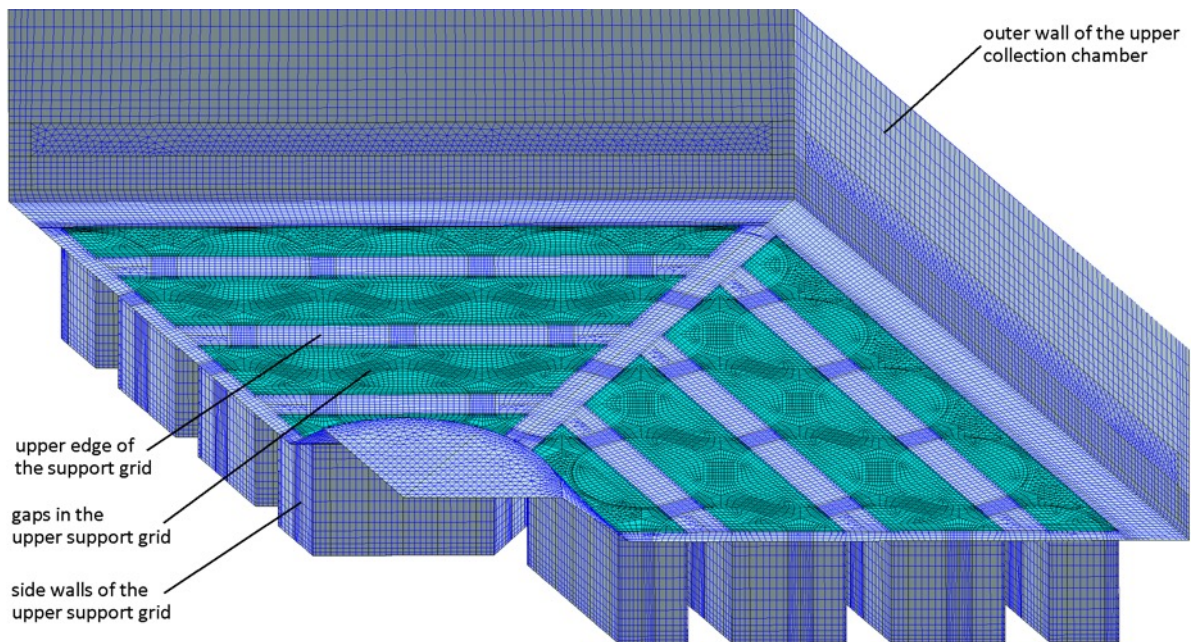
Figure 24: Surface mesh in the upper collection chamber

3.2.2 COMPUTATIONAL MESH QUALITY

The graph in Figure 25 shows the frequency distribution of cells as a function of the skewness parameter. The highest level of skewness reaches a value of approximately 0.86. And like the reflector/shading assembly, the plot shows a significant decrease in cell frequency above a skewness of 0.75, to a value of 80 cells out of a total of 10.53 million.
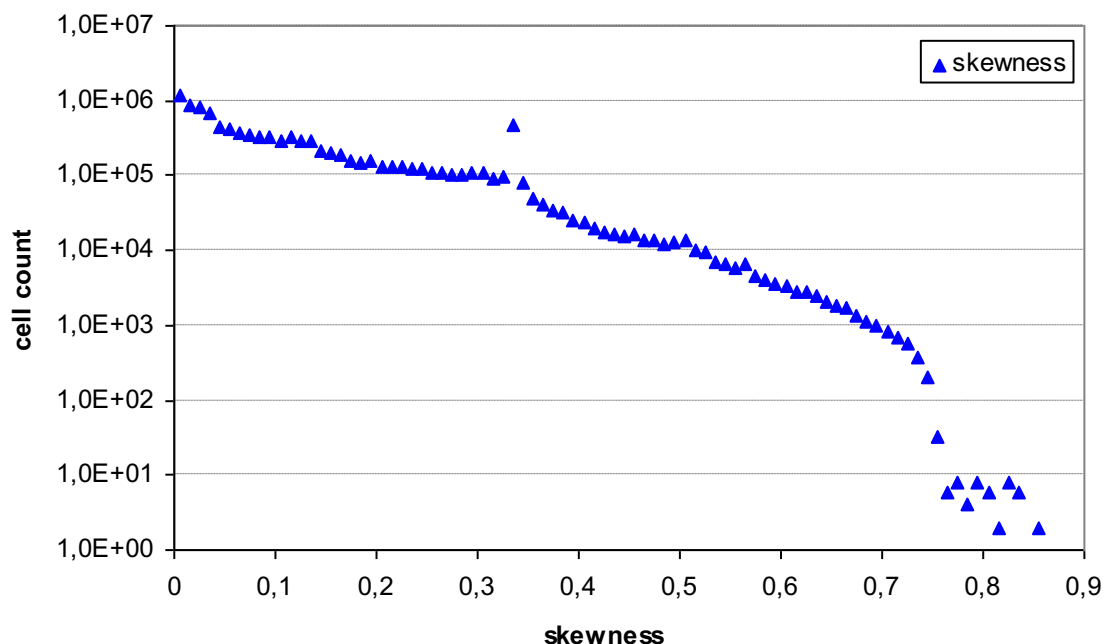
Figure 25: Skewness cells distribution in computational mesh

The graph in Figure 26 shows the distribution of cell frequency in terms of the Aspect Ratio parameter. Its maximum value here is close to 70, which is higher than that of the

reflector/shading assembly. These are the cells that are in the boundary layer near the surface of the control rods in the bottleneck. The number of cells where the value of 50 is exceeded is 5700.
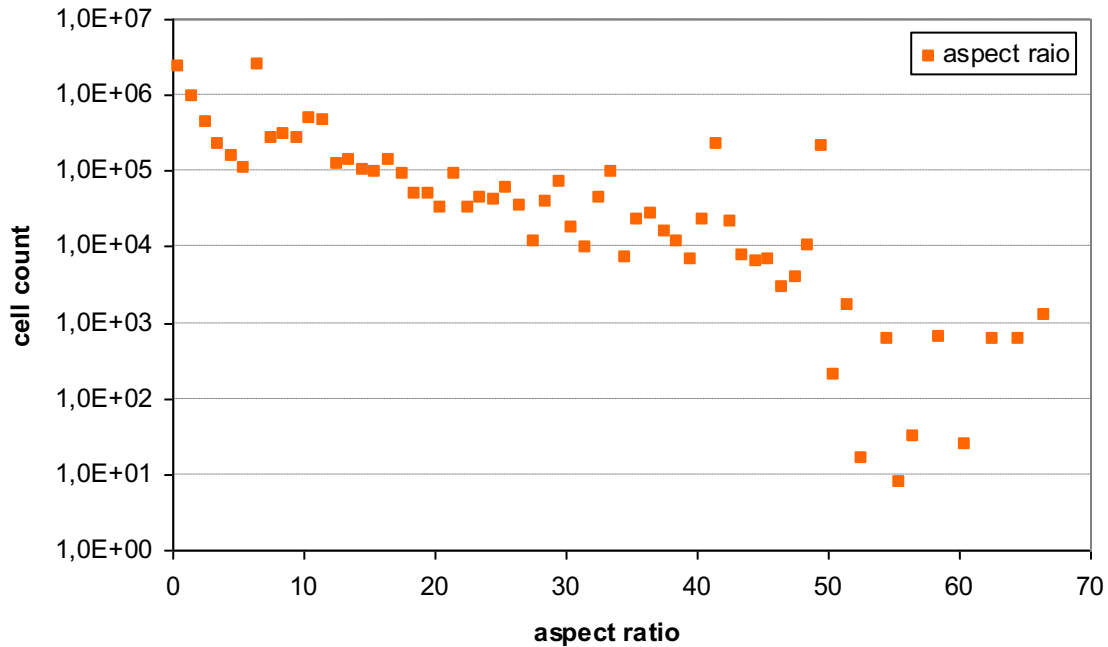
Figure 26: Aspect ratio cells distribution in computational mesh

3.2.3 NUMERICAL MODEL DEFINITIONS

3.2.3.1 Solver settings

The basic settings of the model parameters are identical to the reflector/shading assembly, see Table 1.

3.2.3.2 Settings of thermophysical properties of helium

The thermo-physical properties of the helium is identical to the reflector/shading assembly, see Table 2.

3.2.4 CALCULATION

3.2.4.1 Boundary conditions

Table 4 summarizes the settings of the main boundary conditions of the nominal operating state. The setting of the boundary conditions corresponds to the real conditions in an assembly of this type at time t=0 s. As in the case of the reflector/shielding assembly, the mass flux is set as the corresponding fraction of the known bypass flow, i.e., outside the fuel assemblies. Pressure and temperature are only used to determine helium density and viscosity.

Table 4 Setting of boundary conditions

Location	Condition	Note
Helium inlet	Velocity inlet	Velocity magnitude was set to 0.5055 m/s The velocity inlet condition was chosen for better numerical stability. The velocity was determined based on mass flux, density and inlet flow cross section.
Helium outlet	Pressure outlet	Static pressure was set at 0 Pa.
The inner walls of the model	Wall	Standard stationary wall
The outer walls of the model	Wall	Standard stationary wall
Plane of symmetry	Symmetry	

3.2.4.2 Solution and results

As in the case of the reflector/shielding assembly, the aim was to verify the possibility of simulating the different types of assemblies and their possible simplification by using replacement porous bodies. For the creation of a model of the entire reactor core, this approach allows to dramatically reduce the total number of cells of the computational mesh.

The graphs in Figure 27 a Figure 28 provide information on the course of the calculation in terms of stability and convergence. It is clear from both graphs that a completely steady-state solution was not achieved. The convergence condition for scaled residuals (10^{-3}) was not satisfied for the continuity equation, the kinetic energy equation is on the borderline of this condition, see Figure 27.
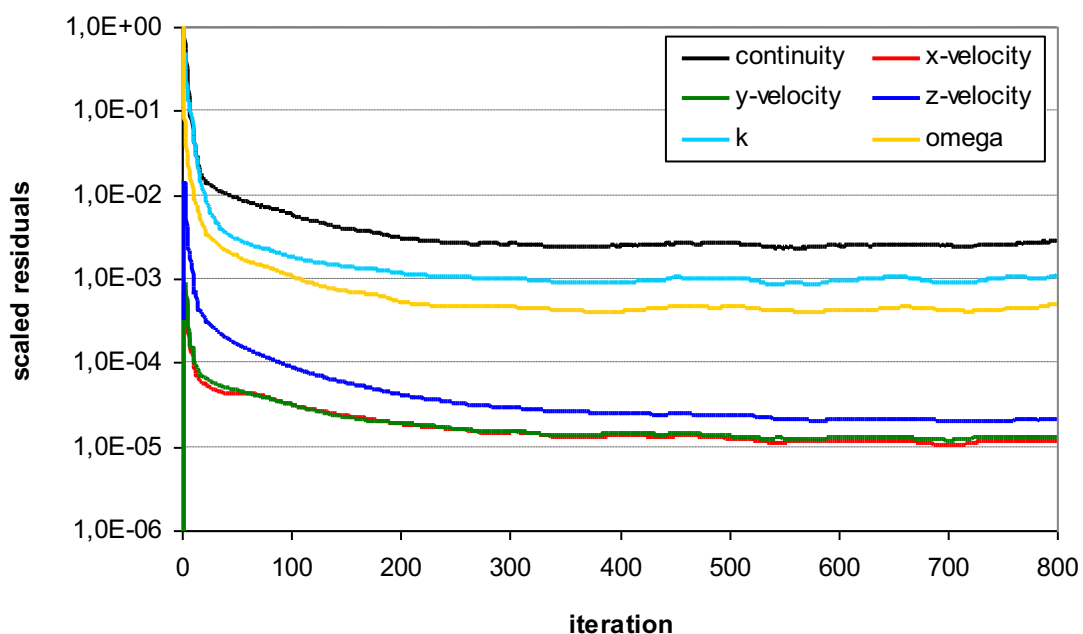
Figure 27: Scaled residuals
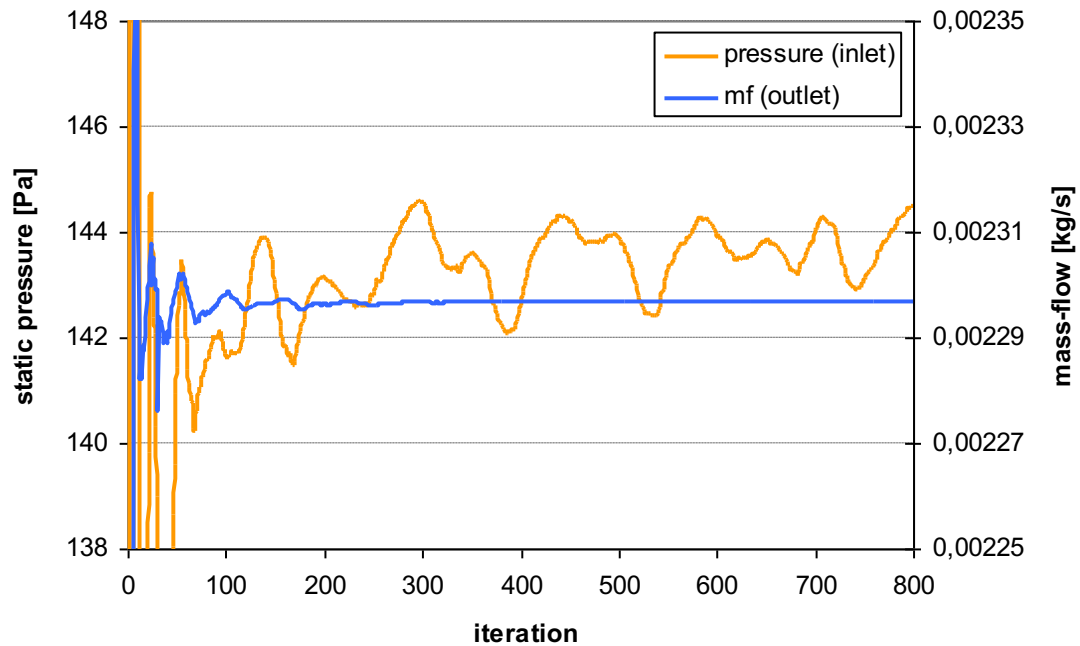
Figure 28: Profile of inlet static pressure and outlet mass-flow

The unsteady behavior is also confirmed by the graph in Figure 28, where the selected monitored variables are plotted. These are the mass flux at the outlet of the simulated domain and the centered value of the static pressure at the inlet of the simulated domain. In the case of the mass flux a steady state has occurred, on the other hand the static pressure profile is slightly oscillating. For these reasons, the problem was further solved in a transient manner, i.e., using a steady-state method with constant boundary conditions. The result of this transient solution is shown in Figure 29, where the same quantities are plotted as in Figure 28.

The oscillation of static pressure in time has been confirmed, at the same level as in the previous steady-state calculation.

The next section of this chapter presents the velocity profiles in the regions that significantly affect the magnitude of the resulting pressure loss.

A very significant change in the nature of the flow is represented by the beginning of the part of the assembly that contains the neutron shielding blocks. Figure 30 shows the helium velocity distribution on a cross section located 1 mm upstream of the slot inlet. The concentration of the flow towards the slit can be seen. The velocity-z distribution shows a sharp drop in velocity outside the slit region. The velocity-xy distribution, on the other hand, shows an intense crossflow as the helium stream recedes towards the slit.
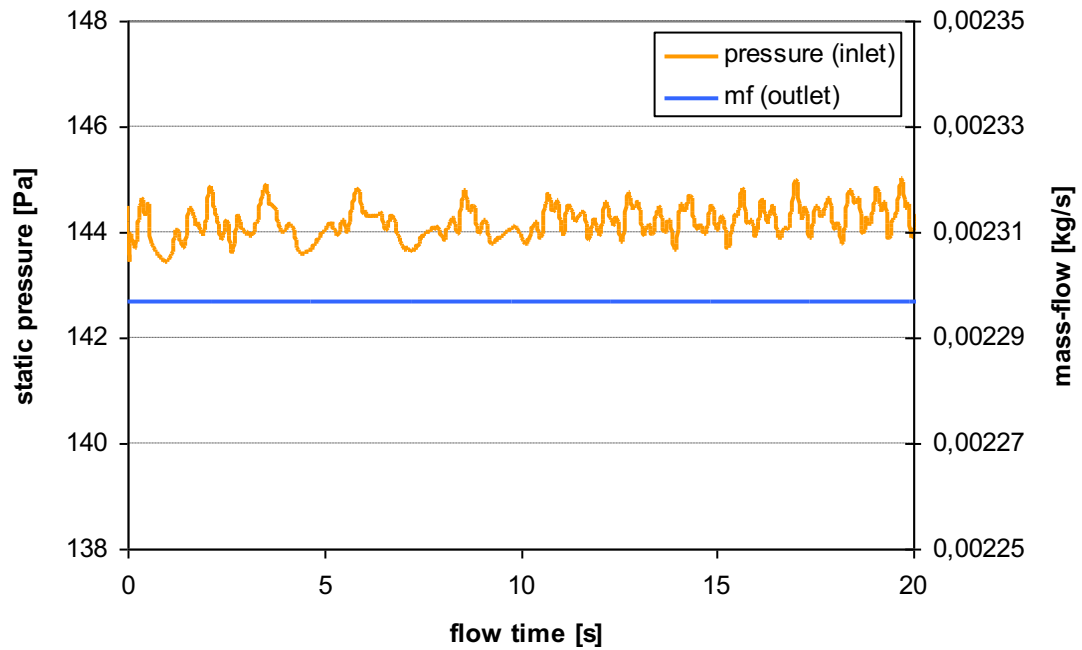
Figure 29: Time profile of inlet static pressure and outlet mass-flow
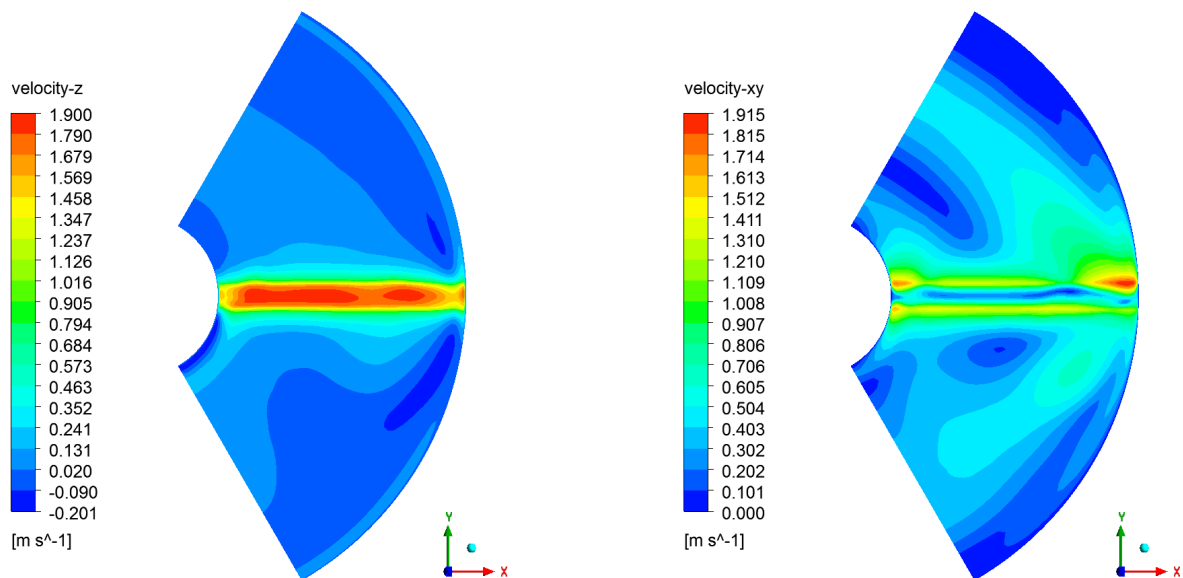
Figure 30: Velocity-z and velocity-xy distribution before inlet of gap in shielding

Figure 31 shows the velocity distribution in the gaps of the support plate at 1 mm from its lower edge. The nature of the flow is still strongly influenced by the inflow of helium through the gap in the shield.
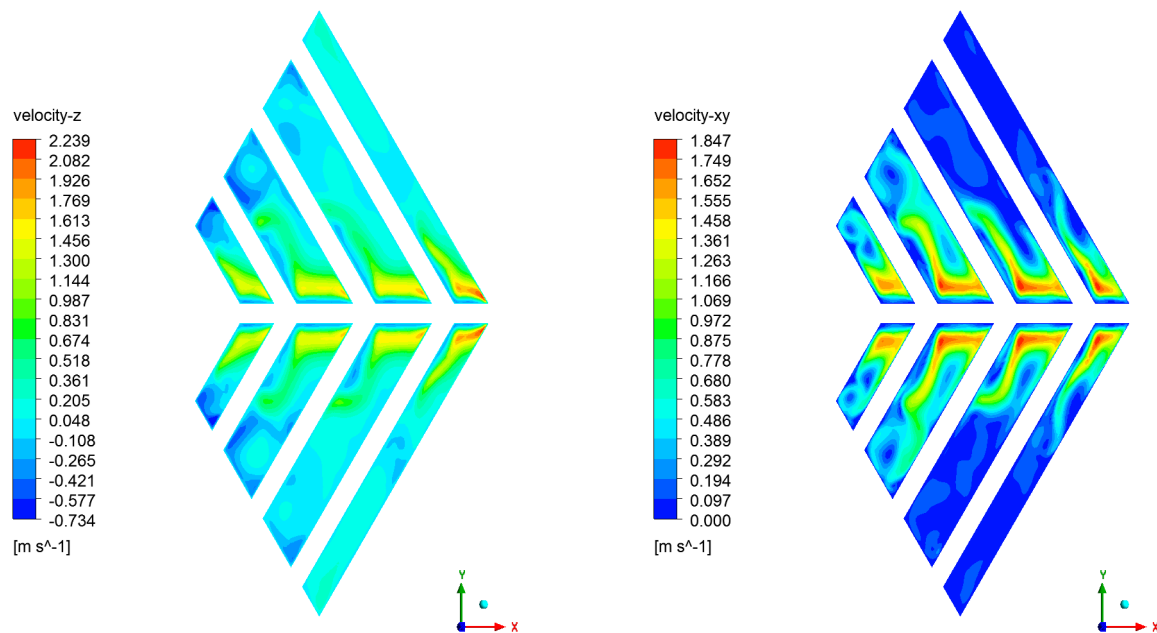
Figure 31: Velocity-z and velocity-xy distribution after inlet to lower support grid

Figure 32 shows the flow development immediately after the inlet between the control rods. The characteristic here is the gradual flattening of the velocity profile and the rapid decrease in crossflow intensity.
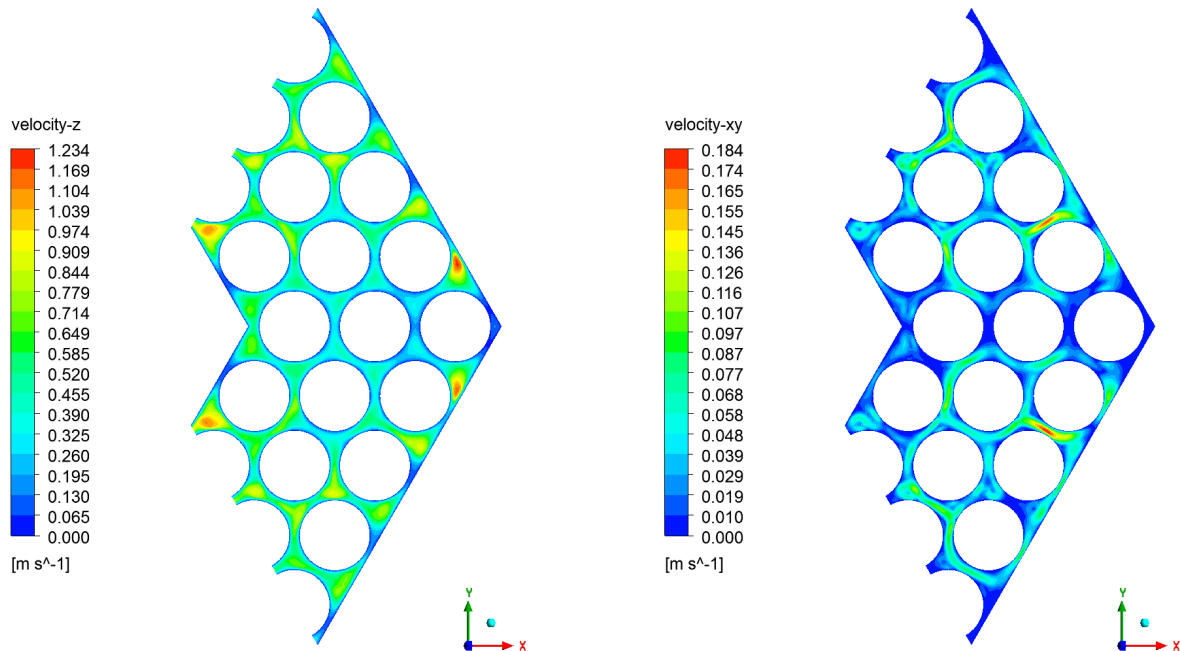
Figure 32: Velocity-z and velocity-xy distribution 50 mm after beginning of control rods

Figure 33 shows the flow in the gaps of the support plate. The velocity distribution here is very strongly influenced by the helium discharge from the space between the control rods, which rest on the grid at their end.
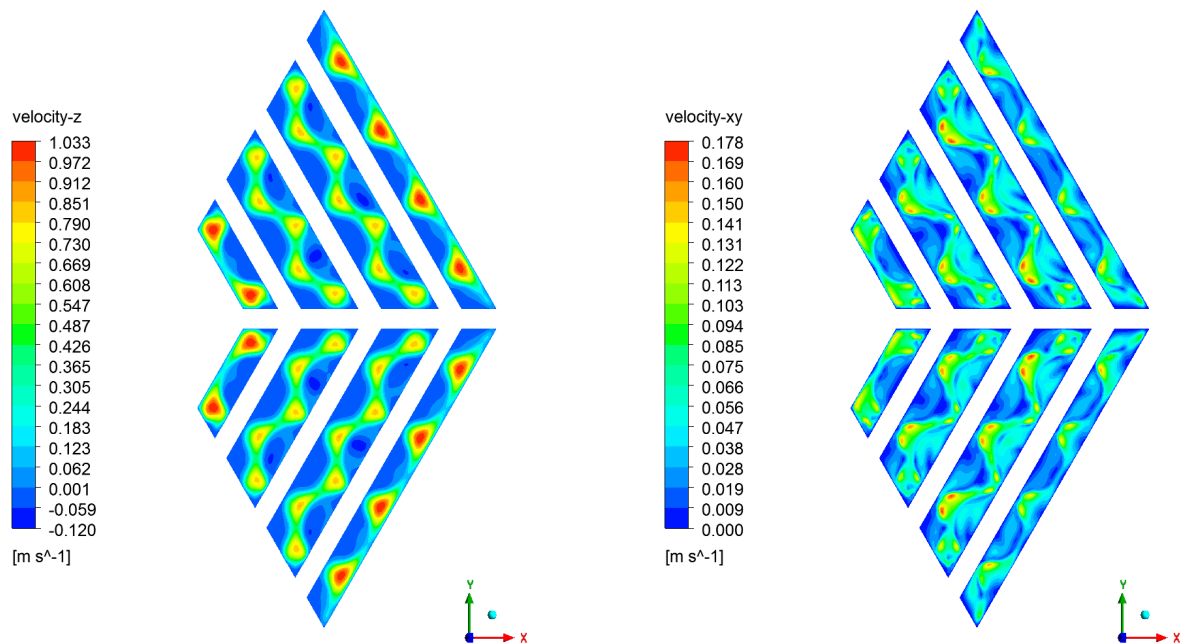
Figure 33: Velocity-z and velocity-xy distribution 1 mm above lower edge of support grid

The above effect of the outflow from the channels between the control rods is still clearly observable in the upper chamber above the support grid in the form of local maxima. With increasing distance from the support grid, however, this effect disappears, and the velocity profile gradually evolves into a standard shape with higher velocities in the center and lower velocities near the walls, as shown in Figure 34.
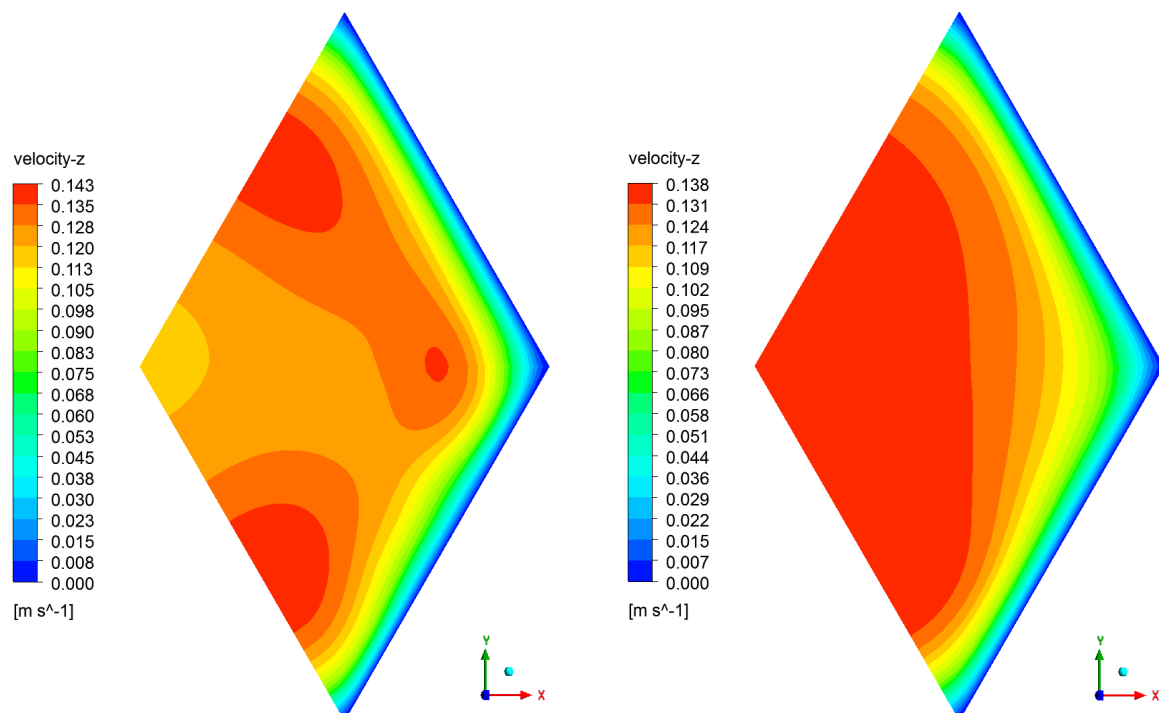
Figure 34: Velocity-z distribution 300 and 500 mm above upper edge of support grid

The graph in Figure 35 shows the variation of the total pressure (static + dynamic component) of helium over the height of the reflector/shielding assembly. This change is related to the value of the static pressure defined at the exit of the computational domain, therefore the value at the exit differs slightly from zero. The use of total pressure here is dictated by changes in the flow cross section and as a result the ratios of the two components (static and dynamic) change.

As was the case with the reflector/shielding assembly, the influence of the individual parts of the assembly and their pressure losses can be detected. The frictional loss in the inlet channel is very small. In contrast, as expected, the greatest loss is in the section between the shading blocks. Here, not only frictional losses in the narrow channels are evident, but also local losses due to dramatic changes in flow direction and velocity. The frictional loss in the area with the control rods is then less than 15 % of the total loss.
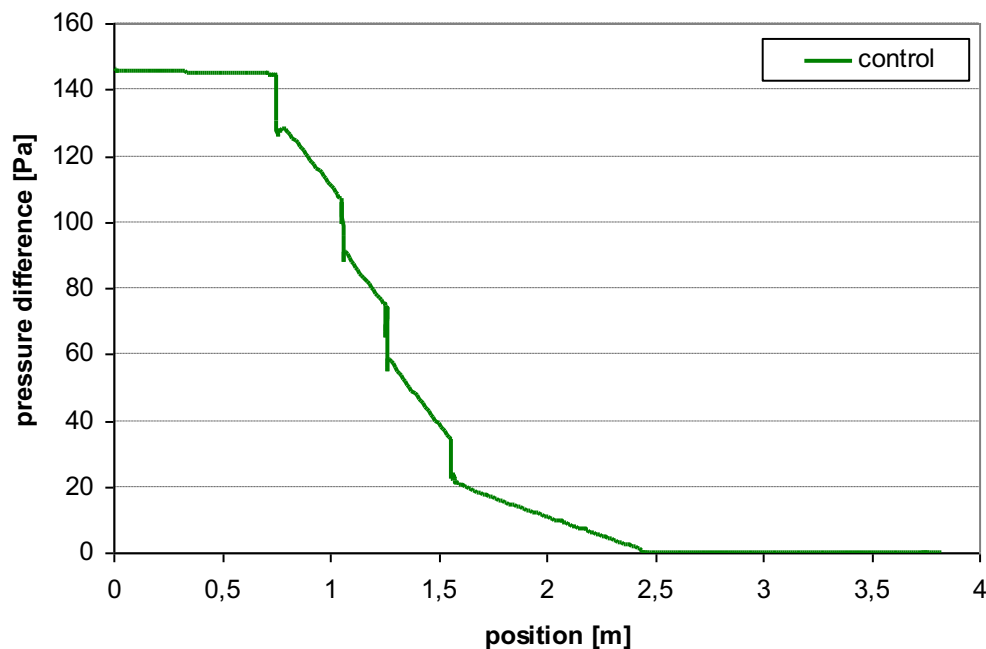
Figure 35: Total pressure profile along of reflector/shielding assembly

3.3 FUEL ASSEMBLY

This chapter describes the creation of detailed models and the calculation of the pressure losses in the fuel assemblies. The fuel assemblies consist of two different parts. One part consists of inlet and outlet shielding sections with helical channels, which are indicated by black rectangles in Figure 36. This section is used to capture neutrons leaving in the axial direction. The second section is the core region with the fuel rods, indicated by the red rectangle in Figure 36

Due to the considerable geometrical complexity of the whole fuel assembly, its simulation was divided into two separate problems. The first task was the simulation of the active part of the fuel assembly with fuel rods. From the point of view of the size of the computational mesh, this is a very challenging task that had to be solved in sections, as will be described below. The next task was the simulation of the distribution chamber

with the lower support grid. This is a geometrically complex section that was created separately. This subdivision will be followed throughout this chapter.
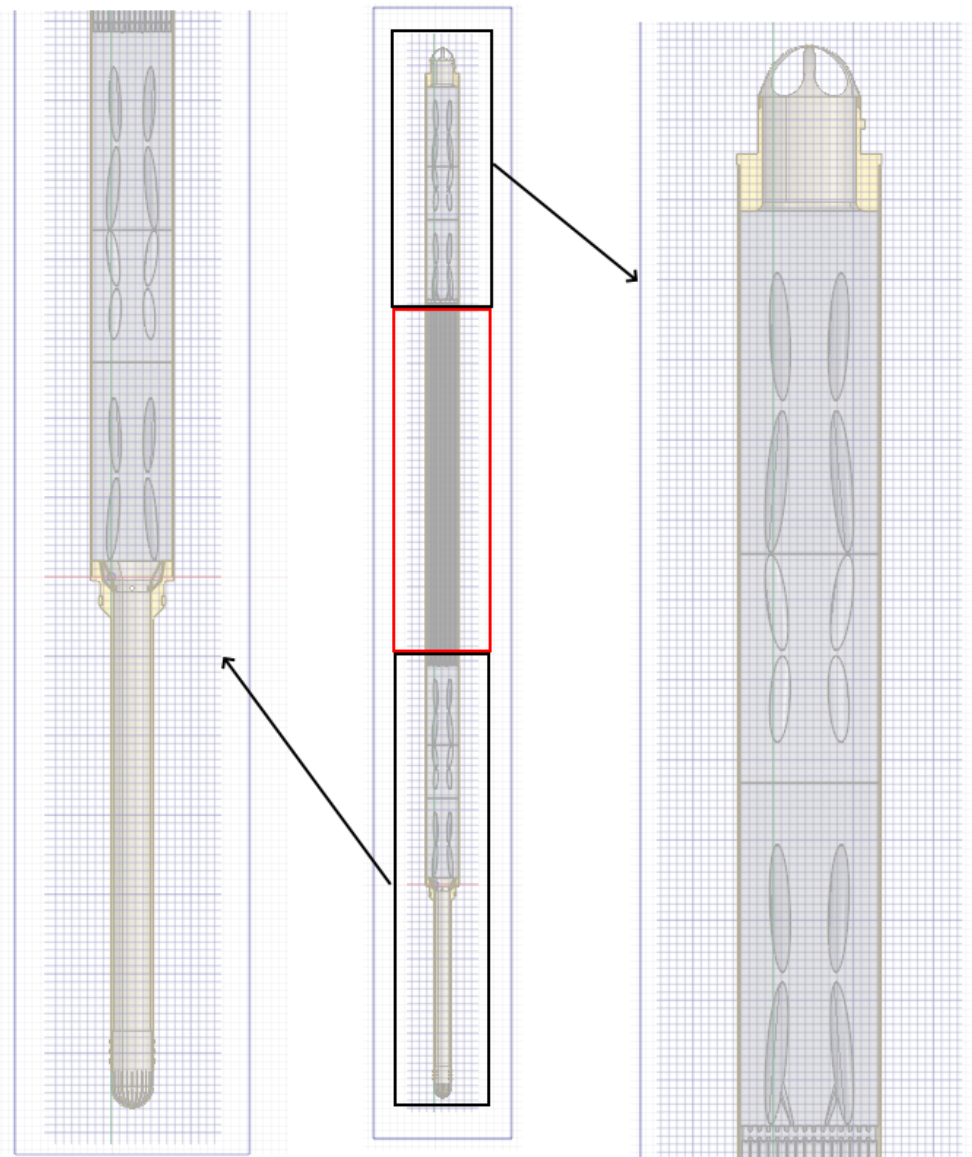
Figure 36: Geometric model of the fuel assembly

3.3.1 *SUPPORT GRID*

3.3.1.1 Geometry and Mesh

The fuel rods are fixed in the assembly by two spacer grids, see Figure 37. A simplified computational model was developed to determine the pressure losses of the spacer grids.

As shown in Figure 38, the geometry exhibits periodicity. For this reason, it was possible to proceed with the calculation of only one part of the diamond-shaped cross-section by selecting appropriate boundary conditions, thus reducing the computational effort. To achieve a steady flow, an additional length of 100 mm in front of the spacer and 200 mm behind the spacer was considered.
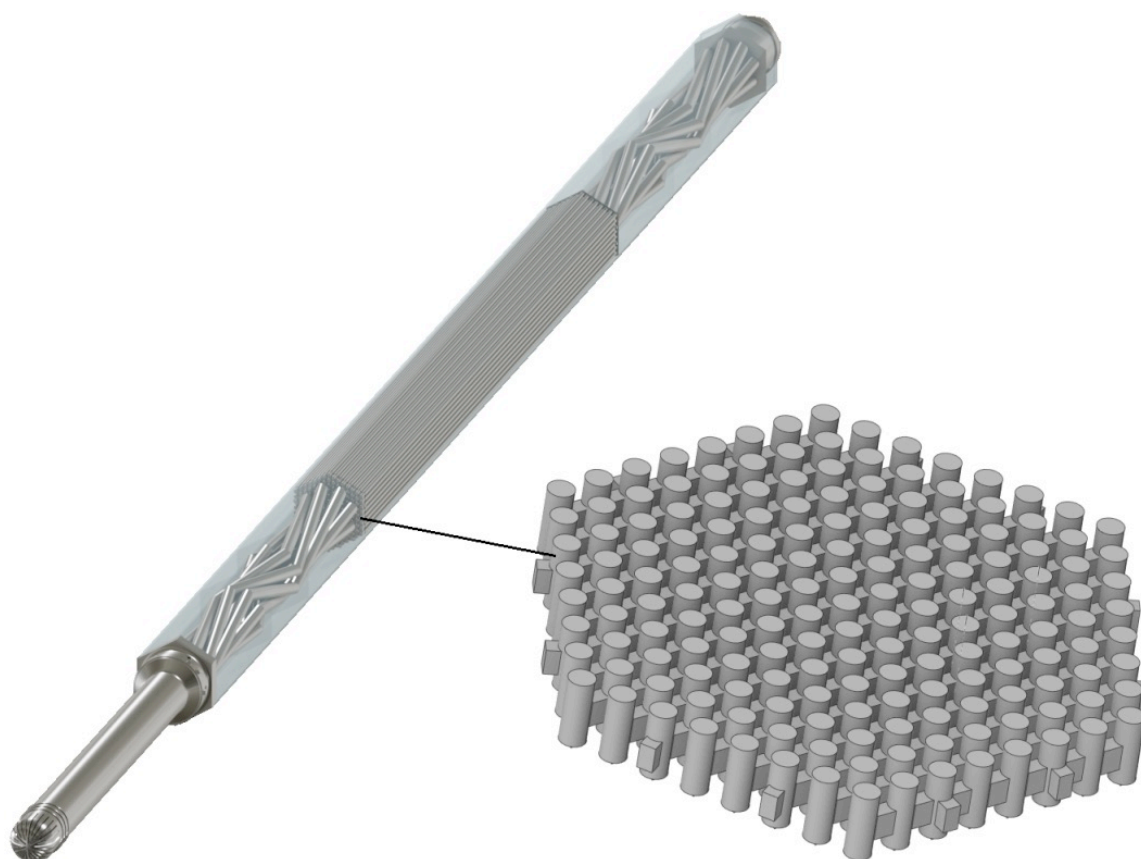
Figure 37: Design of support grid [3]
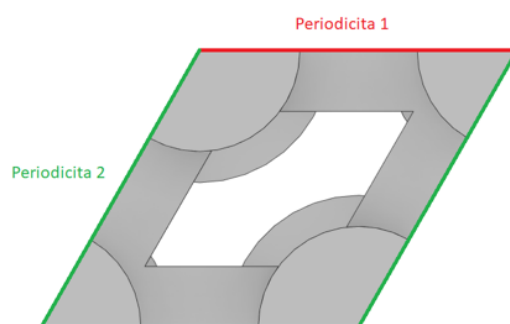
Figure 38: Detected periodicity

In terms of computational mesh design, the use of polyhedral cells was adopted with respect to geometry, see. Figure 39
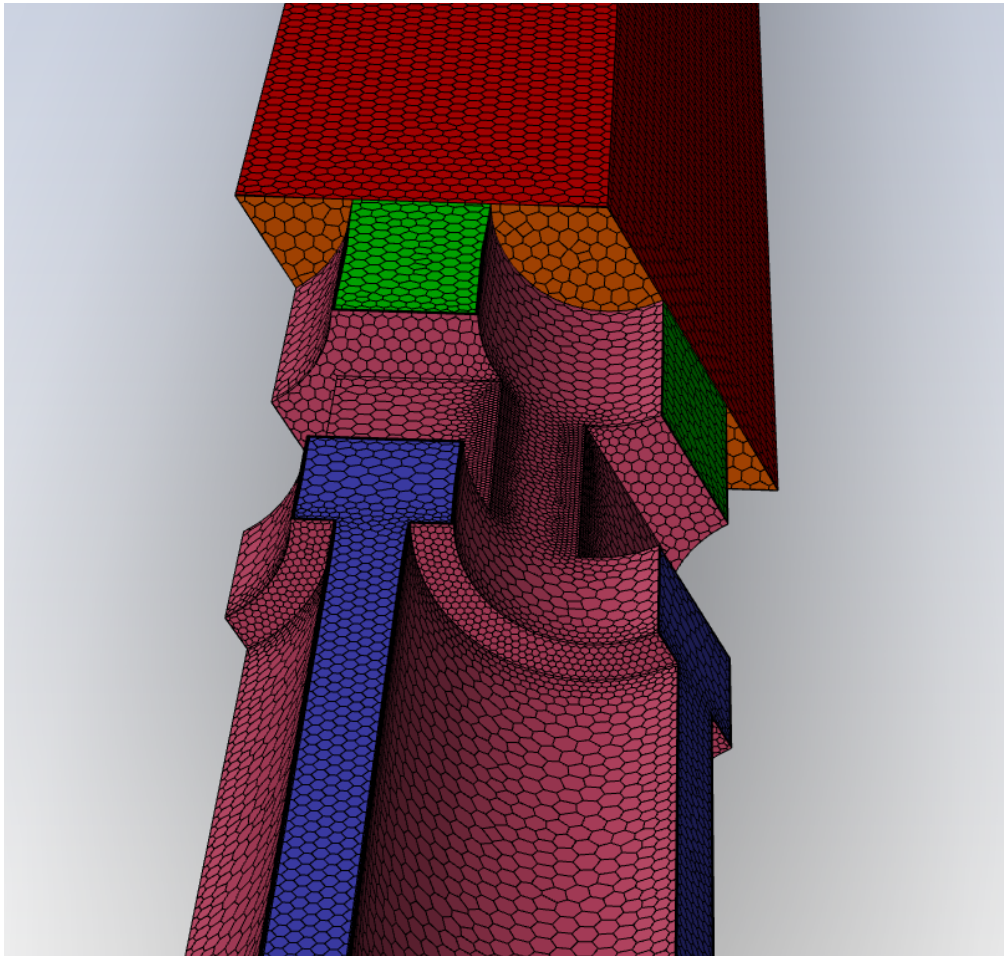
Figure 39: Detail of surface mesh

3.3.1.2 Computational mesh quality

The graph in Figure 40 shows the frequency distribution of cells as a function of the skewness parameter. The highest level of skewness is around 0.825. 208 cells exceed the observed value of 0.75, which is less than 0.05% of the total 440872 cells.

From the graph in Figure 41 the maximum values of the Aspect Ratio parameter are around 130, but these are single cells located in the boundary layer at the walls of the channels passing through the reflector.
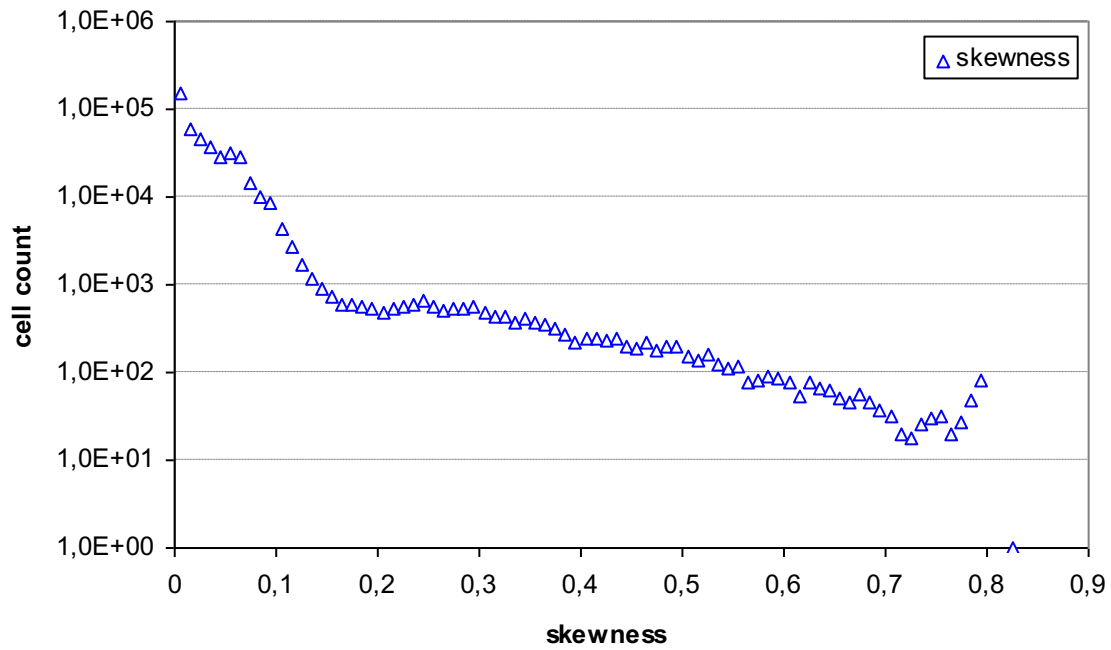
Figure 40 Skewness cells distribution in computational mesh
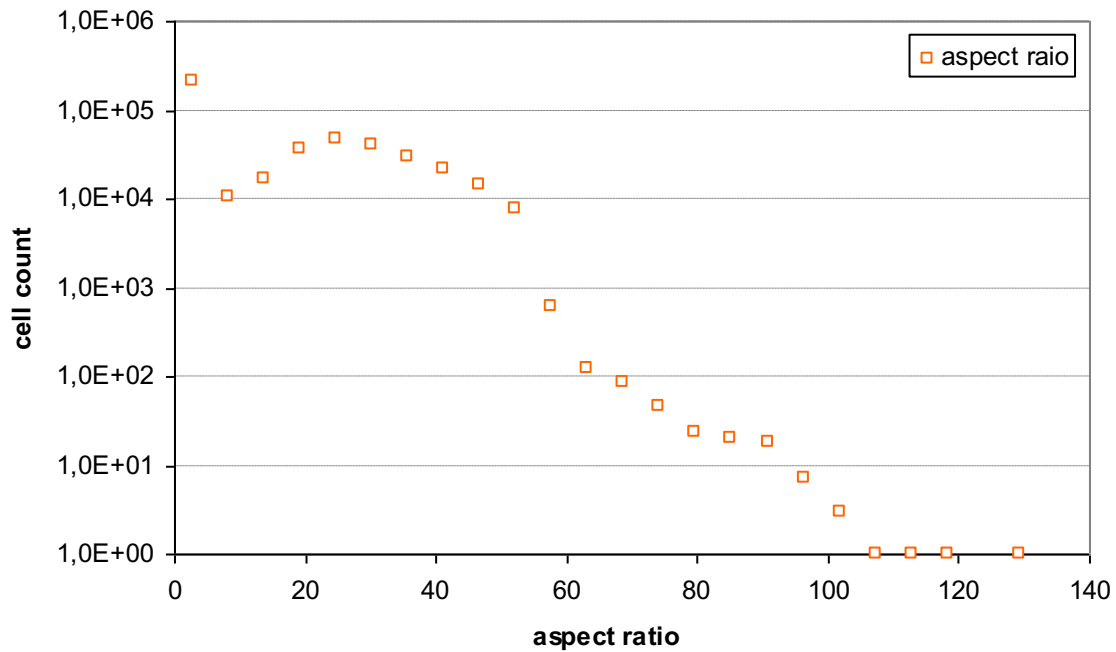
Figure 41 Aspect ratio cells distribution in computational mesh

3.3.1.3 Numerical model definitions

Solver settings
The basic settings of the model parameters are identical to other types of assemblies, see Table 1.

Settings of thermophysical properties of helium

The thermo-physical properties of the helium are identical to other types of assemblies, see Table 2.

3.3.1.4 Calculation

Boundary conditions

The settings of the main boundary conditions of the nominal operating condition are summarized in Table 5. The settings of the boundary conditions correspond to the real conditions in an assembly of this type at time t = 0 s. The mass flux is determined as the corresponding fraction of the known mass flux in the fuel assemblies. A symmetry condition was applied to the model boundaries. Although the solved geometry is periodic rather than symmetric, the inaccuracy caused is negligible.

Table 5 Setting of boundary conditions

Location	Condition	Note
Helium inlet	Velocity inlet	Velocity magnitude was set at 10.6 m/s The inlet velocity condition was chosen for better numerical stability. The velocity was determined based on mass flow, density, and inlet cross section.
Helium outlet	Pressure outlet	Static pressure was set at 7150000 Pa.
The outer walls of the model	Wall	Standard stationary wall.
Planes of periodicity	Symmetry	Even to the geometry is periodic rather than symmetric; the symmetry boundary condition was used. The inaccuracy caused is negligible.

Solution and results

The graphs in Figure 42 and Figure 43 provide information on the progress of the calculation in terms of stability and convergence capability. Both graphs show that a steady-state solution of the problem has been achieved. The graph in Figure 42 shows the profiles of the weighted residuals for the solved equations, i.e., the continuity equation, the equations for the individual velocity components and the equations for the quantities describing the turbulence. The conditions for a sufficient level of convergence of the solutions have been met. The convergence process is also confirmed by the plot in Figure 43, which shows the gradual steady state of the output velocity.
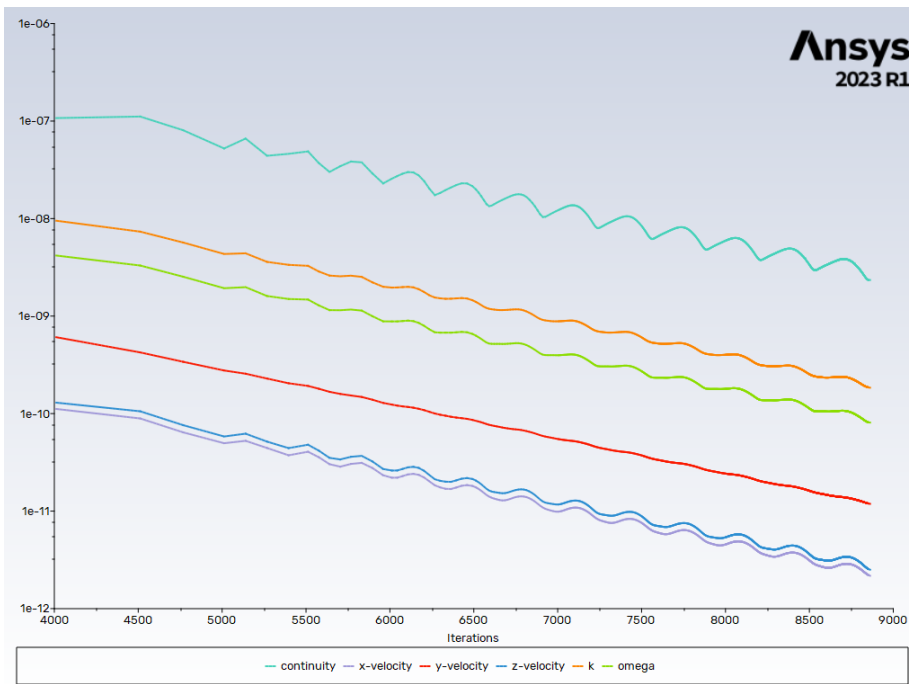
Figure 42: Scaled residuals
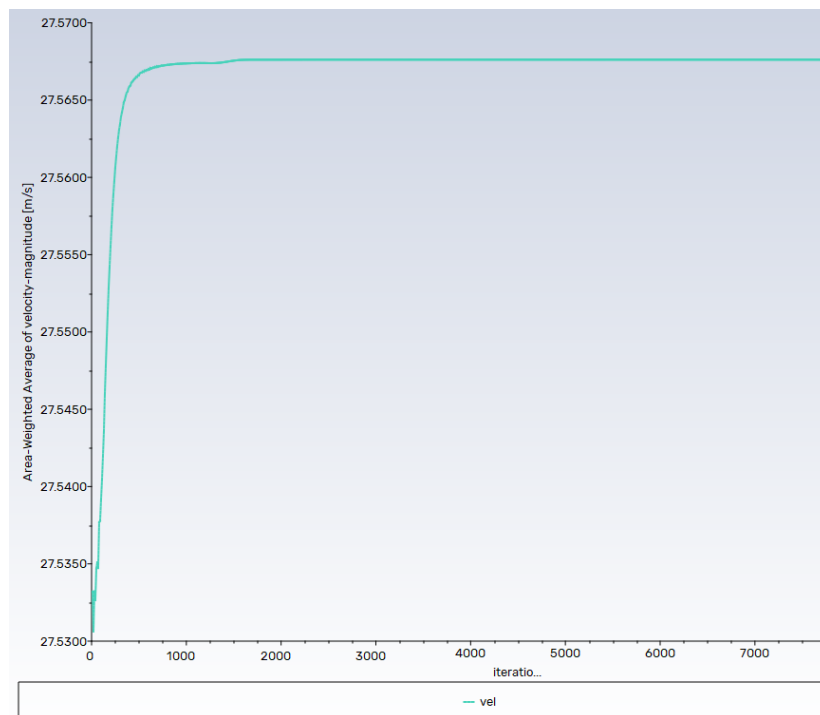
Figure 43: Time profile of average velocity magnitude in the outlet

One of the main objectives of the simulation shows the magnitude distribution in the grid space. From the velocity distribution in front of the grid the inlet was simulated at a sufficient distance and the flow here is no longer visibly affected by the set conditions. Furthermore, there is a noticeable grid effect that significantly affects the flow field distribution behind the grid. The longitudal course of the total pressure loss is shown in

Figure 45. The magnitude of the effect of the spacer grid on the pressure loss can be seen in the graph, which reaches approximately 4100 Pa.
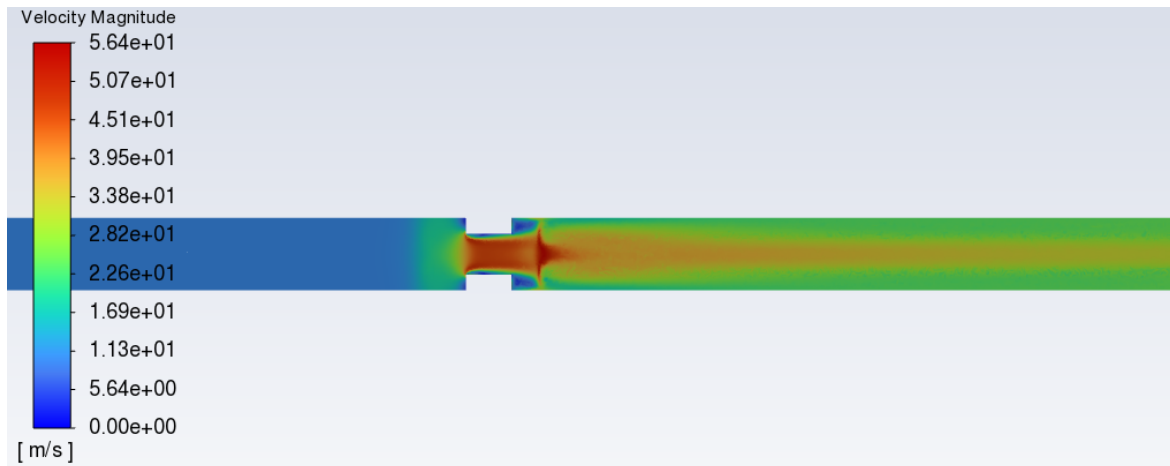
Figure 44: Velocity magnitude distribution in the grid passage
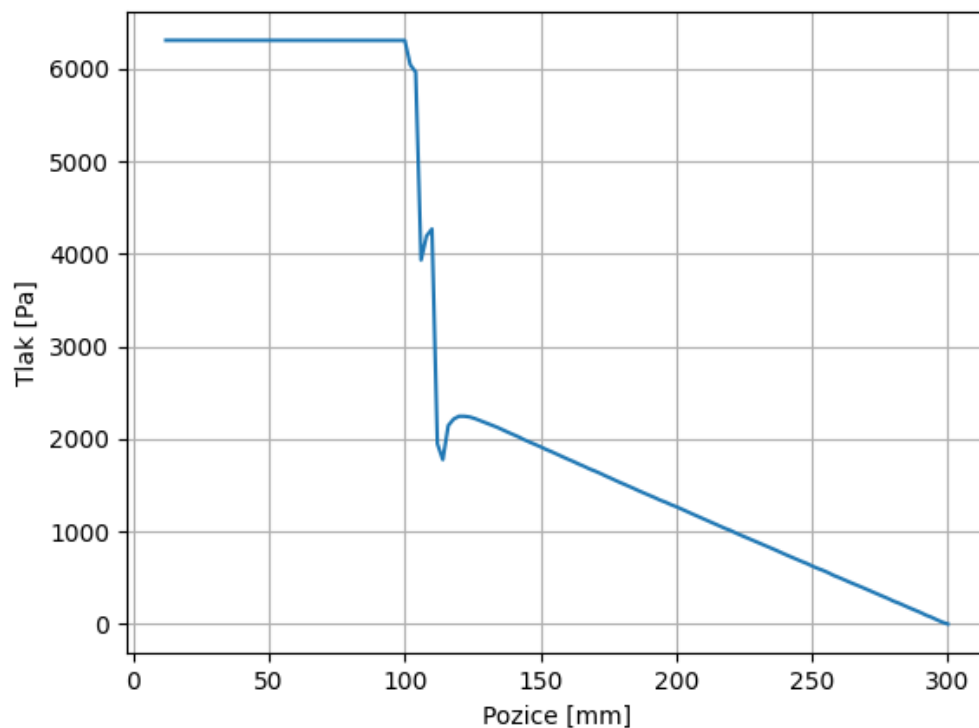
Figure 45: Total pressure profile along of support grid and its surroundings

3.3.2   REACTOR CORE

3.3.2.1 Geometry and Mesh

The core part of the assembly consists of a total of 168 rods, inside which the fission chain reaction will occur during operation and will therefore be the source of heat. The covering of the rods is wrapped with wire, see detail in Figure 46. The wire has two functions here.

Firstly, it provides stabilization of the fuel rods in space, preventing unwanted bending of the rods due to thermal expansion, and secondly it intensifies the heat transfer to the coolant.
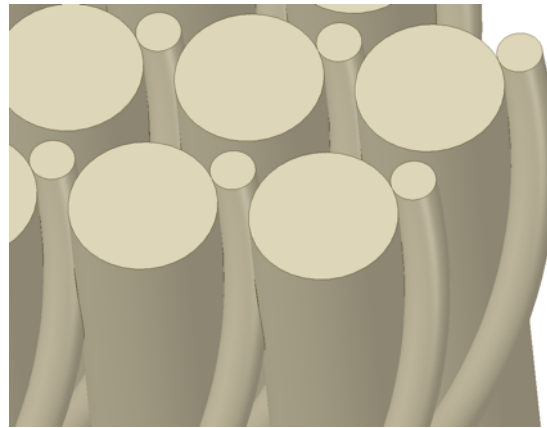
Figure 46: Detail of the fuel assembly with wire

For the CFD model, the geometry of the CAD model needed to be further simplified and modified - in particular, modelling the detailed wire geometry would have been very complicated. The spiral wires, see Figure 47 left, together with the fuel rods, create tangential contact in the geometry, which causes the generation of highly deformed cells when generating the computational mesh and increases the total number of cells significantly. The combination of these two facts led to a suitable modification of the geometry that does not cause a significant change in the behavior of the bypassed coolant. The circular cross section of the wires was therefore converted to a square cross section, thus solving the above problems. A final view of the modified fuel wire geometry can be seen in Figure 47 right.
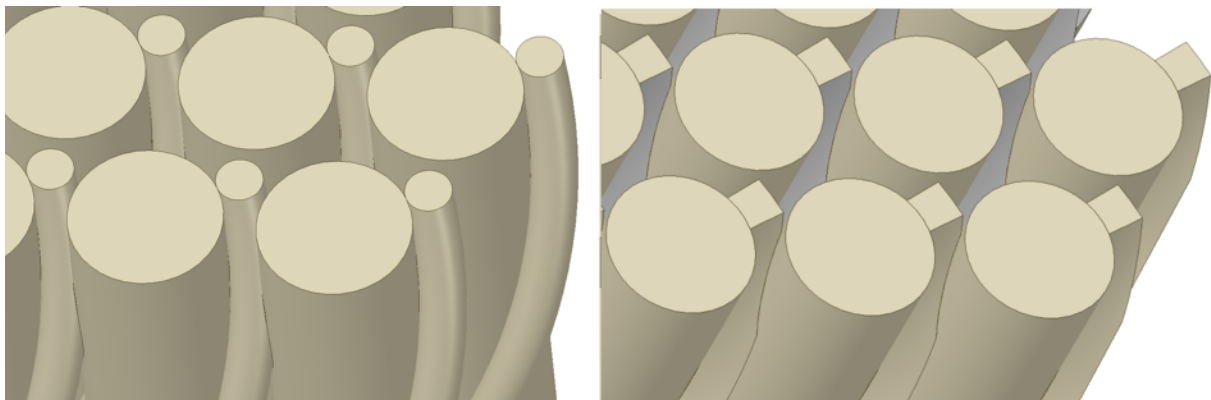
Figure 47: Detail of assembly wire area modifications - original geometry (L), modified geometry (P)

The square wire profile has a side size equal to the diameter of the original wire. The spacing of the fuel rods and other elements have been retained. The dimensions of the geometry after modifications can be seen in Figure 48.
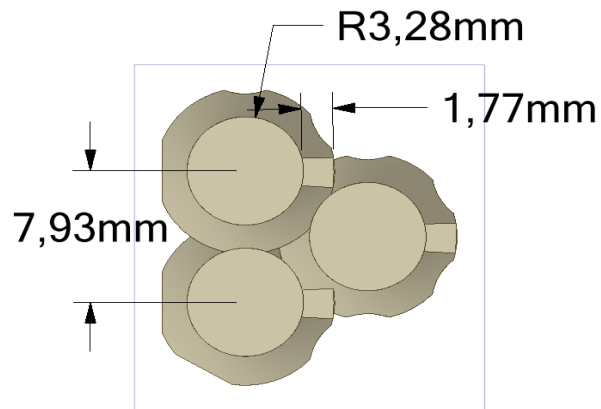
Figure 48: Geometry dimensions after modifications

Another simplification in the creation of the computational model was the division of the fuel area by height into 20 blocks. This division is based on the number of turns of the spiral wire - each block corresponds to one turn. The modelled region will therefore be solved with a periodic boundary condition, which means that the profile of the coolant flow at the outlet of the previous block is used as the input condition for the next block. One block is 64.88 mm high and is shown in Figure 49.
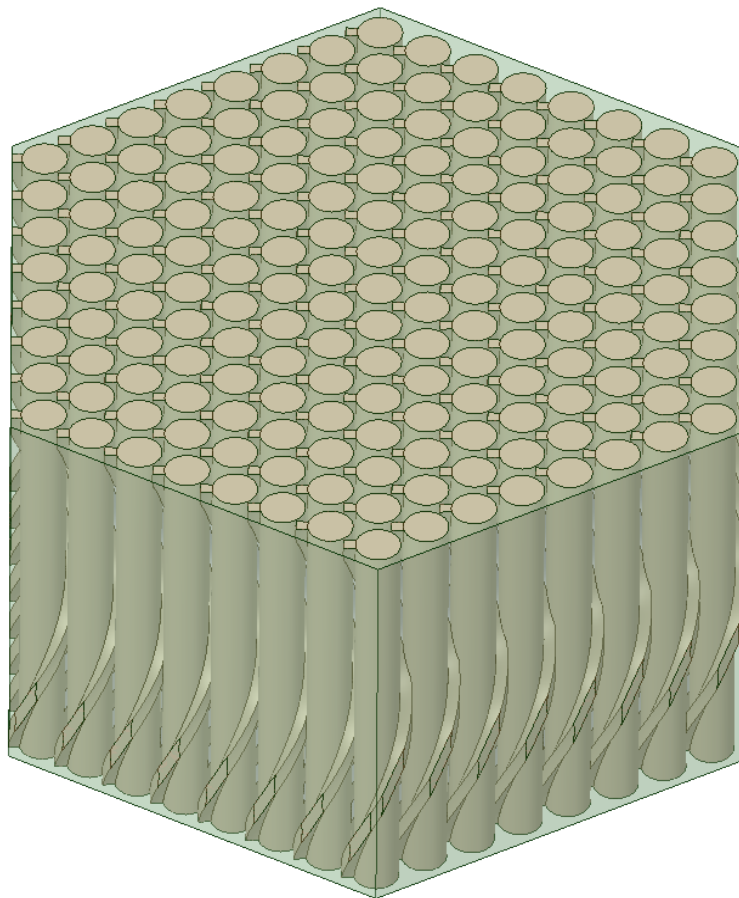
Figure 49: Computational model of one block

The computational mesh was created in Fluent Meshing 19. The standard procedure used in flow zones, i.e. the preparation and creation of the surface mesh, the creation of a prismatic boundary layer at the surface of the walls and the subsequent filling of the core volume space of the solved area with tetrahedral cells, which are then algorithmically converted into polyhedral cells, was used for the mesh creation. The solid parts were modelled without boundary layers, respecting the surface network generated for the flow-through part (to preserve the conformal mesh).

A view of the surface mesh is shown in Figure 50. The size of the surface cells was formed in the range of 0.2 - 2 mm with a maximum skewness of 0.56. On the surface mesh, a constraint on the *Aspect Ratio* parameter was subsequently defined for the boundary layer with a value of 10. The volumetric computational mesh of one block includes 7.56 million cells of the flow portion and 4.78 million cells of the solid portion, i.e., the model includes a total of 12.34 million volume cells.
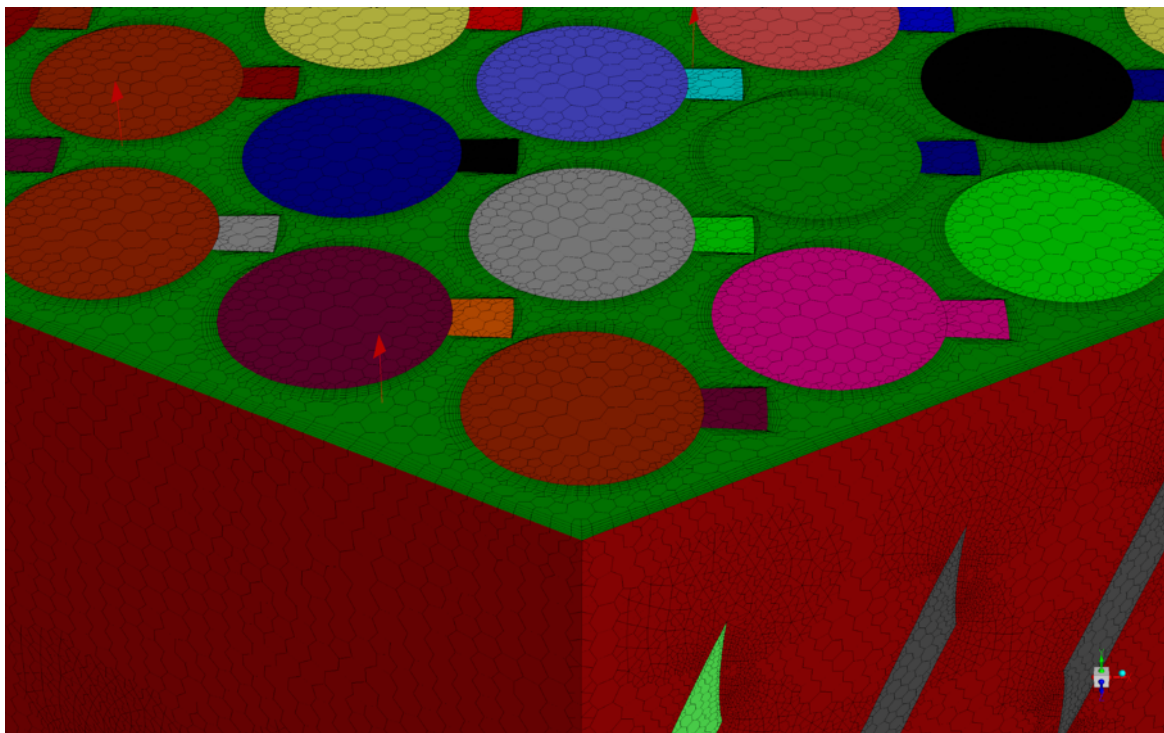
Figure 50: Detail of the surface mesh of one block

3.3.2.2 Computational mesh quality

The graph in Figure 51 shows the distribution of cell skewness in the computational mesh for both the solid and flow-through portions. The maximum skewness values are 0.77 for the computational mesh in the solid part and 0.94 for the mesh in the flow-through part. Due to the complexity of the geometry, it was not possible to keep the maximum level of skewness below 0.9 as generally recommended. However, the number of cells exceeding this limit is negligible and includes only 27 cells. The more significant increase in frequency, which is clearly observable in the graph, occurs below this threshold.

For the Aspect Ratio parameter, whose distribution of cells in the computational mesh can be seen in the graph in Figure 52, there is a significant difference between the maximum value for the solid and flow-through portions. The maximum value is around 5. In contrast, the maximum value for the fluid is close to 350. The number of cells where the Aspect Ratio parameter exceeds 100 is around 2000. These are strongly flattened cells located near the surface of the walls. In such locations, as mentioned earlier, even such high values do not primarily cause complications with the convergence of the calculation and/or deterioration in the quality of the results obtained.
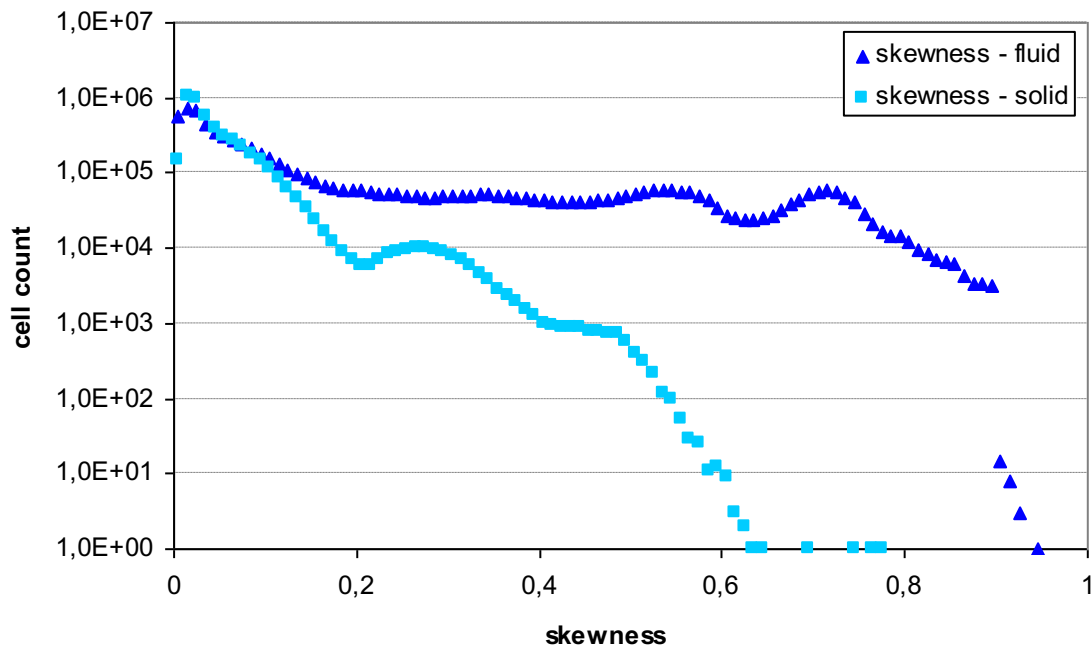
Figure 51 Skewness cells distribution in computational mesh
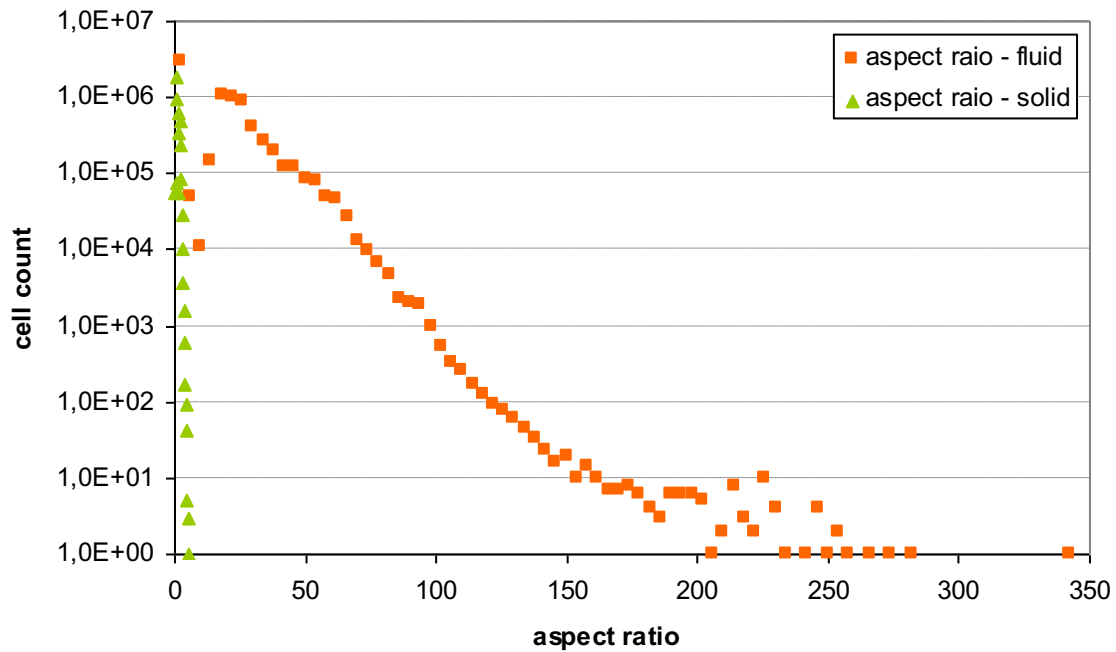
Figure 52 Aspect ratio cells distribution in computational mesh (fluid zones)

3.3.2.3 Numerical model definitions

Solver settings

The settings of the basic parameters of the numerical models used are summarized in Table 6. The choice of individual parameters is based on recommended values or on experience gained from previously solved and similar problems. In addition to the physical parameters, it was also necessary to consider the scope of the problem to be solved when setting up the numerical model.

Table 6: Setting of the basic numerical parameters of the calculation

Parameter	Setting	Note
Time dependence	Steady state	Due to the size of the network of one block and the number of solved blocks it was not realistic to calculate the problem as fully transient, but even in the case of steady state the solution achieved relatively good convergence.
Solver	Pressure-based	The flow is simulated as incompressible, and the thermo-physical properties are only temperature dependent.
Pressure-velocity coupling	SIMPLEC	
Discretization schemes	Gradient – least squares cell based	First-order discretization schemes are usually not precise enough and can only be used to start the calculation and give indicative results.
	Pressure – Second Order	
	Ostatní – Second Order Upwind	
Turbulence model	*k-ω* SST	Due to its robustness, the k-ω model with shear stress transport better handles the simulation of near-wall flow.

44

Settings of thermophysical properties of helium

The thermo-physical properties of the helium are identical to other types of assemblies, see Table 2.

3.3.2.4 Calculation

Boundary conditions

Except for the first block, the velocity, temperature, and pressure profiles from the previous block are used at the input of each region. Constant boundary conditions are considered at the inlet of the first block, which are a mass flux of 0.647 kg/s and a temperature of 260 °C. The setting of the boundary conditions is summarized in v Table 7.

Table 7 Setting of boundary conditions

Location	Condition	Note
Helium inlet	Mass flow	Mass flow set at 0.647 kg/s.
	Temperature	Absolute temperature was set at 260 °C.
Helium outlet	Outflow	
The inner walls of the model	Wall	Standard stationary wall.
The outer walls of the model	Wall	Standard stationary wall.
Plane of periodicity	Periodicity	

Solution and results

The problem was solved as a steady-state problem. The convergence criteria were met for each block. The progression of the weighted residuals when solving the first block can be seen in Figure 53.
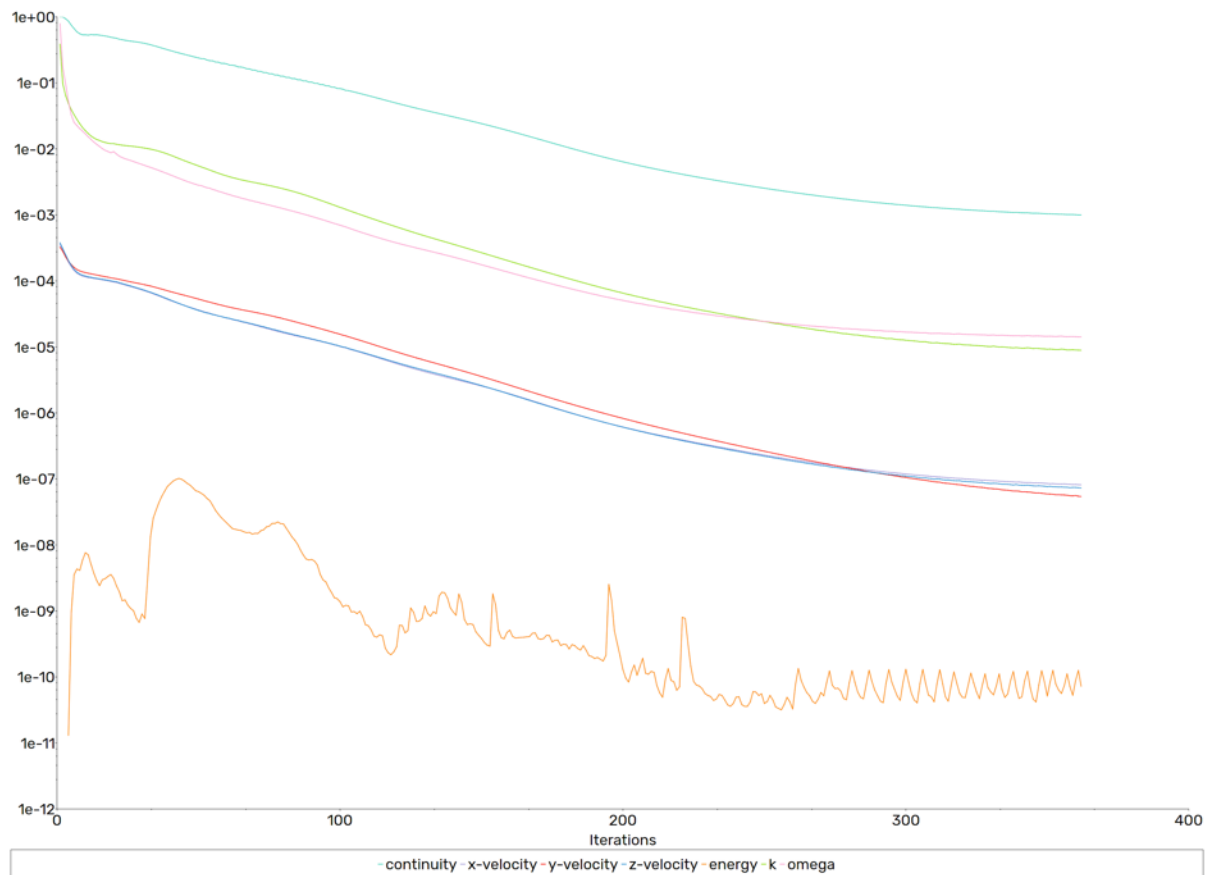
Figure 53: Scaled residuals

One of the main objectives of this simulation was to determine the pressure loss of the entire fuel assembly. Figure 54 shows the pressure loss in the axial direction in the studied area. The total pressure drop corresponds to the sum of the pressure losses of the individual blocks and is approximately 45 kPa.

The velocity field distribution at the end of the first simulated section is also shown. From Figure 55, it is clear, that the effect of wrapping the fuel rods with spirally twisted wire is very pronounced. There are 2 effects observed. The first is a partial radial relocation of the coolant stream to areas with lower pressure drop (along the walls of the assembly) caused by the inertia of the rotating stream. The second effect is the different symmetry of the coiled wires and the hexahedral shape of the assembly, which causes an asymmetric distribution of the velocity profile along the walls of the assembly. Moreover, this distribution gradually rotates along the height.
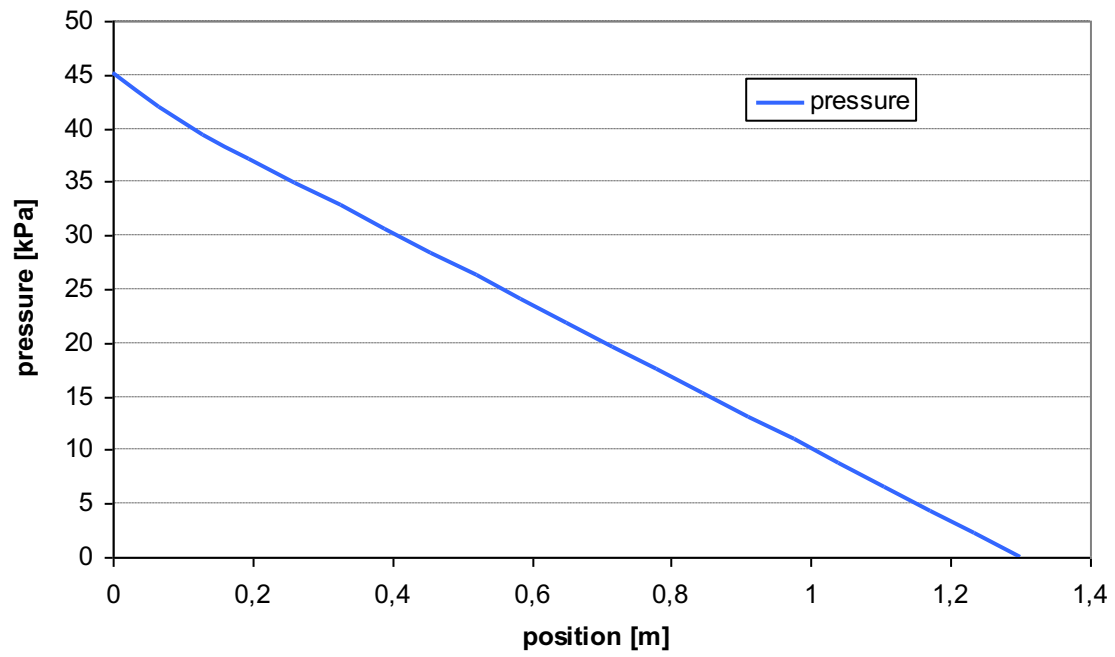
Figure 54: Pressure profile along active part of fuel assembly
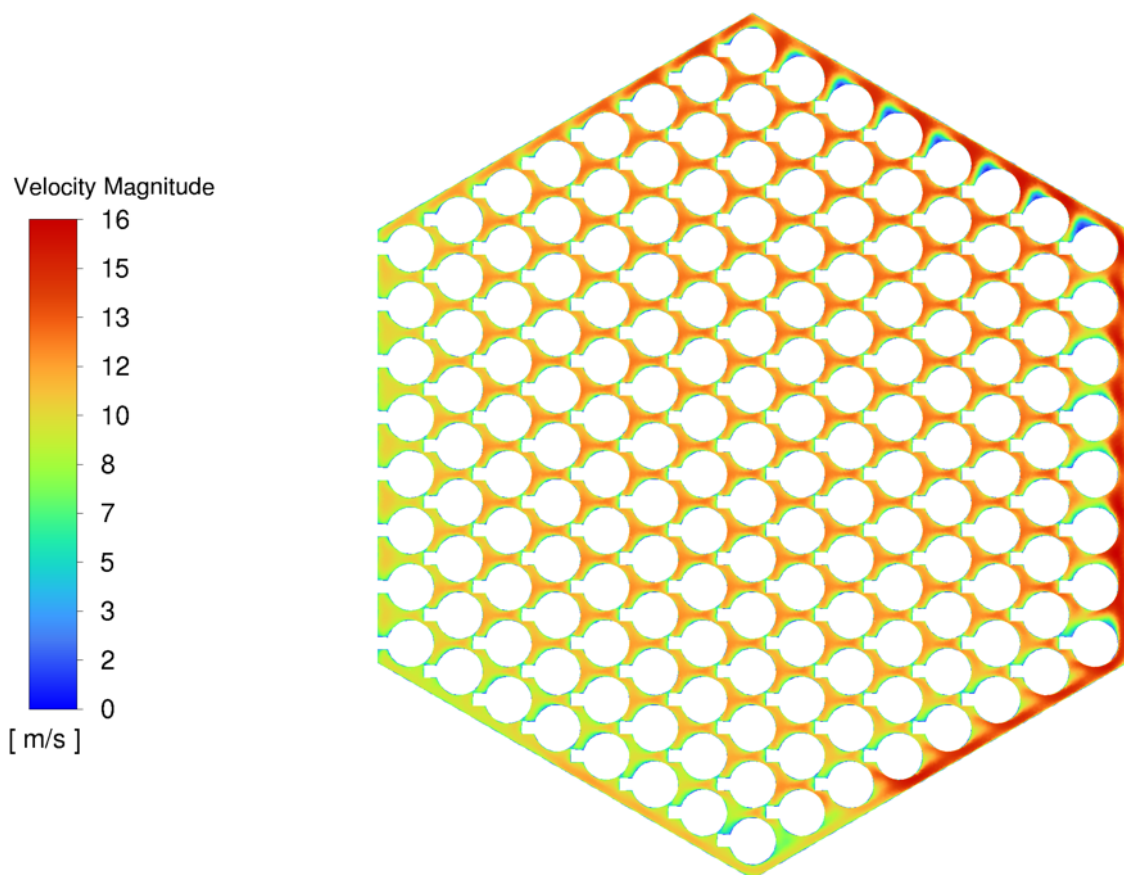
Figure 55: Velocity field at the 1st block outlet

4 LOFA SCENARIO

The scenario was created in advanced process simulation software Apros, which is widely used as a tool for modelling and dynamic simulation of nuclear power plants. The scenario model developed in Apros has been complemented with the results obtained on the CFD model of the PIROUETE system (PIv ROd bUndlE Test faciliTy at bmE). This is a successful implementation of two new heat transfer coefficients correlations that have significantly improved the agreement between the different approaches (Apros vs ANSYS Fluent). A detailed description and compilation of the results of the CFD model of the PIROUETE system are given in the Appendix.

4.1 GEOMETRY AND MESH

Figure 56 shows the simulated domain, which consists of the reactor core, a simplified model of the lower mixing chamber (lower plenum) and a simplified model of the upper mixing chamber (upper plenum). The reactor core, see Figure 2, exhibits a periodicity with an angle of 120°. This symmetry has been exploited to save computational capacity requirements.
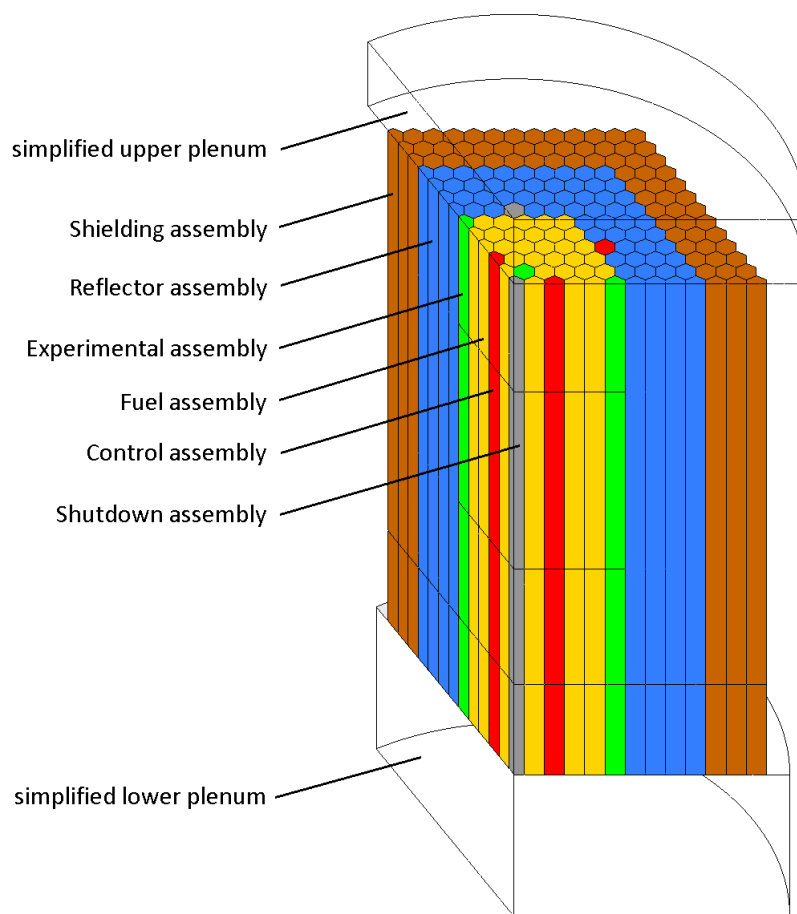
Figure 56: Simulated domain

The shape and dimensions of the simulated lower mixing chamber are based on the source input data defined by the Aros system code calculations [6]. The simplified upper mixing chamber is simulated for numerical reasons so that a single continuous output condition can be defined.

The geometry of the assembly is also simplified. The assemblies are replaced by volumes in the shape of hexagonal prisms, which are divided in height into a lower part, located in the carrier plate, and an upper part, located in the reactor core. The fuel assemblies are further divided in height into a lower shield, an active fuel section and an upper shielding. For ease of computational mesh design, this division is partially reflected in the other types of assemblies that are surrounded by the fuel assemblies. The so-called subkey dimension corresponds to the spacing of the fuel assemblies in the zone. The gap between the assemblies cannot be simulated with a given simplification of the geometry.

Porous bodies are defined in the assembly replacement volumes, which allow the desired hydraulic resistance of each assembly type to be set. The pressure losses for each type of assemblies were determined by detailed CFD calculations, see previous sections. The reactor operating modes, on the other hand, define the flow rate through the fuel assemblies that provides the required removal of the generated heat. It is assumed that these resulting differences between the flow characteristics of the different assembly types will be resolved by appropriate shielding of the assemblies. Therefore, for the scenario considered, the pressure losses are defined based on the helium mass flow distribution requirements between the fuel assemblies and the other assemblies (collectively referred to as bypass) using the outputs from the Apros [6].

Figure 57 shows the layout of the surface computational mesh at the interface of the lower mixing chamber and the core. In all types of assemblies, a mesh based on hexahedral cells in the shape of a general tetrahedral prism was used. In fuel assemblies where significantly higher flow velocities are expected, the mesh density was partially increased and a smaller cell thickness was used in the boundary layer at the walls of the assemblies.

Figure 58 shows the layout of the computational mesh in the transition area between the lower mixing chamber and the bottom of the assemblies. The figure shows a partial increase in the density of the mesh at the interface between the lower and upper parts of the assemblies. This densification allows to solve a wider range of problems that may be sensitive to the input conditions, especially in cases of non-uniform flow distribution, higher flow rates or backflow.
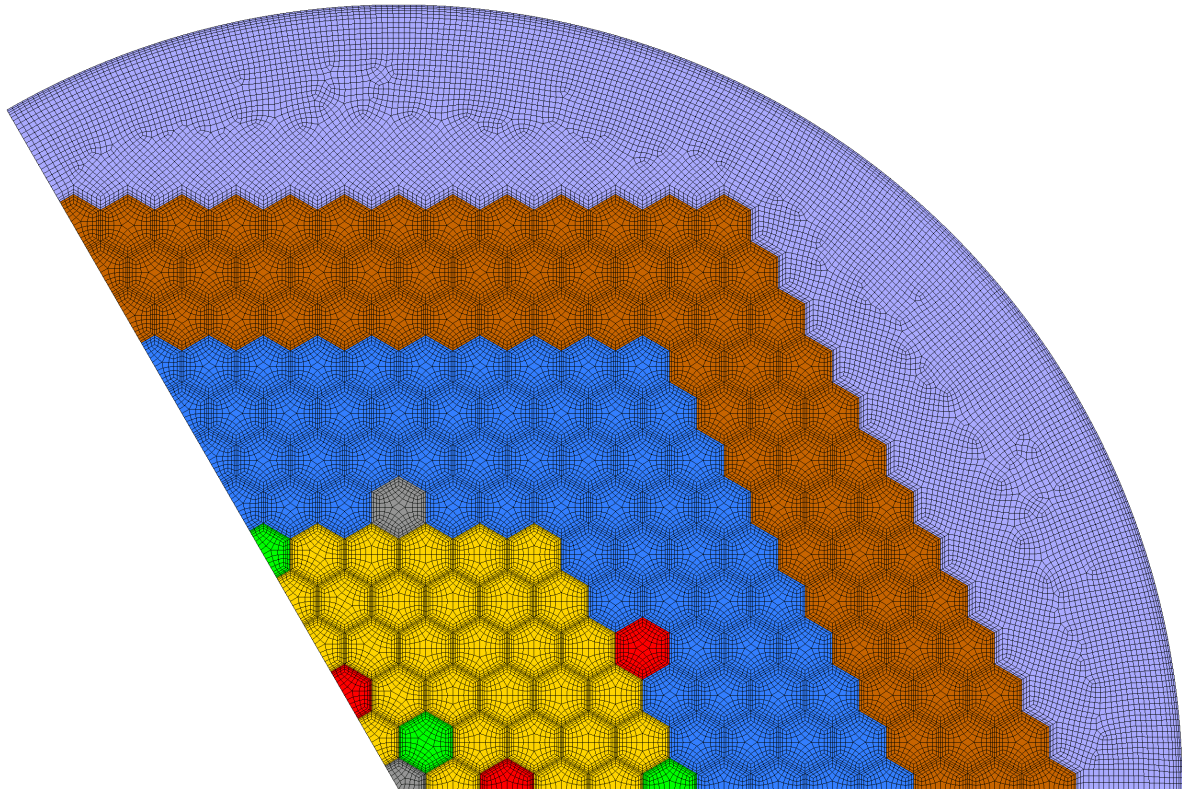
Figure 57: Surface mesh at the core cross-section plane
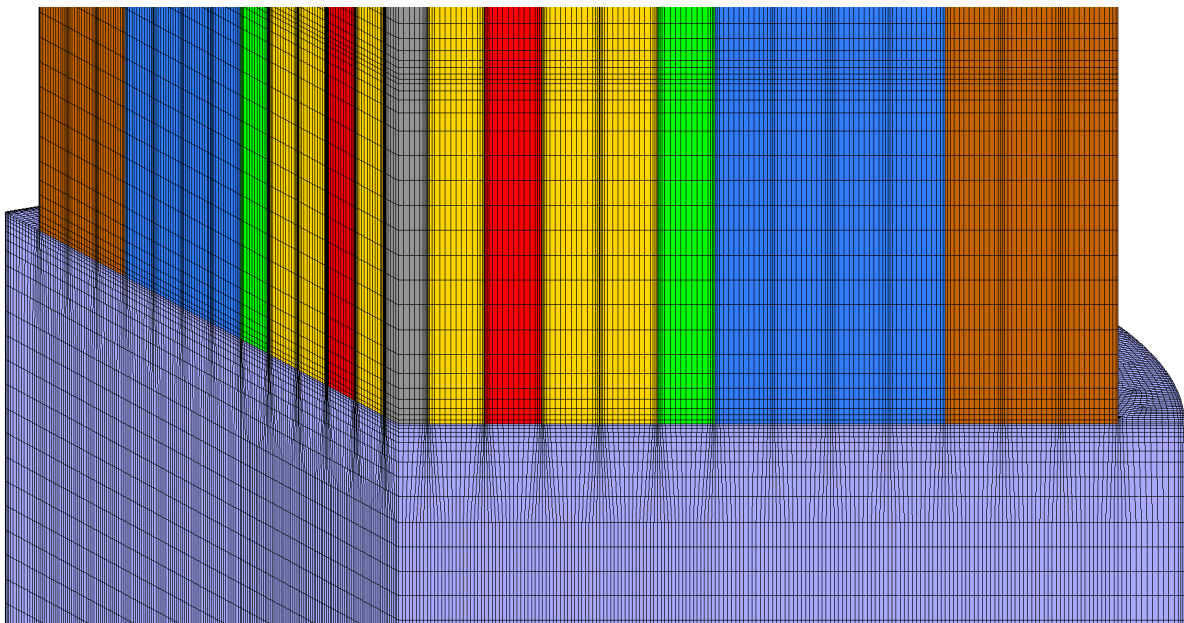
Figure 58: Surface mesh in the area of lower plenum and lower part of assemblies

4.2 COMPUTATIONAL MESH QUALITY

The graph in Figure 59 shows the frequency distribution of cells as a function of the cell skewness parameter. The highest level of skewness reaches a value of approximately 0.57. Moreover, even skewness exceeding 0.5 has only 340 cells out of a total of 4.17 million.
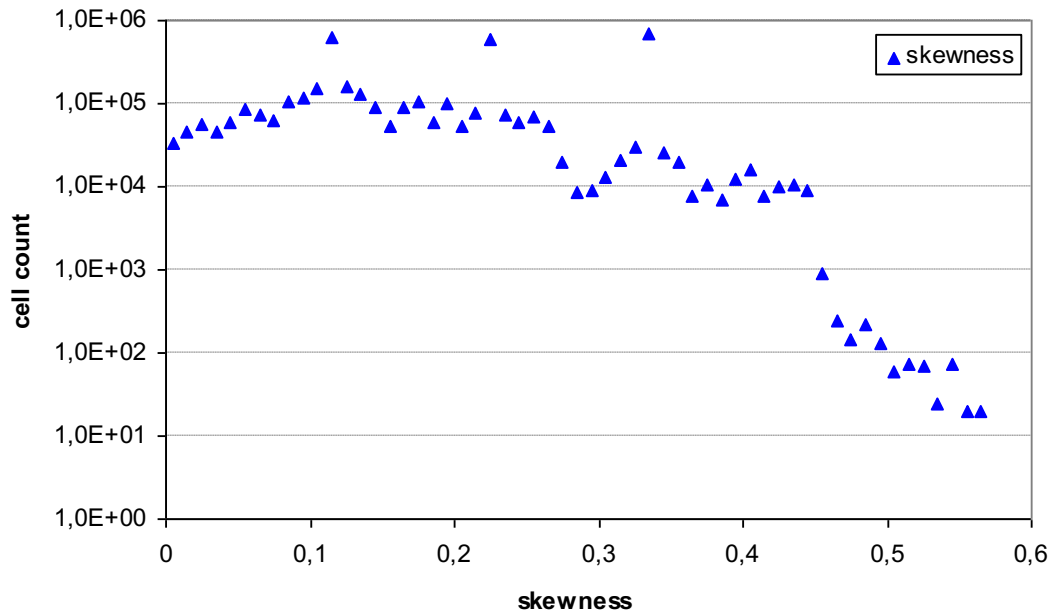
Figure 59: Skewness cells distribution in computational mesh

The graph in Figure 60 shows the frequency distribution of cells in terms of the Aspect Ratio parameter. It is clear from the graph that the maximum Aspect Ratio values are slightly above 30. These are the cells located in the boundary layer near the walls of the assemblie. This has succeeded in significantly reducing both the total number of cells and the demands on computational capacity and time.
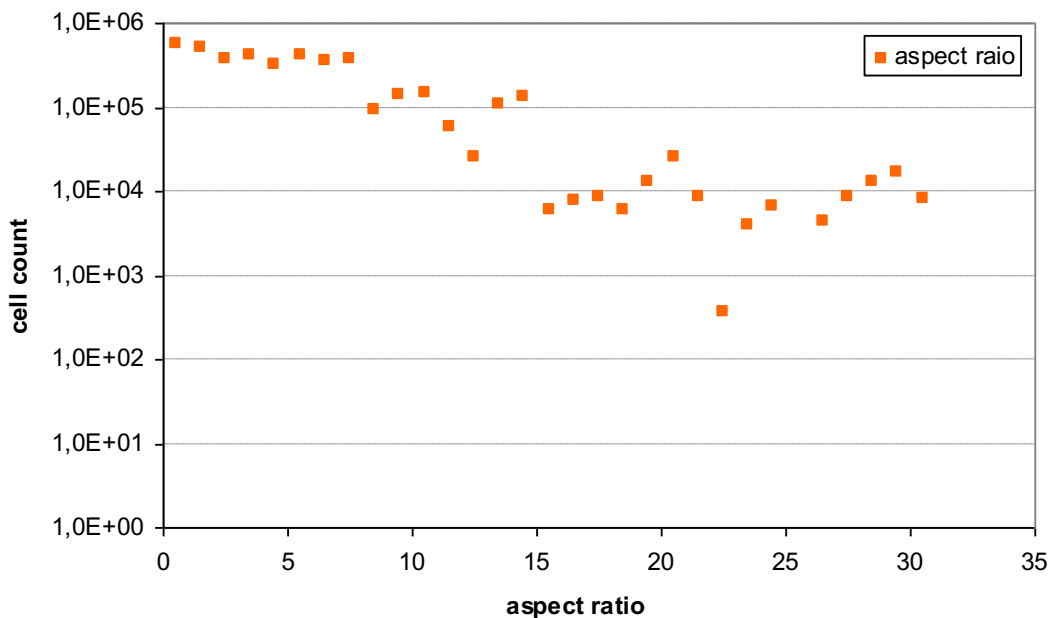
Figure 60: Aspect ratio cells distribution in computational mesh

4.3 NUMERICAL MODEL DEFINITIONS

4.3.1 SOLVER SETTINGS

Table 8 summarizes the settings of the basic parameters of the numerical model used.

Table 8 Setting of the basic numerical parameters of the calculation

Parameter	Setting	Note
Time dependence	Stationary simulation, transient simulation	The boundary conditions are time dependent, and the problem is therefore solved as a transient simulation. The steady state solution was used only in the context of calculating the state at the beginning of the simulated scenario.
Solver	Pressure-based	The flow is simulated as incompressible and the thermal-physical properties are dependent only on temperature.
Pressure-velocity coupling	SIMPLE, PISO	The scheme used depends on whether the steady state or transient process was simulated and also on the behavior of the calculation.
Discretization schemes	Gradient – least squares cell based	
	Pressure –second order or body force weighted	
	Others – second order upwind	
Turbulence model	k-ω BSL (low Reynolds)	The k-ω BSL model has a good ability to approximate a steady-state solution, which can then be used as an initial state for a defined scenario.

4.3.2 SETTINGS OF THERMOPHYSICAL PROPERTIES OF HELIUM

A method referred to as piecewise linear was used to define the properties of the materials as a function of temperature. In this method, material properties are calculated by linear interpolation between two adjacent defined values. The graphs in Figure 61 and Figure 62 show the temperature dependence of each helium property as defined in the calculation.
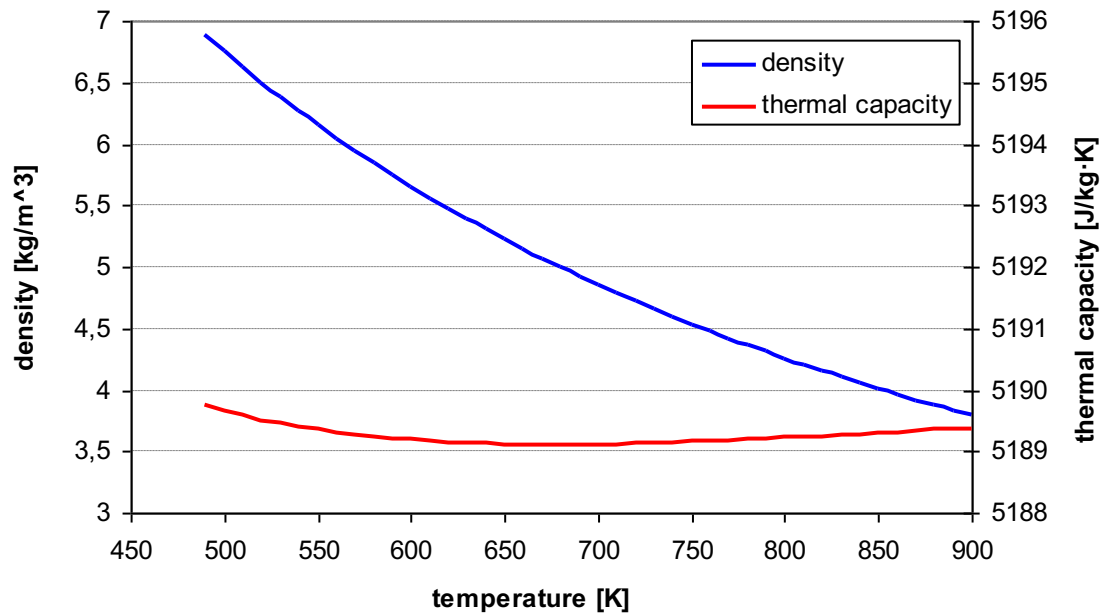
Figure 61: Helium density and thermal capacity
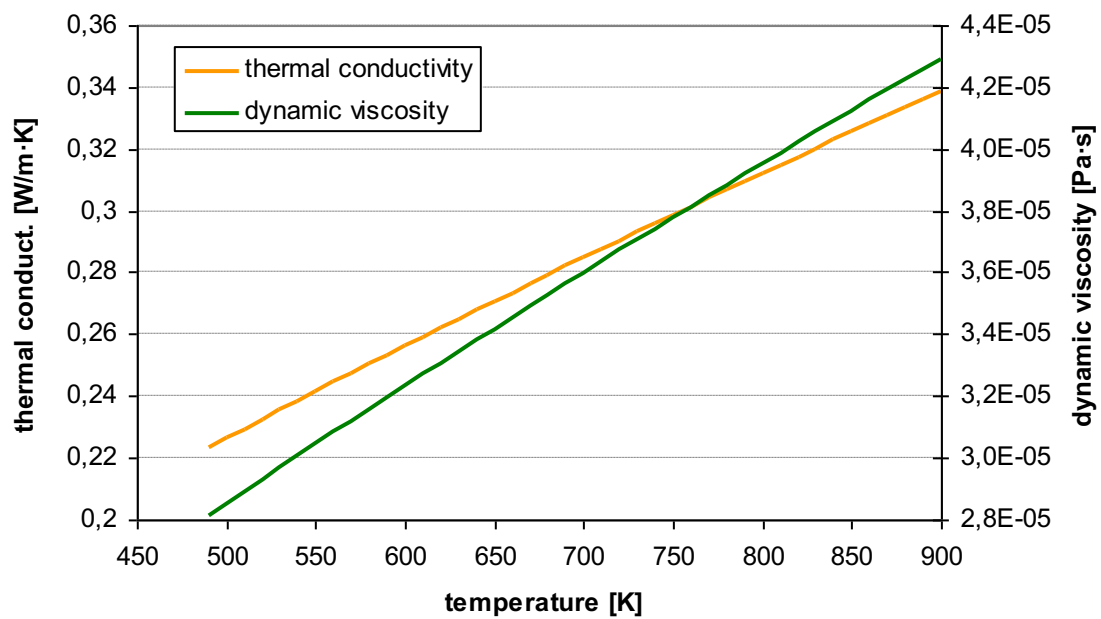
Figure 62: Helium thermal conductivity and dynamic viscosity

4.4   CALCULATION

4.4.1   BOUNDARY CONDITIONS

Table 4 summarizes the settings of the main boundary conditions for the simulation of the nominal operating condition and the subsequent transient scenario.

Table 9 Setting of boundary conditions

Location	Condition	Note
Helium inlet	Mass-flow inlet	Mass-flow and temperature was defined via profiles, see Figure 63
Helium outlet	Pressure outlet	Static pressure was set at 0 Pa
Walls of the assemblies	Wall	Standard adiabatic stationary wall (defined with thickness 0 m – thin wall)
The outer walls of the model	Wall	Standard adiabatic stationary wall
Plane of symmetry	Symmetry	
Fuel assemblies	Volumetric heat source	Time dependence was defined via profile, see Figure 64 Spatial distribution, see Figure 65 and Figure 66, was defined via Fluent expressions

The following graphs on Figure 63, Figure 64, Figure 65 and Figure 66 show the setting of the boundary conditions mentioned in the table above, i.e. time profile for helium inlet temperature and mass-flow, time profile for thermal power of core, axial distribution of core power and radial distribution of core power.
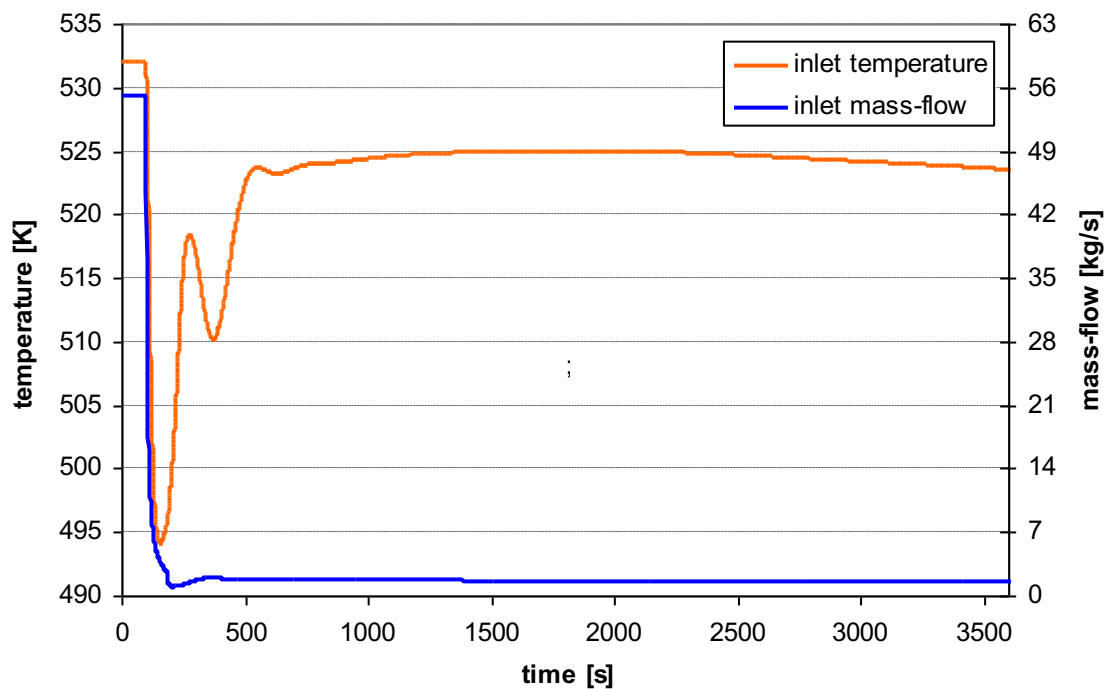
Figure 63: Time profile of inlet temperature and mass-flow [6]
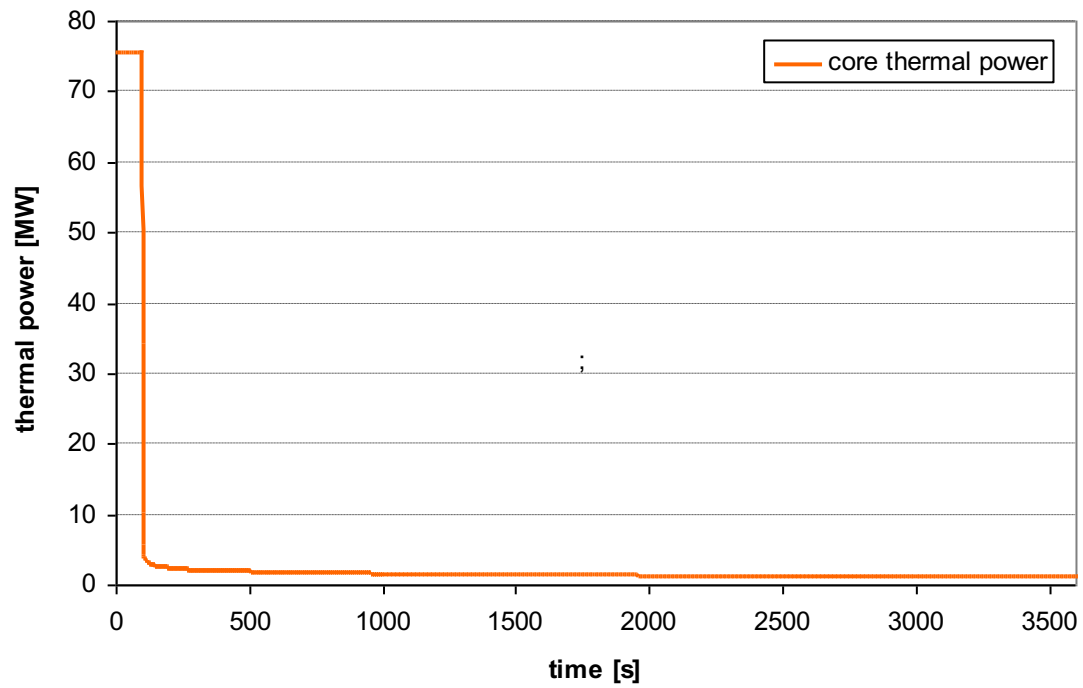
Figure 64: Time profile of core thermal power [6]
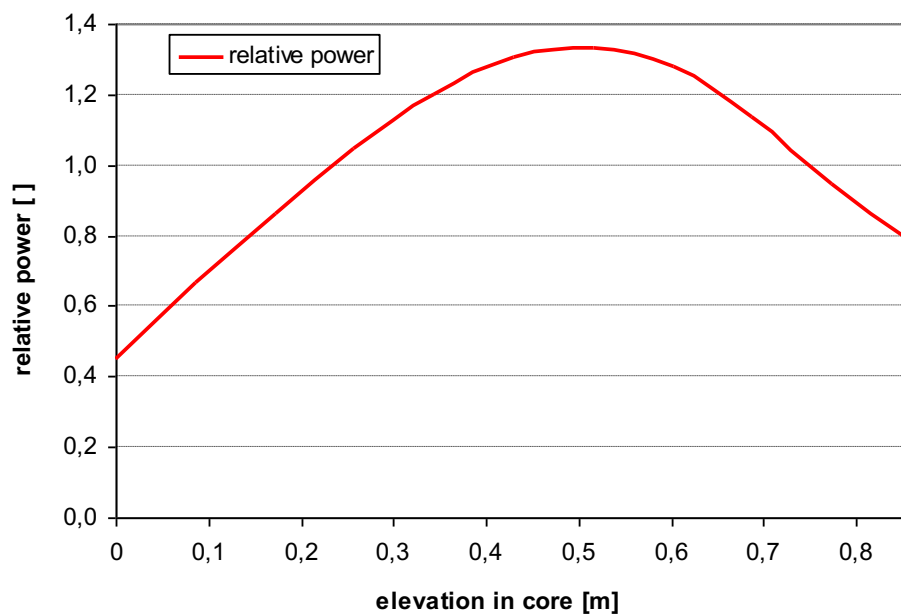
Figure 65: Core axial power distribution [7]
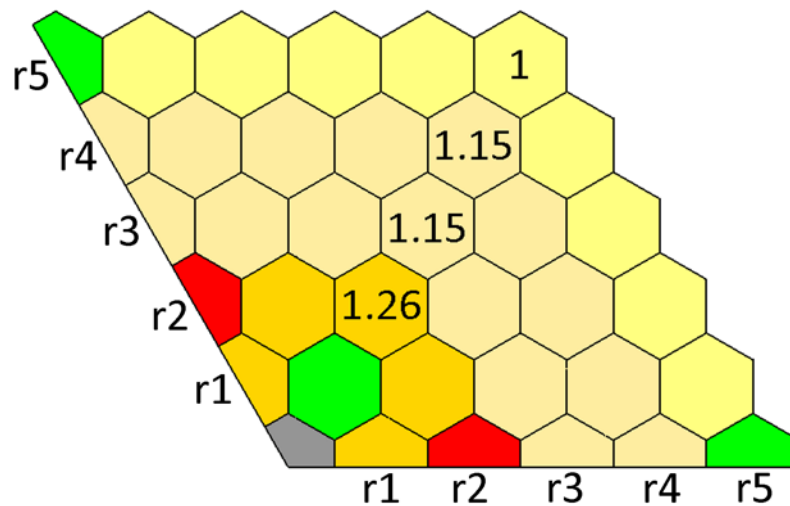
Figure 66: Core radial power distribution and numbering of fuel cassette rows [7]

4.4.2 SOLUTION AND RESULTS

One of the objectives of the work was to evaluate the distribution of the helium flux across the core during a given transient scenario. Important here is the ability to monitor the mass fluxes through each type of assembly and the temperatures at their outlets. In the case of more detailed monitoring of the monitored parameters, it is also possible to analyze the results in the individual fuel assemblies, whose labels can be seen in Figure 66.

The monitoring of the temperature at the outlet of each type of assemblies and each row of fuel assemblies can be seen in the graph in Figure 67. A rapid temperature rise can be seen between approximately times t = 100 to t = 350 s. The reason of this rise is due to the different trends in the decrease in zone power and helium flow rate. The core power decreases much faster than the helium flow rate in the first stages after shutdown. For example, for time t = 130 s, the core power is less than 4 % of the nominal power. In contrast, the helium flow rate reaches 12% of the nominal value. This leads to a very rapid cooling of the core, which is clearly visible in the graph.

The situation changes at about time t = 180 s, when the helium flow rate drops from 5% of nominal to less than 2% in about 20 s. This change can be partially observed in the Figure 63. The residual heat output of the zone is about 3% of nominal for t = 180 s and decreases very gradually. The helium flow is insufficient here and there is a rapid temperature rise at the fuel assembly's outlet. However, with time the helium flow rate increases again slowly and the helium temperatures at the assembly outlet, which reach their maximum at about t = 340 s, start to decrease again. The maximum temperature of 845.6 K is reached in the first row of subassemblies at time t = 335.5 s. Further oscillations are observed. However, their intensity is very small.
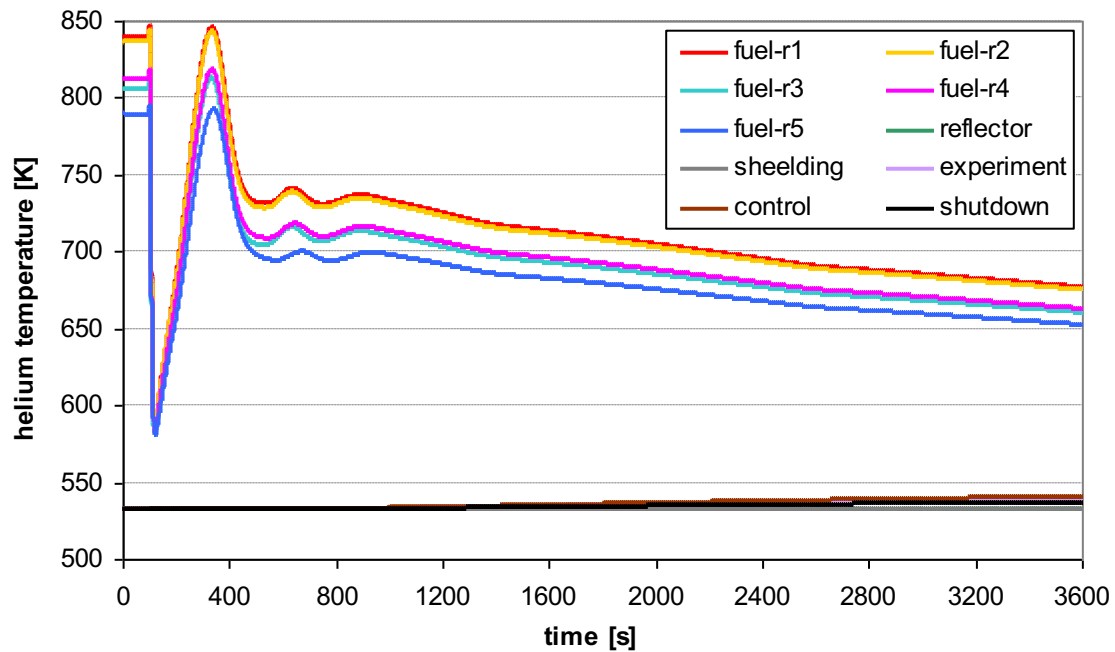
Figure 67: Time profiles of temperature at the end of individual groups of assemblies

The graph also shows a gradual slight increase in temperature at the bypass outlets. Mutual heat transfer between the assemblies is excluded by the adiabatic boundary condition. Thus, the likely cause may be parasitic mixing of hot helium from the upper mixing chamber into the cold assembly outlets, due to the intense mixing in the chamber and very low velocities at the bypass outlet.
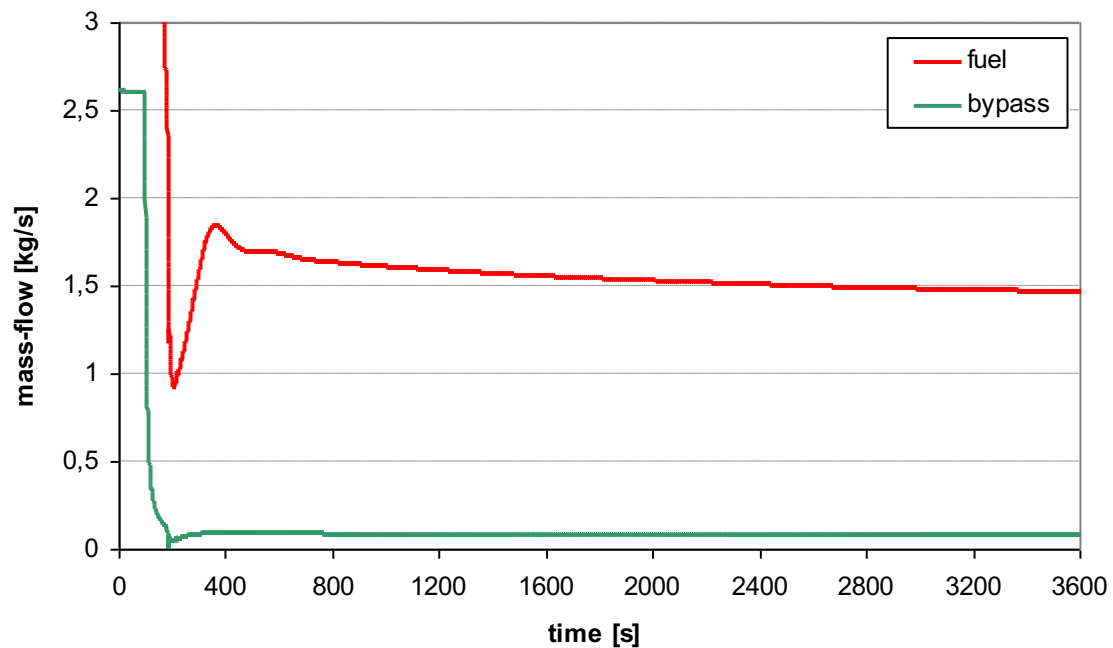
Figure 68: Time profiles of mass-flow in fuel and bypass

Another of the monitored parameters is the mass flow through the assemblies. The graph in Figure 68 shows the time evolution of the mass flow through the fuel assemblies and the bypass.
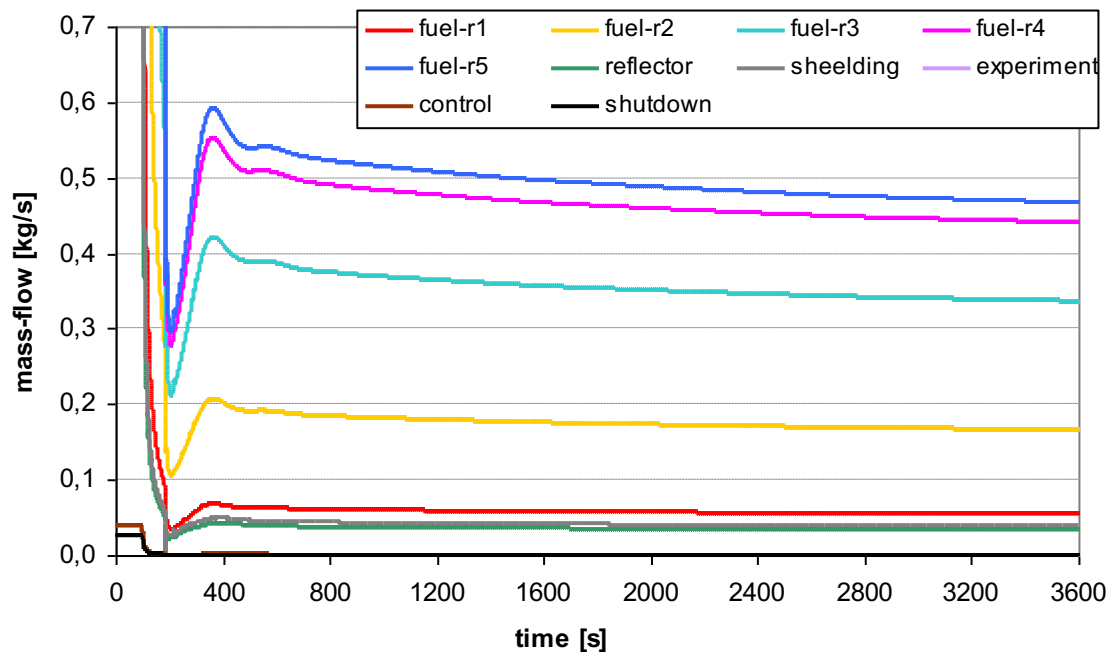
Figure 69: Time profiles of mass-flow in the individual groups of assemblies

A more detailed view of the flow distribution is provided by the graph in Figure 69 Here the mass flow through the fuel assemblies is divided into sub-flows for each radial row, see Figure 66. Similarly, the mass flow designated as bypass is divided into sub flows by all remaining assembly types. As can be seen from the figure, the mass fluxes within the bypass are quite negligible.

The distribution of velocity-z and temperature at the end of the reactor core at time t = 100 s, which represents the beginning of the simulated transient, is shown in Figure 70. It can be seen that the temperature distribution at the exit of the assemblies follows the radial power distribution, see Figure 66. In the case of the flow velocity, row 5, which is adjacent to the reflector assemblies, shows a slightly lower flow through the individual assemblies. Analyses have shown that there is a very intense crossflow at the inlet to this outermost row of assemblies due to helium overflow from the reflector and shielding assemblies, which have much higher hydraulic resistance. As a result, the inlet cross-section is partially flooded by the resulting vortices and the helium flow is lower than in the inner rows of assemblies where the flow is already smoother.
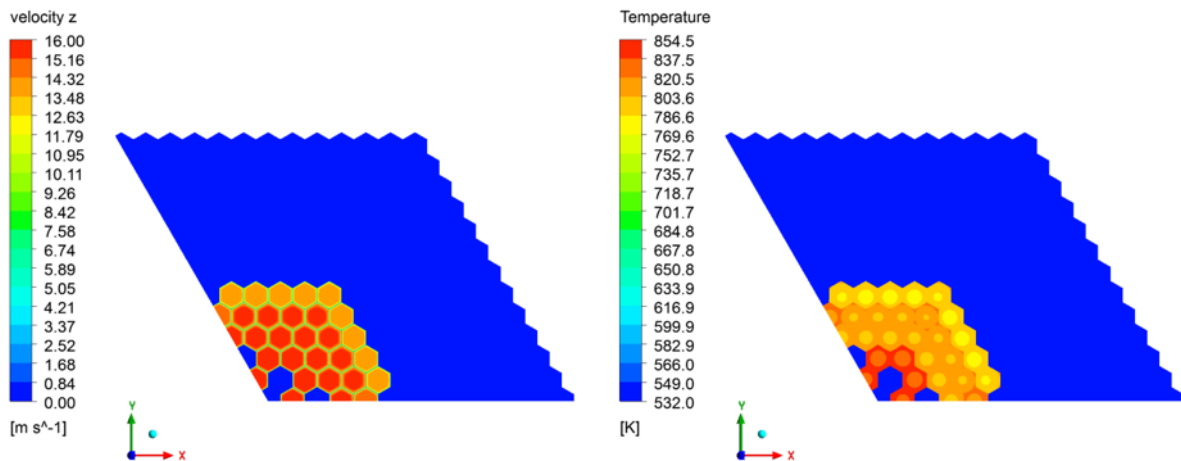
Figure 70: Velocity-z and temperature distribution at the end of core (t = 100 s)

A more detailed distribution of velocity-z and temperature in the fuel assemblies themselves at the mid-height of the core and at the end of the core is shown in Figure 71 and Figure 72. The figures confirm the above temperature and flow rate distributions. It can also be seen that temperatures near the walls of the assemblies reach higher values than in the center of the assemblies. This is because the output of the assemblies is simulated as a volumetric heat source, which is constant throughout the cross section of the assembly. The rate of helium heating is then dependent only on its velocity, which is lower near the walls.
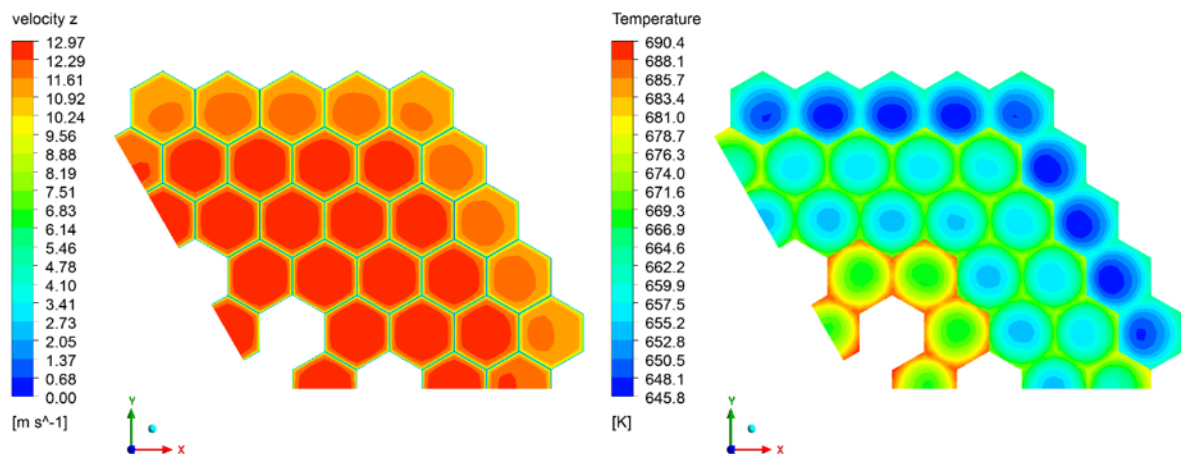
Figure 71: Velocity-z and temperature distribution at the half of core (t = 100 s)
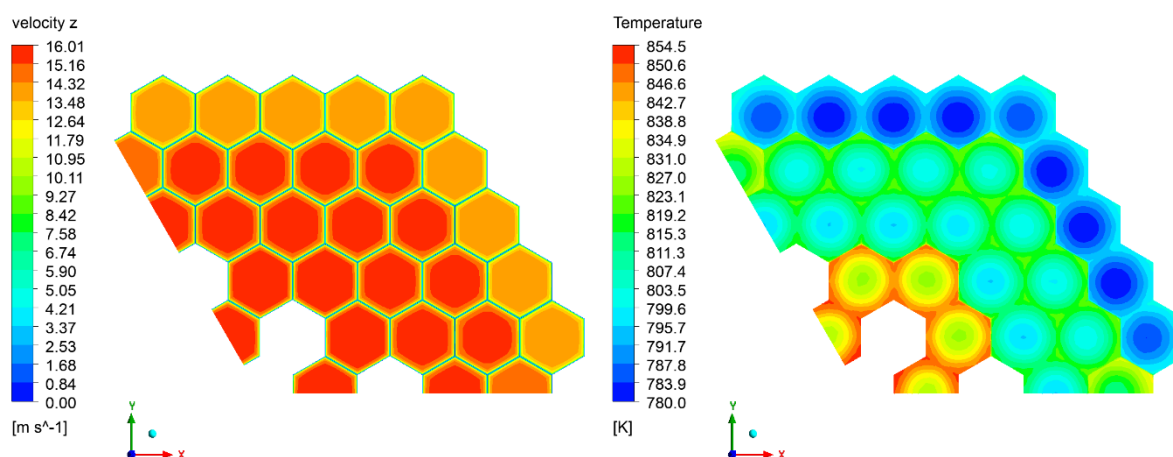
Figure 72: Velocity-z and temperature distribution at the end of core (t = 100 s)

5 CONCLUSIONS

The main objective of Deliverable 3.10 was to provide a CFD study of the core cooling under the selected LOFA scenario. For this purpose, detailed models of each type of assemblies were created in the first phase and pressure drop analyses were performed on them. In the second phase, a simplified model of the core area of the ALLEGRO reactor was created and used to simulate the LOFA scenario.

Detailed models of all basic fuel assembly types (reflector/shielding, control/shutdown and fuel assembly) determined the theoretical pressure drops at nominal operating conditions of 14 Pa (reflector/shielding), 145 Pa (control/shutdown) and 53 kPa (fuel assembly, including two support grids), respectively. The results show that the fuel assembly presents an order of magnitude higher pressure drop compared to the other assemblies. Due to the need to ensure the required flow characteristics during the operating conditions, the further design of the core is expected to appropriately implement orifices in each type of assemblies to meet the thermohydraulic requirements. The achieved pressure drops in the individual assembly types are thus the main basis for the subsequent design of the orifices, which modify the pressure drops according to the operational requirements.

The CFD model of the core area included a simplified part of the lower and upper mixing chambers in addition to the core itself. Input values for the simulation of the selected LOFA scenario were specified using Apros simulations. These are the temperature in the lower mixing chamber and the mass flow rates through the fuel and all remaining assemblies in the core. The drag coefficients in the individual porous zones simulating pressure drops were sequentially adjusted so that the total hydraulic drag of each assembly type would provide the required coolant distribution as specified.

As a result of the simulations performed on the model of the core area, the mass and temperature profiles at the core outlet during the scenario were determined. The simulations determined the maximum temperatures reached during the simulated LOFA accident scenario to be 845.6 K, which is lower than the temperature defined at the beginning of the scenario.

Based on the results obtained, it can be concluded that the main objective of Deliverable 3.10 was met. The developed CFD model of the core area is ready for the simulation of transient flow and thermohydraulic analyses of LOFA scenarios. In addition, new correlations of heat transfer coefficients for the Apros program were developed in D3.10 using the supporting CFD models, which were used to determine the input conditions of the LOFA scenario for the CFD calculations of the entire core.

6 REFERENCES

[1] Gerschenfeld, A., Forgione, N., & Thomas, J. Multi-scale simulations of liquid metal systems. Thermal Hydraulics Aspects of Liquid Metal Cooled Nuclear Reactors, 361–382, 2019

[2] Koryčanský, R., Vácha, P. ALLEGRO Core Design Visualization. Technical report. ÚJV Řež, a.s., 2023

[3] Complete set of CAD models of the individual assemblies of ALLEGRO reactor, UJV Řež, a.s., 2022

[4] ANSYS Fluent Users Guide, Release 2022/R1 Ansys Inc., Southpointe, 2600 Canonsburg, PA 15317, USA, January 2022

[5] ANSYS Fluent Theory Guide, Release 2022/R1. Ansys Inc., Southpointe, 2600 Canonsburg, PA 15317, USA, January 2022

[6] LOFA scenario dataset, Apros program, BME, Budapest, 2023

[7] Core information dataset, UJV Řež, a.s., 2023

APPENDIX

BME-NTI-1003/2023

SAFEG WP3.5 SUPPORT REPORT
ALLEGRO GAS COOLED FAST REACTOR ROD BUNDLE INVESTIGATIONS DURING NORMAL AND LOFA CONDITIONS WITH CFD AND PIV METHOD

Institute of Nuclear Techniques, Faculty of Natural Sciences, Budapest University of Technology and Economics
Műegyetem rkp. 3, H-1111 Budapest, Hungary

V3.0

Name	Occupation	Institution	Contact
Gergely Imre Orosz	**PhD student**	**BME NTI**	**orosz@reak.bme.hu**
Mathias Peiretti	MSc student	BME NTI/ Politecnico di Torino	matthias.peiretti@edu.bme.hu
Boglárka Magyar	BSc student	BME NTI	bogi0614@gmail.com
Dániel Szerbák	MSc student	BME NTI	szerbakdani@gmail.com
Dániel Kacz	PhD student	BME NTI	kacz.daniel@reak.bme.hu
Béla Kiss	Research assistant	BME NTI	kiss@reak.bme.hu
Gábor Zsíros	Research assistant	BME NTI	zsiros@reak.bme.hu
Bendegúz Kopp	Research assistant	BME NTI	kopp@reak.bme.hu
Prof. Attila Aszódi	Professor	BME NTI	aszodi@reak.bme.hu

Budapest, Hungary, 2023.07.24.

NOMENCLATURE

ATF	ACCIDENT TOLERANT FUEL
BME	BUDAPESTI MŰSZAKI AND GAZDASÁGTUDOMÁNYI EGYETEM – BUDAPEST UNIVERSITY OF TECHNOLOGY AND ECONOMY
BPG	BEST PRACTICE GUIDELINES
GFR	GAS COOLED FAST REACTOR
GIF	GENERATION IV INTERNATIONAL FORUM
GOFASTR	EUROPEAN GAS COOLED FAST REACTOR PROJECT
HTR-PM	HIGH TEMPERATURE GAS-COOLED REACTOR - PEBBLE-BED MODULE
LDA	LASER DOPPLER ANEMOMETRY
LMFR	LIQUID METAL FAST REACTOR
LOCA	LOSS OF COOLANT ACCIDENT
MIR	MATCHING OF REFRACTORY INDEX
MVG	MIXING VANE SPACER GRID
NTI	NUKLEÁRIS TECHNIKA INTÉZET – INSTITUTE OF NUCLEAR TECHNIQUES
PIROUETTE	PIV ROD BUNDLE TEST FACILITY AT BME
PIV	PARTICLE IMAGE VELOCIMETRY
PWR	PRESSURIZED WATER REACTOR
RANS	REYNOLDS-AVERAGED NAVIER–STOKES
SMR	SMALL MODULAR REACTOR
V4G4	VISEGRÁD GROUP COUNTRIES FORM G4 CENTRE OF EXCELLENCE FOR JOINT R&D IN GENERATION-4 NUCLEAR REACTORS
VVER	VODO-VODYANOI ENERGETICHESKY REAKTOR – WATER COOLED AND WATER MODERATED POWER REACTOR

TABLE OF CONTENT

1. INTRODUCTION

In order to close the nuclear fuel cycle, the development of reliable Generation 4 reactors is vital. A fourth-generation demonstration gas cooled fast reactor named ALLEGRO has been long under development with the support of the European Union (GIF [1], GOFASTR [2]). During this time, several projects have addressed the challenging thermohydraulic of this reactor. The development started in collaboration of European research institutes, universities and companies in the 2000's. In the near past the demonstrator reactor has been developed by a consortium named V4G4 Centre of Excellence [3], associating several research organizations and companies from Slovakia, Czech Republic, France, Poland and Hungary. In the framework of the latest European project (SafeG [4]), the research programme was relaunched in 2020.

The demonstrator reactor is designed to meet the technological criteria for the future GFR 2400 MW_{th} reactor. It is worthy of note, that the demonstration reactor now being developed, has a power of 75 MW_{th}, which fits in the current trend of SMR reactors. If the technology proves to be mature, an improved version of the ALLEGRO reactor could be attractive to industrial users as an SMR.

The working medium of the reactor is helium (at 7 MPa), as in the current HTR-PM reactor designed by the Institute of Nuclear and New Energy Technology (INET) of Tsinghua University [5]. The main difference between ALLEGRO and HTR-PM is the core design and the power density. The European GFR has more than 28 times bigger power density, namely 92 MW/m^3. The ALLEGRO core will be operated without any moderator material. This core design goes hand in hand with the fast neutron spectrum and the possibility of a more efficient fuel cycle. Nevertheless, the disadvantage is the lack of thermal inertia, which appears in the HTR-PM reactor due to the large mass of graphite present in the reactor. In case of a Loss of Coolant design basis accident (LOCA) a rapid core coolant pressure and density loss can cause overheating of the core. These accident situations have been studied in great detail by a team of experts using various computer codes [6] [7] [8].

The main parts of the reactor and its cooling loops can be seen in Figure 1/a. The system consists of two main heat exchangers (gas-water) and three decay heat exchangers (gas-water) above the core. During the test run, the prototype main (gas-gas) heat exchanger will also be tested (red one). The hot and cold ducts of the reactor are concentrical pipes, which can create special circumstances in some accident situations. Hot duct break transient scenarios can lead to core bypass flows and were investigated by Mayer in recent studies [6].

According to the current agenda of the reactor development, the ALLEGRO reactor and the main equipment will be tested step by step. This is also true for the reactor core, which has three different core configurations during the operation. The first technical configuration of the core will be made of MOX type assemblies with a milder operational temperature (560 °C) [6] [9]. These assemblies are designed with stainless steel fuel cladding and wire wrapped helical spacers. This fuel type was investigated in detail within the ESTHAIR program [9]. In the next stage of the core development, the core will mainly consist of MOX fuel, with some prototype refractory ceramic fuel assembly for irradiation and performance tests.

In the final stage of the operation, the core will be made of refractory ceramic composite fuel assemblies. It is needed to operate the assemblies at a high temperature with enough safety margins. The final composition of the silicon-carbide based fuel claddings is currently under development and could be also a good candidate in accident-tolerant fuel (ATF) cladding for PWRs [10]. The refractory assembly consists of 91 fuel rods with a diameter of 9.1 mm. The fuel rods are arranged in triangular lattice with a pitch distance of 11 mm. The cross-sectional

view of the assembly can be seen in Figure 1/b. Four honeycomb spacer-grids hold the fuel elements in their positions (Figure 1/c). The height of the spacers is 26 mm and the distance between them is 246 mm.

Our previous publications deal with the special heat transfer processes in refractory fuel assemblies [11] [12] [13]. Unfortunately, these studies were purely simulation based with very limited validation possibilities.
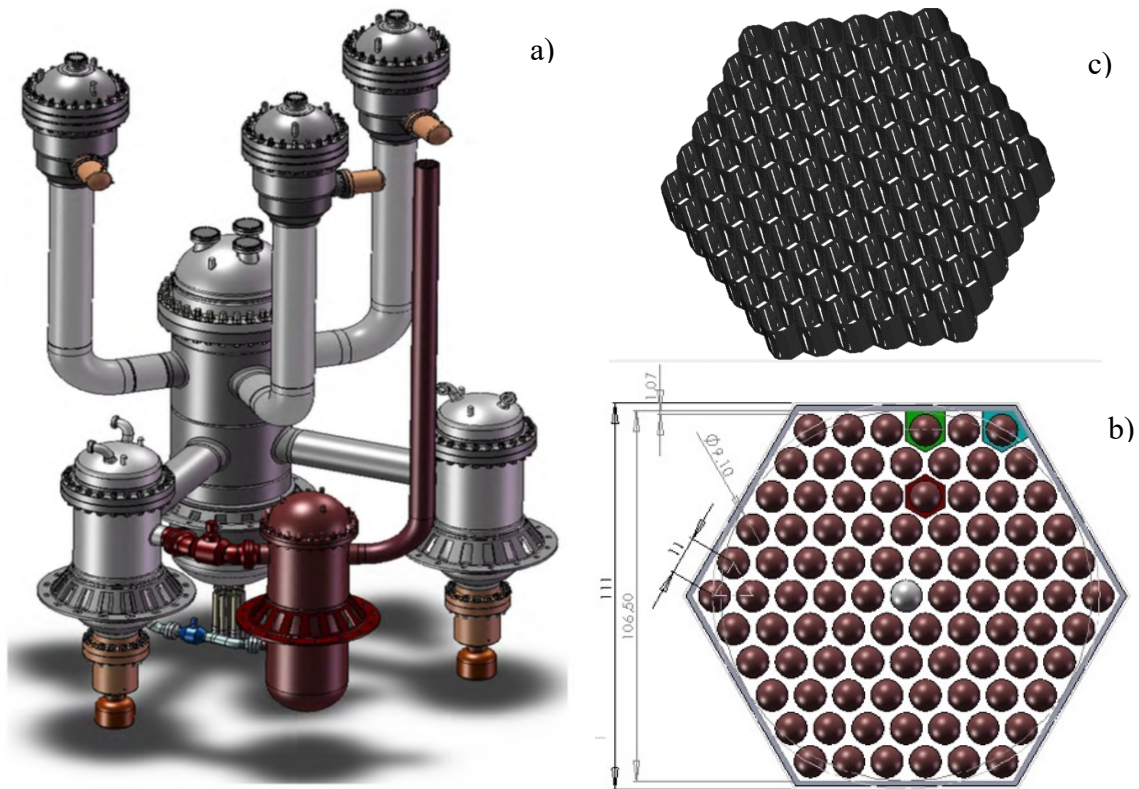
Figure 1: The design of the ALLEGRO reactor (a), the cross-sectional view of the refractory fuel assembly (b) and the geometry of the spacer-grid (c)

A recurring issue in the field of Computational Fluid Dynamics (CFD) code application is the question of code and model validation. The flow cross-sections of narrow grid rod bundles (such as the ALLEGRO bundle) are tight, so using high-resolution measurement techniques is recommended. Non-invasive measurement techniques such as LDA [14] [15] and PIV are used in many cases in rod bundle measurements. For the same reasons, this paper presents studies carried out using PIV measurements and CFD simulations.

The international literature is currently dominated by PIV measurements of square lattice rod bundle geometries. Triangular fuel pin arrangements have been investigated primarily only by Hassan and co-authors [16] [17] [18] with measurements on a fourth generation LMFR fuel model. For gas-cooled pebble bed reactors, PIV studies have already been carried out on the subject of flow fields in the bed [19], but for a gas cooled fast reactor with triangular fuel lattice, there is a lack of publication. Therefore, this paper concentrates on this specific issue.

2. PIROUETTE SYSTEM DESCRIPTION

2.1. INTRODUCTION OF THE MEASUREMENTS

PIROUETTE (PIv ROd bUndlE Test faciliTy at bmE) is a test facility that was designed to investigate the emerging flow conditions in various nuclear fuel assembly rod bundles. The measurement method is based on Particle Image Velocimetry (PIV) with Matching of Refractory Index (MIR) method. The system can reproduce the flow conditions of several VVER and Generation IV reactor types.

The coolant of the ALLEGRO rector is helium with 70 bar pressure and the nominal operating temperature is 800 °C. Our test facility cannot operate on these conditions; therefore, similarity principles were used to replicate the desired flow conditions. The similarity principle was based on the Reynolds numbers; thus, the working fluid of the PIROUETTE facility can be altered from helium to water. The Reynolds numbers in the ALLEGRO GFR assembly are approximately ~16 800, while in our measurements with the PIROUETTE facility it is up to ~22 500, meaning that the facility can reproduce flow conditions similar to the ALLEGRO GFR core. The experimental rod bundle contains 7 rods in a triangular lattice.
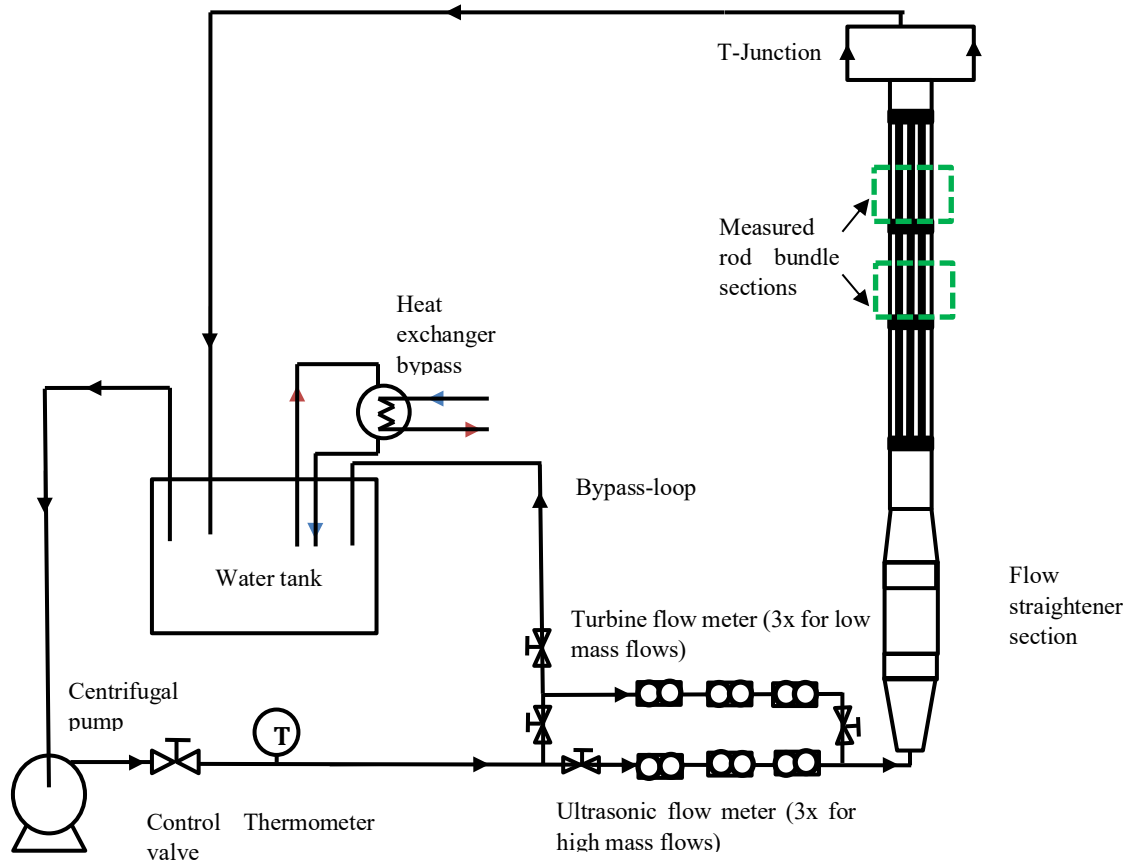
Figure 2: The schematic of the PIROUETTE facility

The structure and the main parts of the test facility can be seen in Figure 2. The installation contains a 1 meter long vertically arranged seven pin rod bundle in the test section. The water flow is provided by the main centrifugal pump (Type: Wilo MHIL 903, Power:1,1 kW, Q_{max}: 14 m^3/h [20]). Some of the power of the centrifugal pump is dissipates into the turbulent flow,

causing the rise of the temperature in the test loop. To provide a constant test loop water temperature, a bypass heat exchanger loop is installed into the facility. The water temperature was controlled and kept at 30 ±1 °C with the heat exchanger during the measurements.

From the pump, the water flows to a ball valve with a nominal diameter of ¾ inch (DN 32). The ball valve is not suitable for fine control of the mass flow and therefore it is followed by an angled seat valve. The fine control valve is followed by three identical HYDRUS ultrasonic flowmeters [21]. Multiple volumetric flow meters can increase the accuracy of the volumetric flow measurement, which is very important for setting the inlet boundary condition for CFD calculations.

A bypass loop was installed to the main pipeline to create lower volumetric flow rates for the LOFA conditions. The ultrasonic flow meter cannot measure precisely flow rates lower than 2.5 m³/h, therefore 3 redundant turbine type flow meters (DIGMESA 141402-99 [22]) were installed in the bypass loop. The excess water was returned to the central water tank.

The measuring channel section and the pump flow control subsystem were connected by KPE pipes with an inside diameter of 26 mm. From here, the water was fed through the diffuser cone to the flow straightening section. The flow straightener reduces disturbances caused by mechanical, measuring and pipe-lining equipments.

The 1 meter long seven-rod bundle was installed in the test channel section. A removable roof has been designed on the test channel section for easy access. This is necessary to allow the change of the rod geometry, for example, different types of spacer grids and mixing vanes. A T-junction was placed after the test section, and the medium discharges to the water tank through other pipelines. The sematic of the test facility can be seen in Figure 2 and the 3D model in Figure 3. In Figure 3, the 7-pin rod bundle is also presented with the TWISTED type MVG. The MVG is coloured black to reduce the reflection of laser light during the PIV measurements.
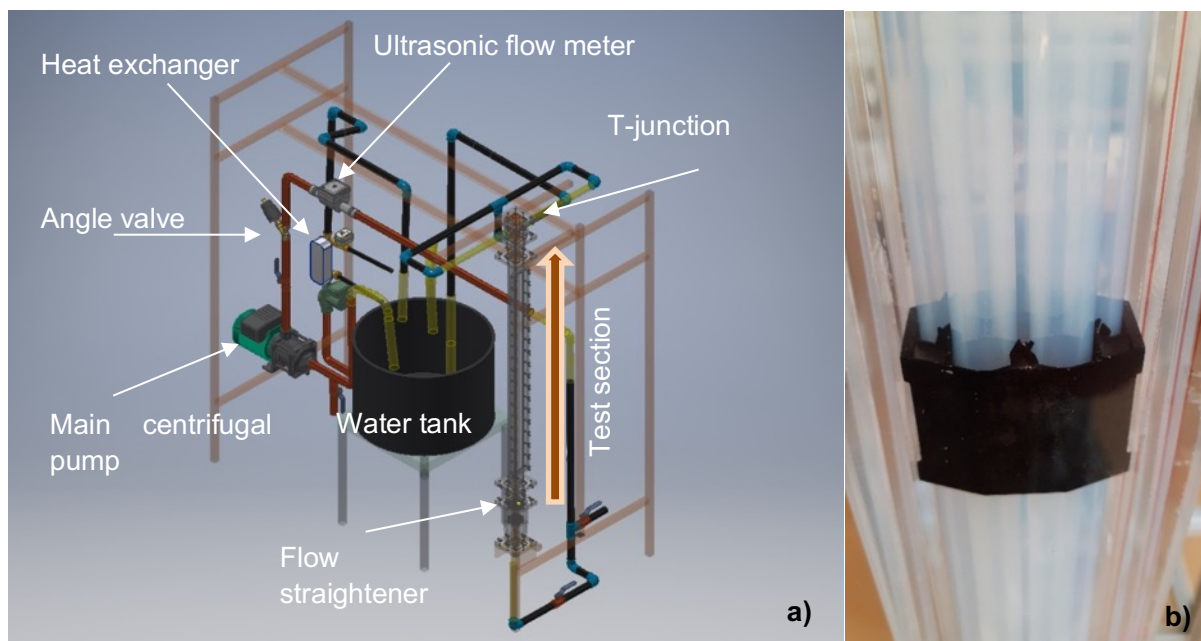
Figure 3: The structure of the PIROUETTE facility (a) and the rod bundle within with TWISTED type MVG (b)

The test section is designed to easily interchange the measurement channel and the associated confuser and diffuser connectors. The flow straightener includes two straightener grids and a deflector cone to restrict the flow from the effects of the pipe elbows upstream of the test section. A confuser adapter part is located above the straightener part. At the exit of the confuser, the cross-section of the channel is the same as the cross-section of the measuring channel section. This avoids problems caused by sudden cross-section changes.

The cross-section of the measuring channel is a little bigger than the reactor type under investigation, but on the basis of the similarity theory [23], the hydraulic parameters are exactly the same. The 1 meter long test bundle is made of FEP (Fluorinated Ethylene Propylene) to meet the refractory index of water. The FEP polymer has a refractive index of 1.33, nearly the same as the working medium (water). The outer and inner diameters of the rod are 10/6 mm, and the inside of the rods was filled with ultrafiltrated water. The diameter of the ALLEGRO refractory fuel rod is 9.1 mm. Therefore, the upscaling ratio of the channel was 10/9.1=1.0989. The rods are connected with pins into the first and fourth spacer grids, and the spacer grids are connected to the channel wall with groove fitting.

The distance between the spacers is 296 mm. The spacers were designed according to the ALLEGRO GFR assembly spacers, with slight modifications to fit the measurement requirements. The wall thickness of the spacers is 0.8 mm. The grids were made using high resolution 3D printing method (SLA) with special rigid composite resin. Thanks to 3D printing, spacer geometries can be easily varied and extended with different types of mixing vane. The ALLEGRO spacer has been equipped with TWISTED and SPLIT type vanes in the presented tests.

The spacer contains 6 vanes in the regions of the edge of the rod bundle. The base of one vane is 2 mm long, the total height of the vanes are ~3 mm in the SPLIT and ~ 4mm in the TWISTED type spacer. The inclination of the vanes is 30° to the axial direction. An important criterion in the design is that the vanes do not touch the rods, which is why there is a curved cut-out at the end of each vane.

Our preliminary research has shown that TWISTED vanes are more effective than SPLIT ones under ALLEGRO relevant conditions [24]. Our current measurements aim to test this claim more accurately.
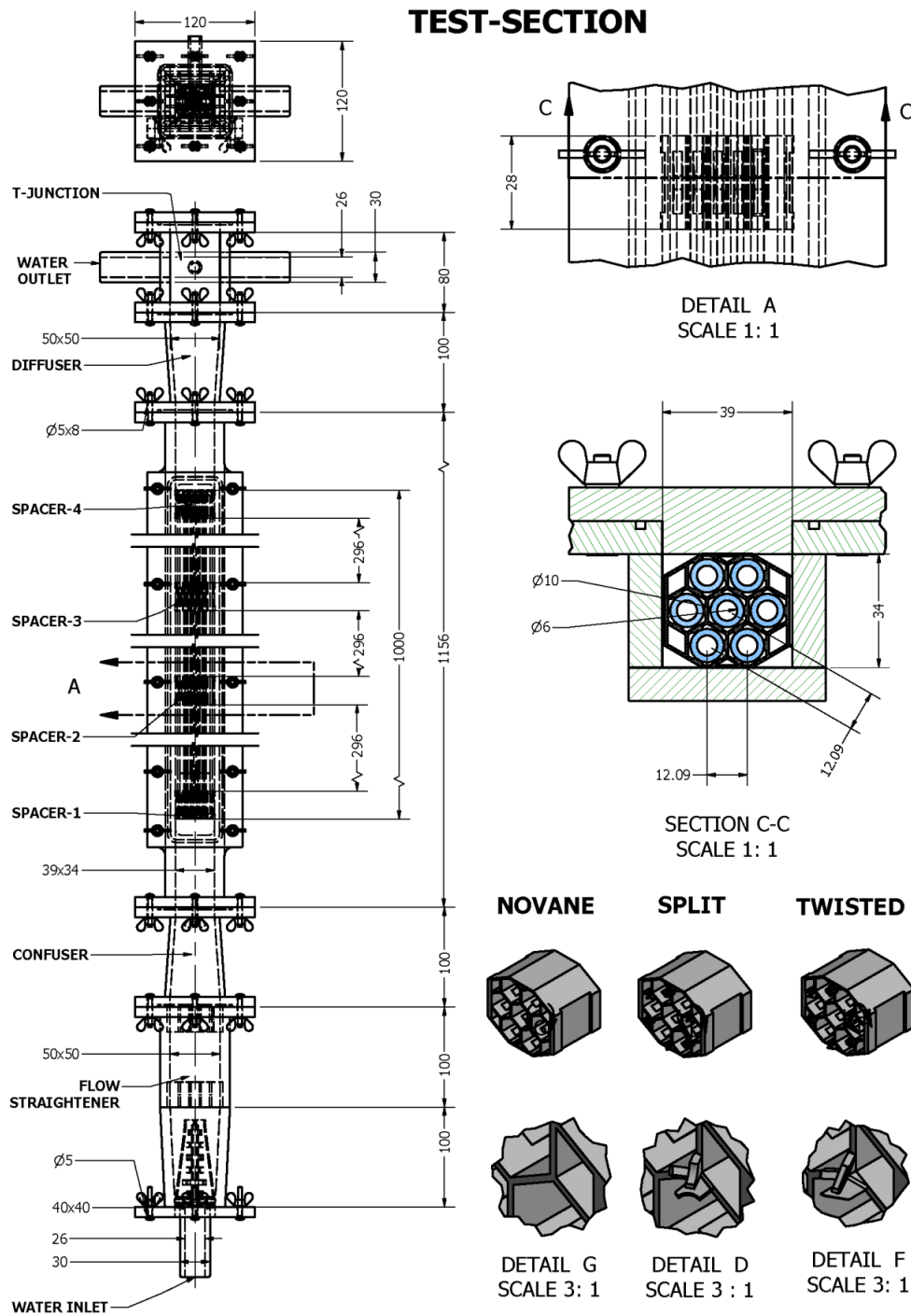
Figure 4: Compilation of the test section

2.2. PIV SYSTEM

The PIV measurement system includes the following components:

- tracer particles: polyamide spheres with an average diameter of d = 50 μm [25],
- light source subsystem: Litron Nano L PIV dual Nd:YAG laser (maximum pulse energy: 135 mJ, wavelength: 532 nm, pulse length: ~6 ns, maximum flash frequency: 15 Hz) [26],

- beam guide arm and beam forming optics [27],
- image capture subsystem (camera): SpeedSense Lab 110 high-speed digital camera, resolution: 1 megapixel (1280x800), frame rate: 1630 fps, buffer: 12GB [28],
- Synchronizer: Dantec Timer Box (80N77) [29],
- Synchronisation, image capture and processing software: Dantec DynamicStudio, latest stabile version 6.6 [30],
- camera and beam-optics positioning systems.

2.3. MEASUREMENT PROCEDURE

The rod bundle measurements were performed in the vertical measurement channel. Figure 5 shows the schematic layout of the experiment with the TWISTED type MVG. The plane of illumination intersects the two outer rods. The illuminated volume is ~1,5 mm wide. Information on the flow processes can be gathered from this volume in the measurements. This special feature of the experiments should also be taken into account in the PIV experiment – CFD simulation comparisons.

As it was mentioned above, in the case of our current measurements, the illumination plane intersects the outer two or the inner three rods. The camera sees perpendicular to this plane.

Before starting the measurements, a so-called target sheet was placed in the appropriate position in the channel. The target sheet is a specially printed dotted and laminated paper sheet. Knowing the diameters of the dots and their positions helps to recover the real physical dimensions from the camera images. Using points of different diameters on the target, we can identify the coordinate axes. After a sufficient number of points have been detected, the conversion from pixel to millimetre distance is done automatically by a software [30].
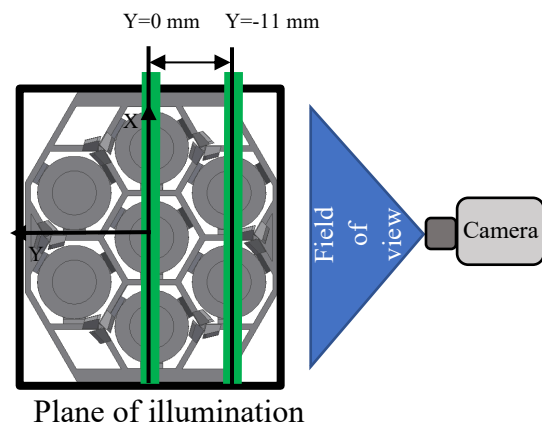
Figure 5: The schematic layout of the investigated planes

In the rod bundle measurements, 2000 image pairs were recorded in the vicinity of the spacer grids. The downstream region after the 2nd and 3rd spacers was captured. We aimed to observe the effect of the different spacer types. The quality of the images at the beginning of data acquisition is insufficient because the lasers have a "warm-up" time requirement. Therefore, the first 100 image pairs were discarded from the 2000 image pairs captured.

To get a sufficiently detailed picture of the flow field, post-processing of the raw images is necessary. Figure 6 shows the steps of image processing. The first image shows the raw image (Figure 6/1). In the first step, an average image of 1900 image pairs were created (Figure 6/2). This average image was extracted from each image to reduce the effect of the elements that are present in each image (shadows, glitches and static elements). The result is shown in the Figure 6/3.

Laser light is not uniform in intensity along the length of the illuminated plane. Figure 6/4 image shows an image processed by "image balancing" to correct this unevenness of illumination. Since not all static elements can be eliminated from the images in this way, the static parts and regions not included in the flow field have to be masked out with digital masks

during post processing. Figure 6/5 row shows the masked image, where only the polyamide particles that move with fluid are visible.

After these steps, the individual image pairs were used to create the instantaneous vector fields separately. These vector fields show the chaotic velocity distribution typical in turbulent flow (Figure 6/6). From these 1,900 vector diagrams, we created the time-averaged vector field describing the flow region downstream of the spacer (Figure 6/7). With this method, the time-averaged velocities can be obtained, and the temporal fluctuations of the velocity vectors can be estimated. In this way, not only assigning a vector value to a given pixel can be made, but also its statistics will be known. However, we cannot accurately determine the distribution of the turbulent kinetic energy, because the 2D measurement loses the information provided by the third velocity component.
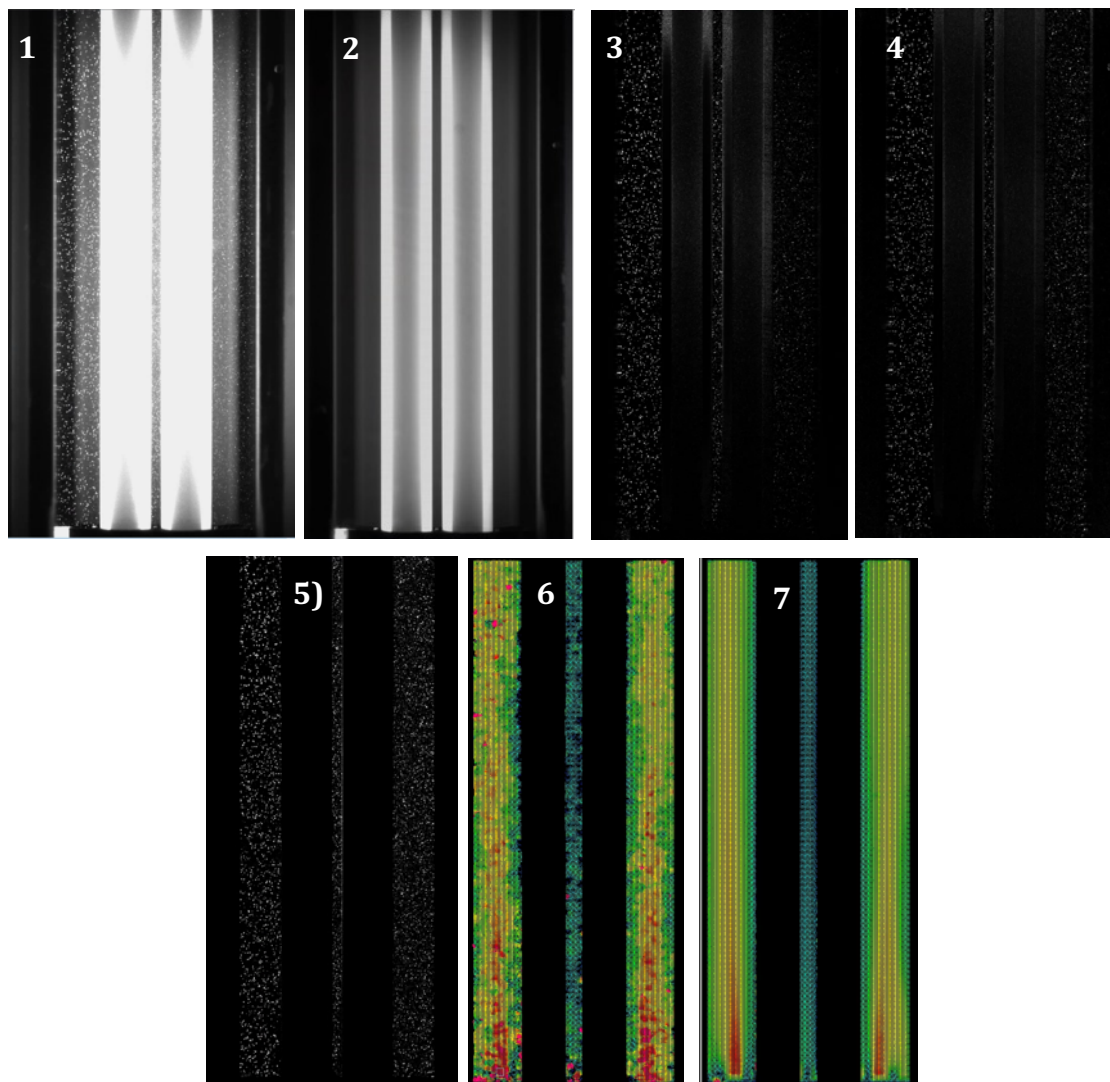
Figure 6: The steps of the image post-processing

3. ESTIMATION OF UNCERTAINTY IN PIV MEASUREMENTS

In PIV experiments, the velocity of the seeding particles is measured instead of measuring the velocity of the flowing fluid. The density of the particles is approximately equal to the density of the liquid. In this case, the diameter of the particles is 50 micrometres. Two digital images of the particle distribution are taken, from which the two-dimensional vector field can be calculated. The time interval between the two images can vary from a few microseconds to several milliseconds, depending on the velocity of the main flow.

While processing the captured image pairs, the velocity is assumed to be uniform in the interrogation areas during the image pair recording period. Knowing the delay between the recorded images and the displacement of the particles, the velocity vectors can be correlated to the interrogation regions using correlation methods [31].

Using calibration, the displacement (measured in pixels) can be converted to a metric value using the following formula [32]:

$$u = \alpha \frac{\Delta X}{\Delta t} + \delta u \qquad (1)$$

Where: u is the physical velocity [m/s], α [m/pixel] is the conversion factor for magnification, ΔX [pixel] is the displacement of the recorded image, and Δt [s] is the time elapsed between the two images being recorded. The magnification factor α was determined by the calibration target. δu is difficult to detect systematically and is usually classified as an uncertainty factor rather than a measurement parameter.

In general, the measurement setup can be broken down into four subsystems:

- Calibration subsystem: converts the displacement in pixels into displacement in metric,
- Visualization: trace particles, illumination,
- Image recording: digital camera,
- Image processing: cross-correlation method, vector field calculation, etc.

The uncertainty in the target variables (flow velocities) is most affected by errors from the four subsystems.

To achieve sufficiently accurate measurements, the estimates of random and systematic errors should be determined at the 95% confidence level and the resulting quadratic error function should be generated. This allows us to estimate the measurement uncertainty with 95% confidence.

Each element in equation (1) is subject to systematic and random errors, which introduce bias into the result and give the uncertainty of the measured value. Using the appropriate literature, a detailed uncertainty analysis was carried out, which included the following sources [33] [32] [34] [35] [36] [37]:

- Error sources and sensitivity factors for magnification α
  - Reference length identification
  - Error caused by the image recording system
  - Error due to de-warping was neglected
- Error sources and sensitivity factors of ΔX image displacement
  - Error due to illumination
  - Error caused by the image recording system
  - Image processing, calculation of displacement
- Error sources and sensitivity factors of Δt time delay

- ▪ Error sources of the delay generator (timer) timing
- ▪ Error sources of the laser pulse timing
- Error sources and sensitivity factors of δu velocity difference
  - ▪ Flow following ability of the particles (trajectory)
  - ▪ Three-dimensional effects
  - ▪ Uncertainty due to volume flow adjustment
- The effect of sampling

In the respect of the average flow velocity in the rod bundle (2.0112 m/s, see in Table 1), the error of our measurement is ~ 0.22 m/s (~10.58% of the average velocity). The relative error is naturally larger in the lower velocity sections (along walls) since most of the sources of error in the uncertainty analysis are constant, and few depend on the actual velocity vector of the measured flow.

Main parameters		Calibration	
Area investigated	105 x 40 mm^2	Calibration length on target l_{sel}	31.5 mm
Average flow velocity w	2.0112 m/s		
Flow cross section A	828.7 mm^2	Calibration length on the visualisation plane L_{sel}	365 pixel
Flow rate Q	1.66667 l/s	Magnification α	0.08630137 mm/pixel
Flow visualisation		**Image recording**	
Trace particle	Polyamide spheres	Kamera	
Average diameter d_p	0.05 mm	Resolution	1280 x 800 pixel
Average density	1.02 g/cm^3	Frame rate	1690 Hz
Light source	Litron Nano L PIV duál Nd:YAG laser	Objective	Nikon 60mm f/2.8 Micro-NIKKOR AF-D
Laser shot energy	138 mJ	Distance from the plane of illumination l_t	260 mm
Laser plane width	1.5 mm	Angle of perspective φ	11.41 °
Pulse frequency	15 Hz		
Time interval	50 µs		
Data processing			
Pixel value analysis	Cross correlation method		
Interrogation area	16 x16 pixel		
Search area	8 x 8 pixel		
Sub-pixel analysis	three-point Gaussian fit		

Table 1: Some basic data for the measurement system error calculation

3.1. ERROR PROPAGATION PRINCIPLES

To achieve sufficiently accurate measurements, the estimates of random and systematic errors should be determined at a 95% confidence level, and a quadratic error function should be generated from them. This allows us to estimate the measurement uncertainty with 95% confidence.

Each element in equation (2) is subject to systematic error and random error, which introduce bias into the result and add uncertainty to the measured value. This is described by the following quantities [33] [38] [39] [35] [36] [37]:

- The precision of a measurement is the closeness of the measured values when successive measurements are taken under identical conditions. Precision can be characterized by the measurement uncertainty, random error (precision index, random error), whose sign is S.

- The accuracy of a measurement is an expression of how close the measured value is to the true value of the quantity to be measured. Accuracy is not known, nor is the true value, and can be estimated by determining the bias error/limit, the latter quantity being denoted by B

The value determined by the measurement is a function of the measured parameters X_i: $r=f_{(X1,X2,....XJ)}$. The following example shows the uncertainty of two measured parameters, x and y. Both measured values have a statistical error around the mean value μ_x and μ_y distributed according to a Gaussian function (ε). The systematic error β is unknown and cannot be measured, although it can be estimated from past experience. It can be assumed that the systematic error varies with different measurement occasions and has a distribution that is either Gaussian, uniform, or takes some other form. On this basis, a selected measured parameter can be described as follows.

$$x_i = x_{real} + \beta_{xi} + \varepsilon_{xi} \tag{2}$$

$$y_i = y_{real} + \beta_{yi} + \varepsilon_{yi} \tag{3}$$

And we can introduce the:

$$\delta_{ri} = r(x_i, y_i) - r(x_{real}, y_{real}) \tag{4}$$

If we decompose the error around the real value of r into a Taylor series, we get:

$$\delta_{ri} = \theta_x \beta_{xi} + \theta_x \varepsilon_{xi} + \theta_y \beta_{yi} + \theta_y \varepsilon_{yi} \tag{5}$$

where θ_x and θ_y are the sensitivity factors for x and y, respectively. The sensitivity factors are the contribution of a given error to the accuracy and can be written in general terms as follows:

$$\theta_i = \frac{\partial r}{\partial x_i} \tag{6}$$

$$u_{ri}{}^2 = \theta_x{}^2 b_x{}^2 + \theta_y{}^2 b_y{}^2 + 2\theta_x \theta_y b_{xy} + \theta_x{}^2 S_x{}^2 + \theta_y{}^2 S_y{}^2 \tag{7}$$

where u_{ri} is the combined standard uncertainty, $b_x{}^2$ and $b_y{}^2$ are the variances of the standard systematic errors, $S_x{}^2$ and $S_y{}^2$ are the standard deviations of the errors, and b_{xy} is the covariance. Generalizing the above formula and writing it as a function of variance, we obtain:

$$D^2[g(\xi)] = M[(\Delta g)^2] = \sum_{i=1}^n \left(\frac{\partial g}{\partial \xi}\right)^2 D^2(\xi_i) \tag{8}$$

Where ξ_i is the directly measured data, $g_{(\xi)}$ is a function that relates the directly measured data to the target parameter being sought, D^2 is the variance of g around ξ_i. This is the general form of the error propagation [35].

The covariance of random errors is considered to be zero, so formula (8) can be decomposed as follows:

$$B_r^2 = \theta_x{}^2 B_x{}^2 + \theta_y{}^2 B_y{}^2 \tag{9}$$

$$S_r^2 = \theta_x{}^2 S_x{}^2 + \theta_y{}^2 S_y{}^2 \tag{10}$$

The ASME standard considers the covariance of b_{xy} standard systematic errors to be zero [39] [36]. The systematic error factors are not known, so the estimation must be done by taking into account all sources of error and all variables: the upper estimate of the elementary systematic error (B_{jk}) is called the acceptance criterion. The acceptance criterion is defined at the 95% confidence level. The overall systematic error of the parameter X_j will be as follows:

$$B_J = \left(B_{J1}^2 + B_{J1}^2 + B_{J1}^2 \ldots + B_{JM}^2\right)^{1/2} \tag{11}$$

S_x or S_y will be the standard deviation around the mean value of the parameter you are looking for:

$$S_{\overline{X_\iota}} = \left\{\left[\frac{1}{N(N-1)}\right] \sum_{i=1}^{n}(X_{ik} - \overline{X_\iota})^2\right\}^{1/2} \tag{12}$$

The 95% confidence level of error estimate summarises the random and systematic uncertainties as follows.

$$U_{RSS} = [B_r^2 + t_{95}S_r{}^2]^{1/2} \tag{13}$$

Or at the 99% level:

$$U_{ADD} = B_r + t_{95}S_r \tag{14}$$

$t_{95}=2$, if N>30.

3.2. UNCERTAINTY SOURCES AND SENSITIVITY FACTORS IN THE RESPECT OF MAGNIFICATION

To determine the magnification factor α, a calibration target was placed at the measurement position. Using a digital image of the target, metric distance information can be recovered from the pixel image.

3.2.1. IMAGE DISTANCE OF REFERENCE POINTS:

The image distance of reference points consists of reading the distance of two points with an accuracy of 0.5 pixel, and therefore $\sqrt{0.5^2 + 0.5^2} = 0.707$ [pixel] will be the total accuracy. The corresponding sensitivity factor can be determined as follows [38]:

$$\frac{\partial \alpha}{\partial L_{sel}} = -\frac{l_{sel}}{L_{sel}^2} = -\frac{31{,}5[mm]}{365\,[pixel]^2} = -0.00023644\,[mm/pixel^2] \tag{15}$$

where L_{sel} [pixel] is the reference length in pixels measured in the image and l_{sel} [mm] is the real length of the reference distance. The calibration target was created using an inkjet printer, where an error of 2% was assumed for a target width of 31.5 mm (accuracy = 0.63 mm). The sensitivity factor is [38]:

$$\frac{\partial \alpha}{\partial l_{sel}} = \frac{1}{L_{sel}} = \frac{1}{365 \text{ [pixel]}} = 0.002739 \text{ [1/pixel]} \tag{16}$$

3.2.2. UNCERTAINTIES ARISING FROM THE IMAGING SYSTEM

There are two main components to an image capture system: the digital camera that takes the pictures and the lenses that attached to it. The distortion caused by the lenses is about 0.5% of the total recorded reference [38]. The type of Nikon 60 mm f/2.8 Micro-NIKKOR AF-D lens we used is exactly the same as the PIV system lens used in reference [38], so the accuracy due to lens distortion was assumed to be 0.005xLsel = 1.825 [pixels]. The sensitivity factor is calculated according to formula (17).

On the CCD panel of a digital camera, pixels are arranged in rows and columns. The distortion is caused by manufacturing inaccuracies in the CCD sensor because the pixels are not always equally spaced due to manufacturing inaccuracies. The precision ranges from 0.0033 pixels and the accuracy from 0.017 pixels (or 1/300 pixels, ~ 50 nm [37]) to 100 nm or 0.006 pixels, the latter value being considered as an upper limit. The value of 0.0056 pixels [38] will be used as the accuracy. As suggested in [38], additional sources of error arise from the design and operational characteristics of the CCD, which should be considered to include the inaccuracy due to the inaccuracy of the reference length reading.

Additional sources of error, such as dark current, open rate, noise, can be expected from the design and operational characteristics of the CCD. These are taken into account when reading the image distance according to [38].

If the calibration plane and the laser plane (measurement plane) are in a small angular misalignment, a slight distortion will result. For small angles $\theta = 0.035$ rad (accuracy = 2° = 0.035 rad), the recorded distance l_{sel} will be smaller by $l_{sel} \theta^2$. The magnification then takes the following form:

$$\alpha = \frac{l_{sel} - l_{sel}\theta^2}{L_{sel}} \tag{17}$$

and the sensitivity factor:

$$\frac{\partial \alpha}{\partial \Delta\theta} = -2\frac{l_{sel}\,\theta}{L_{sel}} = -2\frac{31.5[mm] \cdot 0.035[rad]}{365\,[pixel]} = -0.006041[mm/pixel] \tag{18}$$

3.2.3. ERROR RESULTING FROM DE-WARPING RECONSTRUCTION

The de-warping error usually occurs when images are taken through a container with a curved surface. In this case, the lens effect of the outer surface of the tank must be compensated for by de-warping reconstruction. Since there are no images taken through curved surfaces in our own measurement geometry, we do not need to take into account the warping distortion due to the lensing effect of curved surfaces. The camera looks perpendicular to the wall of the rectangular channel under the measurements.

3.2.4. ERROR SOURCES AND SENSITIVITY FACTORS FOR ΔX DISPLACEMENT

The displacement ΔX is affected by the current positions of the tracer particles, the properties of the image processing system, and the properties of the illumination system.

3.2.5. ERROR DUE TO THE ILLUMINATION

The spatial and temporal fluctuations of the illumination plane affect the observed position of the particles. According to the literature [33] [32], the variation is 1/10 of the particle diameter, which in our case is 0.1dp = 0.005 mm. Since two consecutive images must be considered, the absolute accuracy $\sqrt[2]{2 \cdot 0.005^2} = 0.007 \; mm$. From equation (1), the velocity can be calculated as follows:

$$u = \frac{\Delta x}{\Delta t} = \alpha \frac{\Delta x}{\Delta t} \tag{19}$$

The displacement in the picture is due to:

$$\Delta X = \frac{\Delta x}{\alpha} \tag{20}$$

The sensitivity factor will be:

$$\frac{\partial \Delta X}{\partial \Delta x} = \frac{1}{\alpha} = \frac{1}{0.08630137 \left[\frac{mm}{pixel}\right]} = 11.5873 \; [pixel/mm] \tag{21}$$

3.3. UNCERTAINTIES ARISING FROM THE IMAGE CAPTURE SYSTEM

The error due to optical distortion has already been taken into account in section 2.2.2. The accuracy for distortion due to CCD technology is 0.0056 pixels. As shown in section 2.2.2 the sensitivity factor is 1 [38]. Additional sources of error due to the design and operational characteristics of the CCD should be considered as sub-pixel analysis accuracy [38].

3.3.1. IMAGE PROCESSING, DISPLACEMENT CALCULATION

The calculation of the particle displacement uses the sub-pixel analysis methodology to determine the position of the correlation peaks at a resolution below 1 pixel. The accuracy of sup-pixel analysis is a function of several factors. Based on the analysis presented in the literature [38], the uncertainty of the sub-pixel analysis is 0.033 and 0.017 pixels and the sensitivity factor is 1.

The effect of smoothing due to the selection of the interrogation area is an accuracy of 0.008 pixels and a sensitivity factor of 1 [38].

3.3.2. ERROR SOURCES AND SENSITIVITY FACTORS FOR THE Δ𝑇 INTERVAL

Δt is the time interval between the two images, which has two sources of error: the timing of the laser pulses and the error of the interval, which is determined by the timer box properties.

3.3.3. UNCERTAINTY DUE TO THE DELAY GENERATOR (TIMER) TIMING

An error due to inaccuracy of the timer can be determined from the description of the current device. If this is not available, [38] also provides recommendations for this value. The accuracy of the Dantec Timer Box 80N77 pulses used is 12.5 ns [40]. The sensitivity factor is 1 [38].

3.3.4. UNCERTAINTY DUE TO THE TIMING OF THE LASER

During the operation of the lasers a so-called jitter phenomenon is typical, which is the inaccuracy of the timing of the laser pulse. Information on the accuracy of jitter can be found in the manual of the light source [41]. Again, if the available data are unclear or inaccurate, the literature suggests a definition here [38]. According to the documentation of the Litron Nano L

135-15 PIV laser used in our measurements, the jitter is less than 0.5 ns and this is taken into account for accuracy and precision [79]. The sensitivity factor is 1 [38].

3.4. ERROR SOURCES AND SENSITIVITY FACTORS FOR THE ΔU SPEED DIFFERENCE

3.4.1. UNCERTAINTY DUE TO THE FLOW FOLLOWING ABILITY OF THE TRACER PARTICLE

There are two sources of errors due to the flow following capability of the tracer particles, one is the source of error due to the inertia (acceleration following) of the particles, which is a problem for rapid direction changes, and the other is due to the settling velocity of the particles. Based on the literature search, the acceleration following can be defined by the frequency response of the particles. In practice, this means that acceleration following shows how a particle behaves in a flow situation with sinusoidally varying velocity, i.e. how it tracks the motion of a fluid with time-varying velocity. This skill depends, among other things, on the specific density of the particle and the particle size. Gravitational settling is negligible except in the case of low velocity flows. According to the literature [42], if the relative density $(0.56 < \rho\_p/(\rho\_f \approx 1 < 1.62))$ is in the appropriate range, the particle has good tracking properties. In our case, the density of the polyamide is 1.02 g/cm^3 and the relative density is 1.035, so it can be considered as a good tracker.

According to Stokes' law, the settling velocity can be calculated as follows:

$$\overrightarrow{U_g} = d_p{}^2 \frac{(\rho_p - \rho_f)}{18\mu} \vec{g} = 0.00005 \ [m]^2 \frac{(1030\left[\frac{kg}{m^3}\right] - 995.71\left[\frac{kg}{m^3}\right])}{18 \cdot 7.98 \cdot 10^{-4}[Pa \cdot s]} \overrightarrow{9.81} \left[\frac{m}{s^2}\right] \cdot 1000 = 0.05854 \left[\frac{mm}{s}\right]$$

(22)

where g is the acceleration due to gravity, μ is the dynamic viscosity of the fluid, ρ_p and ρ_f are the particle and fluid densities, d_p is the particle diameter. In our case, the settling velocity is 0.059 mm/s and acts only in the direction parallel to the gravitational acceleration, with a sensitivity factor of 1.

3.4.2. THREE-DIMENSIONAL EFFECTS ON PERSPECTIVE OF VELOCITY

A particle moving in a finite-thickness plane of light does not necessarily move in a two-dimensional plane; the flow-tracking particle may have a velocity component perpendicular to the plane of light. The measured velocity can be described as follows:

$$w_m = w + v \cdot tang\varphi \qquad (23)$$

where v is the velocity component perpendicular to the plane. The angle of perspective can be estimated from the distance between the target plane and the objective, and the width of the captured images. If the out-of-plane velocity component is 1% of the mean flow velocity (w), then the velocity magnitude can be calculated as follows [38].

$$w \cdot tang\Theta = 0.001 \cdot 2.01125 \left[\frac{m}{s}\right] \cdot tang(11.41°) = 0.406 \ [mm/s] \qquad (24)$$

The sensitivity factor is 1.

3.4.3. UNCERTAINTY DUE TO VOLUME FLOW ADJUSTMENT

One form of inaccuracy in the measurements is due to the measurement of the volume flow and the flow cross-section. Based on the law of continuity:

$$w = \frac{\dot{Q}}{A} \tag{25}$$

where w is the main velocity component of the flow, Q is the volumetric flow and A is the cross-sectional area (828.67 mm^2). The flow cross-section is 6.33% based on the manufacturing dimensions and our measured values and has a value of 52.44 mm^2. The sensitivity factor:

$$\frac{\partial w}{\partial A} = -\frac{\dot{Q}}{A^2} = -\frac{1.666E6\left[\frac{mm3}{s}\right]}{828.67^2[mm^4]} = -2.427\left[\frac{1}{smm}\right] \tag{26}$$

The error from the volumetric flow measurement was reduced by connecting 3 volumetric flow meters of the same type in series to the test equipment. We measured their data using a measurement program we developed. Based on the time average of the results (which fluctuate slightly over time), the desired flow rate of 6000 l/h was set. The maximum deviation of the flow rate control observed during our measurements was 1.07%, so conservatively an error of 2% was assumed. This is much smaller than the manufacturer's recommended measurement error of 5% for 1 flow meter [43]. Thus, this method was used to reduce the inaccuracy resulting from the adjustment of the volumetric flow. The sensitivity factor:

$$\frac{\partial w}{\partial \dot{Q}} = \frac{1}{A} = \frac{1}{828.669[mm^2]} = 0.001207[mm^{-2}] \tag{27}$$

3.5. ERROR SOURCES DUE TO SAMPLING

It is a general procedural methodology for PIV measurement to generate the results from the average of several image pairs. Many publications discuss the need to sample these image pairs in such a way that the variance of the final result is sufficiently small. In his doctoral thesis, Yamaji Bogdan examined in detail the effect of the number of samples taken on the accuracy of the result [33]. His investigations show that the variance of the measured velocity is less than 5% after 500 image pairs and that 1000 image pairs produce reliable results. Since in our case, the flow velocities are higher and the degree of turbulence is higher, we calculated the results from the time average of 1900 image pairs to be absolutely sure [33]. The vector fields computed separately from 1900 image pairs were subjected to a coherence filter, which excluded incoherent vectors. Therefore, in reality, the time averaging was done from fewer data points (about 1400-1900) from 1900, and their number varies from pixel to pixel.

For a selected point (NOVANE type vane, 1D distance from the second spacer and -15 mm from the origin of the flow channel), the standard deviation of the axial velocity vector σ=0.74303 [m/s] based on the PIV measurement system:

$$SD_{mean} = \sigma/\sqrt{N} = 0.74303[m/s]/\sqrt{1657} = 18.2536 \left[\frac{mm}{s}\right] \tag{28}$$

Where N is the number of samples (N=1657).
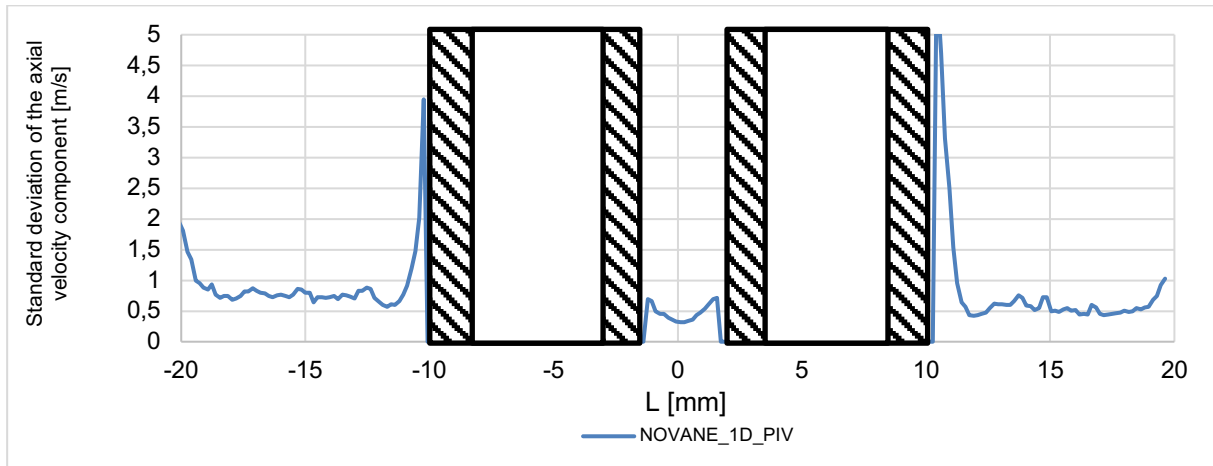
Figure 7: Standard deviation of the axial velocity component along a given evaluation line in the NOVANE grid type measurements at 1D distance after the second spacer

In Figure 7, we plot the line wise distribution of the standard deviation σ for clarity. It can be seen that the uncertainties increase along the walls and the values are higher than in the inner regions of the channels.

3.6. ERROR CALCULATION SAMPLE FOR A SELECTED POINT

In this subsection, a calculation procedure is presented for a selected point located: the NOVANE vane type, at a distance of 1D from the second spacer and -15 mm from the origin of the flow channel. At this point, the w (axial direction velocity component) is 3.325 m/s = 3325 mm/s.

Parameter	Sub-system	Error source	Absolute accuracy [B_{ij}]	Absolute precision [S_{ij}]	Sensitivity factor [θ]
α magnification factor	Calibration	Reading of reference point	B_{11}=0.707 [pixel]	-	$\theta_{11} = -0.00023644\ [mm/pixel^2]$
		Physical distance	B_{21}=6.3E-1 [mm]	-	$\theta_{21} = 0.002739\ [1/pixel]$
		Optical distortion	B_{31}=0.005xLsel=1.825 [pixel]	-	$\theta_{31} = -0.00023644\ [mm/pixel^2]$
		CCD distortion	B_{41}=0.0056 [pixel]	-	$\theta_{41} = -0.00023644\ [mm/pixel^2]$
			B_{51}=0.035 [rad]	-	$\theta_{51} = -0.006041[mm/pixel]$
ΔX displacement in the image plane	Data recording	Angle of calibration plane and illuminated plane	B_{12}=0.00707 [mm]	-	$\theta 12$=1/α= 11.5873 [pixel/mm]
			B_{22}=0.0056 [pixel]	-	θ_{22}=1
	Data processing	Displacement calculation	B_{13}=0.017 [pixel]	S_{13}=0.033 [pixel]	θ_{13}=1
		Smoothing by interrogation	B_{23}=0.008 [pixel]		θ_{23}=1
Δt time delay	Data recording	Timer jitter	B_{42}=1.25E-08 [s]	S_{52}=5E-10 [s]	θ_{42}=1
		Laser jitter	B_{52}=5.00E-10 [s]		θ_{52}=1
δu velocity difference	Measurement principle	Gravitational settling	B_{13}=0.05854 [mm/s]	-	θ_{13}=1
		Three-dimensional effects on perspective of velocity	B_{23}= 0.406 [mm/s]	-	θ_{23}=1
	Volume flow adjustment	Flow cross-section	B_{33}=52.44[mm2]	-	θ_{33}=-2.4271[1/smm]
		Volume flow adjustments	B_{43}=3.33E-6 [m³/s]	-	θ_{43}=0.001207[mm⁻²]

Table 2: Summary of PIV subsystem uncertainties

Calculated using the values in Table 2:

$$B_\alpha = [(B_{11}\theta_{11})^2 + (B_{21}\theta_{21})^2 + (B_{31}\theta_{31})^2 + (B_{41}\theta_{41})^2 + (B_{51}\theta_{51})^2]^{1/2}$$
$$= \Big[(0.707\,[pixel] \cdot -0.00023644)^2 + (6.3E-1\,[mm] \cdot 0.002739\,[\tfrac{1}{pixel}])^2$$
$$+ (1.825\,[pixel] \cdot -0.00023644)^2 + (0.0056\,[pixel] \cdot -0.00023644)^2$$
$$+ (0.035\,[rad] \cdot -0.006041[mm/pixel])^2\Big]^{1/2} = 0.001799452\,[\tfrac{mm}{pixel}]$$

$$\boldsymbol{B_\alpha = 0.001799452\,[\tfrac{mm}{pixel}]}$$

$$\boldsymbol{S_\alpha = 0}$$

$$B_{\Delta X} = [(B_{12}\theta_{12})^2 + (B_{22}\theta_{22})^2 + (B_{13}\theta_{13})^2 + (B_{23}\theta_{23})^2]^{1/2}$$
$$= [(0.00707\,[mm] \cdot 11.5873\,[pixel/mm])^2 + (0.0056[pixel] \cdot 1)^2$$
$$+ (0.017 \cdot [pixel]1)^2 + (0.008\,[pixel] \cdot 1)^2]^{1/2} = 0.08424\,[pixel]$$

$$\boldsymbol{B_{\Delta X} = 0.08424\,[pixel]}$$

$$\boldsymbol{S_{\Delta X} = [(S_{13}\theta_{13})^2]^{1/2} = [(0.033\,[pixel] \cdot 1)^2]^{1/2} = 0.033\,[pixel]}$$

$$B_{\Delta t} = [(B_{42}\theta_{42})^2 + (B_{52}\theta_{52})^2]^{1/2} = [(1.25E-08\,[s] \cdot 1)^2 + (5E-10\,[s] \cdot 1)^2]^{1/2}$$
$$= 1.251E-08\,[s]$$

$$\boldsymbol{B_{\Delta t} = 1.251E-08\,[s]}$$

$$\boldsymbol{S_{\Delta t} = [(S_{52}\theta_{52})^2]^{1/2} = [(5E-10[s] \cdot 1)^2]^{1/2} = 5E-10[s]}$$

$$B_{\delta u} = [(B_{23}\theta_{23})^2 + (B_{43}\theta_{43})^2 + (B_{43}\theta_{43})^2]^{1/2} = [(0.406\,[mm/s] \cdot 1)^2 + (52.44[mm^2] \cdot$$
$$-2.4271\,[1/(smm4)])^2 + (3.33E-6 \cdot 0.0012067)^2]^{1/2} = 127.27\,[mm/s]$$

$$\boldsymbol{B_{\delta u} = 127.27\,[mm/s]}$$

The contribution of different factors to uncertainty:

$$B_\alpha/\alpha = 0.001799452\,[\tfrac{mm}{pixel}]\Big/0.0863017\,[\tfrac{mm}{pixel}] = 2.085\%$$

$$B_{\Delta X}/\Delta X = 0.08424\,[pixel]/2.0265[pixel] = 4.65\%$$

$$B_{\Delta t}/\Delta t = 1.251E-8\,[s]/5E-5[s] = 0.025\%$$

$$B_{\delta u}/\delta u = 127.27[\tfrac{mm}{s}]/3325\,[\tfrac{mm}{s}] = 3.827\%$$

$$B_u/U = \sqrt{(B_\alpha/\alpha)^2 + (B_{\Delta X}/\Delta X)^2 + (B_{\Delta t}/\Delta t)^2 + (B_{\delta u}/\delta u)^2} =$$

$$\sqrt{(0.02085)^2 + (0.04648)^2 + (0.00025)^2 + (0.04236)^2} = 0.0602 = 6.02\%$$

$$S_\alpha/\alpha = 0$$

$$S_{\Delta X}/\Delta X = 0.033[pixel]/2.0265\,[pixel] = 1.63\%$$

$$S_{\Delta t}/\Delta t = 5E-10[s]/5E-5\,[s] = 0.001\%$$

$$S_{\delta u}/\delta u = 0$$

$$SD_{mean}/U = 18.2536\,[\tfrac{mm}{s}]/3325\,[\tfrac{mm}{s}] = 0.55\%$$

$$S_u/U = \sqrt{(S/\alpha)^2 + (S_{\Delta X}/\Delta X)^2 + (S_{\Delta t}/\Delta t)^2 + (S_{\delta u}/\delta u)^2} =$$

$$\sqrt{(0)^2 + (0.0163)^2 + (0.00001)^2 + (0)^2} = 0.0182 = 1.82\%$$

$$\boldsymbol{U_{uSSR}/U = \sqrt{(B_u/U)^2 + (2 \cdot S_u/U)^2 + (SD_{mean}/U)^2} = 0.0687 = 6.87\%}$$

The selected sample count point is marked in Figure 8. The relative error of the measurement at this point is ~6.87%. This relative error is higher at lower velocities (along walls), as most sources of error in the uncertainty analysis are constant and few depend on the actual velocity vector of the measured flow.
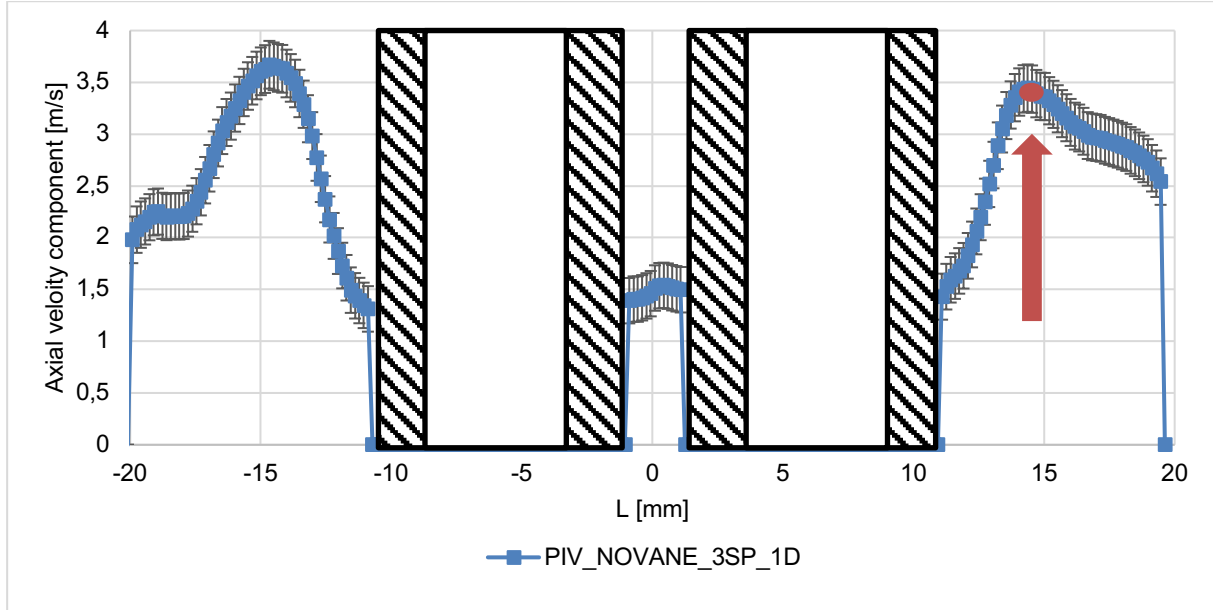
Figure 8: Axial velocity profiles after the second spacer for the NOVANE grid at 1D distance after the grid
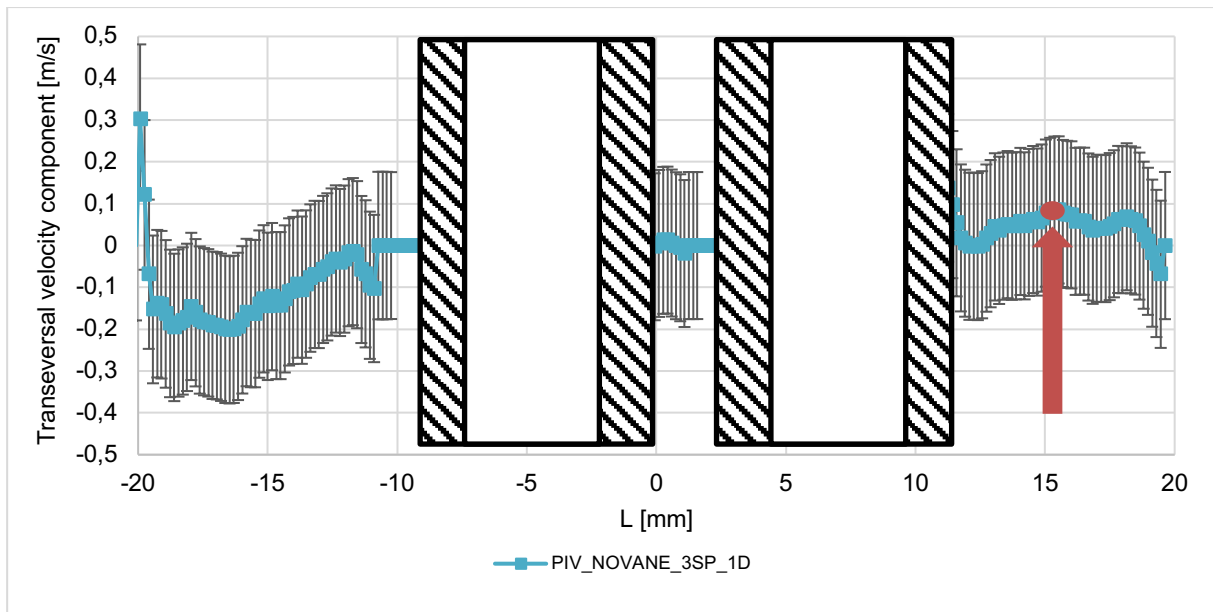
Figure 9: Transverse velocity profiles after the second spacer for the NOVANE grid at 1D distance after the grid

The error of the transverse velocity component is also plotted in Figure 9. Since the velocity values are much smaller in absolute value for the lateral velocity vectors, the uncertainties are also larger. In the error analysis of the transverse velocity components, the uncertainty from gravity settling and volumetric flow measurements were not considered, as they typically only occur in the axial velocity vectors of the flow.

4. INTERPRETING THE FLOW STRUCTURES BEHIND THE SPACER GRIDS

4.1. INTERPRETATION OF THE 2D VECTOR FIELDS AFTER THE SPACERS

Figures 10 and 11 show the results of our measurements at the heights of the spacers. The position of the plane of the vector fields can be seen in Figure 5. The flow field presented below was captured on a plane positioned at Y=-11 mm. The plane passes through the side channels of the test section, the two outer rods, and the subchannel between the two outer rods. The very top of the spacer grids and the silhouette of the outer mixing vane (marked with white ovals) can be seen in the figures.

The NOVANE grid type uses the vaneless spacer grid as its name suggests. In the flow cross-sections along the wall, two larger jets are observed and the velocity values in the gap between the rods are much lower. The reason behind this phenomenon is that the narrow inner subchannel has a higher flow resistance than the channels in the corners. As a result, more and more water is directed to the channel of the corners and downstream less and less remains in the subchannels between the rods. It can be observed that the velocity of the medium is similar after the second and third spacer. After the third spacer, the velocity is slightly lower due to the pressure loss caused by the wall friction.

The SPLIT grid type also has maximum flow velocities in the corner regions. In the channel between the two rods (marked by the white oval), the effect of the mixing vanes is clearly visible. Immediately after the mixing vanes, a region of higher velocity is visible, indicating the presence of a medium swirled and accelerated by the vanes. The axial velocity peak is shifted close to the grid in this region. A relatively uniform velocity distribution is created downwards the aforementioned region.
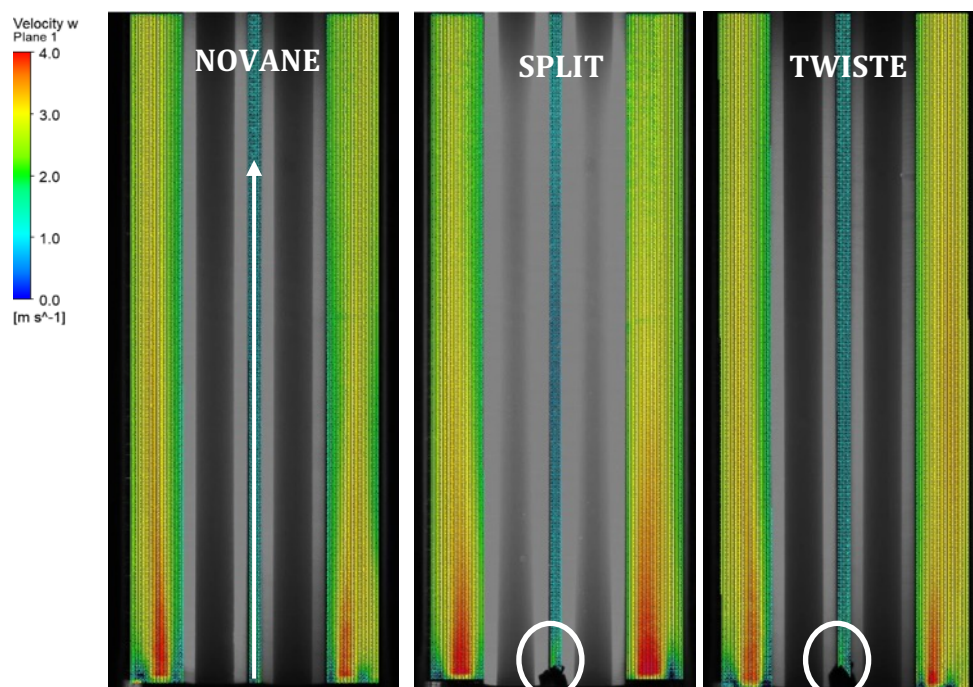
Figure 10: Velocity distributions in the region downstream the second spacer grid
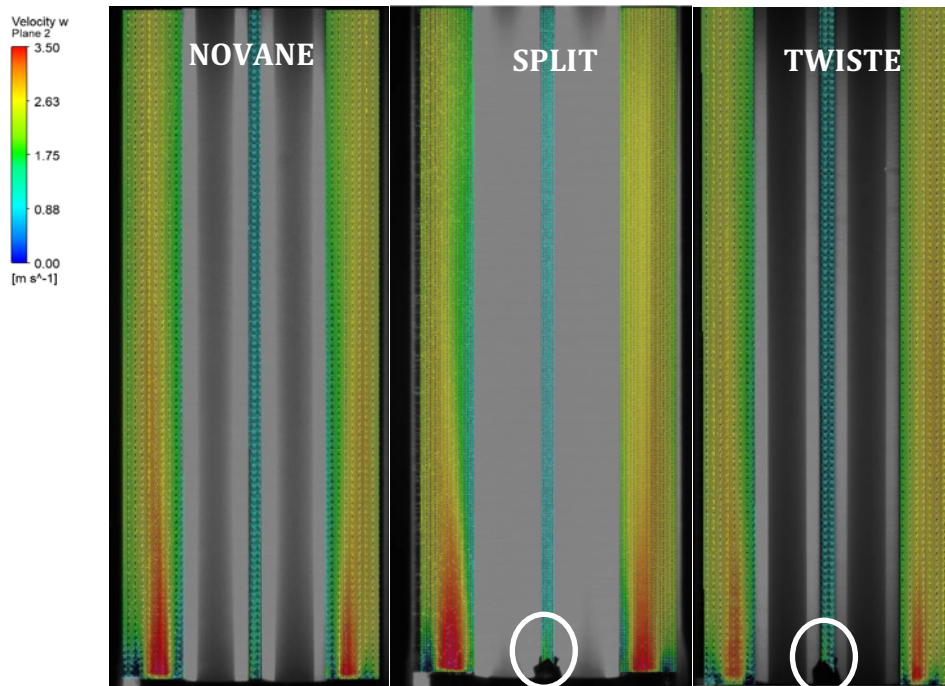
Figure 11: Velocity distributions in the region downstream the third spacer grid

The flow structure created by the mixing vanes can also be observed after the TWISTED spacer grid. The shape of the jets in the channel corners of the TWISTED vanes is similar to that observed for the NOVANE spacer. A relatively even velocity distribution is created in the subchannel between the two rods.

For all the velocity distributions of each vane type, it is observed that the vector field is not symmetric. In the case of spacers with vanes, the reason for this is that the diverse flow created by the vanes drives the medium in a circle along the channel wall. And in the NOVANE case, the cause is the 120° symmetry of the rod-spacer contact point (see in Figure 18), which is not mirror symmetric to the plane (see in Figure 5).

4.2. INTERPRETATION OF CENTRELINE VELOCITY DISTRIBUTIONS

In this section, we investigate the axial and transversal velocities in the subchannel between the two outer rods. The position of the monitor line is shown in Figure 10 (white vertical arrow) In the first figures (Figures 12 to 17), the velocity distributions after the 2nd and 3rd spacers are compared for the respective spacer grid types. This gives an insight into how the consecutive spacers interact. The reference distribution is given by the vaneless NOVANE spacer type.

Figure 12: Axial velocity distributions in the gap between the two rods as a function of height for NOVANE grid type downstream the 2nd and 3rd spacers (monitor line position marked in Figure 10 with white arrow)

Figure 12. shows the axial velocity change as a function of height downstream of the 2nd and 3rd spacers. After the spacers, a maximum is observed, created by the decreasing flow cross-section caused by the spacer, accelerating the fluid. It can be seen that the velocity distributions are identical after the spacers.

Figure 13: Transversal velocity distributions in the gap between the two rods as a function of height for NOVANE grid type downstream the 2nd and 3rd spacers (monitor line position marked in Figure 10 with white arrow)

In Figure 13, the axial distribution of the transversal velocity components is presented. In most parts of the investigated section, the value is around 0 m/s. A milder transversal mixing is visible only in the closest region behind the spacer (the first 15 mm section). The distribution after the 2nd spacer (blue line) shows a larger velocity fluctuation than after the 3rd one. This may be due to the unstable nature of the flow or to the uncertainty of the measurement in the region of interest. This aspect needs to be investigated more. The transversal velocity values measured after the NOVANE grid are generally 2 order of magnitude lower than the axial velocity values.

In contrast, the absolute value of the uncertainties is of a similar order of magnitude (approximately in the range of ~0.18 m/s). The error bars are not presented here due to better observation of the results.
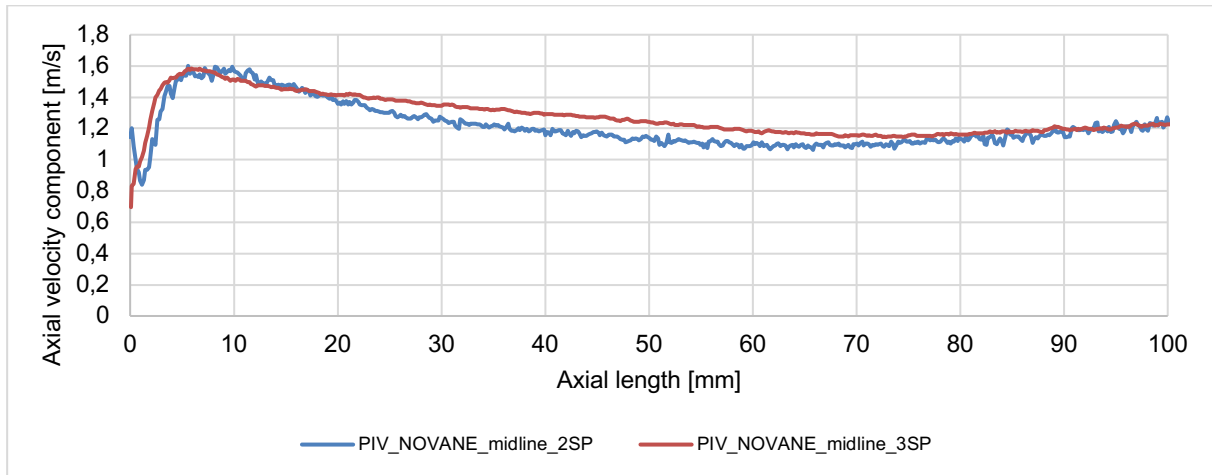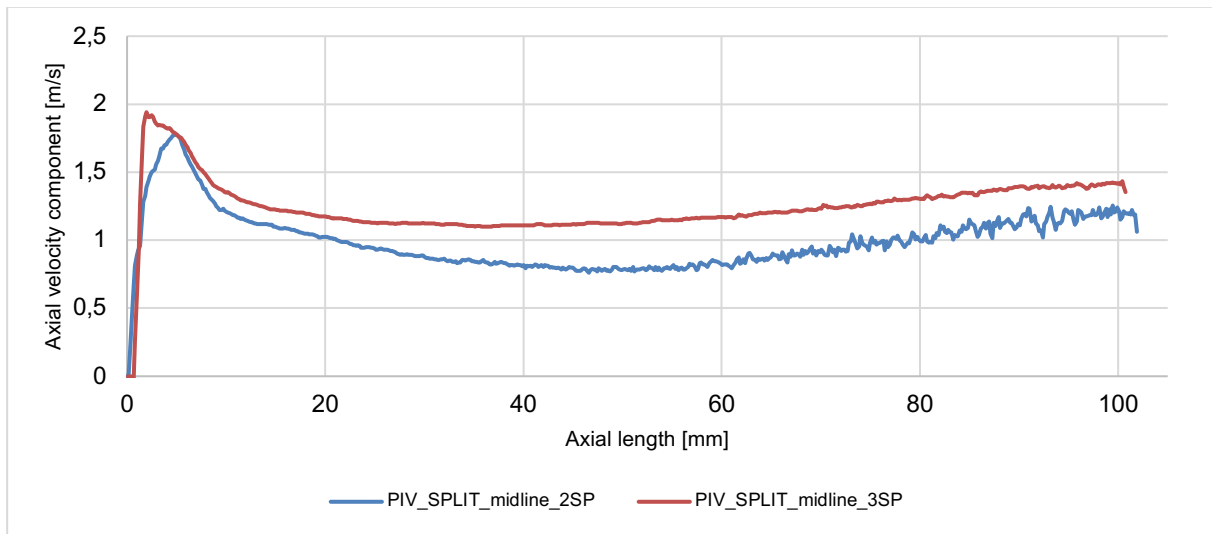

Figure 14: Axial velocity distributions in the gap between the two rods as a function of height for SPLIT grid type after 2nd and 3rd spacers (monitor line position marked in Figure 10 with white arrow)

In Figure 14, the axial velocity values for the SPLIT type case are shown. Also, in this case a peak in the velocity values is observed immediately after the spacer, which is more pronounced after the third spacer. Furthermore, after the third spacer the axial velocity seems to settle to a higher average value. This clearly points to the beneficial effect of the mixing vane, since the average velocity increases in the region with a narrower flow cross-section in the case of the SPLIT vane. This would lead to an improvement in heat transfer.
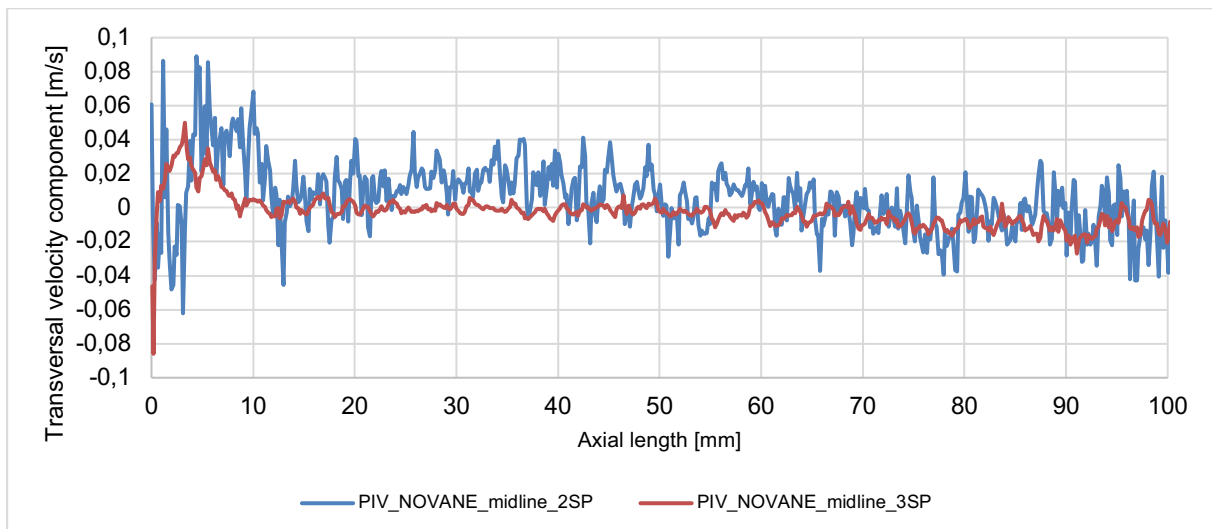

Figure 15: Transversal velocity distributions in the gap between the two rods as a function of height for SPLIT type grid after 2nd and 3rd spacers (monitor line position marked in Figure 10 with white arrow)

Figure 15 shows the transversal velocity distributions after the 2nd and 3rd SPLIT type spacers. After the second spacer, the initial peak value is slightly larger (max=0.22 m/s) than for the third spacer (max=0.12 m/s). About 30 mm after the grid, the transversal velocity values return to around 0 m/s. However, these values are much higher than the transversal velocity values of the NOVANE grid.
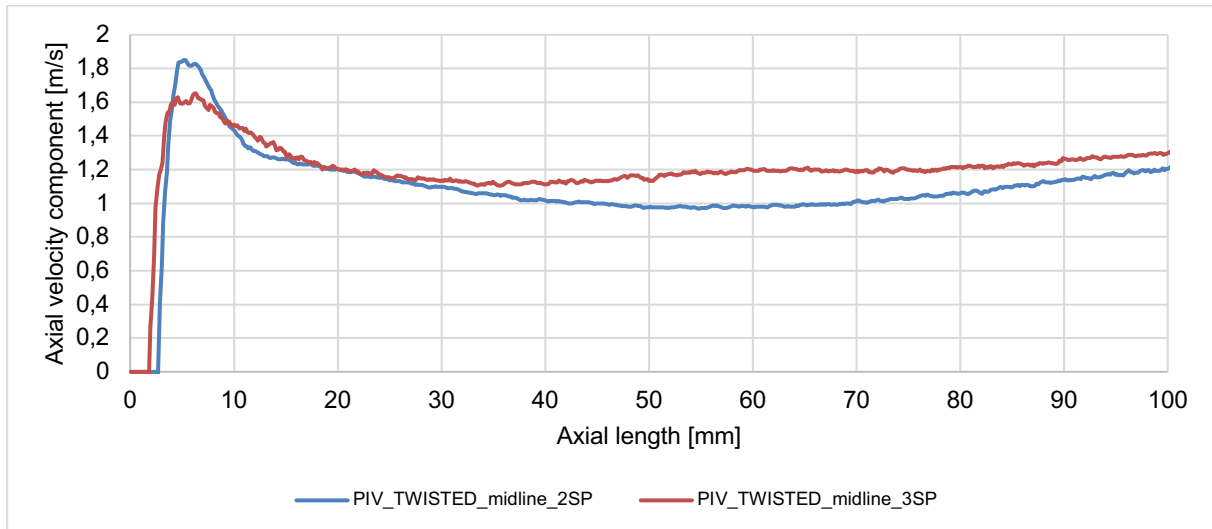
Figure 16: Axial velocity distributions in the gap between the two rods as a function of height for TWISTED type spacers after the 2nd and 3rd grid (monitor line position marked in Figure 10 with white arrow)

The axial velocity distribution of the TWISTED vanes also shows a higher velocity maximum after the second grid, but the average axial velocities are higher after the third spacer.
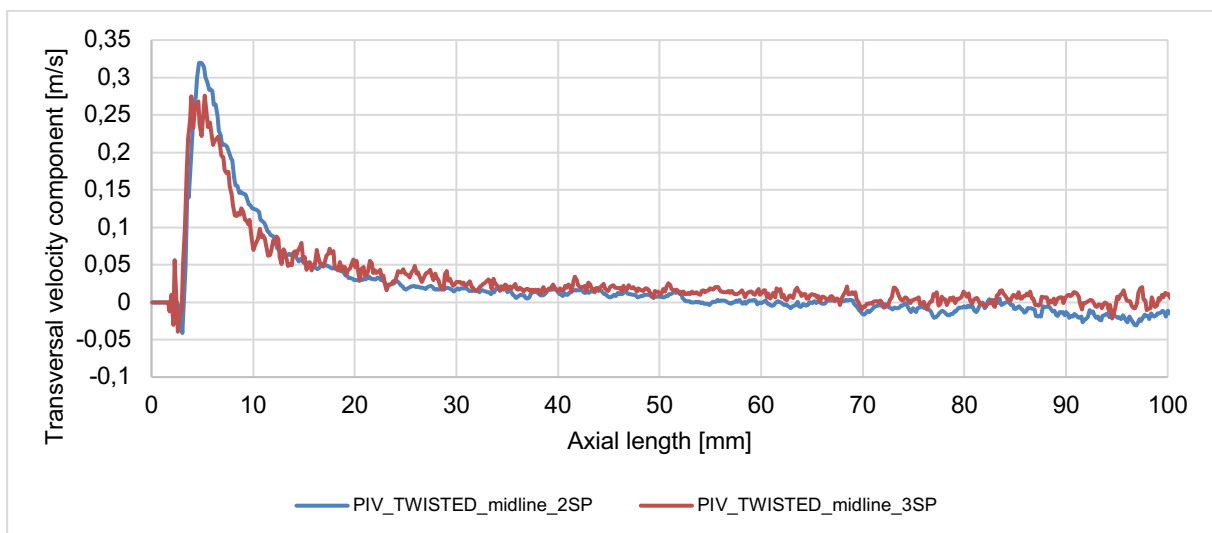
Figure 17: Transversal velocity distributions in the gap between the two rods as a function of height for TWISTED type spacer after the 2nd and 3rd grid (monitor line position marked in Figure 10 with white arrow)

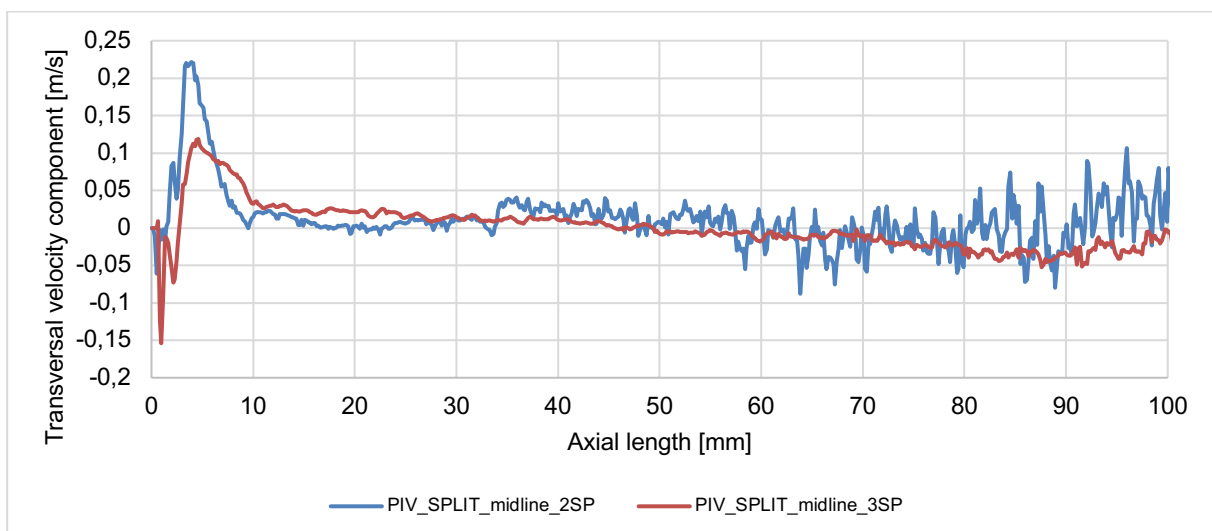Figure 17 shows the transversal velocity decay after TWISTED vanes. It can be noticed that the values are almost identical in the region after two consecutive spacergrids.
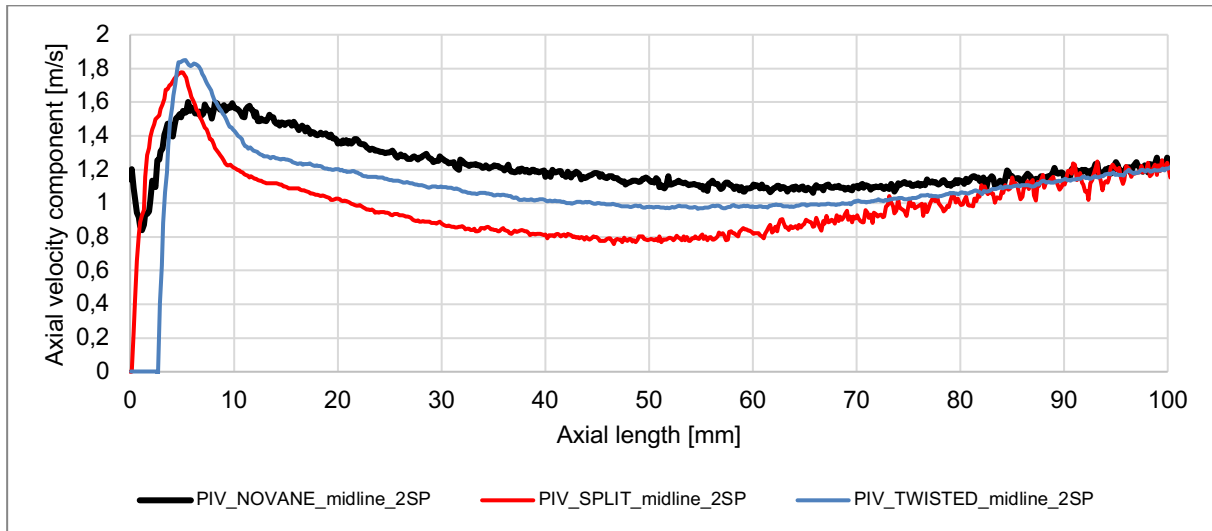
Figure 18: Axial velocity distributions in the gap between the two rods as a function of height in the case of the different grid types after the 2nd spacer (monitor line position marked in Figure 10 with white arrow)

In Figure 18, the axial velocity component distributions can be seen for different spacer types. In cases of the spacers with vanes, the axial velocity peak is notably higher, than the reference NOVANE case. The highest velocity peak occurred by the TWISTED type spacer (see accurate values in Table 3). The velocities along the monitor line also differ far away from the grids, but at 9-10D (90-100 mm) distance, the differences are leveling out. At the distance of 1D-8D, the NOVANE spacer produce the highest axial velocity values, which can be explained by the fact that the NOVANE grid has the lowest flow resistance.
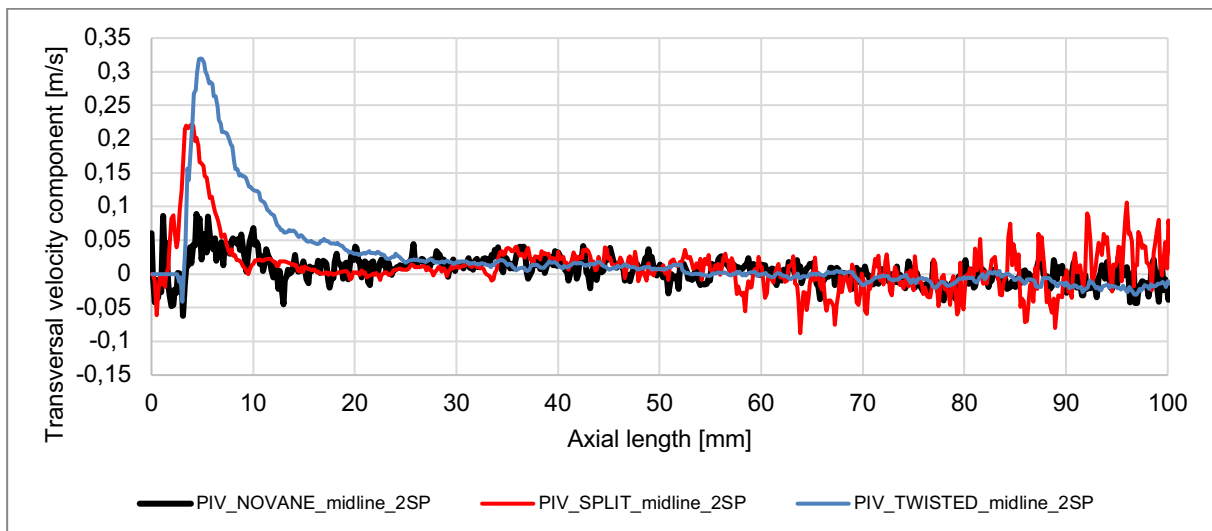
Figure 19: Transversal velocity distributions in the gap between the two rods as a function of height in the case of the different grid types downstream the 2nd spacer (monitor line position marked in Figure 10 with white arrow)

In Figure 19, the transversal velocity values are displayed. It is clear and obvious, that the TWISTED type spacer can produce the highest velocity values after the spacer, and the SPLIT type vane also creates higher values than the NOVANE spacer. The effect of the spacer is

observable in 3D distance in the case of the TWISTED vane, while in case of the SPLIT type vane the strong spike like effect disappears at 1D. In the case of the SPLIT vane, we see larger statistical excursions in regions far from the grid. The NOVANE grid produces values close to zero along almost the entire length tested.

	NOVANE	SPLIT	TWISTED
Maximum axial velocity [m/s]	1.6	1.78	1.85
Line along average axial velocity [m/s]	1.22	0.996	1.089
Maximum transversal velocity [m/s]	0.0891	0.221	0.320
Line along average transversal velocity [m/s]	0.00543	0.0126	0.0205
Pressure difference on 2nd spacer (from CFD) [Pa]	3934	4272.7	4170.3
Relative pressure loss increases to NOVANE 2nd spacer	0 %	8.6 %	6 %

Table 3: Average and maximum velocity values for different grid types

The maximum and average axial and transversal velocities after the second grid are collected in Table 3. Regarding axial velocity, the TWISTED type spacer gives the highest maximum, although the average axial velocity is higher in the case of the NOVANE type spacer. This can be explained by the fact that the spacer with vanes has a higher resistance than the NOVANE spacer. In terms of maximum transversal velocity, the TWISTED type also stands out. Along the monitor line, the TWISTED has an average transversal velocity value of ~1.6 times greater than measured for SPLIT type vanes. The pressure drops for the second grid and the 10D long rod bundle sections are also shown in Table 3. It was not possible to measure these characteristics during the measurements, so the values are given by CFD calculations. The result was calculated with the M3 mesh and the SST turbulence model (see details in Chapter 6) and gives the pressure difference between the lower planes of the grids and the 10D distance after the grid. This allowed the change in pressure loss through the mixing vanes to be monitored. According to the CFD model results, the TWISTED MVG has a slightly lover pressure loss increase, then the SPLIT type MVG.

In light of these results, it can be said that the NOVANE grid can generate higher flow rates in the post-grid region. Our previous research [12] [11] [24] has shown that there are hot spots in the assembly that can be eliminated using mixing vanes. These vanes would only be placed in the spacer grid positions after which these hotspots are formed. In this case, a locally increased heat transfer can result a more favorable temperature distribution. For this purpose, the TWISTED vane has been partially optimized in our previous study [24] and its effect has been demonstrated experimentally with these PIV measurements.

5. CFD MODEL CALCULATIONS OF THE PROUETTE SYSTEM AND COMPARISON TO THE PIV MEASUREMENTS

5.1. CFD MODEL DESCRIPTION

In this chapter, the 3D Computational Fluid Dynamics model of the PIROUETTE system is presented. CFD models have been created in parallel with the design and development of the experimental facility to support the design process and optimize the test section to the research needs and objectives. In addition, CFD models were used to develop the flow straightener, create the spacer mounts, and design the upper T-junction.
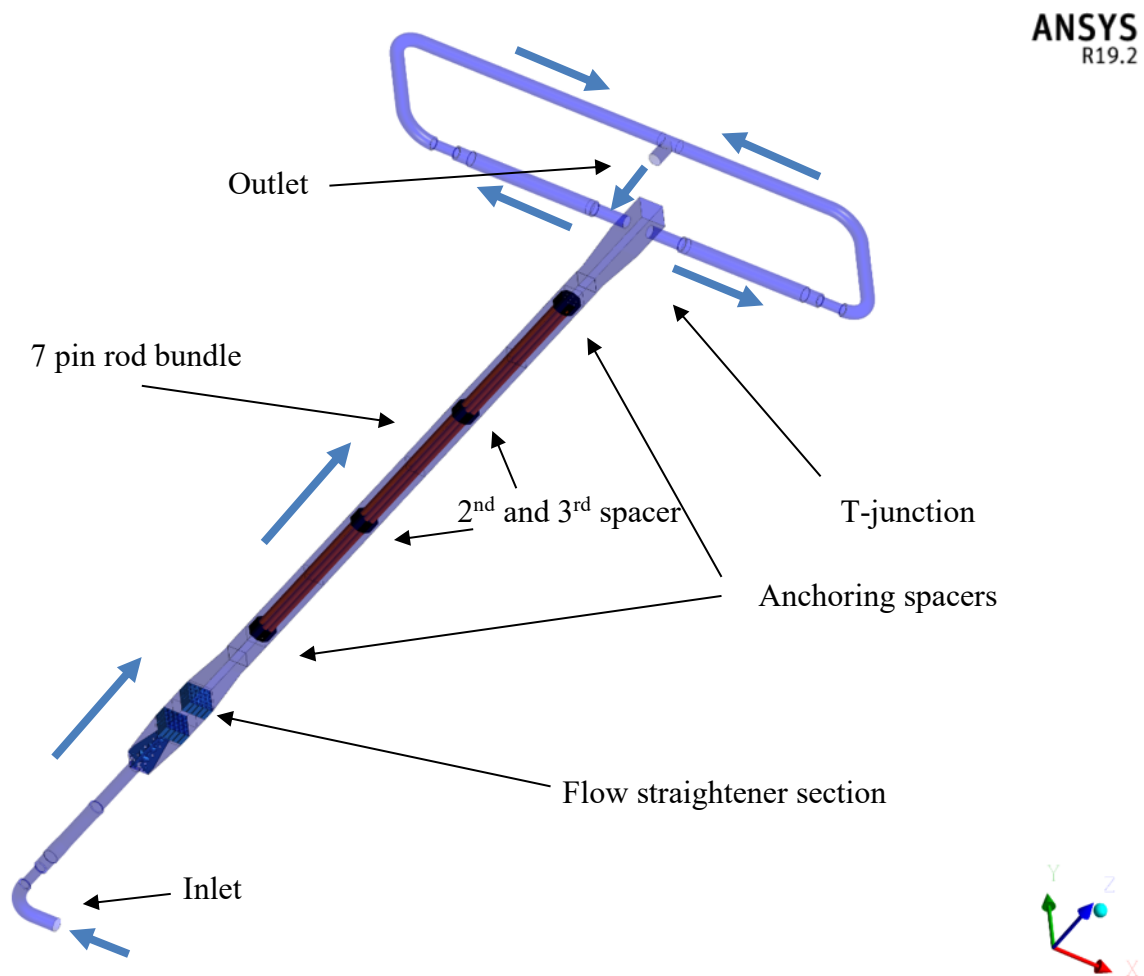
Figure 20: CFD model domain of the PIROUETTE experiment

Figure 20 shows the structure of the 3D CFD model. The Inlet boundary is located at the bottom of the system and includes the inlet pipe elbow. This was necessary in order to take into account possible disturbances caused by the pipe elbow. The flow straightener was deliberately designed with the objective that the elbow no longer had any effect on emerging flow conditions in the rod bundle test section. The pipe elbow is followed by the flow straightener section, including the deflector and the double straightener grid. The straightener is 300 mm long, and

the flow conditions of the part are currently examined in detail during the preparation of an international benchmark exercise [44] within the SafeG EU funded research project.

The CFD model has the same dimensions as in the real facility: the test channel is 1156 mm long and rectangular in cross-section (35 mm x 40 mm). The spacers are 28 mm high and the distance between them is 296 mm. The rods have a diameter of 10 mm. The rod bundle section is connected to the other channel sections from the bottom and top by an adapter with variable cross section. The cross-section of the channel in the T-junction is 50 mm x 50 mm. The fluid flows out of the T-junction in two opposite directions. The by-passing pipe sections are not of equal length due how the channel is fixed in the PIROUETTE facility. This may affect the velocity distribution in the T-junction; therefore, this section has been modelled, too.

The geometry of the spacer grids had to be slightly modified to achieve better mesh quality. The environments of the rod-spacer contact points have to be simplified in the CFD models, as the mesh quality around the rod-spacer contact points was drastically degraded. Figure 21 shows the original and simplified contact points (highlighted with purple ovals). For the simplified rod-spacer contact point, the spacer grid's protruding part is perpendicular to the rod surface, and therefore the wall meshing can be created much more reliably. In the original case, the rod-spacer contact points have a ramp-like rising surface approaching the much smaller contact point. Due to the very small gap between the ramped surface and the rod wall, the wall meshing will be of poor quality. It should be mentioned that this ramped design is necessary to ease the installation of the rod assembly in the experiments. Except for this modification, the geometry of the spacers and the mixing vanes are exactly the same as the 3D printed versions in reality.
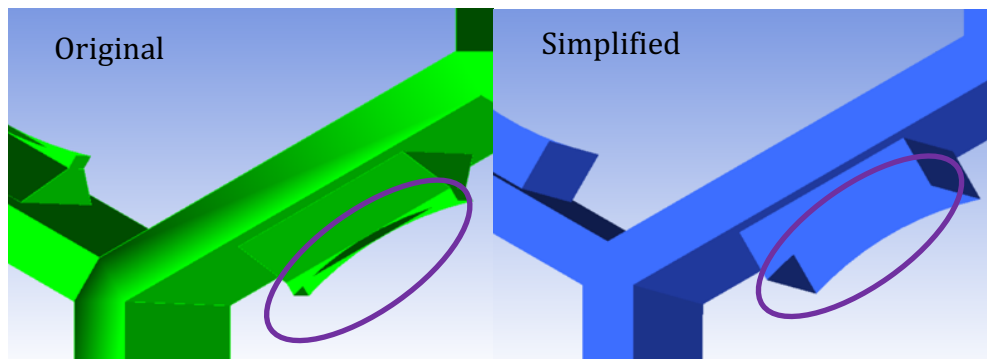
Figure 21: Connection points of the original and the simplified spacer grid

5.2. DEFINITION OF BOUNDARY CONDITIONS

The inlet boundary condition was given as a mass flow rate of 6 m³/h (1.6594 kg/s). The relative pressure at the outlet was defined as 0 Pa. The channel walls, spacers, rods, and straightening elements were assumed to be smooth walls (Smooth Wall). The velocity on the walls was zero (No Slip Wall). The flow was adiabatic and the water properties were determined at 30 °C and atmospheric pressure (Table 4). The different mesh regions were connected via 13 interfaces. This was necessary due to the complexity of the model structure. As primary turbulence model, the SST k-omega turbulence model was chosen. All the calculations were carried out using ANSYS CFX 19.2 code.

Water properties	Value
Temperature [°C]	30

Density [kg/m3]	995.652
Pressure [atm]	1
Dynamic viscosity [kg/m*s]	0.00079773

Table 4: Properties of water in the CFD calculations

5.3. MESH SENSITIVITY STUDY

In this investigation phase, a mesh independence test was performed with 4 models of different mesh densities. The mesh densities were varied only at the rod bundle section of the models. An average mesh resolution was created before and after the rod bundle section based on our experience. Table 5 summarises the properties of the different resolution models. The total model for the M4 mesh already consists of approximately 103 million elements. Considering the computational capacity available in our institute, it is the highest achievable discretisation. In Figure 22, the cross-sectional mesh densities are presented.

The meshes include tetrahedral elements around the spacer with layers of prismatic elements next to the solid walls. Above the tetrahedral region, in the bare rod bundle sections, the mesh consists of prismatic elements in the inner regions with hexahedral layers next to the walls.

	M1	M2	M3	M4
Number of elements in the rod bundle test section	6 914 604	17 999 798	35 74 973	103 436 982
Maximal element diameter [mm]	3	2	0.7	0.5
Properties of the mesh near the walls				
High of the first layer [mm]	0.1	0.08	0.02	0.01
Number of layers [-]	5	6	8	8
Height ratio [-]	1.2	1.2	1.3	1.3
Y+ on rod wall [-]	9.91	3.57	2.69	1.37
Y+ on spacer wall [-]	16.47	10.6	4.06	2.56

Table 5: Basic properties of meshes in the rod bundle
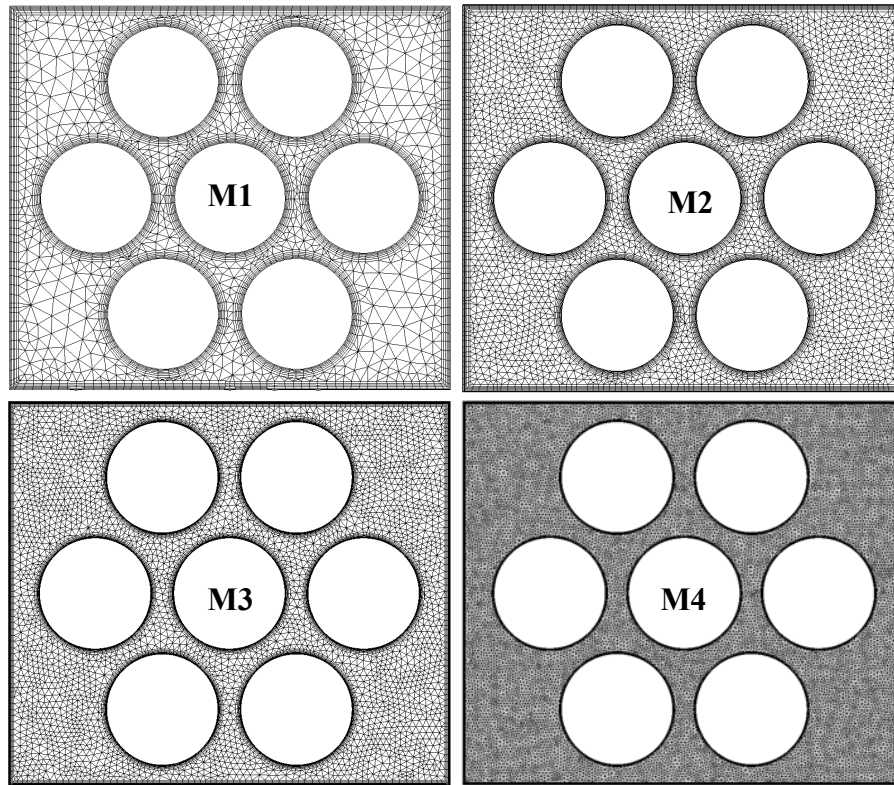
Figure 22: Cross-sectional mesh densities in the rod bundle

The velocity distributions evaluated along a line at different distances downstream of the third spacer grid are compared in the following figures. We have chosen this method for mesh independence studies because the comparison of the computed results with measurements will be presented for similar line-along velocity distributions. The investigated planes are in the same positions as the laser planes of the experiments. Y=-11 mm from the axis of the rod bundle (see Figure 5).
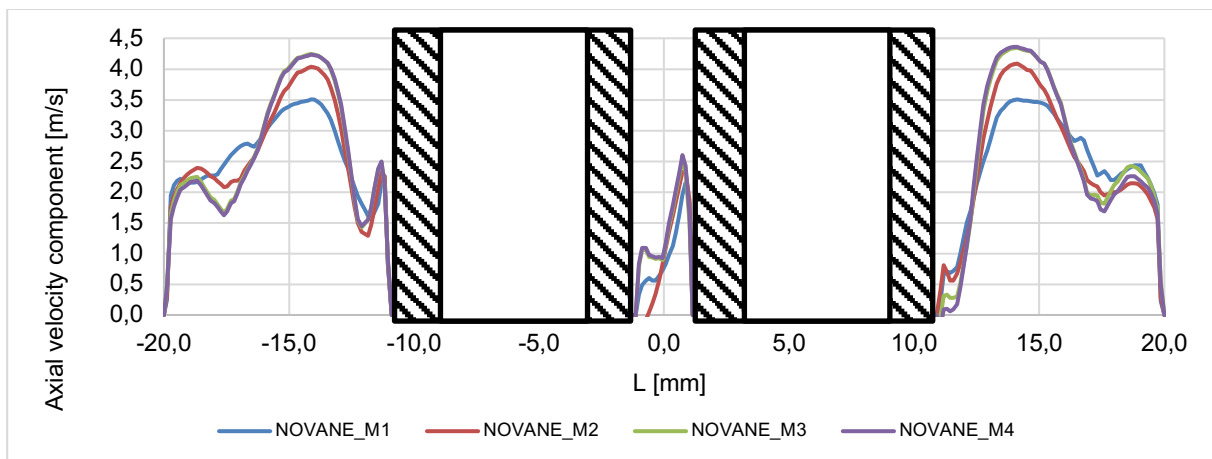
Figure 23: Line-along velocity component distribution 1D (10 mm) downstream the 3rd spacer in the CFD simulation result
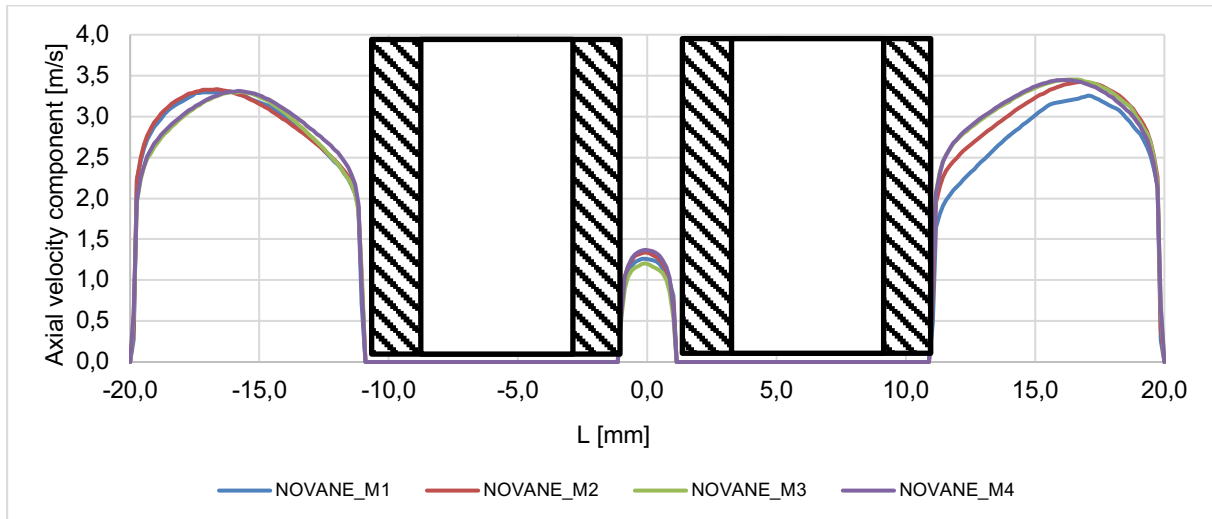
Figure 24: Line-along velocity component distribution 10D (50 mm) behind the 3rd spacer in the CFD simulation result

In Figure 23, the axial velocity components alongside the line at 1D behind the 3rd spacer have been plotted. The distributions are identical in case of M3-M4 meshes. Nevertheless, the M2 mesh also produces a very similar axial velocity pattern between the two rods, while the M1 mesh shows a completely different velocity profile.

Moving away from the grid (Figure 24), there is already a slight difference in the velocity profiles of the two finest meshes, but still the M4-M3 meshes give the closest results. It can also be observed that the velocity profiles calculated in the left outer channel are generally more similar than in the right outer channel. This could be due to the uncertainty of the turbulence model. Based on the line-along profile comparisons, it can be concluded that the results of M1 and M2 meshes differ from the results of the finer meshes. Thus, the M3 mesh was chosen for further investigations, which also avoids the excessive computational demands of the M4 mesh.

5.4. COMPARISON OF CFD RESULTS AND MEASUREMENTS FOR THE NOVANE CASE

In this chapter, the comparison between the measurement and CFD simulation results is presented. It is very important to note here that the comparison of measurements and calculations should take into account the real size of the measured volume, which was also mentioned in Chapter 3.4. In reality, the laser plane has a non-zero thickness, meaning that all seeding particles within the finite laser plane are illuminated and recorded by the camera. Thus, the velocity from the calculations should be taken for the same finite area of the flow field. By default, in CFD post-processing, the evaluation plane has zero thickness, which does not correspond to the real measurement conditions here. Therefore, the line-along velocity distributions of the simulations were extracted from the CFD result files with the help of a short evaluation script. The script extracted the volumetric averaged velocity values with 0.01 mm step intervals from the surroundings of the centrum of the measurement plane. In this way, we could take into account the actual thickness of the measurement plane to make the measurements and the simulations comparable.
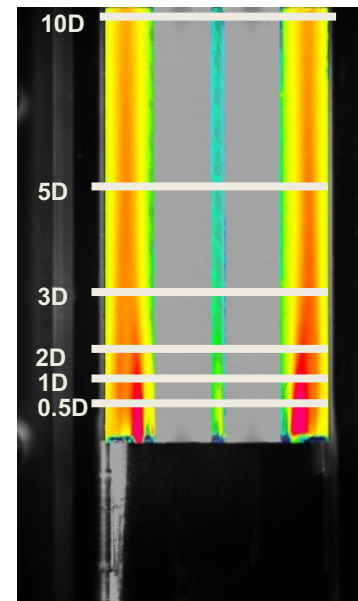
Figure 25: Positions of monitor lines

The positions of the monitor lines can be seen in Figure 25. The comparisons have been made at 0.5, -1, -2, -3, -5, and 10D distance from the top of the spacers.

Figure 26 shows the velocity field above the 2nd NOVANE type spacer grid in case of SST k-ω, BSL Reynolds stress and RNG k-ε turbulence models. The difference between the simulations and measurements is observable. The measurements show that the higher velocity region after the grid disappears relatively soon, while it is observed for a much longer distance in the simulations. The velocities in the inner subchannel are much lower than in the outer ones. This can be seen in the measurements and simulations, as well.

In Figure 27, the results are compared based on the transversal velocities. The transversal distributions plotted on the plane show good agreement in some regions. For example, in the region marked by the red oval, we can see a transversal pattern due to the spacer, which is well observed in both measurements and calculations. In the subchannel on the right, a black oval indicates the positive velocity region, which is also present in the measured and calculated results.

Based on this quantitative comparison, the turbulence models correctly describe the transversal velocities in the section close to the grid. The simulations of the NOVANE spacer show that the effect of the spacer grid is significant at much greater distances, while the measured results suggest that it disappears at a shorter distance.
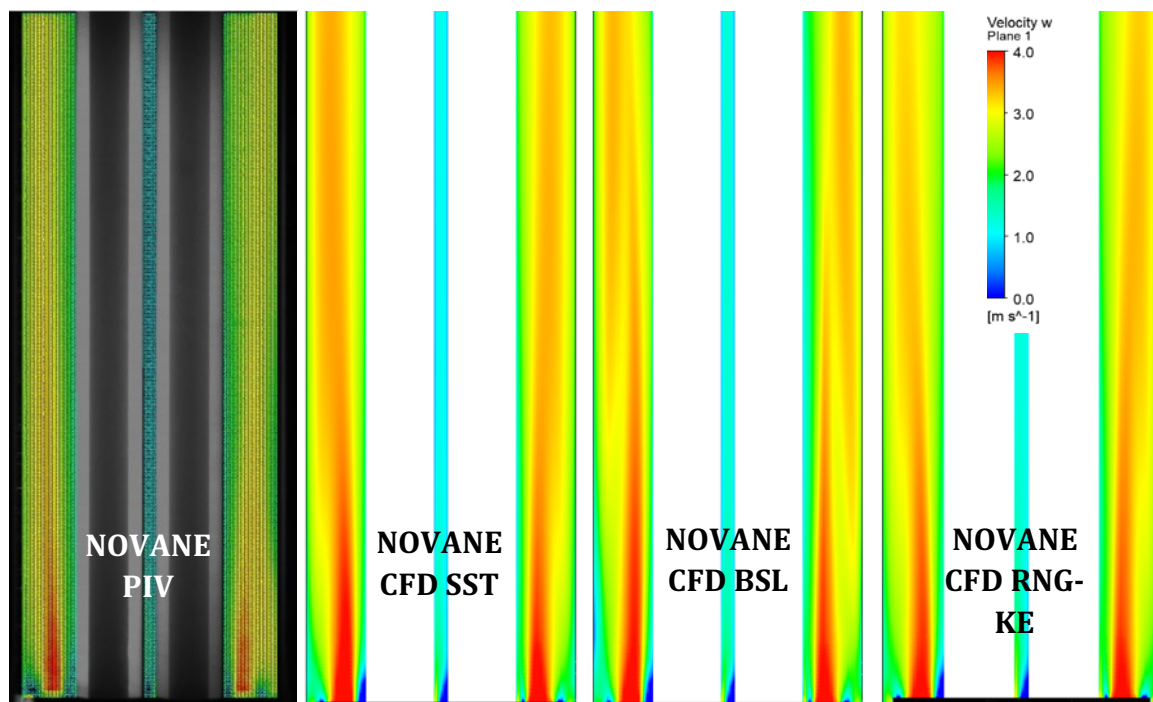
Figure 26: Comparison of axial velocity fields after the 2ⁿᵈ NOVANE spacer grid
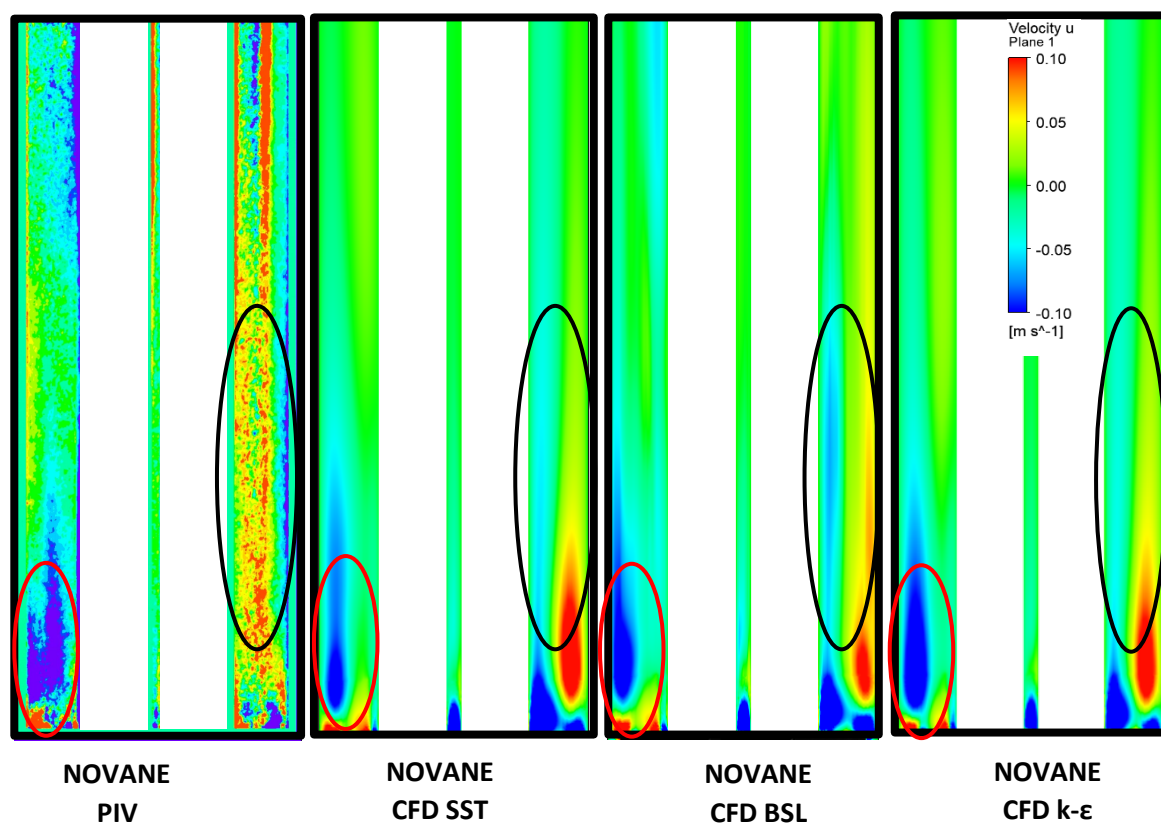
Figure 27: Comparison of transversal velocity fields after the 2ⁿᵈ NOVANE spacer grid
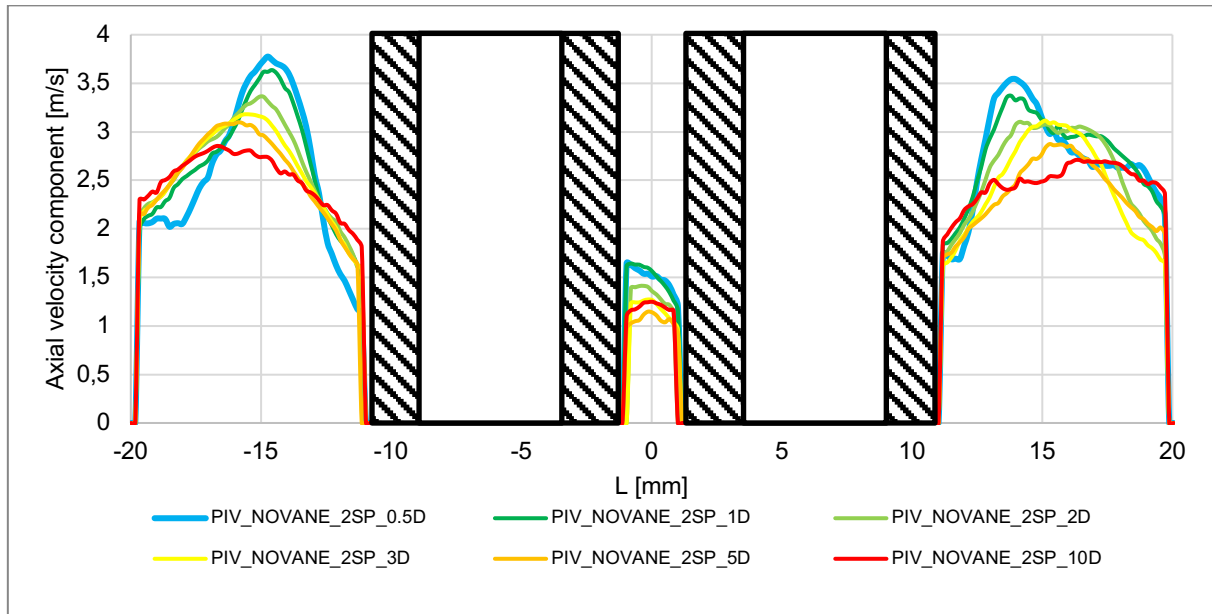
Figure 28: Axial velocity distributions behind the 2nd NOVANE spacer from 0.5 to 10D distances as a function of horizontal position in the PIV experimental results

In Figure 28, the line-along axial velocity distributions are presented in different distances from the NOVANE spacer. The error bars are not presented here to provide a clearer view of the figures. The axial velocities are the highest in the closest monitor line due to the decreased cross-section at the spacer. A progressive reduction in the effect of the grid can be observed. Moving away from the spacer, the velocity profiles become more and more parabolic as in the inner, as also in the outer subchannels.
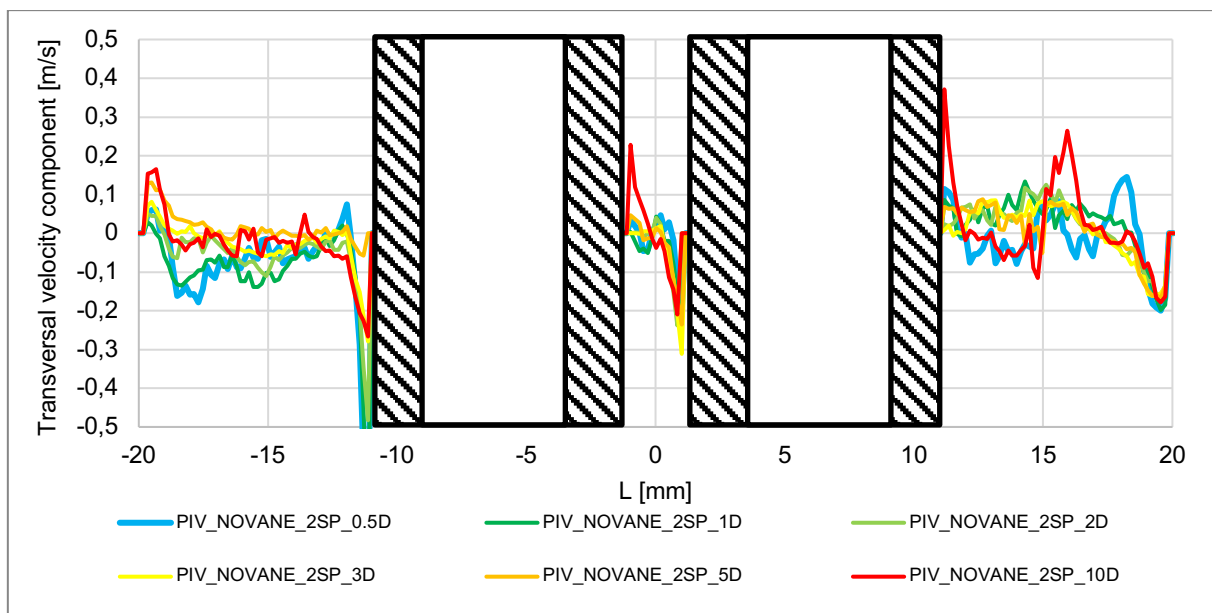
Figure 29: Transversal velocity distributions behind the 2nd NOVANE spacer from 0.5 to 10D distances as a function of horizontal position in the PIV experimental results

The transversal velocities are presented in Figure 29. Despite the surrounding of the walls of the flow channels, the values are close to 0 m/s. The transversal velocities along the walls indicate that the fluid flows toward the inner regions of the channels. The axial velocity values are typically two orders of magnitude higher than the transversal velocities.

Figure 30: Line-along axial velocity component distribution 0.5D (5 mm) behind the 2nd NOVANE spacer grid in the experiment and in CFD simulations using different turbulence models as a function of horizontal position

Figure 31: Line-along transversal velocity component distribution 0.5D (5 mm) behind the 2nd NOVANE spacer grid in the experiment and in CFD simulations using different turbulence models as a function of horizontal position

At a distance of 0.5D, the axial velocity components show good agreement in the outer channels, except for the region near the outer walls (Figure 30). In the inner subchannel, the shape of the velocity profile is already slightly different, and the CFD calculations predict a higher maximum. The transversal velocity profiles are in the same order of magnitude, but their shape is different (Figure 31). Nevertheless, the calculation results are within the measurement error range for almost the entire length of the monitor line. The different turbulence models give similar results at this distance, and it is difficult to determine which one is the correct.

Figure 32: Line-along axial velocity component distribution 1D (10 mm) behind the 2nd NOVANE spacer grid in the experiment and in CFD simulations using different turbulence models as a function of horizontal position

Figure 33: Line-along transversal velocity component distribution 1D (10 mm) behind the 2nd NOVANE spacer grid in the experiment and in CFD simulations using different turbulence models as a function of horizontal position

At a distance of 1D the axial velocities again show good agreement, except for the outer region of the left channel (Figure 32). The axial velocity maximum measured in the inner channel at this distance is already agrees with the calculations. Concerning the transversal velocities, the nature of the velocity profile in the left subchannel is the same, although more significant differences are observed in the right subchannel (Figure 33). Apart from this, the measurements and calculations are within the error range.
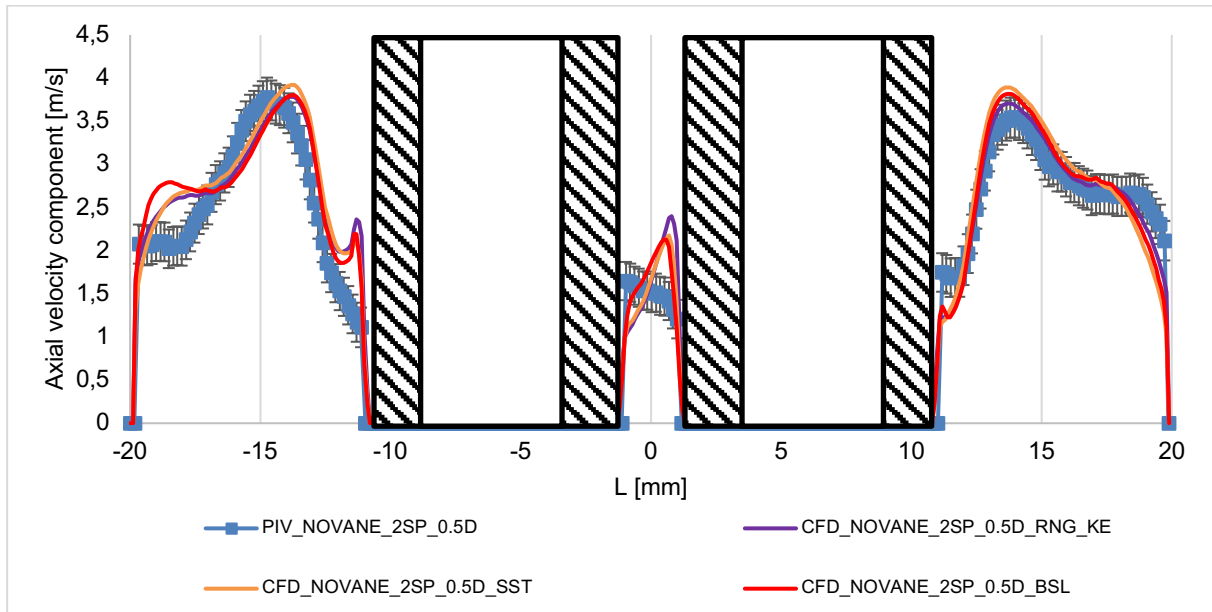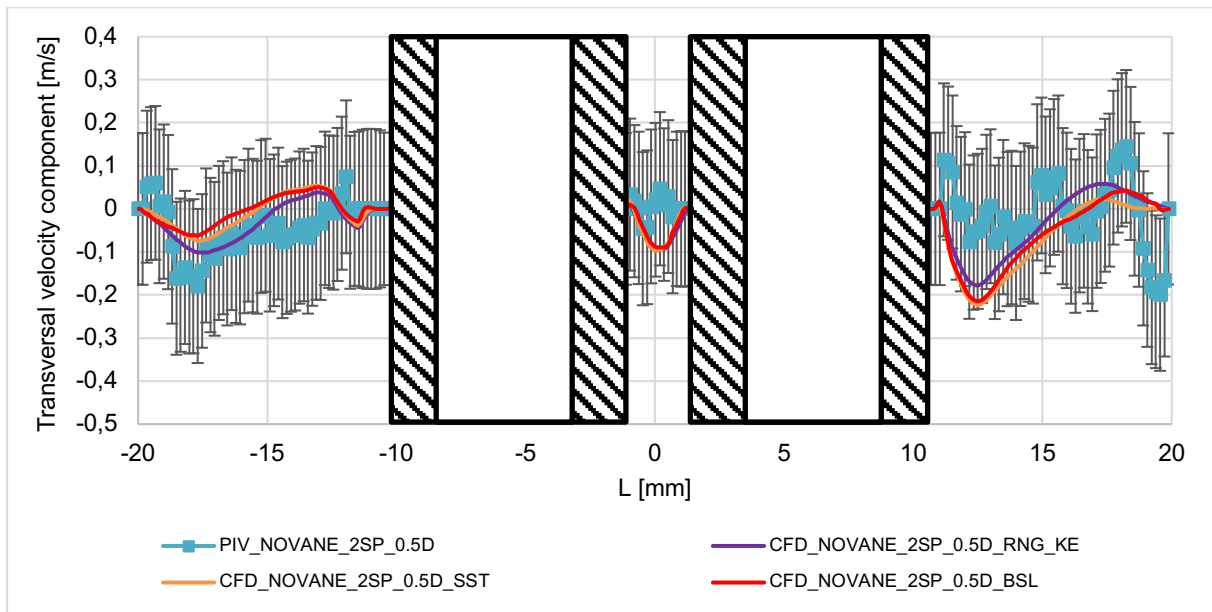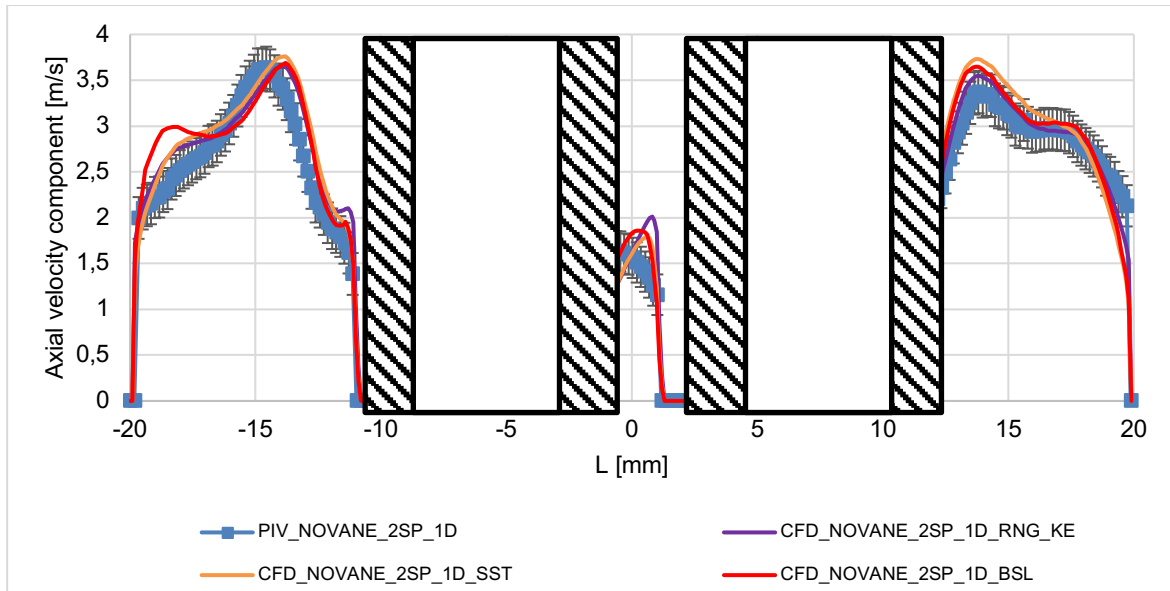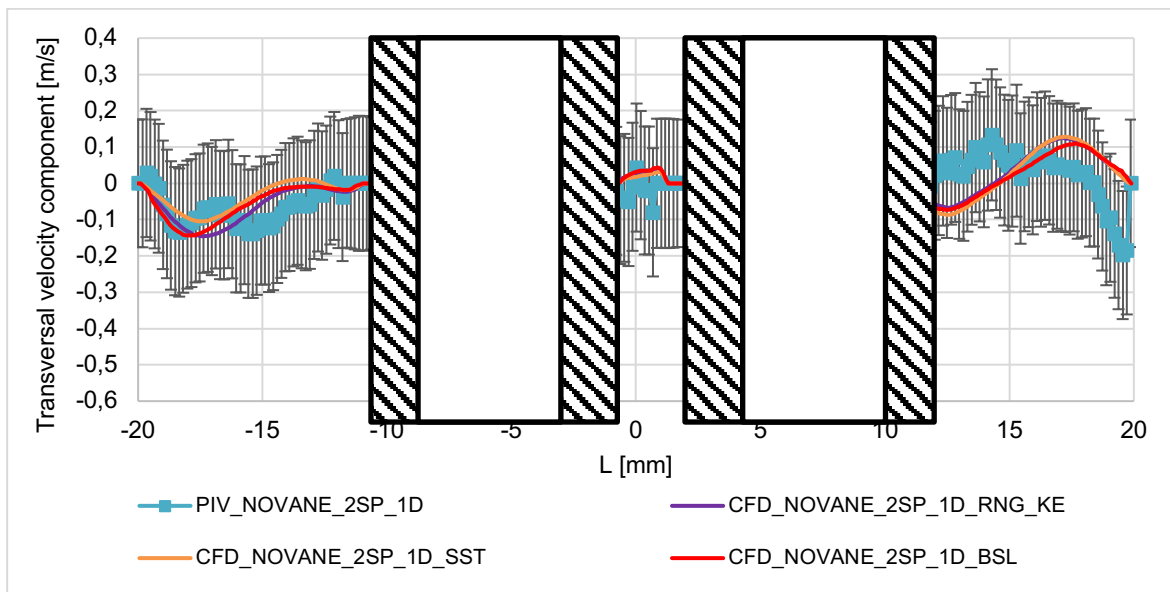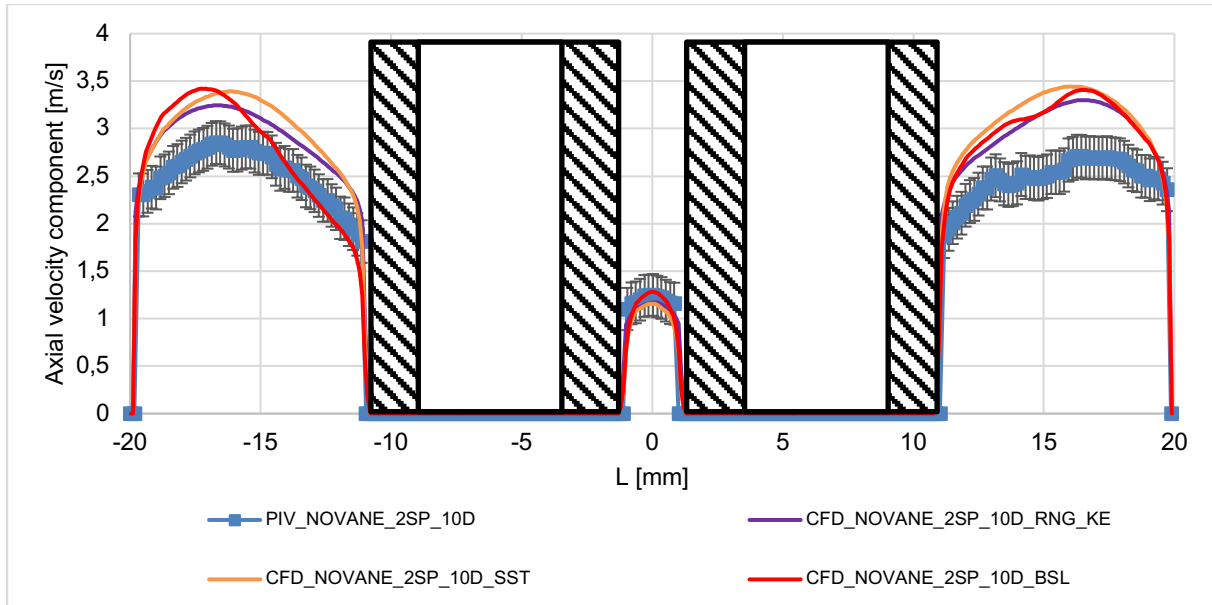

Figure 34: Line-along axial velocity component distribution 10D (100 mm) behind the 2nd NOVANE spacer grid in the experiment and in CFD simulations using different turbulence models as a function of horizontal position

At 10D distance, CFD calculations clearly overestimate the absolute value of the axial velocity components in the outer subchannel (Figure 34). The values are the same in the inner subchannel (between the rods). The three turbulence models also give different velocity profiles. The deviation between the maximum value of the RNG k-ε model output and the measurement is 15.62 %.

As a result, the axial velocity profiles for the NOVANE spacer grid in the near-grid regions showed good agreement with the measurements. The transversal velocity profiles were also in the same order of magnitude as the measurements, although it is pointed out that the relative error of the measurements is much larger.

The experimental results were also evaluated at the laser plane positioned to Y=0 mm where the laser light crosses three FEP rods. If we look at Figure 5, we can see that the two edge rods close to the camera cover the velocity distribution on the Y=0 mm plane. For this reason, the velocity distributions of the inner subchannels were encumbered with more significant errors. Nevertheless, we would like to highlight some exciting results from this measuring position. In Figure 35, the velocity distribution can be seen behind the 2nd NOVANE spacer in the position of Y= 0 mm. In the right outer subchannel a backflow is created by the calming effect of the spacer. The backflow appears in the case of PIV measurement and the simulation made with the k-ε turbulence model. Interestingly, the much more sophisticated SST and BSL models predict an emerging vortex that is not present in the measurement.

In Figure 36, the line-along experimental results are presented in different distances behind the second spacer. According to the measurements, the aforementioned backflow is observable in 0.5 and 1D far from the end of the grid. In the outer subchannels, the flow velocity turns into the axial direction and increases with distance. The inequalities between the two inner subchannels decrease with increasing distance from the spacer.
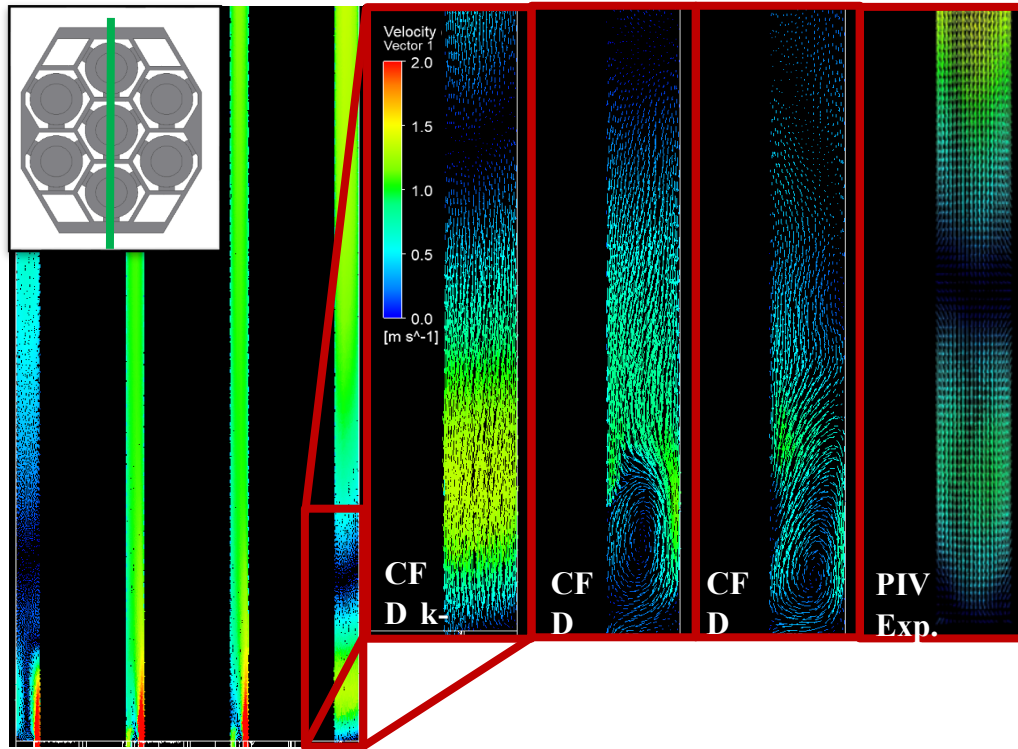
Figure 35: Comparison of axial velocity fields after the 2nd NOVANE type spacer grid in the experimental plane position Y=0
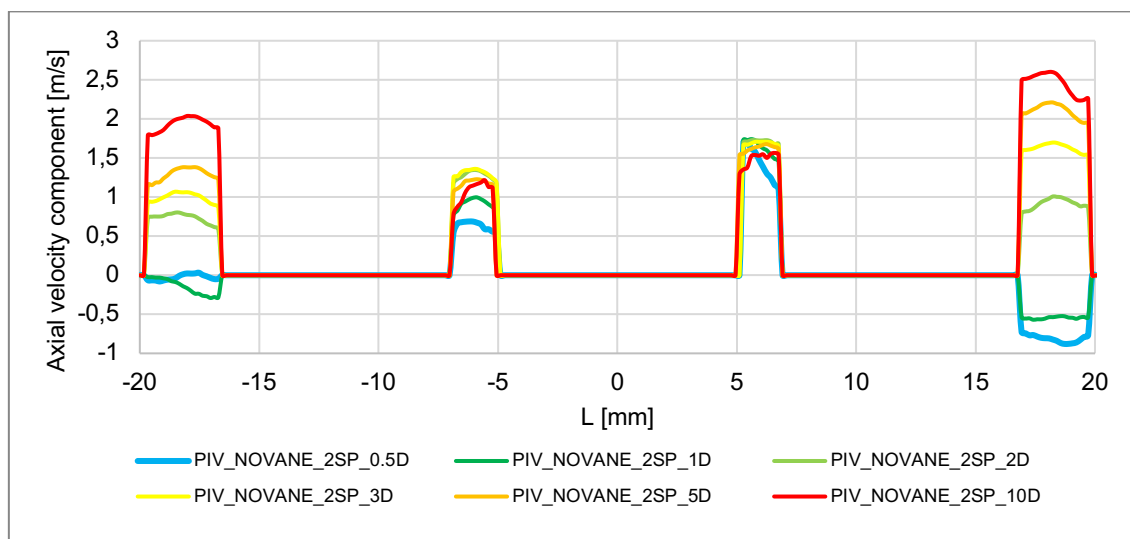
Figure 36: Axial velocity distributions behind the 2nd NOVANE type spacer grid from 0.5 to 10D distances in the experimental plane position Y=0 in the PIV measurements as a function of horizontal position

5.5. COMPARISON OF CFD RESULTS AND MEASUREMENTS FOR THE SPLIT TYPE SPACER GRID

The axial velocity distributions after the SPLIT type grid are shown in Figure 37. There are minor differences between measurements and calculations in the region after the vanes. The measurements suggest that the higher velocity region of the two side subchannels is dissipated quickly, while in the calculations it remains pronounced for much longer.

Figure 38 shows the 2D distribution of the transversal velocity components in the region after the second spacer. The black ovals highlighted in the inner subchannel show a well-traced pattern, which is also reflected in the calculations. The vortex created by one of the external mixing vanes can be seen in this region. Figure 39 shows the cross-sectional secondary flow regime. It can be observed that the laser plane intersects one of the vortices, and the corresponding velocity component of this vortex can be seen in the region marked by the black oval in Figure 38. Good agreement is also found for the positive velocity region in the left outer subchannel (blue dashed line).
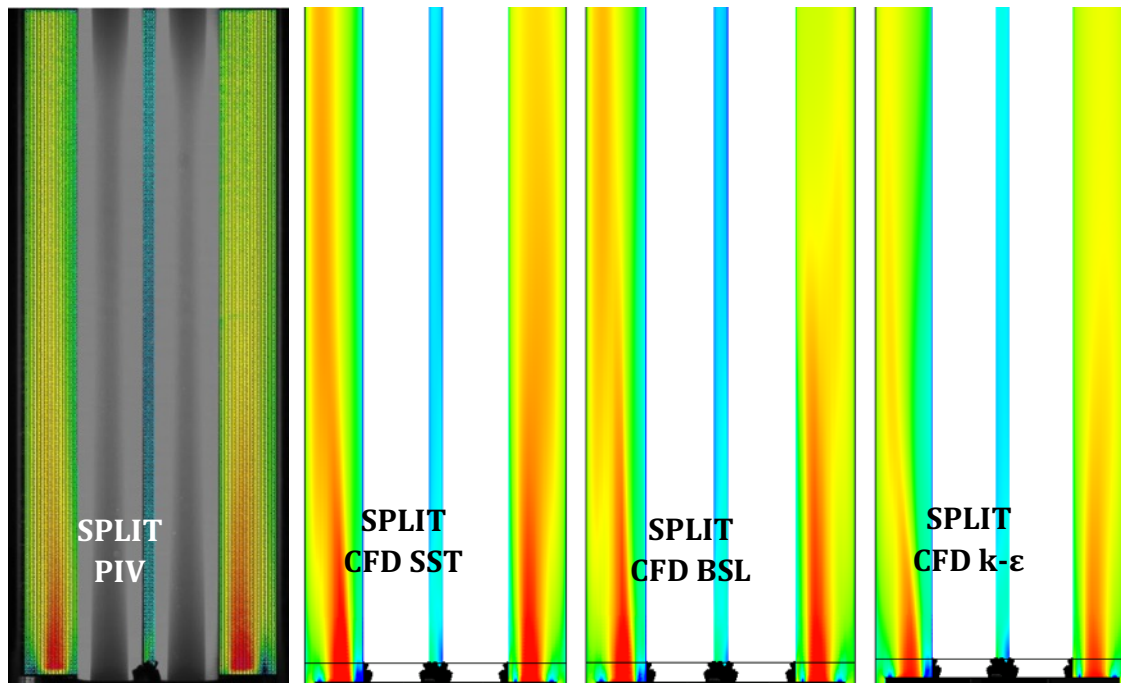
Figure 37: Comparison of axial velocity fields after the 2nd SPLIT type grid

SPLIT PIV   **SPLIT CFD SST**   **SPLIT CFD BSL**   **SPLIT CFD k-ε**
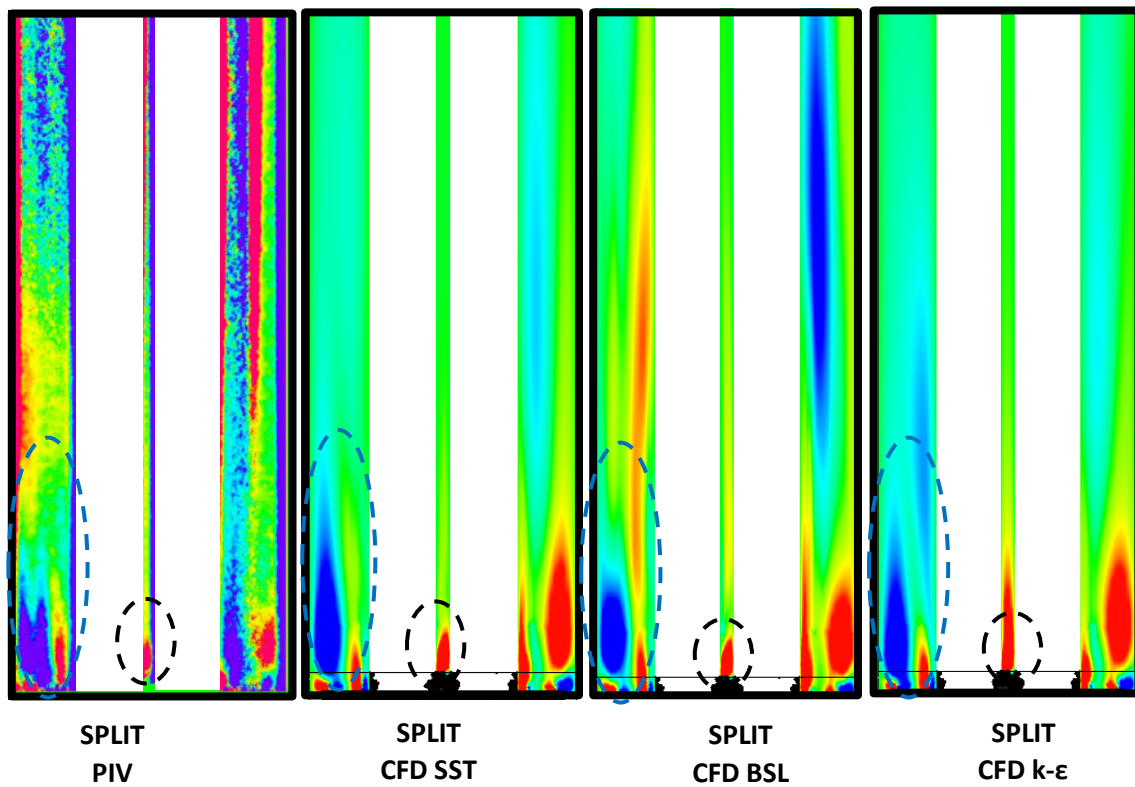
Figure 38: Comparison of transversal velocity fields after the 2nd SPLIT type spacer grid
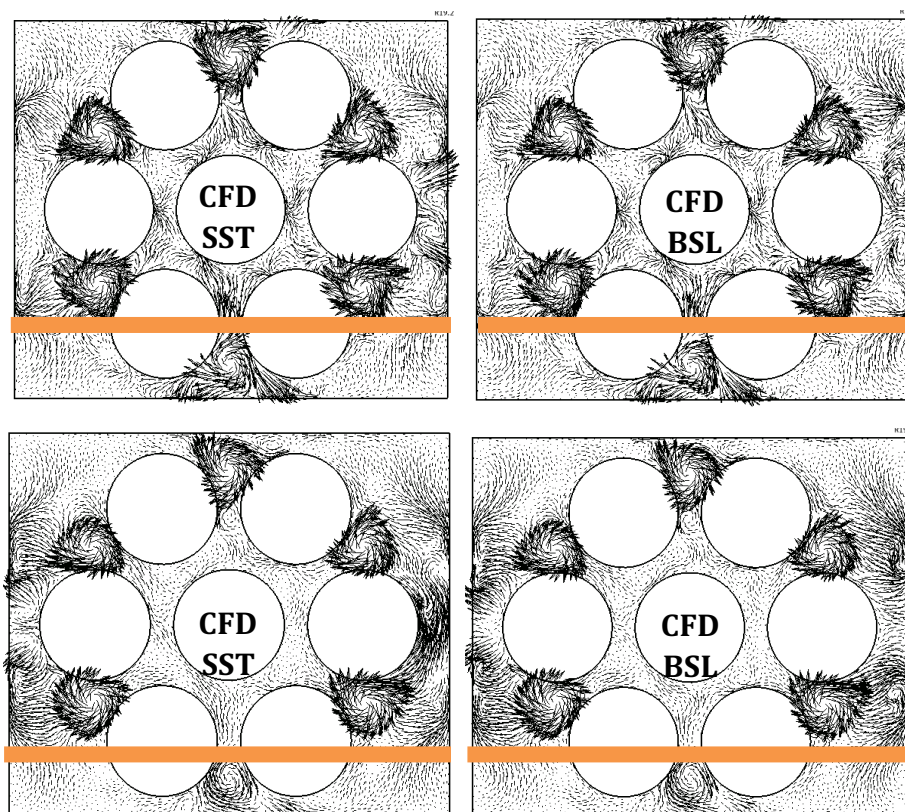
Figure 39: Cross-flow pattern behind the 2nd SPLIT type spacer at 0.5 and 1D distance

Figures 40 and 41 show the results along the monitor lines for the SPLIT type spacer grids. The axial velocities are plotted in Figure 40. Close to the spacer grid, in the right subchannel shows a profile with two local maximum, and between these maximums a local minimum can be seen. The bigger maximum is the one close to the rod wall. On the left outer channel the axial profile contains only one maximum point. As we can see in Figure 40, the velocity profiles in the two edge channel regions are not symmetrical to each other. This is because the SPLIT (and TWISTED) type vanes are set to create a circular flow around the channel wall. Since the cross-section of the channel is rectangular and the positioning of the rods are not rotationally symmetric in the channel, a different flow pattern is observed in the two outer subchannel corners. The asymmetry is observed in the near-spacer region and persists in the far-grid regions. It can be seen that at distances 5-10D, the velocity profile is tilted towards the channel wall in the left channel and towards the rods in the right channel. This profile tilt is also presented in the inner subchannel between the rods. This trend is readily noticeable after the second grid and less pronounced after the third grid.
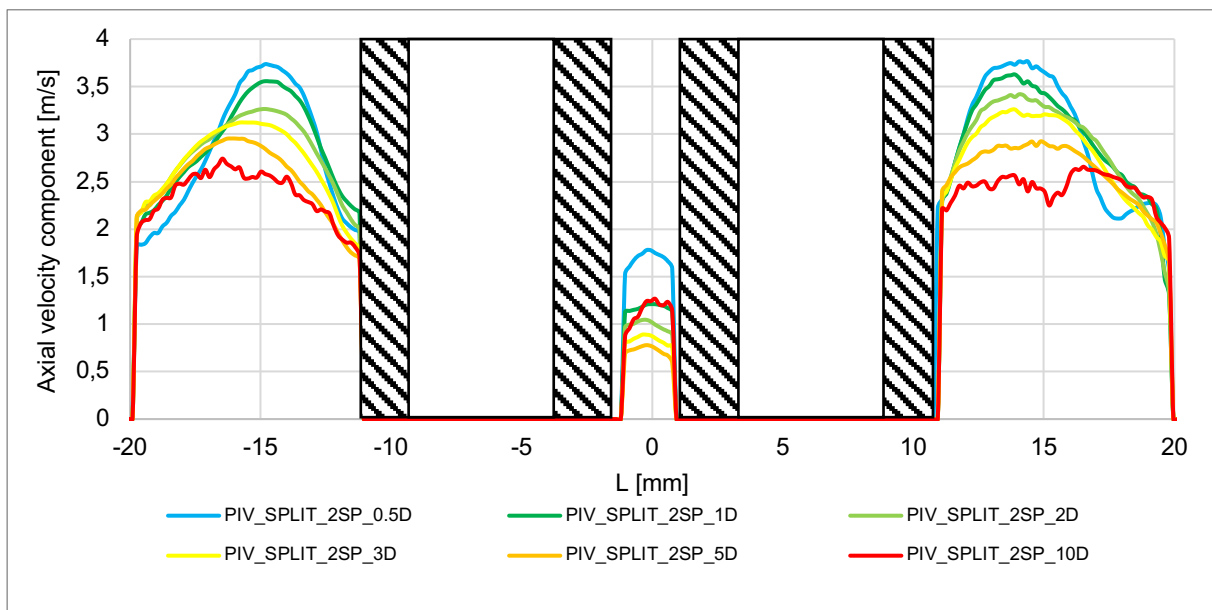
Figure 40: Axial velocity distributions behind the 2nd SPLIT type spacer grid from 0.5 to 10D distances in the PIV measurements as a function of horizontal position
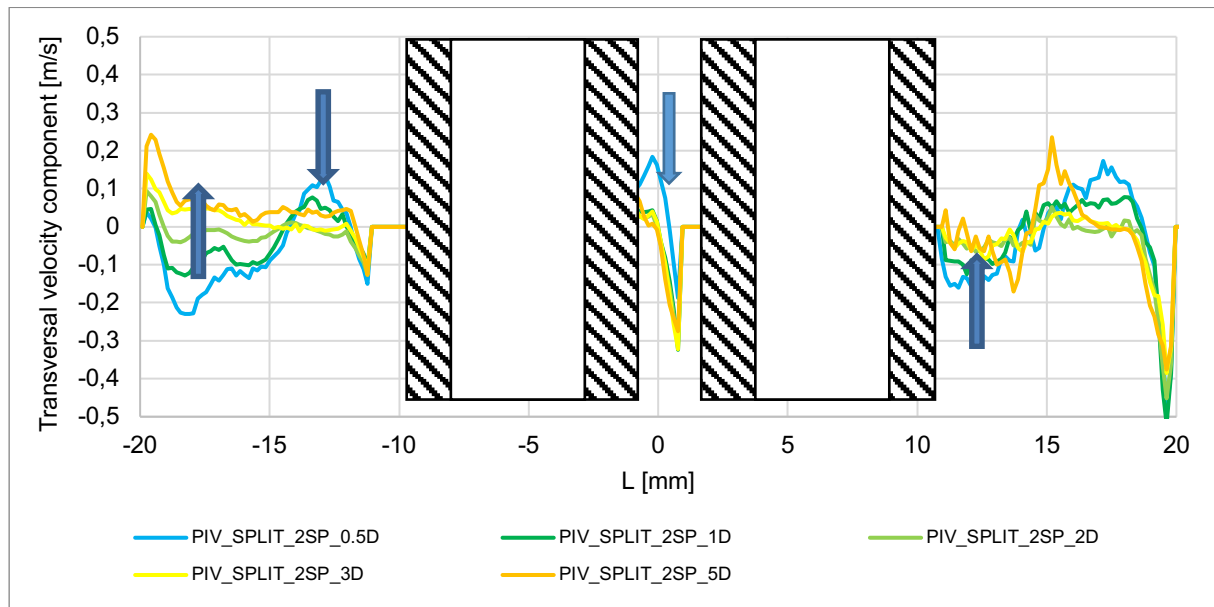
Figure 41: Transversal velocity distributions behind the 2nd SPLIT type spacer grid from 0.5 to 5D distances in the PIV measurements as a function of horizontal position

In terms of transversal velocities, a velocity profile evolution can be seen (marked with blue arrows). In the outer channels, a profile resembling an inverted letter "N" is shown, which flattens out as the flow progresses away from the girds, and settles near 0 m/s. This trend can be clearly seen in the channel between the rods and in the left channel in Figure 41. The mixing effect of the eddies created by the vanes can also be traced in these value series. Compared to the NOVANE spacer grid, the transversal velocity maximum is significantly larger. The error bars are not presented in Figures 40-41.

Figure 42: Line-along axial velocity component distribution 0.5D (5 mm) behind the 2nd SPILT type spacer grid in the experiment and in CFD simulations using different turbulence models as a function of horizontal position

At 0.5D distance from the grid, there is a good agreement between the calculated and measured axial velocity profiles (Figure 42). The velocity maximums are in the same order of magnitude, and the profiles are similar. There is a larger discrepancy in the left subchannel along the wall of the rod (orange dashed oval). The transversal velocity components are also identical except for the region marked above (Figure 43).

Figure 43: Line-along transversal velocity component distribution 0.5D (5 mm) behind the 2nd SPLIT type spacer grid in the experiment and in CFD simulations using different turbulence models as a function of horizontal position
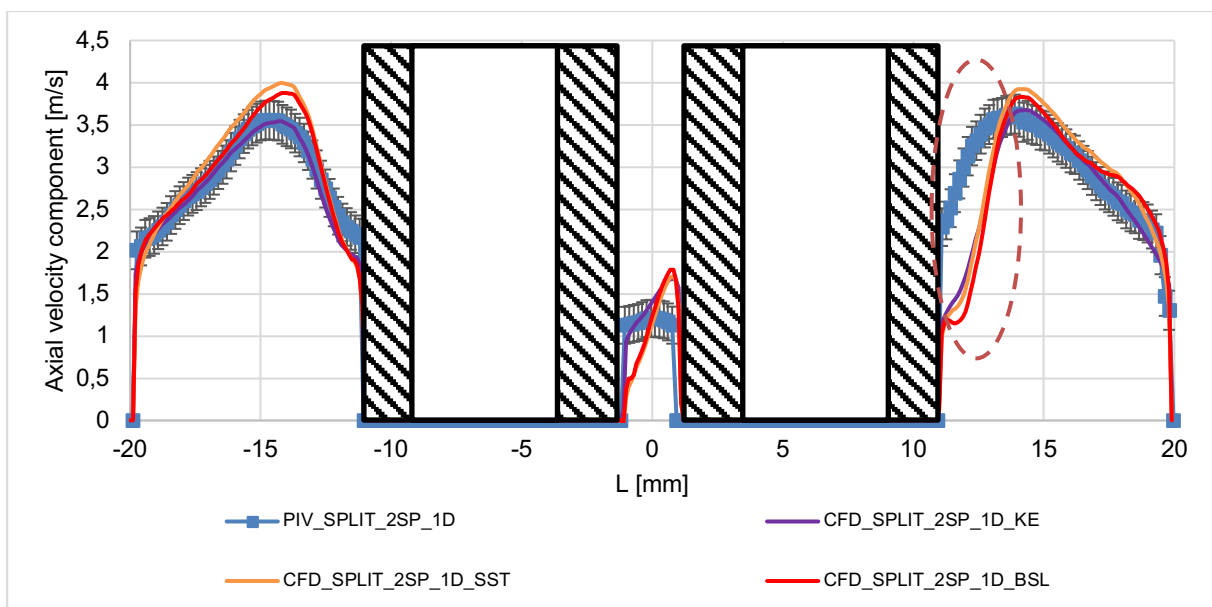
Figure 44: Line-along axial velocity component distribution 1D (10 mm) behind the 2nd SPLIT type spacer grid in the experiment and in CFD simulations using different turbulence models as a function of horizontal position

The profiles taken in 1D distance (Figure 44) agree well with the measurement, except for the abovementioned left subchannel near the rod wall. The axial velocity profile in the right subchannel shows a particularly good agreement between the k-ε model and the PIV measurement data. In the inner channel, the calculations also approximate the measurement well but predict a more strongly sloped profile. Similar profiles can be seen in the case of transversal velocities (Figure 45) in the two outer channels, but the series of values in the inner channel are different. Despite this, the measured and calculated results agree within the error range of the measurements.
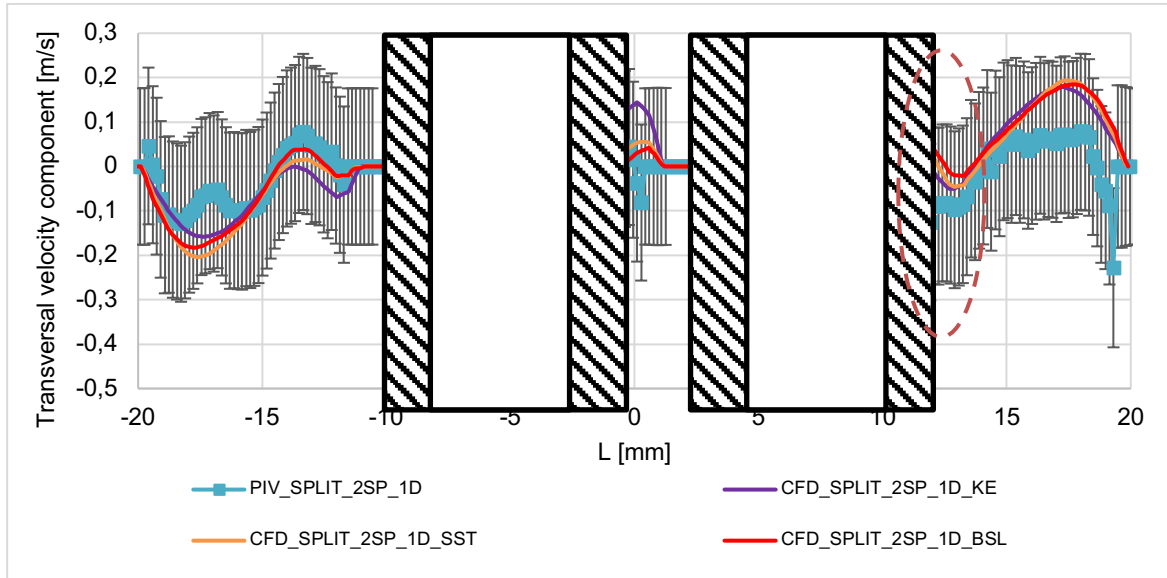
Figure 45: Line-along transversal velocity component distribution 1D (10 mm) behind the 2nd SPLIT type spacer grid in the experiment and in CFD simulations using different turbulence models as a function of horizontal position
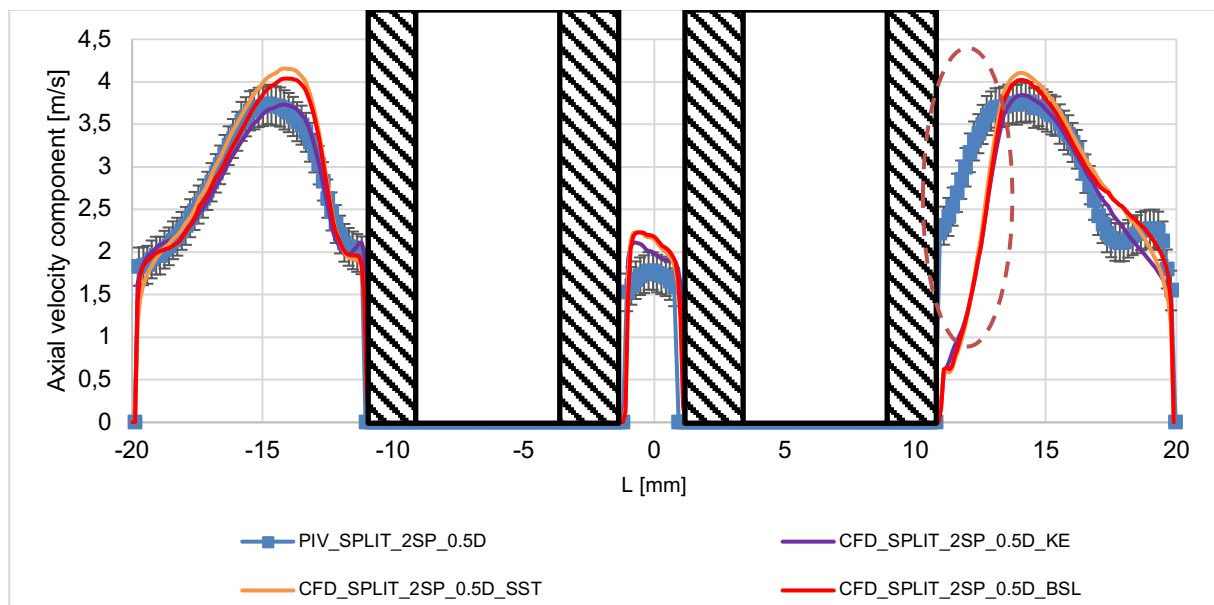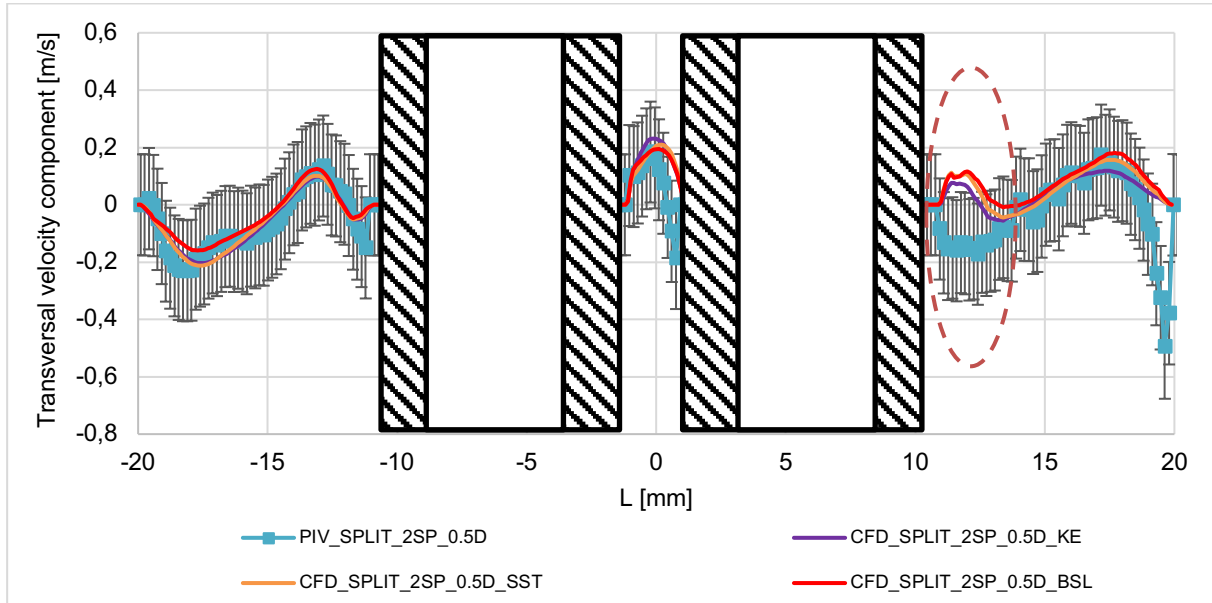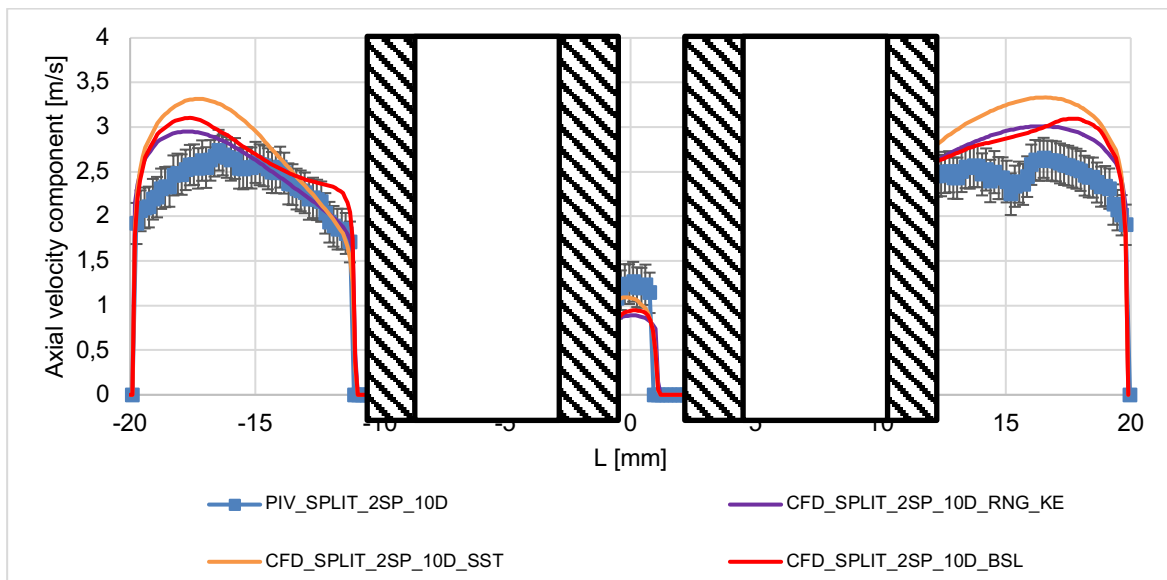
Figure 46: Line-along axial velocity component distribution 10D (100 mm) behind the 2nd SPLIT type spacer grid in the experiment and in CFD simulations using different turbulence models as a function of horizontal position

At 10D distance (Figure 46), the axial profiles are well matched in the inner subchannels, but the discrepancies are larger in the outer subchannel. Even at this distance, the calculations give a higher velocity maximum. The deviation between the maximum calculated by RNG k-ε model and the measurement is 9.82%. It can be concluded that in the regions close to the spacer grid the models and measurements show a good agreement, but further away from the spacer the data series become more and more distant.

In Figure 47, the emerging flow field after the second SPLIT type spacer can be seen at the position of Y=0 mm. In the left outer subchannel, the experiments show a counter-clockwise vortex created by the spacer clamping, which is also presented in the calculations. The more sophisticated turbulence models (BSL and SST) show a smaller clockwise vortex at the top of the bigger main vortex. This second vortex is not present in the measurement.

The line-along velocity distributions are presented in the position of Y=0 mm in Figure 48. As we can see at the 0.5D distance (blue coloured line) in the left outer subchannel, the axial velocity takes both positive and negative values, which can be explained by the presence of the vortex mentioned above. In the right outer subchannel, the axial velocity is negative in the section between 0 to 1D, which means that a reverse flow is observed. In the inner subchannels the velocity profiles do not change significantly (apart from 0.5D distance).

We would like to emphasise that, these steady state calculations are generally good approximation of the measured results, but in many cases, there are inconsistencies. To resolve these discrepancies, we will organise a two-part benchmark exercise in the near future. A description of the first phase of the exercise is already available online [44].
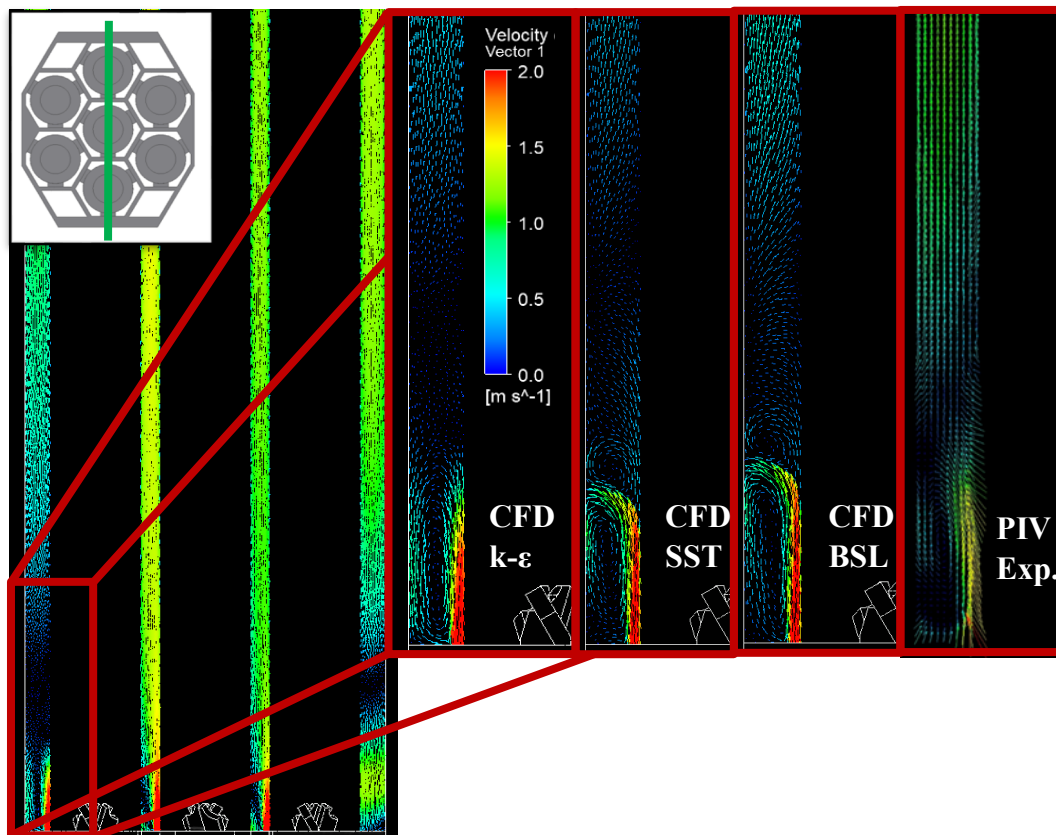
Figure 47: Comparison of axial velocity fields after the 2nd SPLIT type spacer grid in the experimental plane position Y=0

Figure 48: Axial velocity distributions behind the 2nd SPLIT type spacer grid from 0.5 to 10D distances in the experiment as a function of horizontal position

5.6. COMPARISON OF CFD RESULTS AND MEASUREMENTS FOR THE TWISTED TYPE SPACER GRID
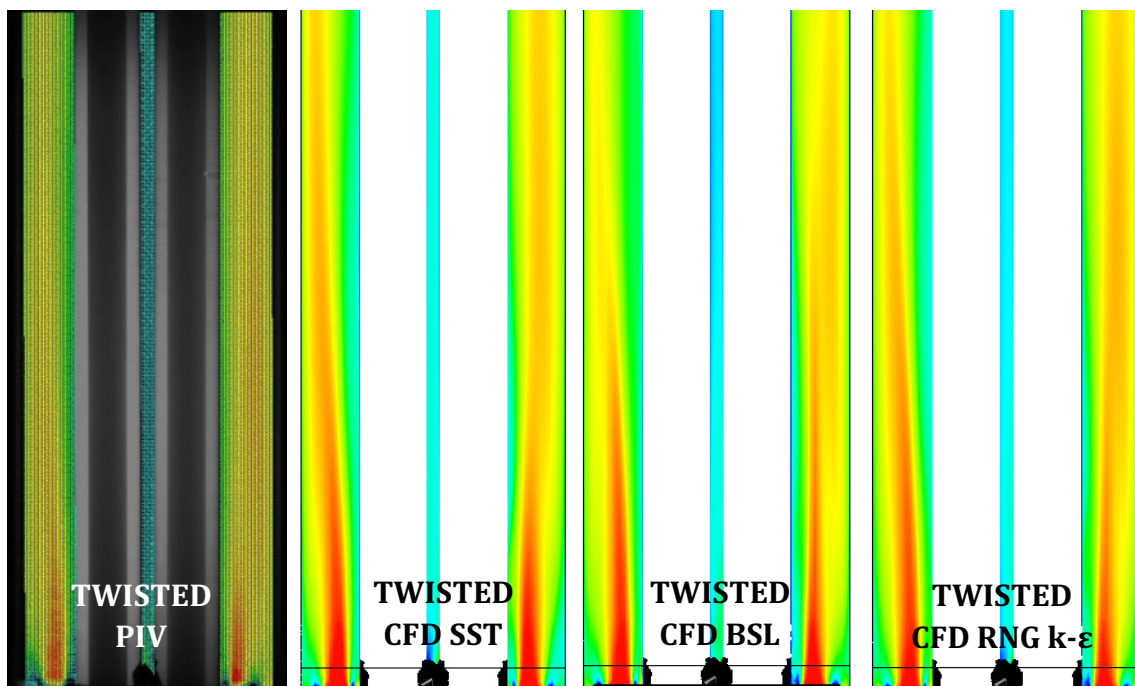
Figure 49: Comparison of axial velocity fields after the 2nd TWISTED type spacer grid
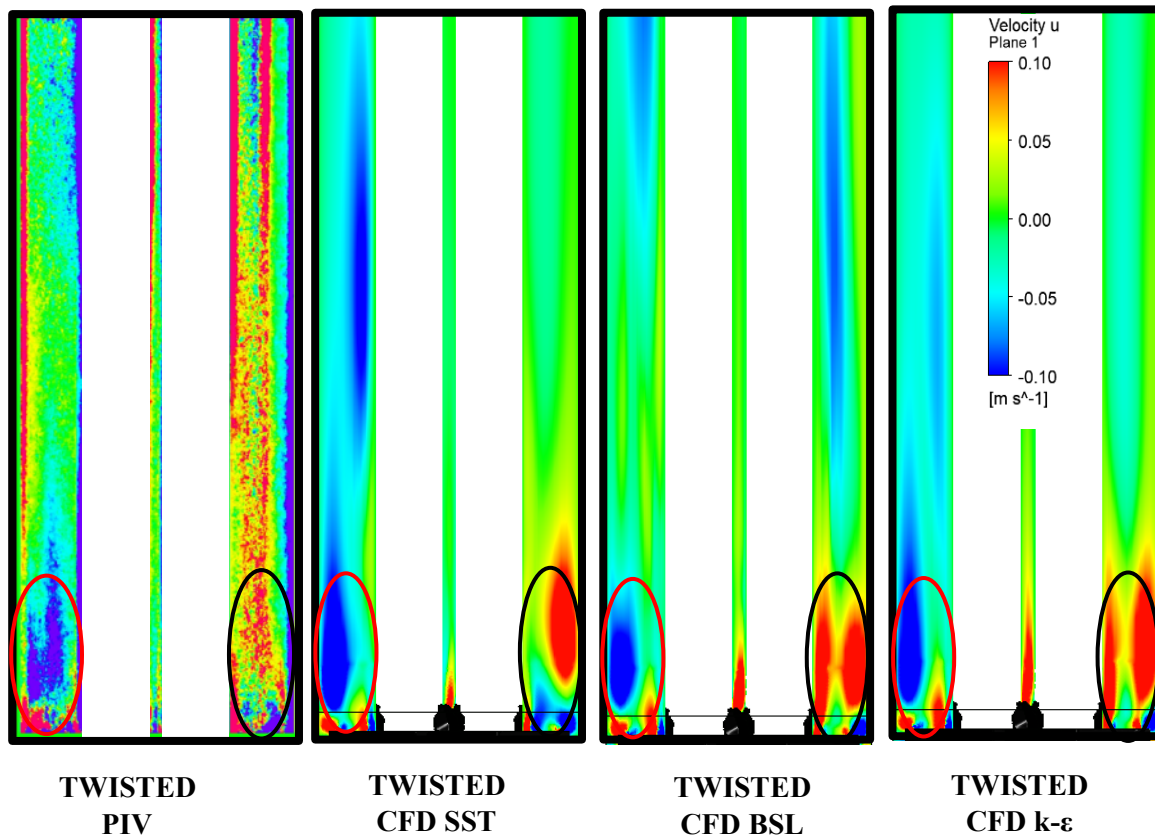
Figure 50: Comparison of transversal velocity fields after the 2nd TWISTED type spacer grid

The SST, BSL and RNG k-ε turbulence models were used to calculate the velocity distribution in the case of TWISTED vane spacer grid. The results of these models are shown in Figure 49. The measurement shows two well-defined cone-like jets in the outer channels after the grid. In contrast, the calculations show a higher velocity region remaining along a longer trace. Similar flow patterns were observed in both the SPLIT and NOVANE cases.

The in-plane distribution of transversal velocities is shown in Figure 50. The red oval flow pattern in the left outer channel can be easily observed in the CFD results. A similar observation can be made for the flow structure in the right outer channel.

In Figure 51, the cross-flow pattern is presented in the case of the TWISTED vane calculations. The effect of the vortices created by the mixing vanes can be seen in the vector fields. Strangely, the vortex that fell within the PIV test domain is much less present in the calculations. In contrast, the presence of vortices created by the other mixing vanes is strong. The reason for this is not clear yet.
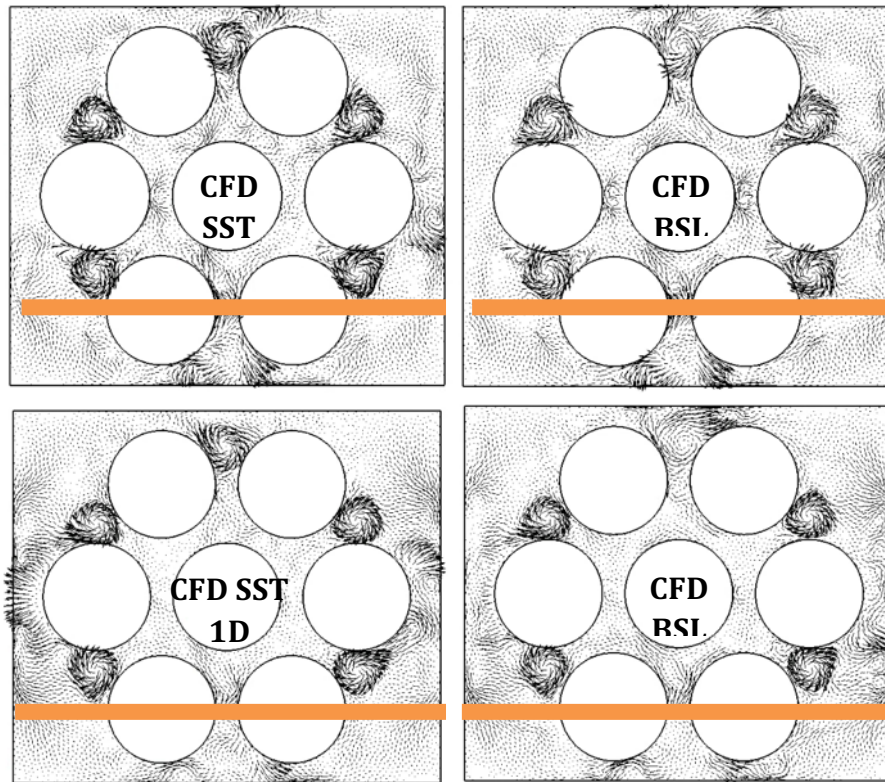
Figure 51: Cross-flow pattern behind the 2nd SPLIT type spacer at 0.5 and 1D distance

Figures 52-53 show the velocity profiles of the TWISTED type spacer grid along the monitor lines. The axial velocity profiles also show that the effect of the grids and mixing vanes decreases with the increasing distance from the grid. It can also be seen that the left and right subchannel profiles are asymmetric and the profiles remain slightly asymmetrically sloped in the far-grid region due to the cross-flow created by the vanes.

In the case of the TWISTED vane, the velocity values in the middle subchannel are higher in the near-grid region, than away from the grid, but the same trend can be seen as for the SPLIT vane.

The region between the two rods is the closest (at 0.5D) to the maximum speed due to the reduction in cross-section caused by the grid and the mixing vanes (Figure 52). Similar velocity profile development can be seen in the measurements with TWISTED type vanes, as in case of the SPLIT type vanes. At a greater distance (at 10D), a profile tilt is also presented in the measurements.
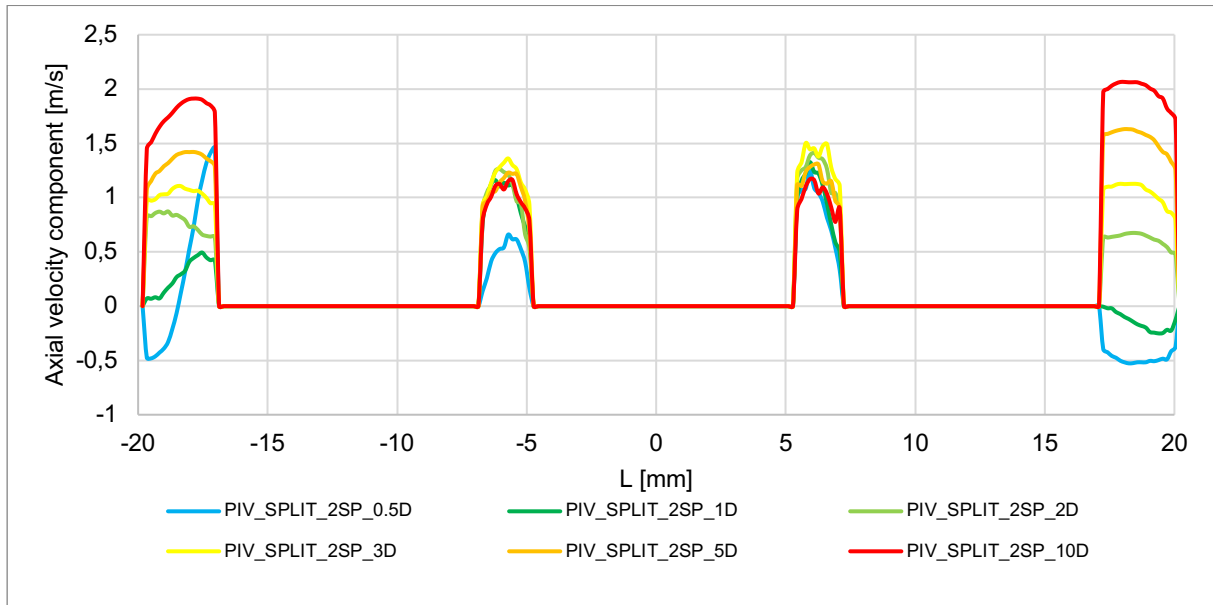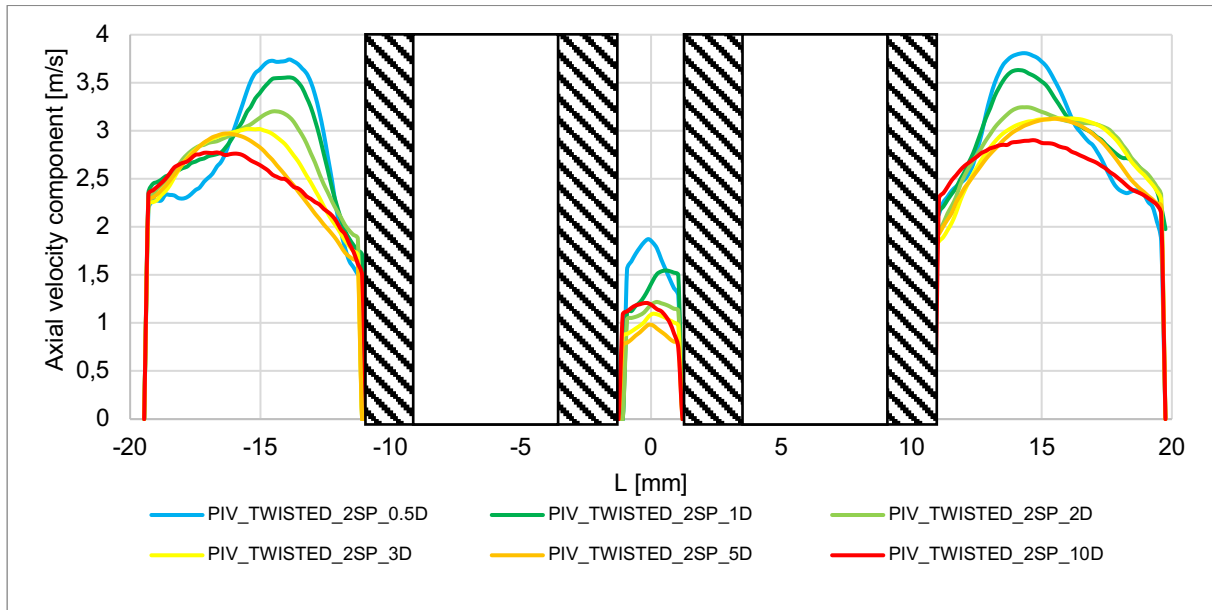
Figure 52: Axial velocity distributions behind the 2nd TWISTED type spacer grid from 0.5 to 10D distances in the experiment as a function of horizontal position
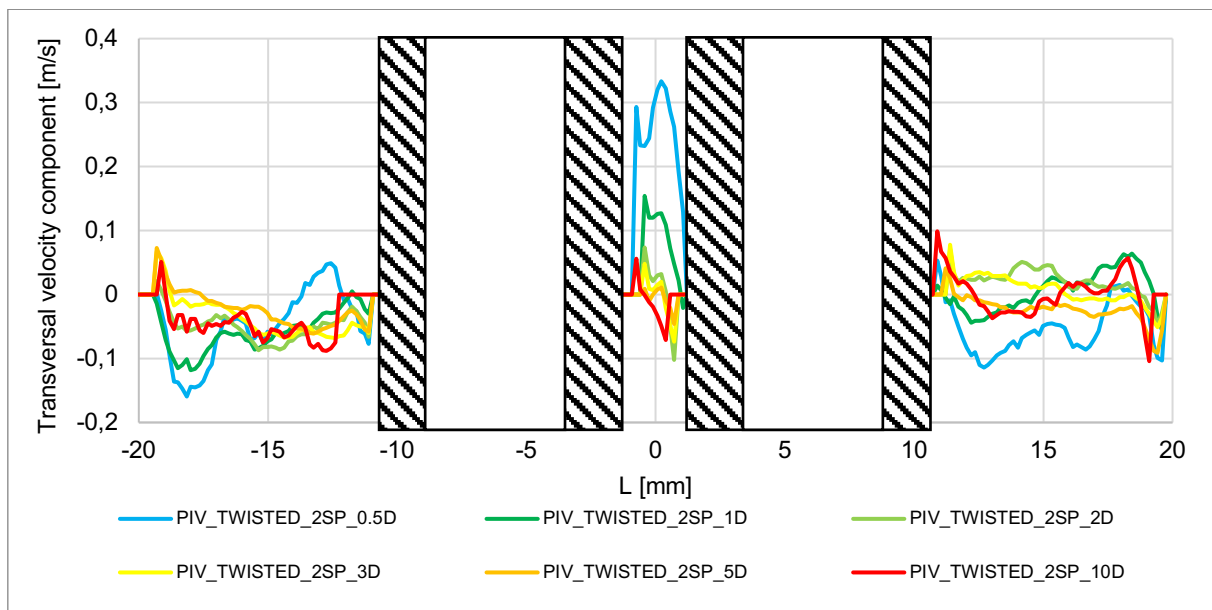
Figure 53: Transversal velocity distributions behind the 2nd TWISTED spacer from 0.5 to 10D distances in the experiment as a function of horizontal position

The profiles of transversal velocities after the second spacer evolve with the distance of the spacer (see in Figure 53). In the inner subchannel the transversal velocity maximum is higher than 0.3 m/s, which decreases with the distance.
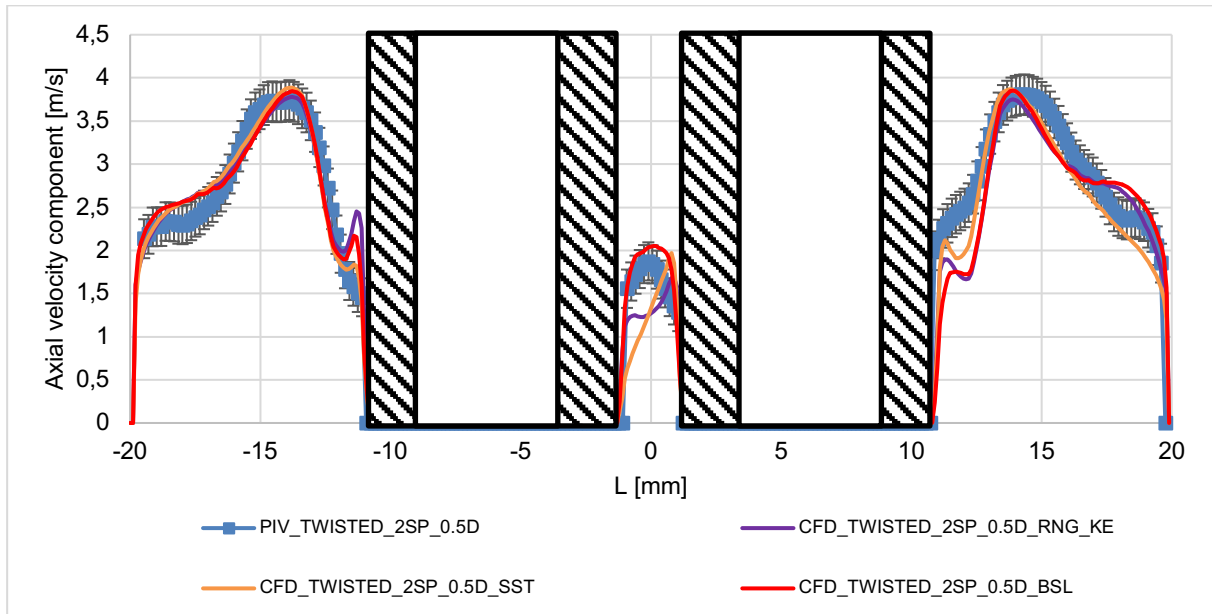
Figure 54: Line-along axial velocity component distribution 0.5D (5 mm) behind the 2nd TWISTED type spacer grid in the experiment and in CFD simulations using different turbulence models as a function of horizontal position
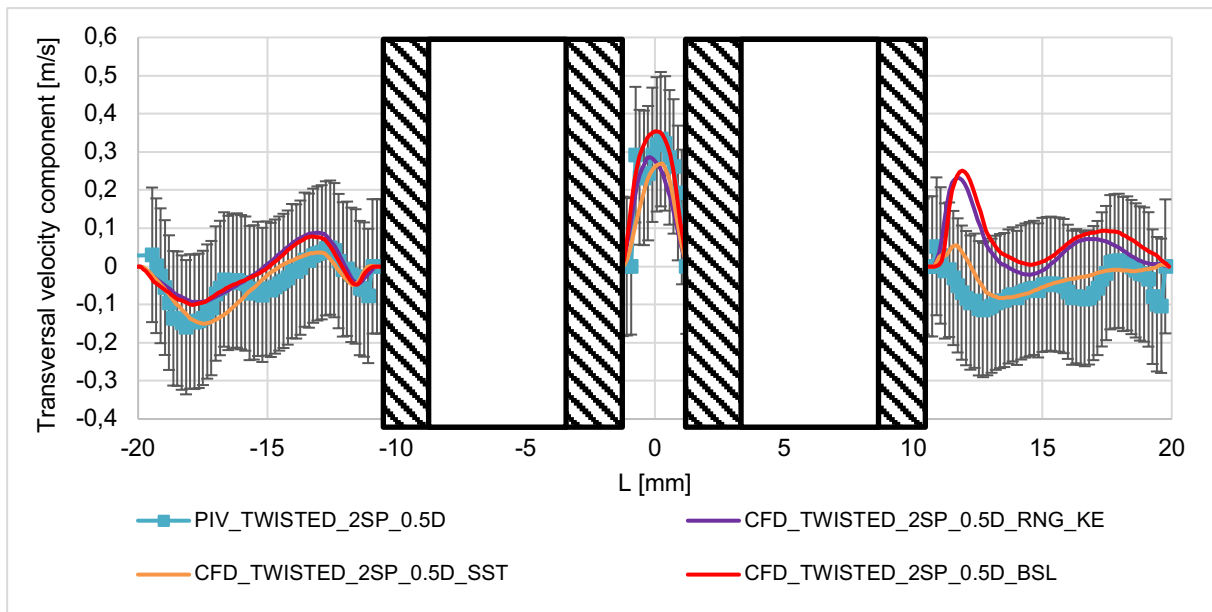
Figure 55: Line-along transversal velocity component distribution 0.5D (5 mm) behind the 2nd TWISTED type spacer grid in the experiment and in CFD simulations using different turbulence models as a function of horizontal position

In the aspect of the CFD code validation, the measured velocity profiles of the near-grid regions in the TWISTED type vane are very well matched with the calculations, both in terms of axial and transversal components (Figure 54 and 55). The absolute values are of the same order of magnitude, and the distributions are similar.

With respect of the axial velocity components in the inner subchannel, the BSL Reynolds stress model approximates the best the measured results. For the transversal components, the SST turbulence model shows a better agreement.
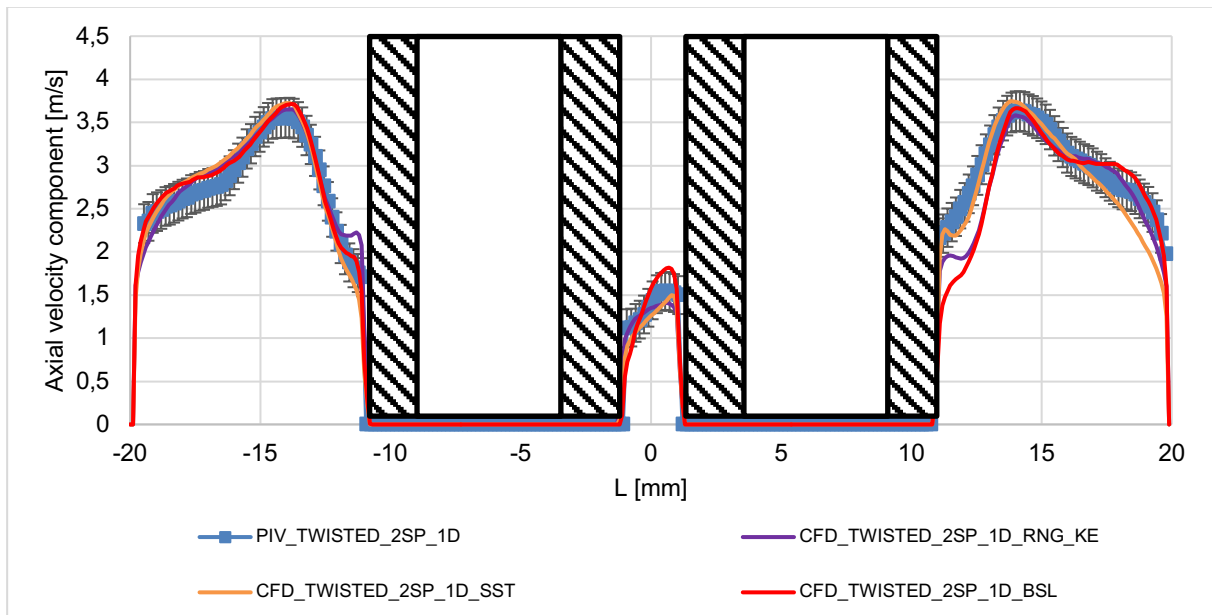
Figure 56: Line-along axial velocity component distribution 1D (10 mm) behind the 2nd TWISTED type spacer grid in the experiment and in CFD simulations using different turbulence models as a function of horizontal position
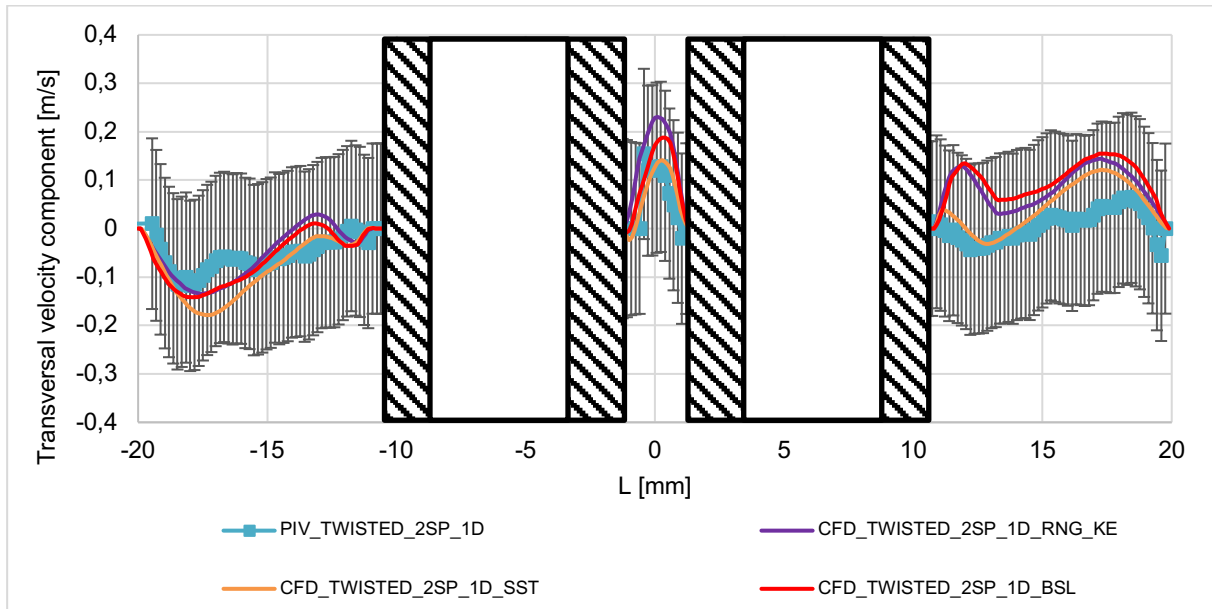
Figure 57: Line-along transversal velocity component distribution 1D (10 mm) behind the 2nd TWISTED type spacer grid in the experiment and in CFD simulations using different turbulence models as a function of horizontal position

At 1D distance from the spacer (Figure 56 and 57), the SST turbulence model gives the closest values to the measurements both in respect of the axial and transversal velocities.
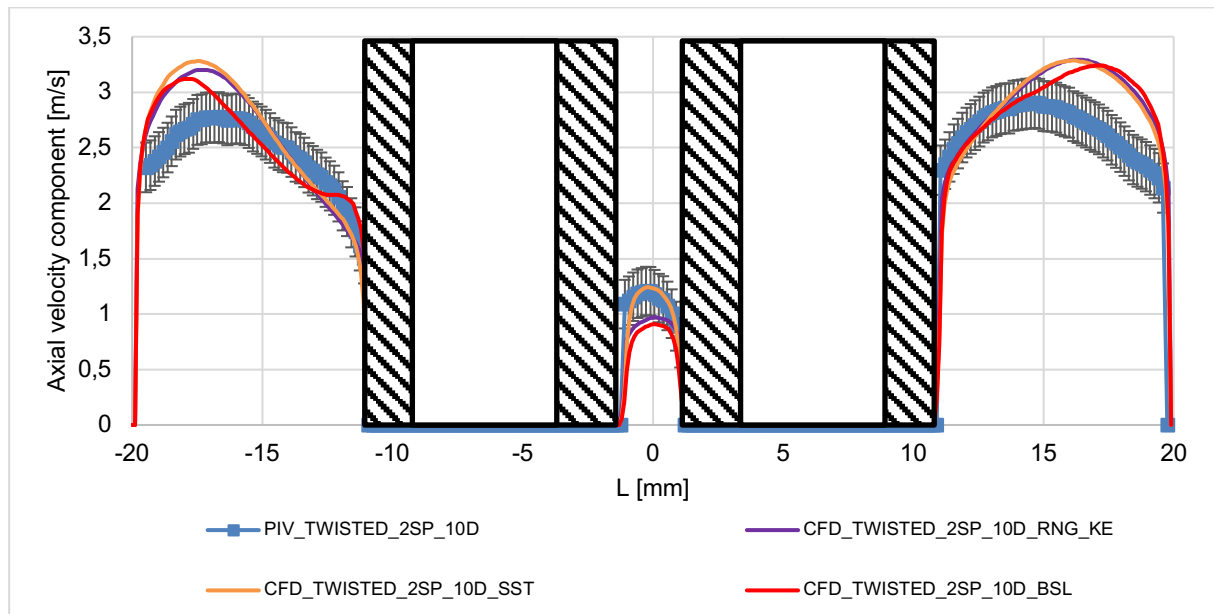
Figure 58: Line-along axial velocity component distribution 10D (100 mm) behind the 2nd TWISTED type spacer grid in the experiment and in CFD simulations using different turbulence models as a function of horizontal position

Far from the spacer at the distance of 10D (Figure 58), the CFD calculations overestimate the maximum axial velocity values. The difference between the measurement and the result of the SST model is about 13%, which is not much larger than the average measurement uncertainty.

In Figure 59, the effect of the TWISTED type spacer is presented in the Y=0 mm illumination plane. In the left outer subchannel, a double vortex is present in the measurement and most of the calculations. The direction of rotation of the first vortex is counter-clockwise, while the second vortex's is clockwise. The least sophisticated k-epsilon model represents these two vortices as one larger vortex. The first vortex is measured to be very close to the grid. The calculations describe this vortex with a much more elongated shape. The BSL Reynolds stress model provides the most similar distribution.

Figure 60 shows the line-along velocity distributions evaluated along the above-mentioned plane. In both of the outer subchannels at 0.5-1D distance, the direction of the axial velocities alternate caused by the detachment vortices visible in Figure 59. The velocity values increase consistently with the distance of the spacer, and the initial differences between the maximums of the internal subchannels also decrease.
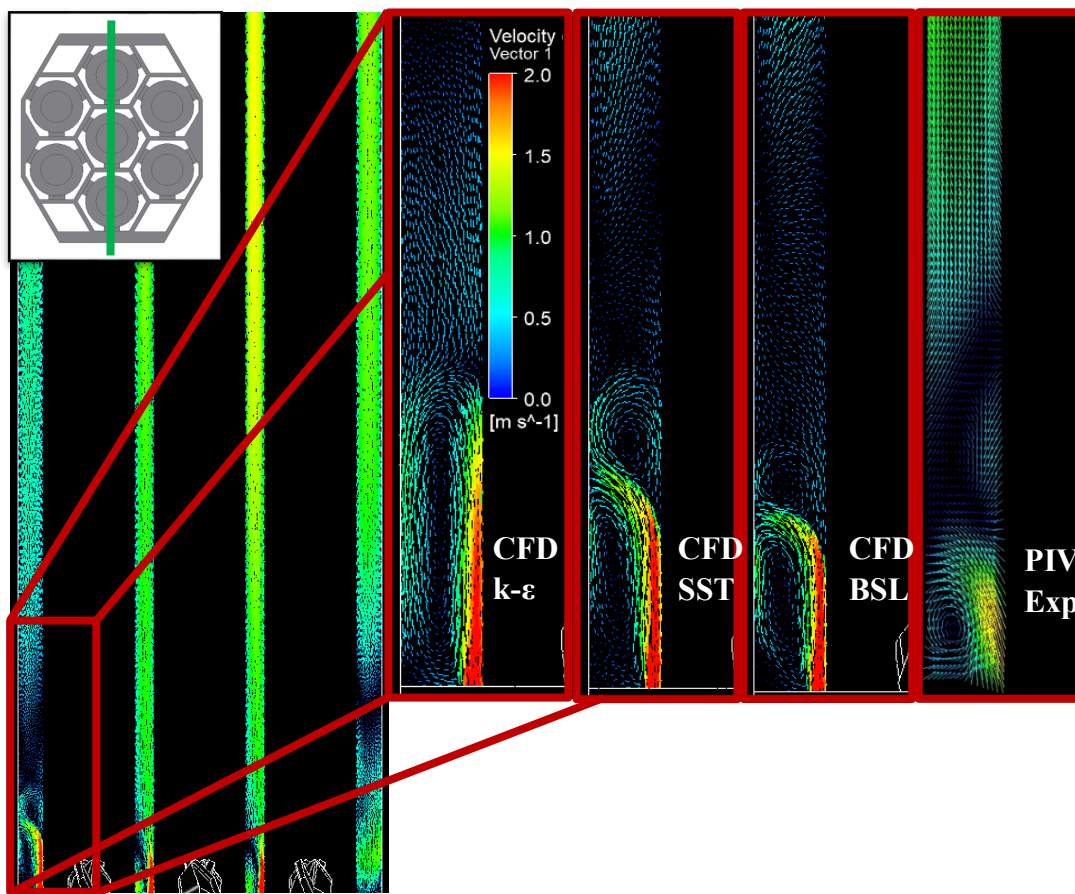
Figure 59: Comparison of axial velocity fields after the 2nd grid TWISTED type spacer in the experimental plane position Y=0
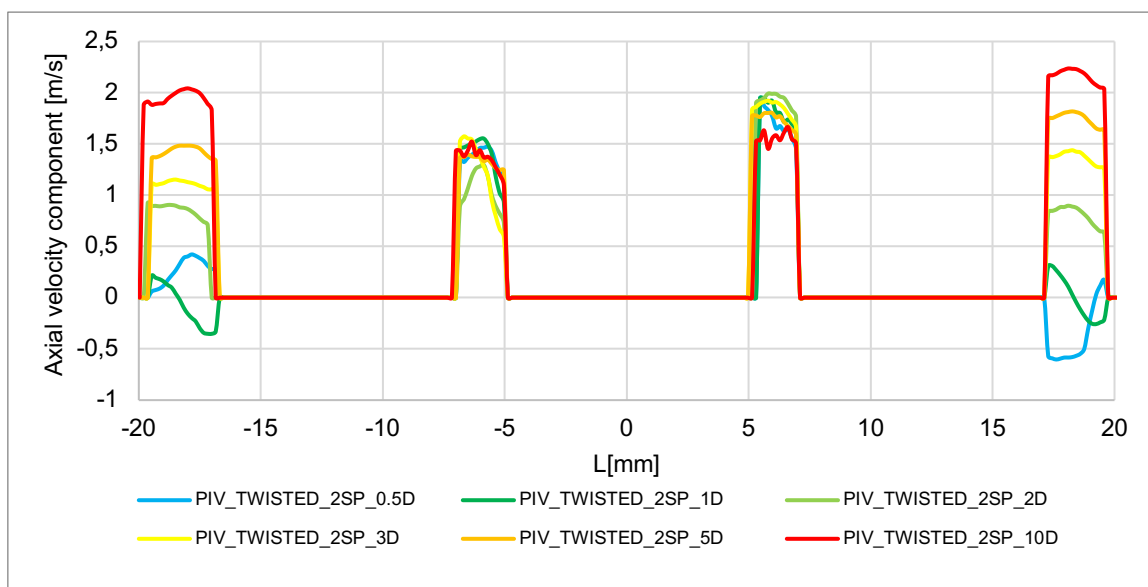
Figure 60: Axial velocity distributions behind the 2nd TWISTED type spacer grid from 0.5 to 10D distances in the experimental plane position Y=0 in the experiment as a function of horizontal position

In this chapter, several CFD simulations have been compared with the PIV measurements. A mesh independence analysis was made to ensure suitable model domain discretisation. A CFD model with acceptable computational requirements has been successfully constructed, describing the most important elements of the PIROUETTE test facility.

Separate simulations have been performed with the different spacer grids and the effects of the turbulence models have been investigated. The results of the computations were compared to the PIV measurements, both in terms of 2D vector fields and velocity distributions along different monitor lines.

The general conclusion we could draw is that the CFD simulations with the applied turbulence models overestimate the axial velocity values for sections far away from the spacer grid. In many cases, the SST turbulence model offered the best results; however, there are some evaluation positions and cases where other models seemed more accurate. There is no single turbulence model which could be declared as most accurate for this purpose.

6. LOFA MEASUREMENTS

The aim of work package 3.5 is to answer the question: how the reactor zone behaves during a LOFA (Loss of Forced Flow Accident) event, where the volume flow of coolant passing through the reactor is drastically reduced. During a LOFA event, the volumetric flow rates decrease with time.

In Figure 61, the core decay heat power and mass flow rates are presented during a LOFA + SBO (Station Black Out) event calculated by Mayer with CHATARE model [7]. As we can see, the core power and the mass flow rate decrease rapidly and exponentially. Approximately 60 s after the starting point of the transient the mass flow rate stabilizes ad driven by natural convection.
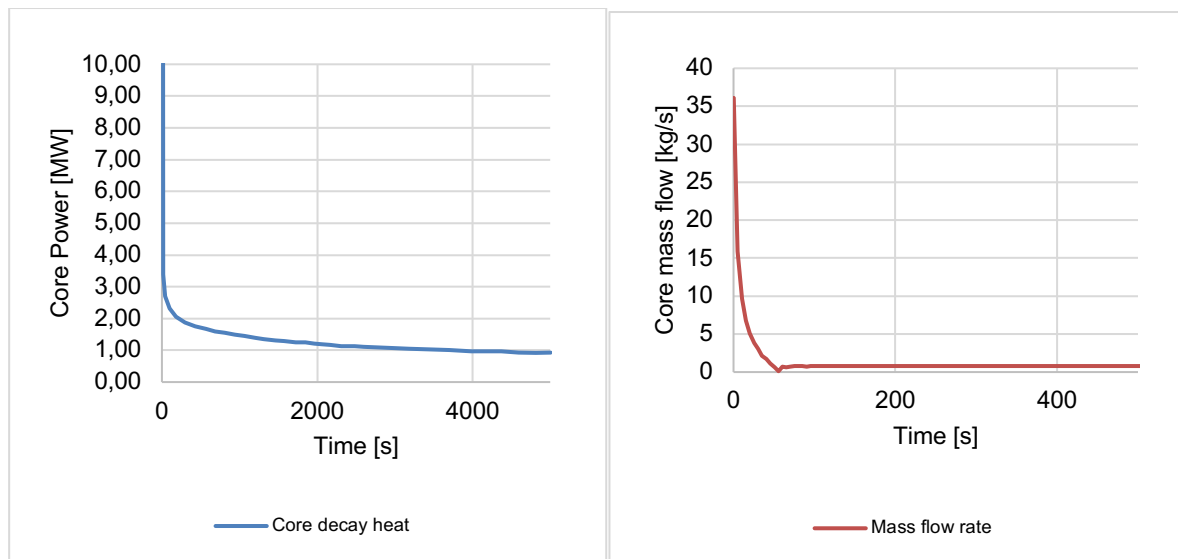
Figure 61: Core decay heat and mass flow rates calculated by CHATARE [45]

The PIROUETTE system is not suitable for the temporal resolution of such a process, but we are able to model operating states associated with dedicated time instants.

Figure 62 shows some of the Reynolds numbers in the fuel assembly during the transient. It is possible to create similar flow conditions of the chosen time instants in the PIV rod bundle. The highest Reynolds number is 22600, and the lowest is 350, which represents the natural convection regime of the accident. The values presented in Figure 62, represent the Reynolds numbers of the fuel assembly in the rod bundle measurements.
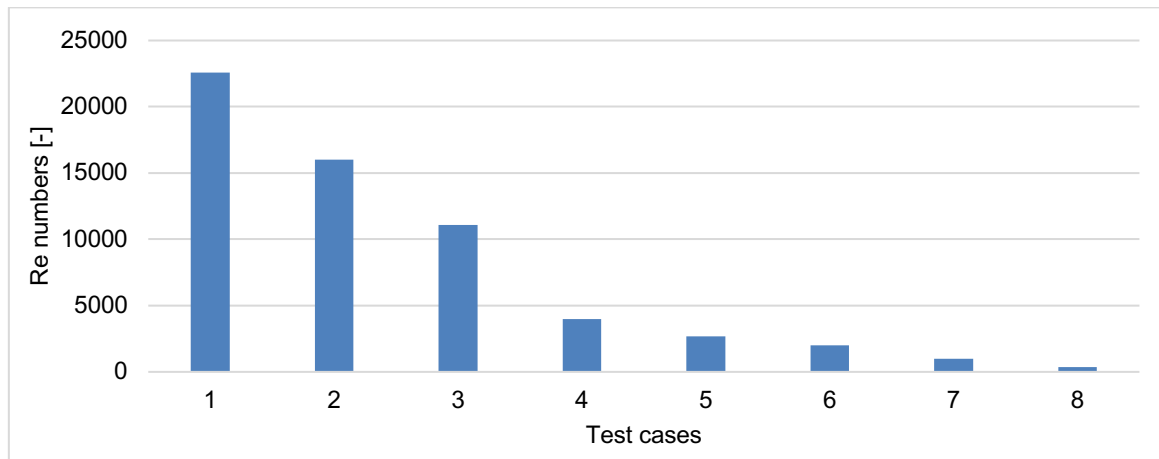
Figure 62: Chosen Re-numbers of the fuel assembly for LOFA measurements

Case-number	Re-number	$W_{average}$[m/s]	Q [m3/h]	Q [l/h]	Δt [µs] time interval
1	22590	2.014248	6.003861	6003.861	50
2	16000	1.426648	4.252402	4252.402	50
3	11072	0.987285	2.942795	2930	70
4	4005	0.357175	1.064629	1060	500
5	2701	0.240924	0.718122	715	600
6	2000	0.178331	0.53155	531.5503	700
7	1000	0.089165	0.265775	265.7752	1000
8	350	0.031208	0.093021	93.0213	1500

Table 6: Main parameters of the test cases

The main parameters of the test cases are collected in Table 6. With the decreasing Re-number, the average flow velocity and the needed flow rate also decrease. The time interval in the lower velocity cases was increased to detect the seeding particle movement in the frame pairs during the measurements.

The measurements were carried out with NOVANE and TWISTED vane spacer grids to investigate the effect of the improved spacer grid without forced flow. The NOVANE grid is the reference case (as before in the previous chapters). The test of the vane spacer grid is necessary because, although we have seen that the mixing vanes have a positive effect in normal operation, the pressure drop on the grids is slightly increased. This effect must be counteracted in the natural circulation-driven operating mode.

The measurements were made behind the third spacer to provide a good basis for comparing the results of CFD simulations.

6.1. INTERPRETATION OF 2D PLANAR VELOCITY DISTRIBUTIONS DURING LOFA BEHIND THE 3RD SPACER

6.1.1. RESULT OF THE NOVANE VANE EXPERIMENT CASES

The velocity flow field behind the 3rd spacer in the case of the NOVNE grid can be seen in Figure 63. The captured field intersects the outer two rods of the rod bundle. In Figure 63, the W-axial velocity flow fields are presented in the case of different Re-numbers. The impact of the decreasing mass flow rates can be clearly observed. As mentioned before, the spacer grids create several higher velocity "jet-like" flow structures due to constriction. This type of flow structure is easily recognizable in high flow rate cases in the NOVANE and TWISTED (Figure 76) type vanes. The different test cases are presented in the same velocity scale to highlight the extent of the decreasing flow rate. There are no visible captured vectors between the two rods in Re=350 case. Obviously, the flow does not stop, but the velocity vectors are relatively small compared to the Re=22 000 case.
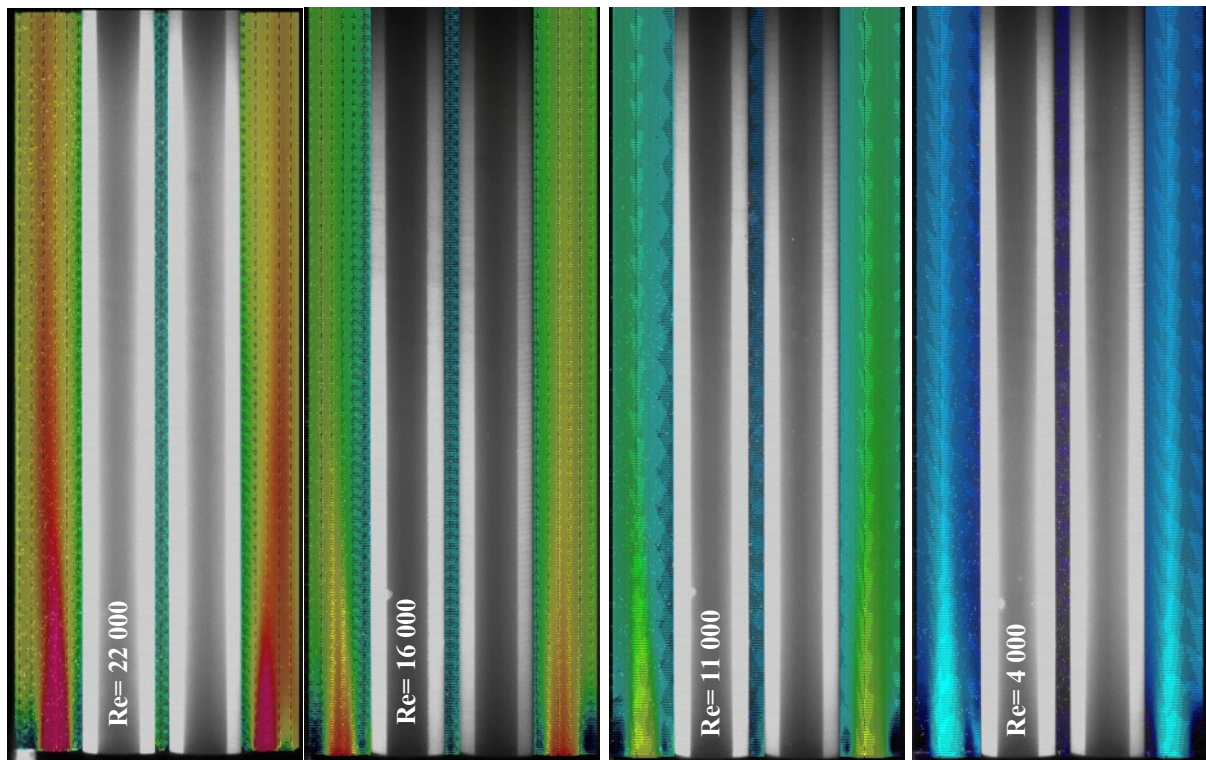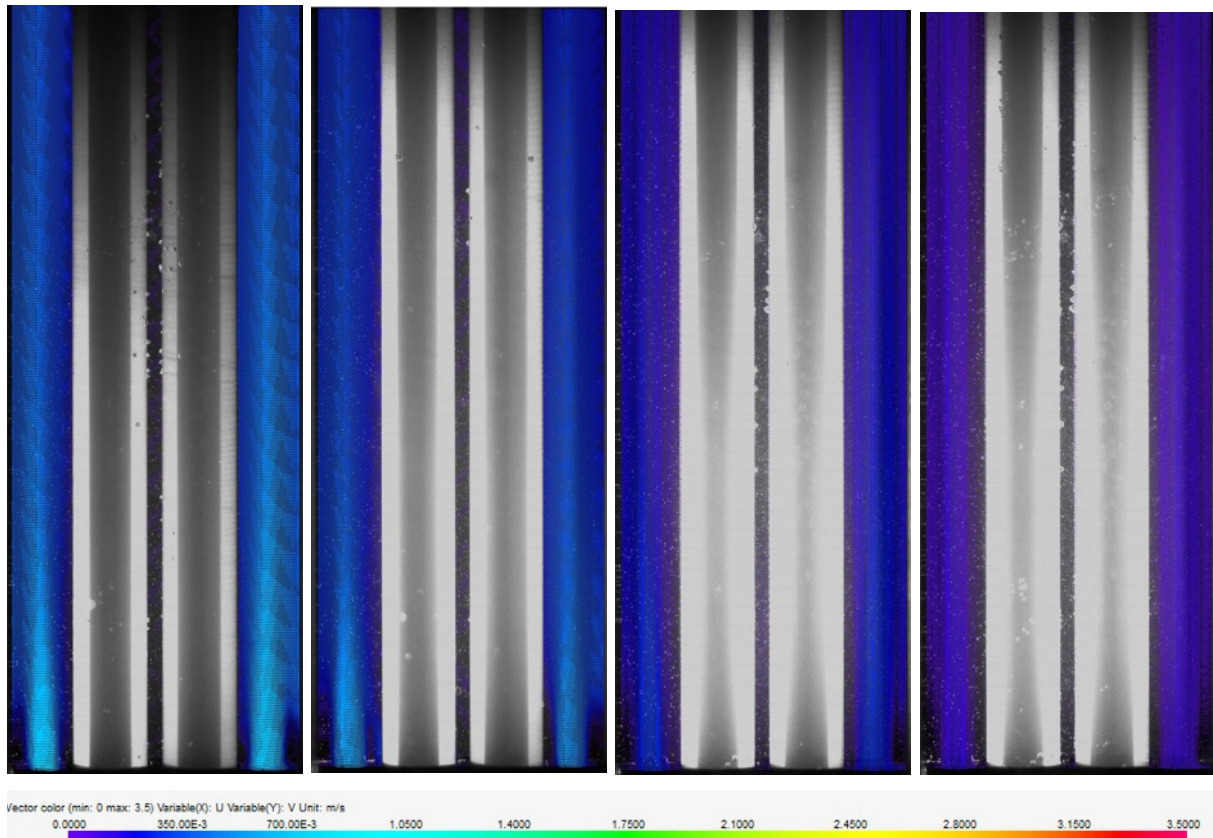
Figure 63: 2D velocity distribution in case of different Re-numbers behind the 3rd NOVANE spacer

In Figures 64-67, line-along velocity distribution scan be seen at 1D distance behind the NOVANE type spacer. In this position, the effect of the spacer is well defined, and is it remains in the different Re-number scenarios. In the middle subchannel (between the two rods), in the case of Re=11-16 000, the axial velocity is in the same magnitude as in the outer subchannels.

In contrast, the velocity drops significantly in the case of lower flow rates. Furthermore, the flows change their direction in some cases. This phenomenon can be observed better in Figure 66, where the line-along velocities were non-dimensioned with the maximal value of the monitor line.

The transversal velocities also decrease step by step with lower flow rate cases. The similarity of the profiles is clearly visible (Figure 65), and the reduction of the transversal velocity amplitudes is also observable.

Figure 64: Line-along axial velocity distribution at 1D distance behind the 3rd NOVANE spacer in different Re-number cases

Figure 65: Line-along transversal velocity distribution at 1D distance behind the 3rd NOVANE spacer in different Re-number cases

In Figure 66, the non-dimensioned velocity profiles are presented. The velocity values were divided by the maximum velocity of the given line and case. In the outer subchannels, the shape of the velocity profiles evolves from typical laminar to fully turbulent. This development is better observable far from the wake of the spacer. In Figure 66 and 70, the analytic solution for laminar flow in annular tube is also presented for comparison. We are aware of the oversimplification of the problem by applying the flow profile formula for annular tubes of

laminar flow, but we can see the tendency of the flow profile evolution with this comparison. In the inner subchannel (between the rods) in the case of the Re=2000, 2700, and 4000 the flow direction is opposite to the main flow. This is clearly not beneficial in terms of safety. Fortunately, these flow states represented by these Re-numbers, are very short-lived and temporary during a LOFA transient.

Figure 66: Line-along dimensionless axial velocity distribution at 1D distance behind the 3rd NOVANE spacer in different Re-number cases
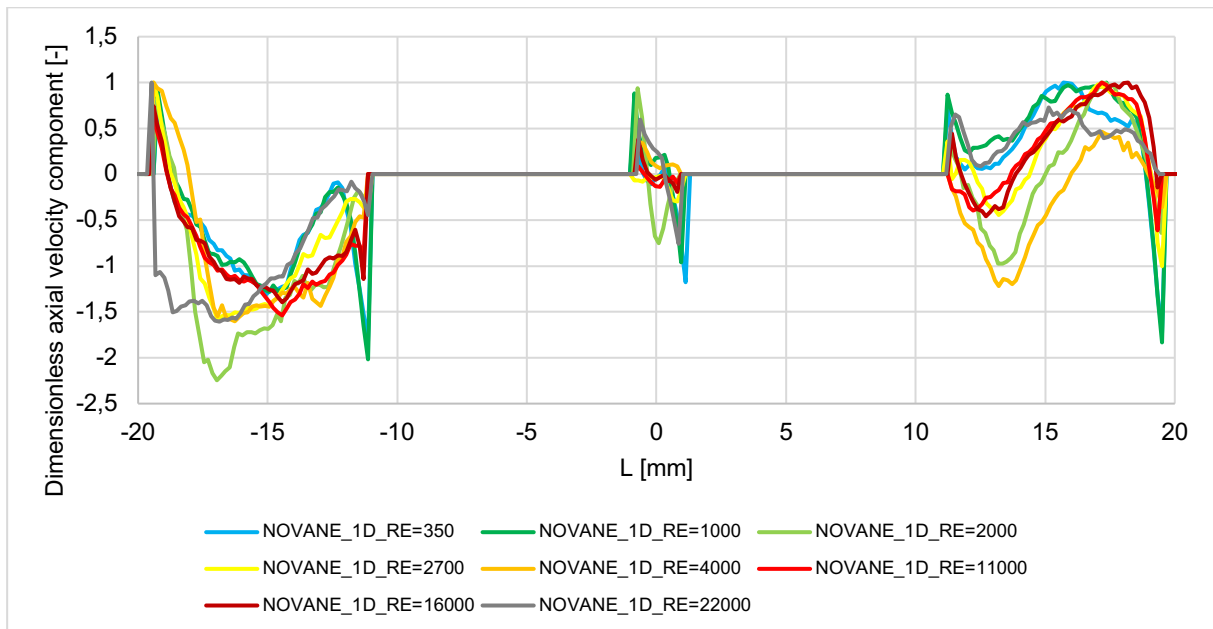
Figure 67: Line-along dimensionless axial velocity distribution at 1D distance behind the 3rd NOVANE spacer in different Re-number cases

Far away from the wake of the spacer the axial velocity profiles are very similar, apart from differences in maximum amplitudes (Figure 68). In contrast to the 1D distance profiles in the inner subchannel, the flow does not change direction at lower flow rates. The observed

backflow at 1D distance is only a local phenomenon. The transversal velocities are lower in the regions close to the spacer grids. The amplitudes of the profiles also decrease with the lower Re- numbers.
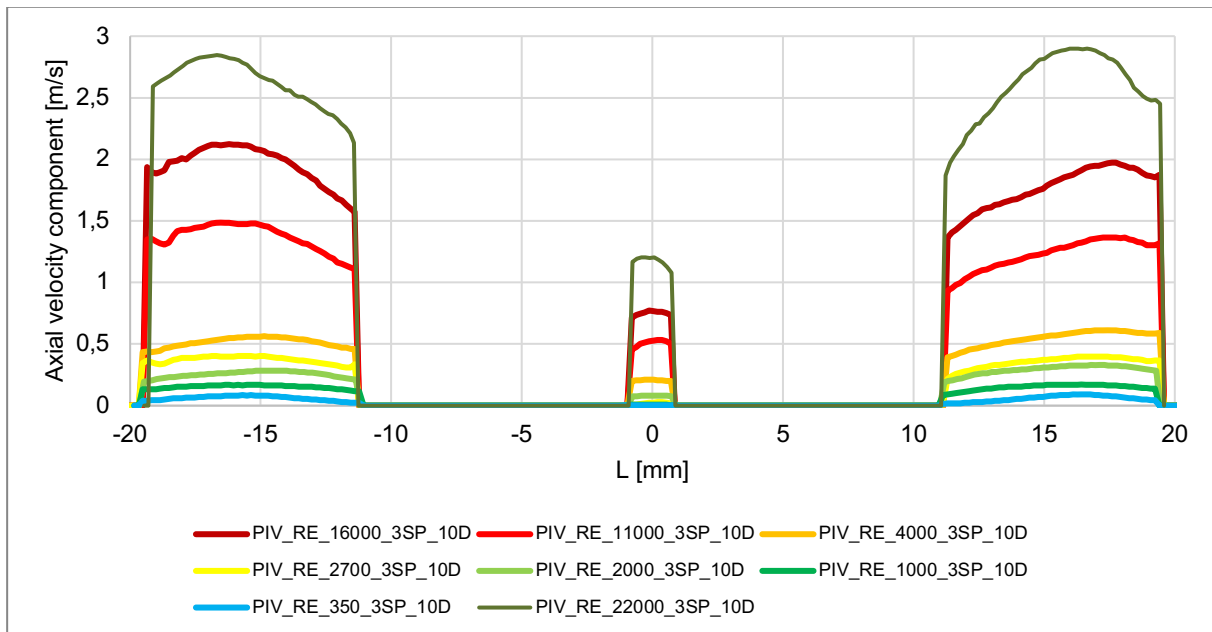
Figure 68: Line-along axial velocity distribution at 10D distance behind the 3rd NOVANE spacer in different Re-number cases
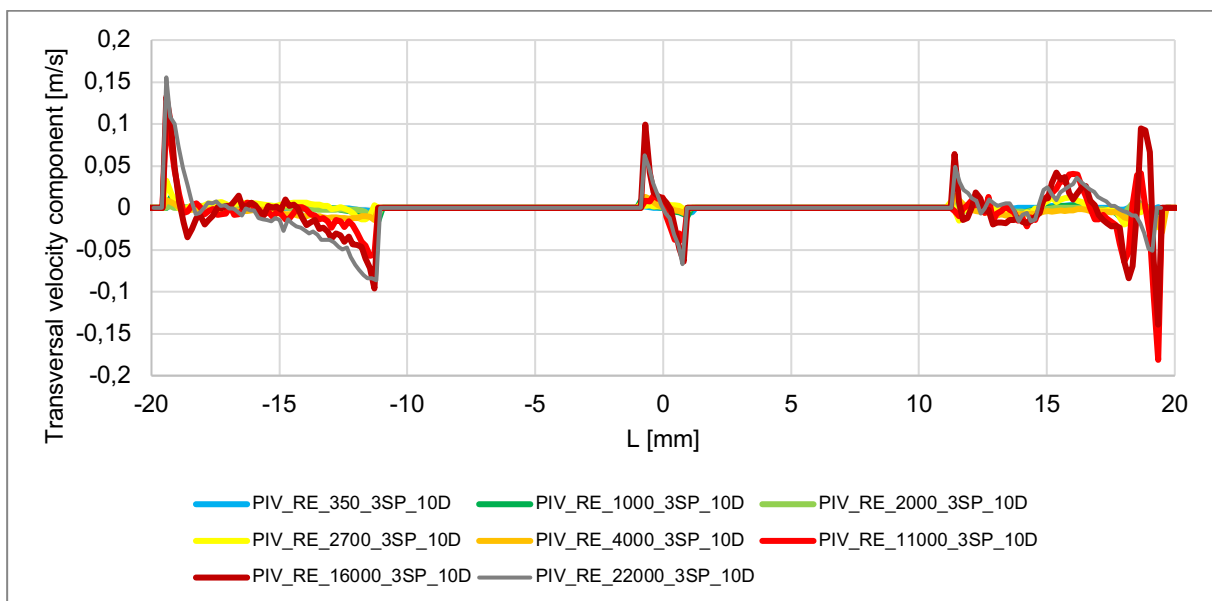
Figure 69: Line-along transversal velocity distribution at 10D distance behind the 3rd NOVANE spacer in different Re-number cases

At 10D distance behind the spacer, the non-dimensioned velocity profiles (Figure 70) are very similar in the outer subchannels in the fully turbulent cases. The analytically calculated laminar flow velocity profile is displayed in Figure 70, as well. The Re=350 case stands out because the nature of the profile is different. The analytical solution and the Re=350 profile is very similar,

but because the analytical solution cannot take into account the complex geometric nature of the rod bundle, the location of the maximum falls elsewhere. The experimental maximum is located closer to the channel wall because the rod bundle has greater flow resistance due to the relatively large surface of the rods.

For these reasons, it can be stated that the flow in the assembly is laminar at a Re number of 350, which is typical for the natural circulation mode. This characteristic must be taken into account since different heat transfer correlations are applicable in the laminar and turbulent cases.
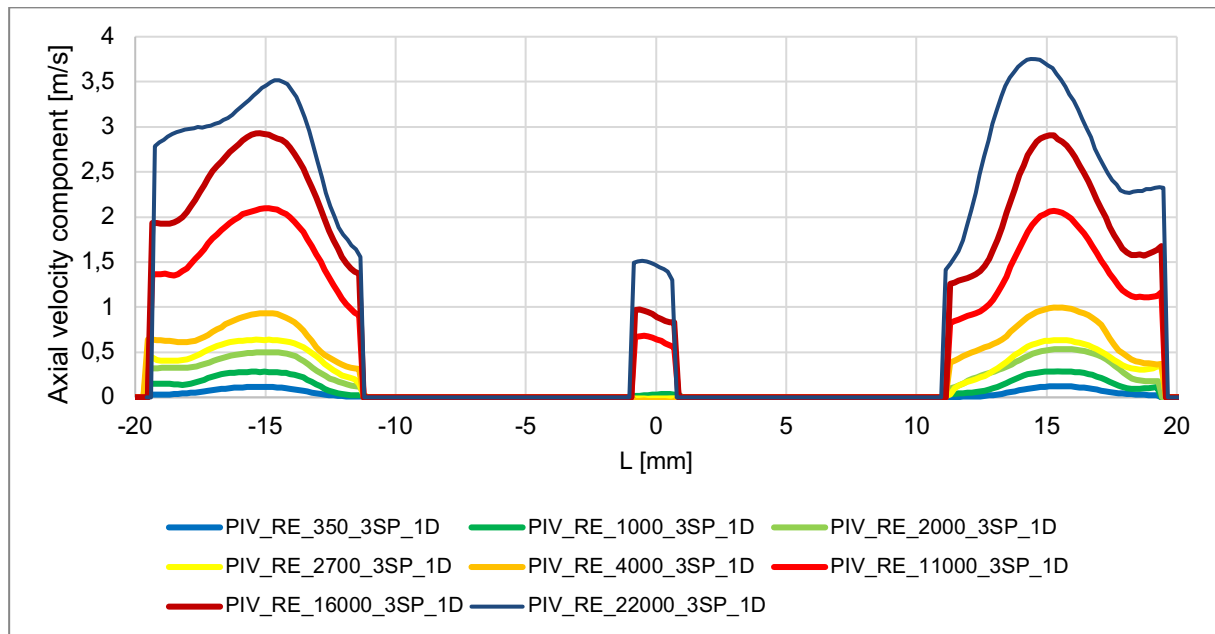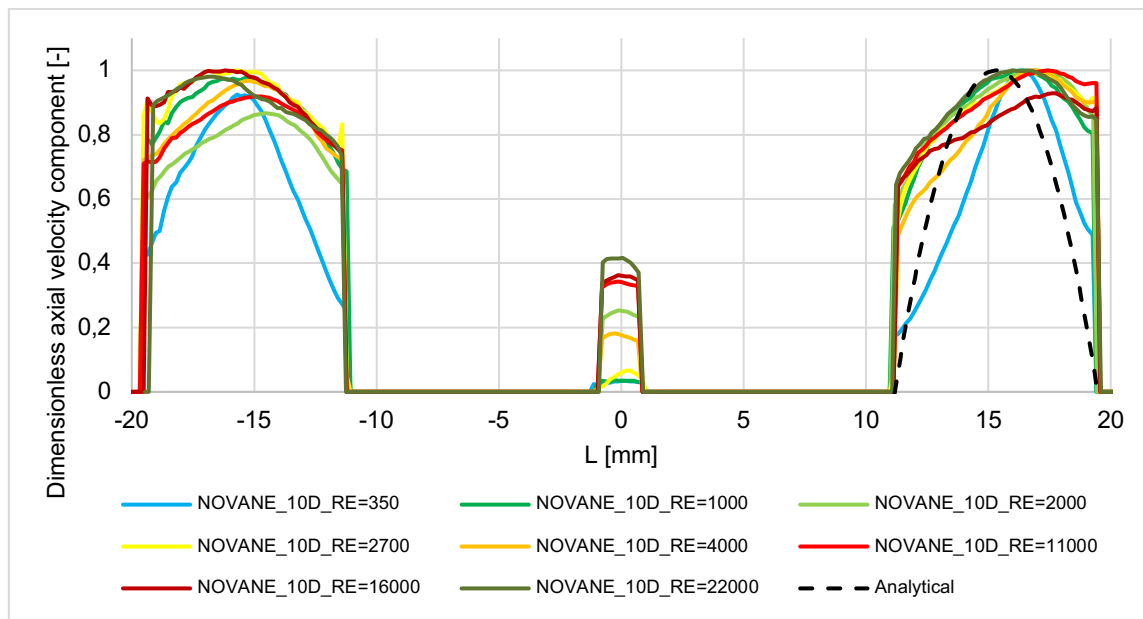

Figure 70: Line-along dimensionless axial velocity distribution at 10D distance behind the 3rd NOVANE spacer in different Re-number cases
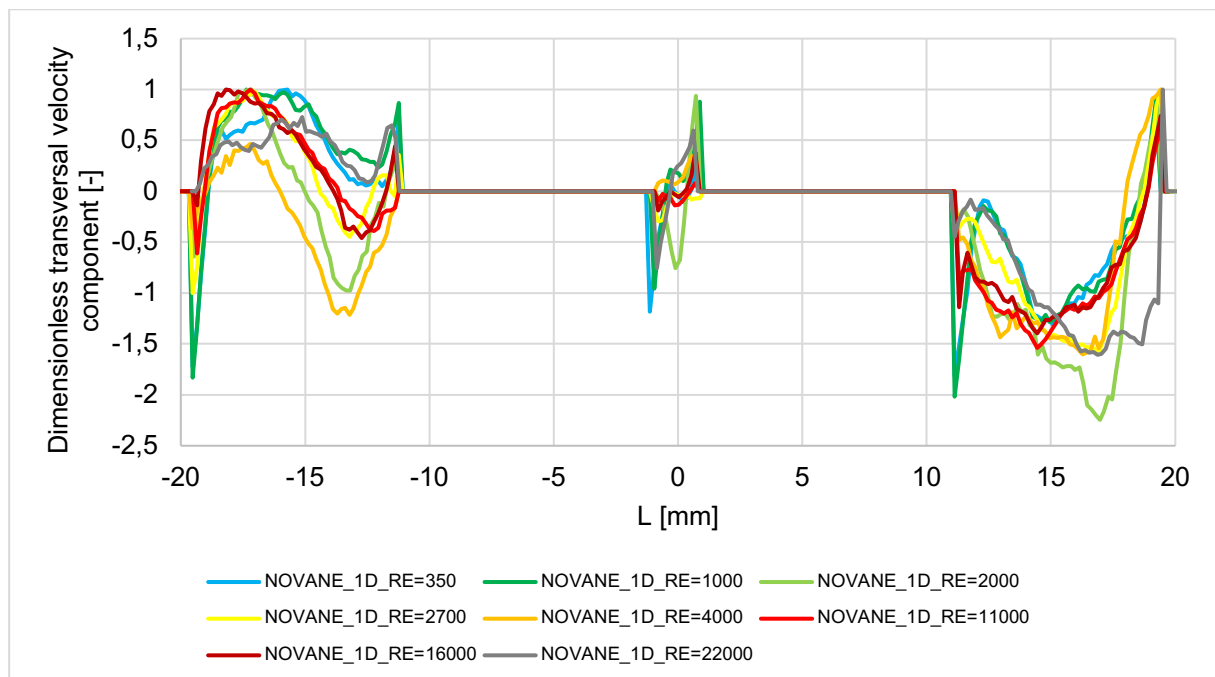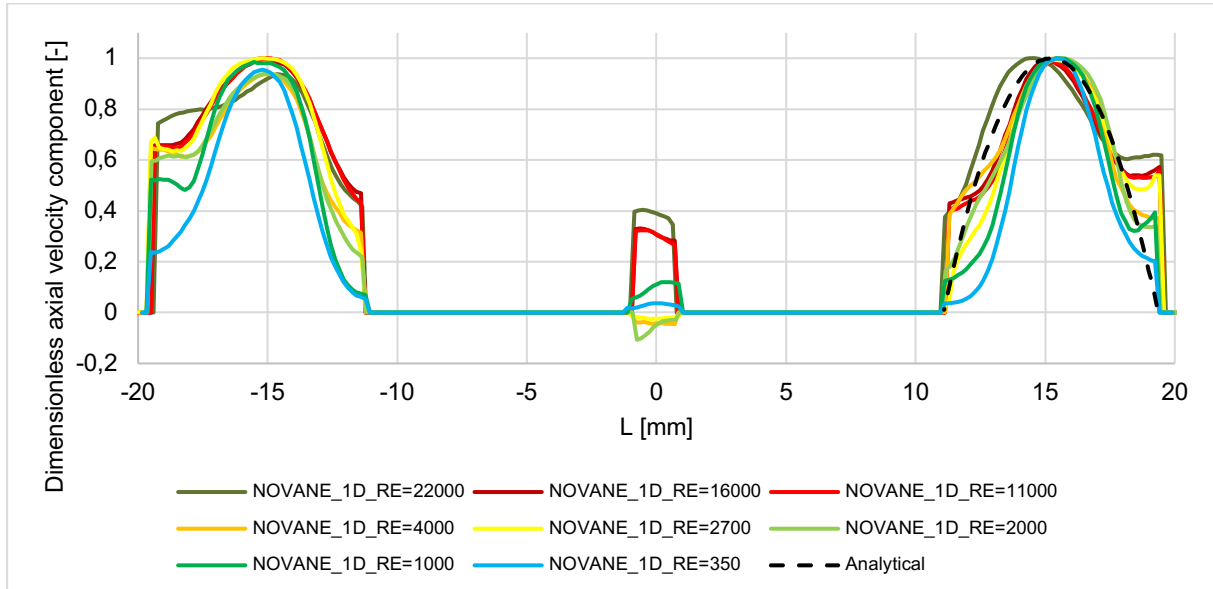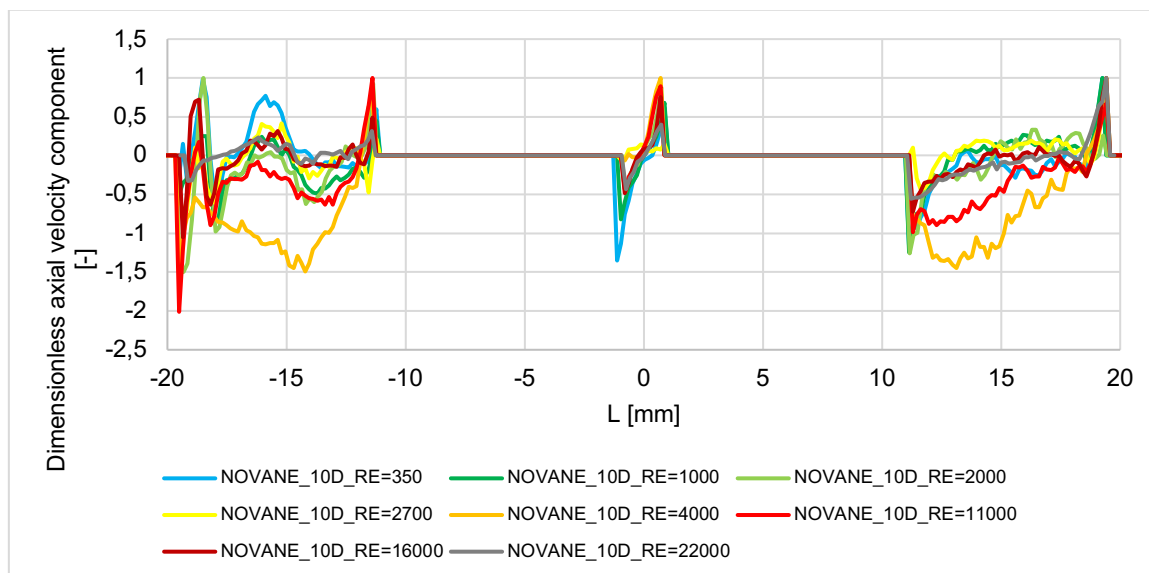

Figure 71: Line-along dimensionless transversal velocity distribution at 10D distance behind the 3rd NOVANE spacer in different Re-number cases

Besides the information on the cross-sectional velocity profiles, it is important to know how the flow field evolves along the inner subchannel (between the rods). The line-along velocity distribution in Z direction was evaluated inside the inner subchannel in the different cases. The runoff of the first 3 cases is very similar in the aspect of the axial and transversal components (Figure 72-73). In this figures, for Re=16 000-11 000, the axial velocity components show a small anomaly at 75 mm height, while for the transversal velocity components a local peak is observed. These are not due to real physical processes, but are anomalies from measurements. A small impurity on the channel wall can produce a similar phenomenon. This could be avoided by reducing the statistical errors, which would require more image acquisitions during measurements.
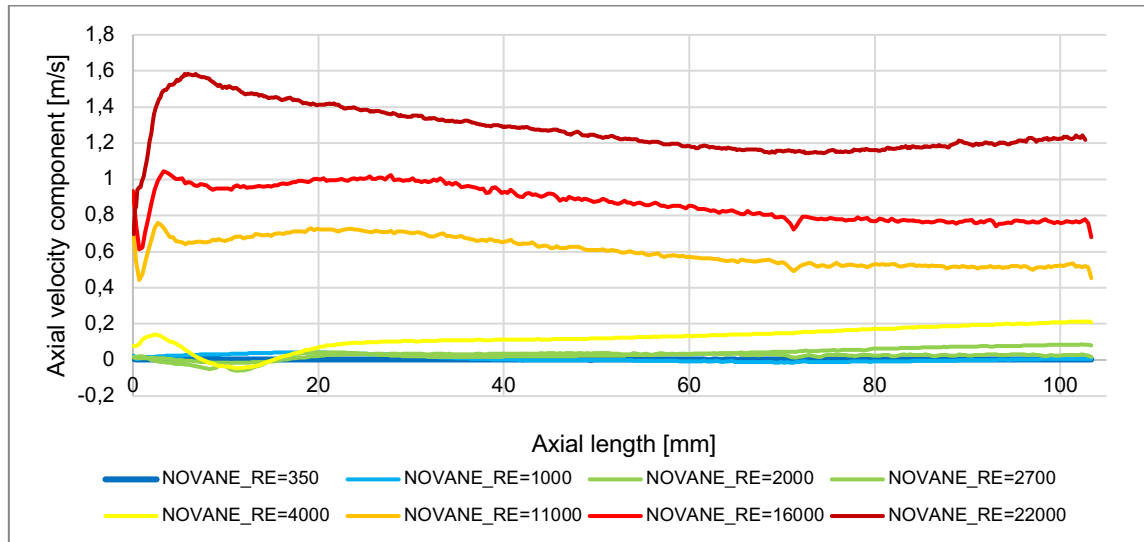
Figure 72: Axial velocity distributions in the gap between the two rods as a function of height for NOVANE type spacers after 3rd grid (monitor line position marked in Figure 10 with white arrow)
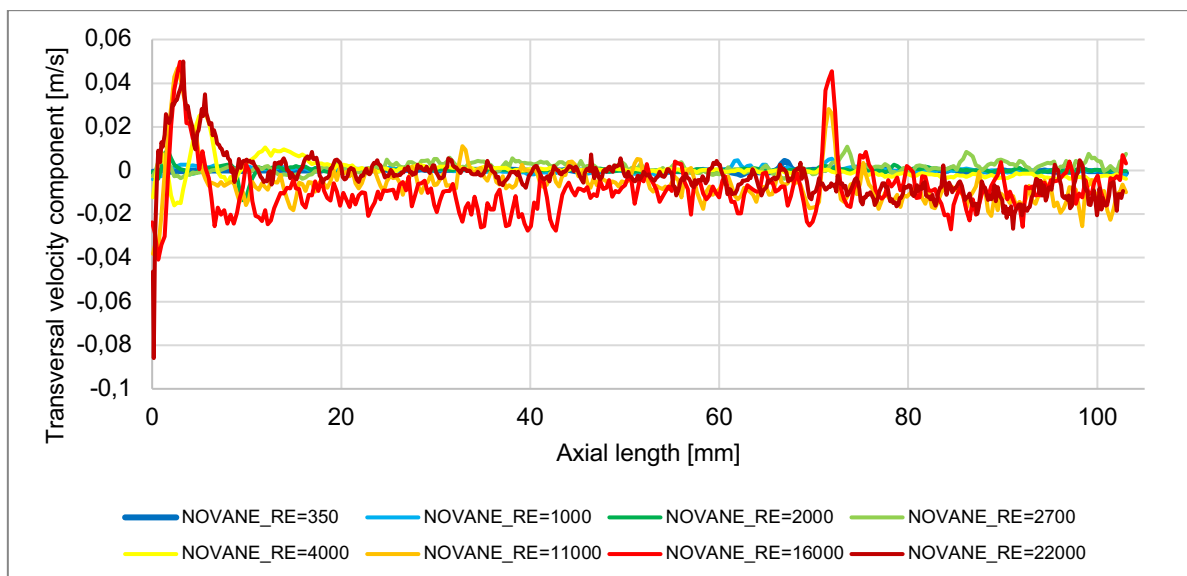
Figure 73: Transversal velocity distributions in the gap between the two rods as a function of height for NOVANE type spacers after 3rd grid (monitor line position marked in Figure 10 with white arrow)

In Figure 74, the non-dimensioned axial velocity distributions can be seen in the middle line of the inner subchannel. These data can provide an overview of the flow directions of this channel in different mass flow cases. In the region of 0-15 mm behind the spacer, significant backflow appears in the measurements at Re=2000, 2700 and 4000. This backflow region near the grid is growing with the lower mass flow till Re=1000 when it disappears. In the case of Re=1000, the backflow region is in the distance between 40-95 mm.
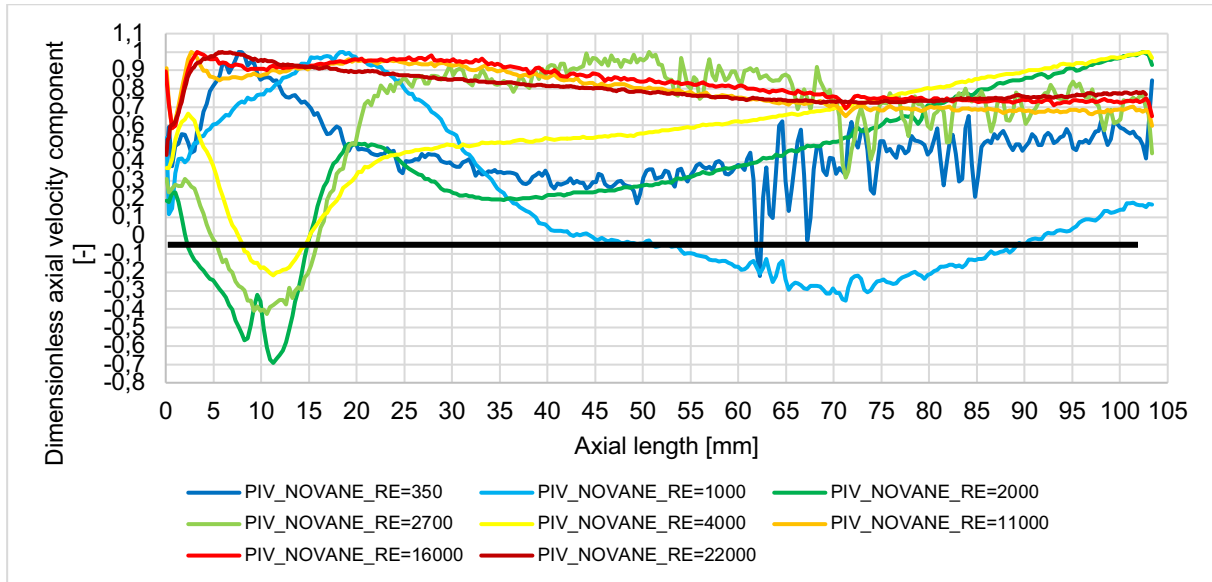
Figure 74: Dimensionless axial velocity distributions in the gap between the two rods as a function of height for NOVANE type spacers after 3rd grid (monitor line position marked in Figure 10 with white arrow)
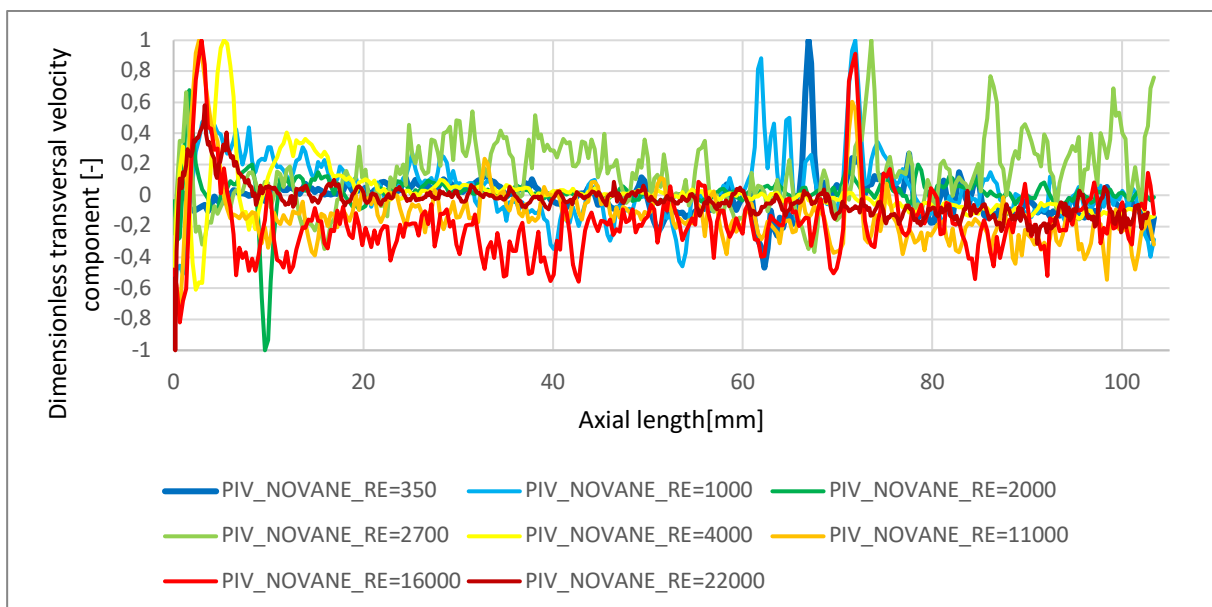
Figure 75: Dimensionless transversal velocity distributions in the gap between the two rods as a function of height for NOVANE type spacers after 3rd grid (monitor line position marked in Figure 10 with white arrow)

In Figure 75, the dimensionless transverse velocity components are shown, similar to the axial velocities. For the different Re-number cases, the transverse velocities approach zero except for small local perturbations.

The conclusion of the NOVANE LOFA experiments are the followings. The PIROUETTE system is capable of capturing flow fields in rod bundles during small mass flow rate conditions. The captured flow field characteristics are very similar in the different mass flow rate conditions till the flow rate decreases to the natural convection driven regime. In this regime, where the Re-number of the flow is approximately 500-700 the flow is laminar. (The minimum Re number is 350). A significant backflow appears behind the spacer between the Re-number cases of 1000-4000.

6.1.2. RESULT OF THE TWISTED VANE EXPERIMENT CASES

As mentioned above, the usage of mixing vanes on spacer grids has a huge beneficial effect of the operation of the fuel assemblies. In normal operation, the enhanced mixing caused by the vanes can increase the heat transfer from the fuel rods to the coolant. On the other hand, it can increase the pressure loss of the assembly by approximately 9 % [24]. The effect of the mixing vanes on lower mass flow rate conditions needs to be investigated.

In Figure 76, the W-axial velocity flow fields presented in the case of different Re-numbers. As in the case of the NOVANE grid, we can observe the impact of the decreasing mass flow rates. The different test cases were presented in the same velocity scale as before. Based on this comparison, no different trends can be seen from those observed in the previous ones. Therefore, we also investigate the effect of TWISTED vane along monitor lines.
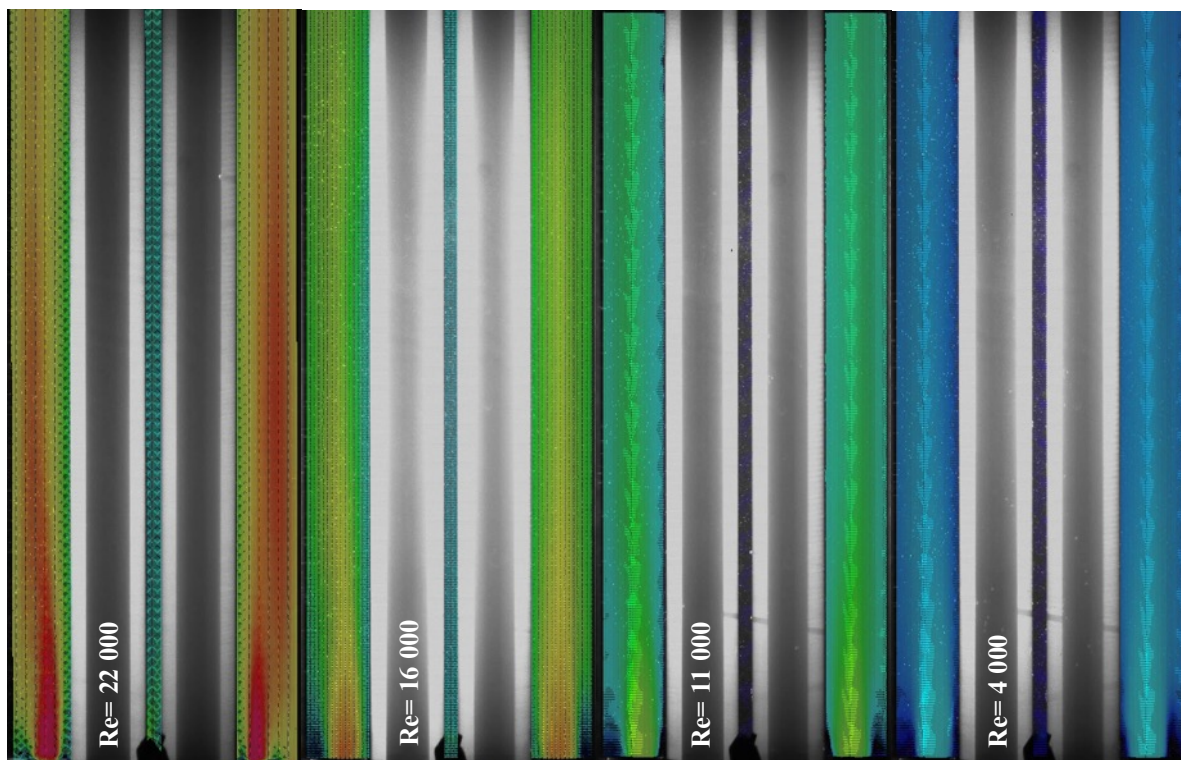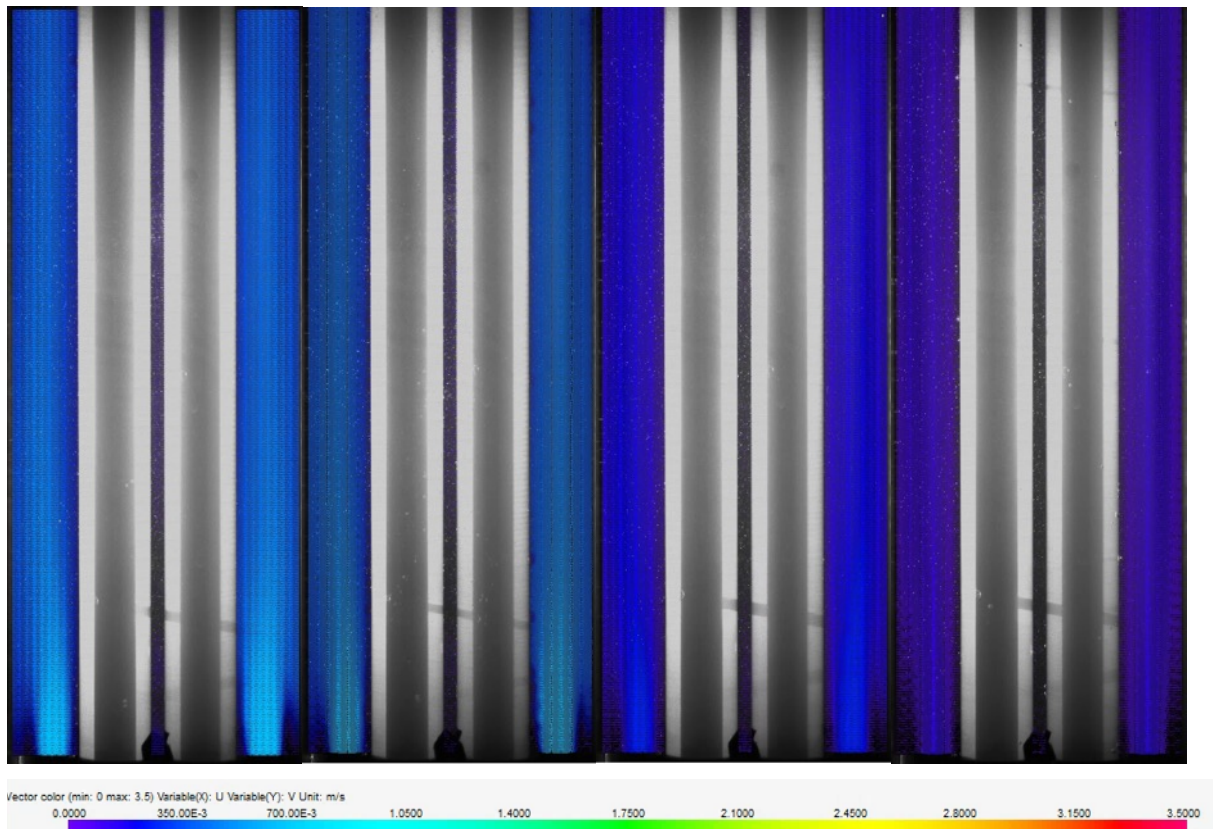
Figure 76: 2D velocity distribution in different Re-numbers behind the 3rd TWISTED spacer

In Figure 77 and 78, the non-dimensioned axial and transversal velocity components are presented at 1D distance behind the 3rd spacer. In the case of the TWISTED spacer grid, a similar trend is observable as in the NOVANE grid. In Figure 77, with the lower Re-numbers the velocity gradients of the 'jets' become steeper and steeper, due to the flow entering into the laminar flow region. In the middle subchannel, the flow does not change direction at 1D behind the spacer, however, the flow velocities are relatively lower than in the outer subchannels. The fact that the flow direction does not change in the middle subchannel (between the two rods) at 1D distance after the grid is a big improvement compared to the NOVANE case (Figure 77).
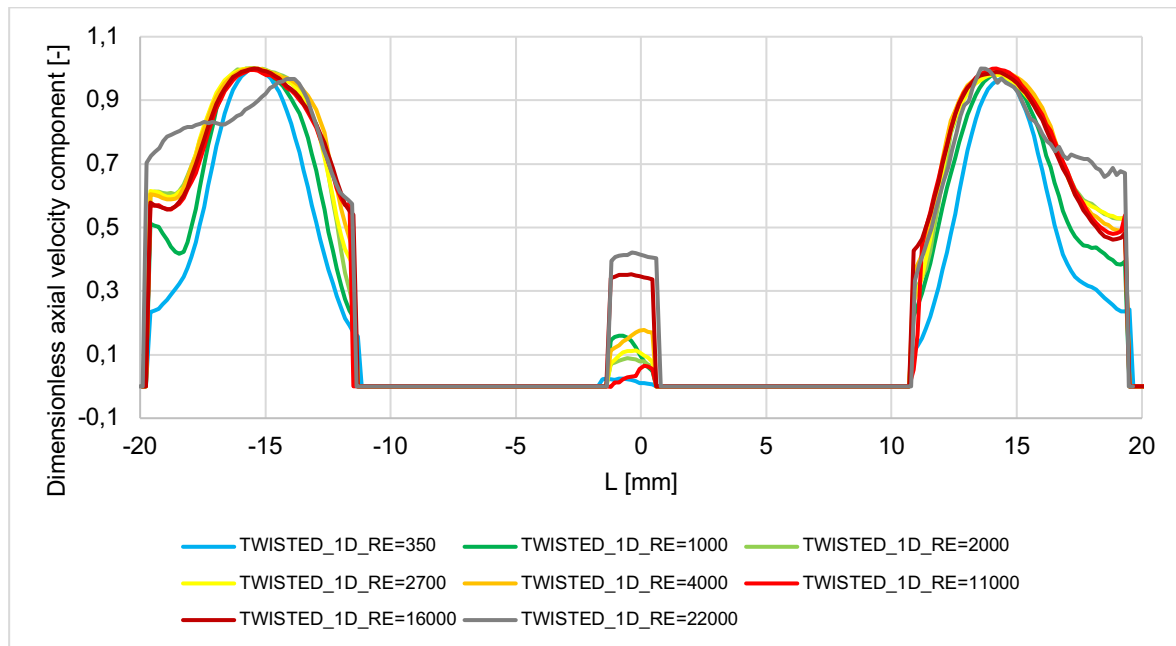
Figure 77: Line-along dimensionless axial velocity distribution at 1D distance behind the 3rd TWISTED spacer in different Re-number cases
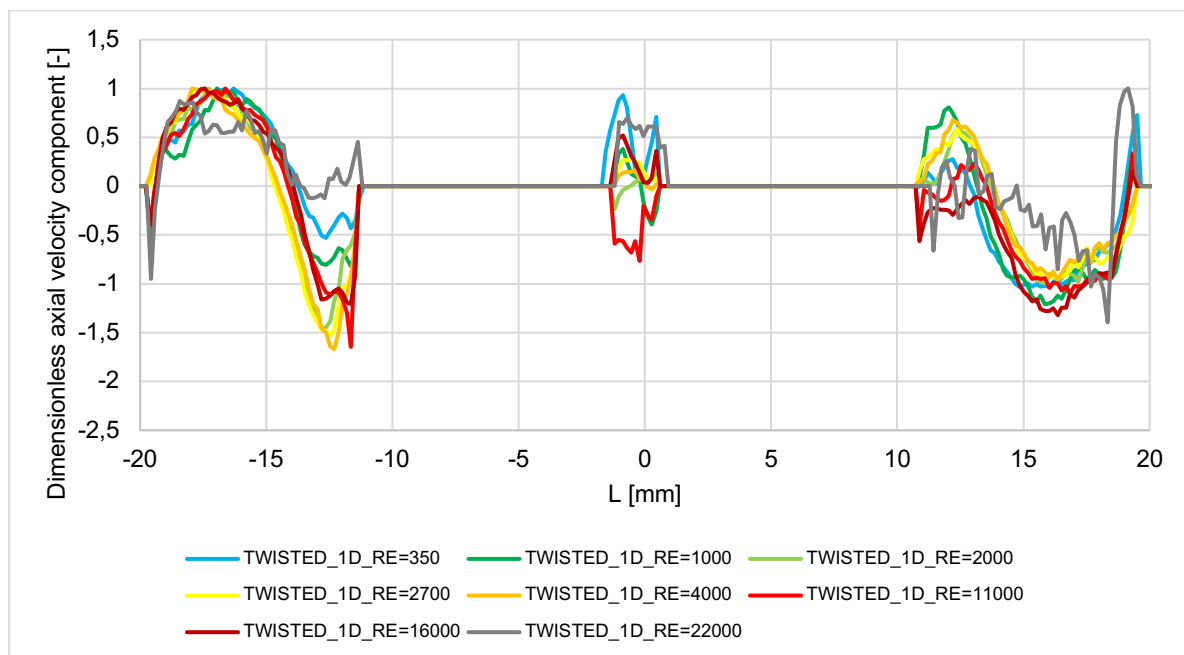
Figure 78: Line-along dimensionless transversal velocity distribution at 1D distance behind the 3rd TWISTED spacer in different Re-number cases

The effect of the mixing vanes on the transversal velocities can be seen (Figure 78). The profiles in different Re-number cases in the outer subchannels are very similar, therefore, we can say that the effect of the vanes remains in case of lower flow rates (especially in the near grid region). This kind of transversal velocity pattern is not presented in the far grid region (at 10D in Figure 80). The values are mostly near 0 m/s in the outer subchannels.

The axial velocity profiles are shown in Figure 79. In the outer subchannels, the profiles are almost self-identical in most cases, but the Re=350 case stands out from the rest. This shows that this case belongs to a different flow regime. It can also be observed that the flow velocity in the inner subchannel is the smallest relative to the outer two in the Re=350 case.

For the inner subchannel, the Re=11 000 measurement case is significantly different from the expected one. The axial velocity values are lower than for Re=4000 (Figure 77). The transverse velocity values also show a different trend than expected (Figure 78). This phenomenon is also observed in the results recorded at longer distances, as well as in the midline velocity distributions.

The cause of this phenomenon is not yet clear, but it is thought that a blockage may have occurred in the spacer grid during the experiment, drastically altering the flow conditions in the very narrow inner subchannel. This blockage could only have been temporary, as this phenomenon is not observed in the other experimental cases.

The PROUETTE system is equipped with pre-filters, but their operation may not be perfect.
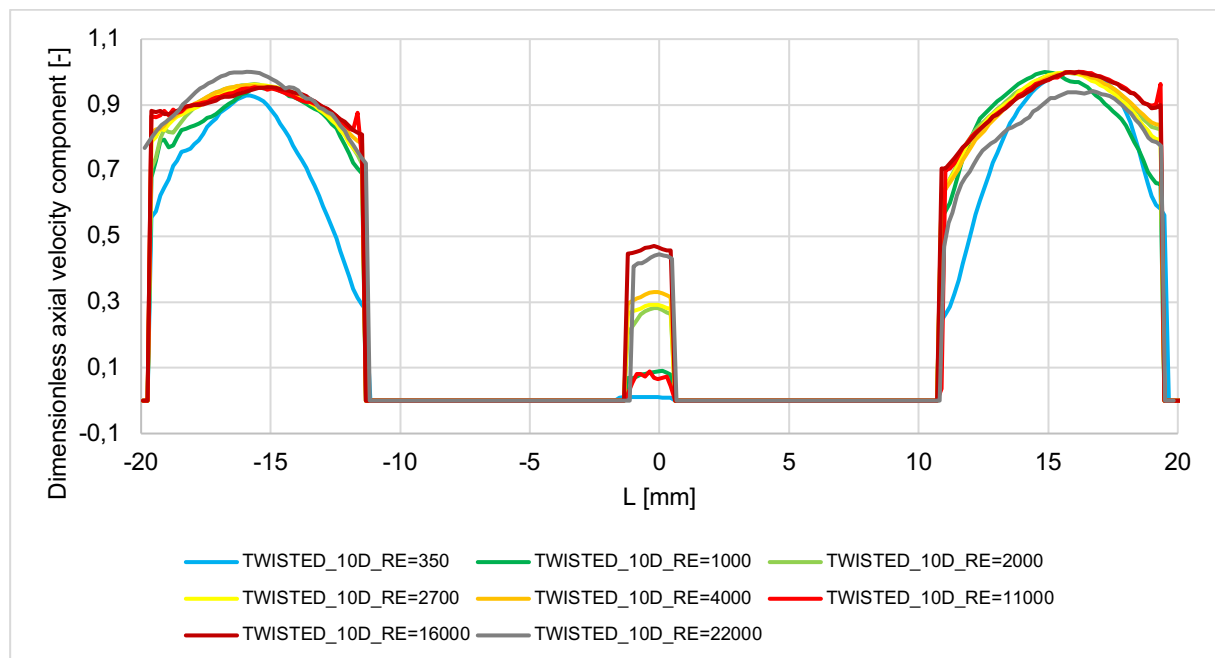
Figure 79: Line-along dimensionless axial velocity distribution at 10D distance behind the 3rd TWISTED spacer in different Re-number cases
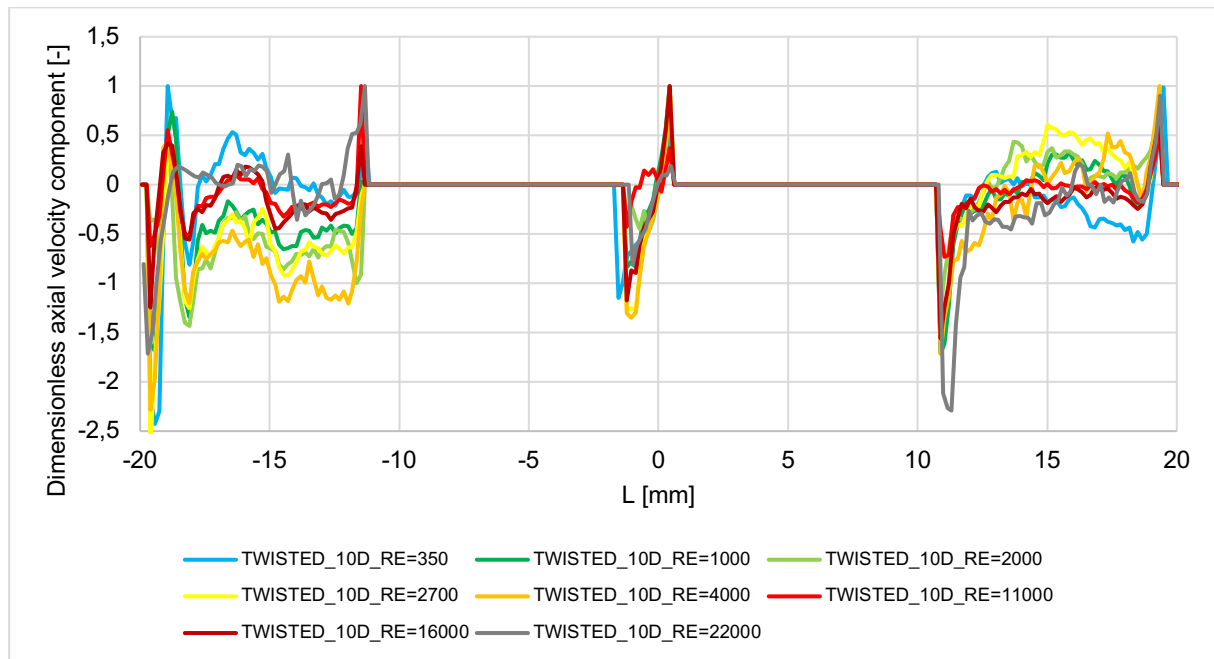
Figure 80: Line-along dimensionless transversal velocity distribution at 10D distance behind the 3rd TWISTED spacer in different Re-number cases

Figure 81 shows the axial velocity distributions in the gap between the two rods (inner subchannel). As the mass flux decreases, the velocities in the inner subchannel also decrease significantly. The absolute value of the transversal velocity component also decreases (Figure 82). The values of the case of Re=11 000 deviates from the other cases.
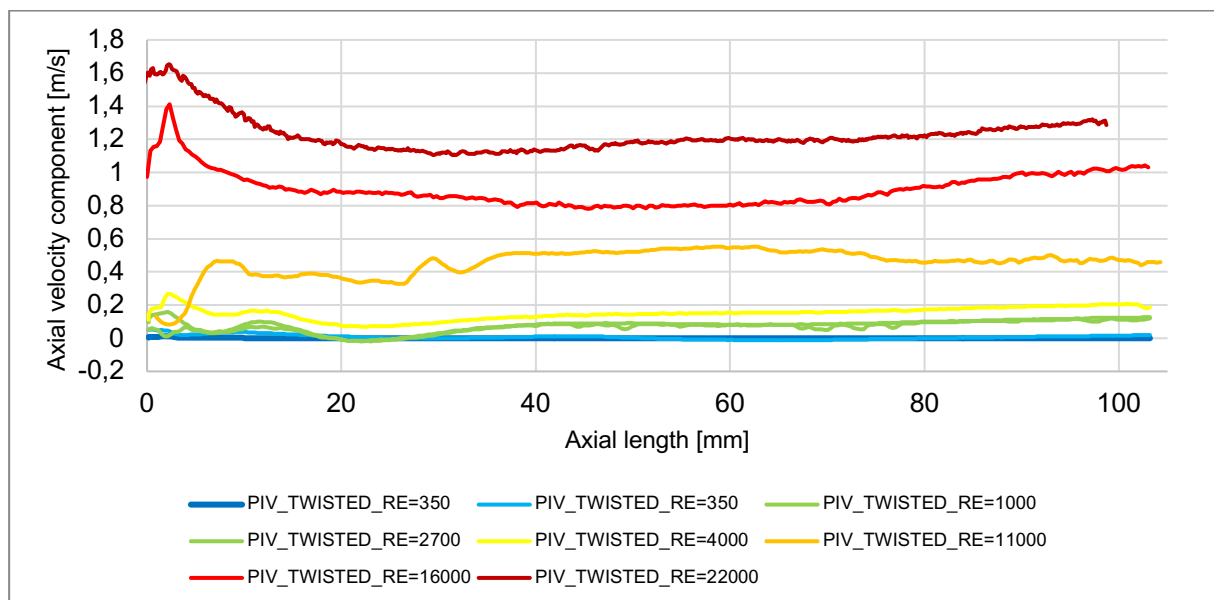
Figure 81: Axial velocity distributions in the gap between the two rods as a function of height for TWISTED type spacers after 3rd grid (monitor line position marked in Figure 10 with white arrow)
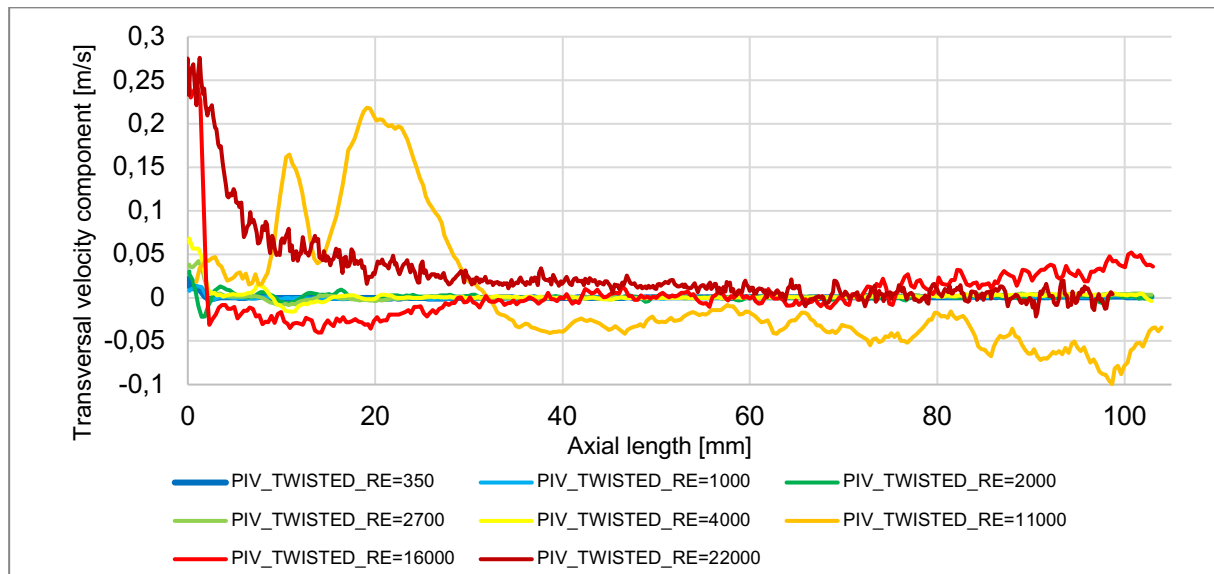
Figure 82: Transversal velocity distributions in the gap between the two rods as a function of height for TWISTED type spacers after 3rd grid (monitor line position marked in Figure 10 with white arrow)

In Figure 83, the relative or dimensionless values are presented in the same location. In the case of NOVANE grid, there are Re-number cases when the flow direction is opposite in some locations along this line. In TWISTED grid case, the Re-numbers where the negative values appear are: 1000-2700.
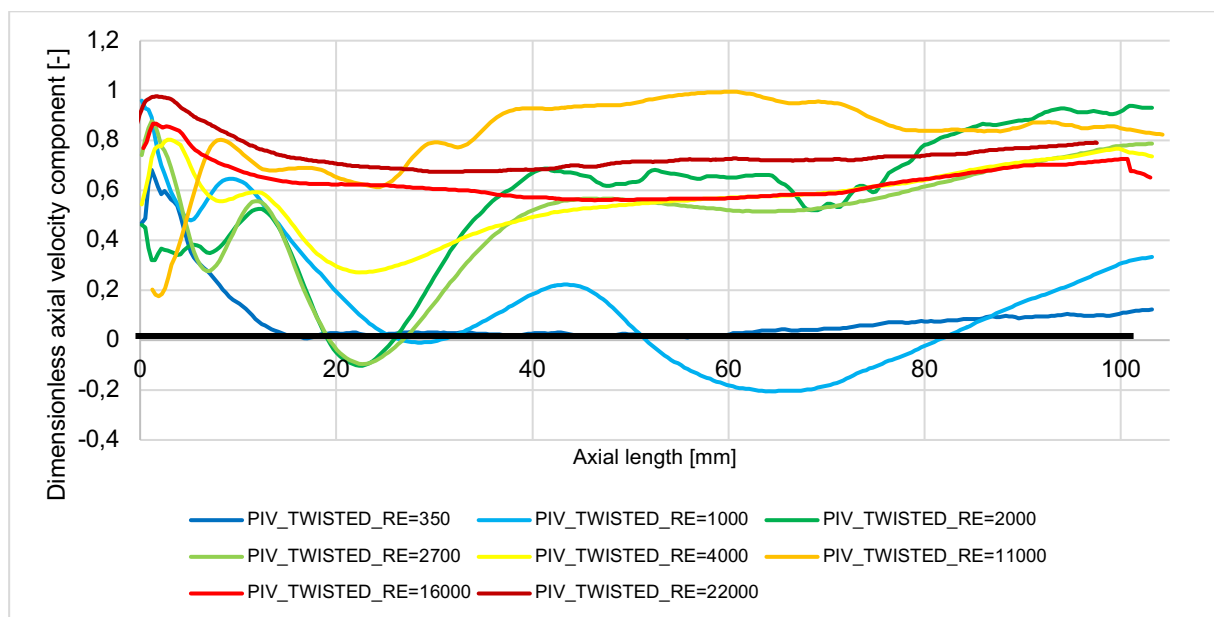
Figure 83: Dimensionless axial velocity distributions in the gap between the two rods as a function of height for TWISTED type spacers after 3rd grid (monitor line position marked in Figure 10 with white arrow)

In Re=2700 and 2000, the backflow region is located between 20 and 25 mm behind the grid, while in the case of Re=1000 is far behind (between 50-85 mm). These observed negative value regions are far smaller than in the case of the NOVANE grid. The relative minimums in the

different grids are: NOVANE = -0.55 [-], TWISTED = -0.1 [-]. Based on these findings, it seems that the backflows are less likely to occur in the case of the TWISTED vane. Further research is needed to understand these processes more deeply.

The dimensionless transversal velocity distributions can be seen in Figure 84. The Re=11 000 case stands out from the distributions of other cases. Unfortunately, the transversal distributions and the axial profiles are not as expected. As we mentioned, we assume that some undetected error may have slipped into this TWISTED vane measurement.

Figure 84: Dimensionless transversal velocity distributions in the gap between the two rods as a function of height for TWISTED type spacers after 3rd grid (monitor line position marked in Figure 10 with white arrow)

6.2. COMPARISON BETWEEN THE CFD CALCULATIONS AND PIV MEASUREMENTS

In this chapter, we would like to introduce the CFD simulation results in the aspect of the PIV measurements. In the 6.2.1 subchapter, the NOVANE results will be compared to the CFD calculations.

If the entire LOFA transient shall be analyzed by subsequent CFD calculations, a turbulence model that can cover the entire Re-number range will be needed. In general, such a model does not exist, but it is worth checking whether the models proposed for the transition range can handle the problem.

The CFD models are identical to the ones introduced in the previous chapters. The inlet boundary conditions were fitted to the different experimental cases. The calculations were performed with M3 mesh resolution. The chosen turbulence model was the SST k-ω. In some cases, we refined the calculation method with the setup the Gamma-Theta model for transitional turbulence, and run the simulation in transient mode. The Re=350 cases were handled with these time and computation effort consuming treatment. In these cases, the initial timestep was 0.001 s. Furthermore, for the Re=350 case, we also run simulations in laminar mode, where no turbulence model is applied by the CFX solver.

6.2.1. RESULT OF THE *NOVANE* VANE EXPERIMENT CASES

In Figure 85, the calculated and measured transversal velocity distributions are compared. The results are displayed on grayscale contours, where the velocity scales are the same in the calculations and experiment results. According to the PIV experiment, in the outer subchannels, two oppositely oriented but symmetrically positioned "angel wing shaped" transverse velocity regions are formed after the spacer. In the steady-state SST calculation (Figure 85, right side), these oppositely oriented regions are asymmetrical, but in the Gamma-Theta transient and in the Laminar calculations are clearly displayed as expected from the measurements.
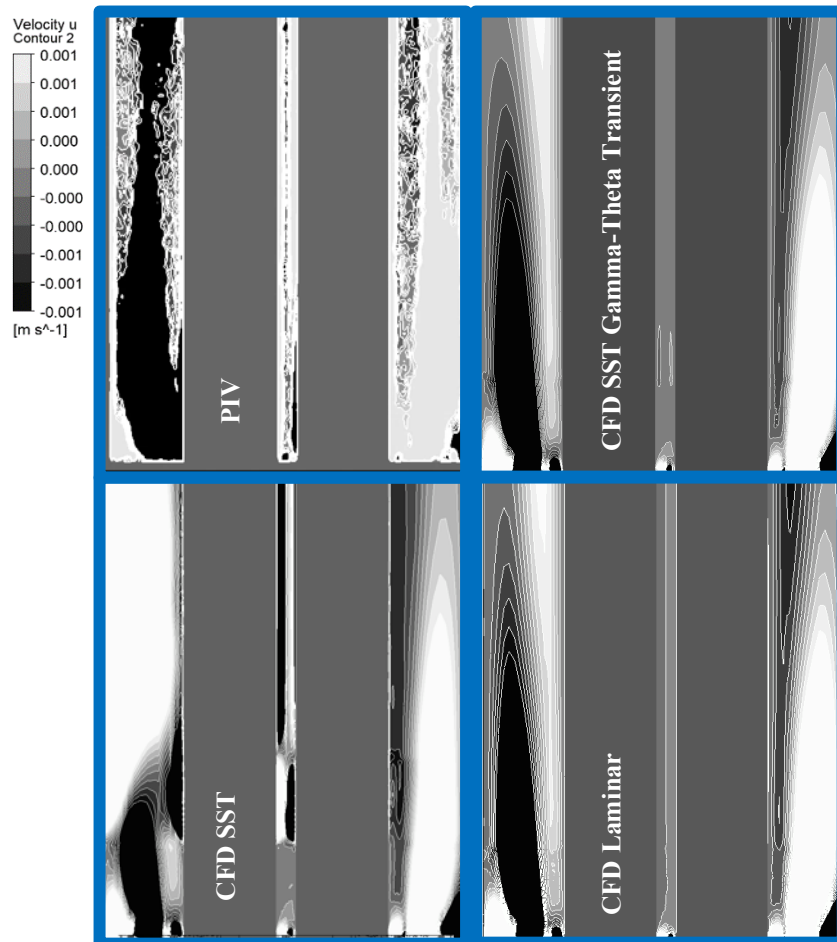
Figure 85: 2D transitional velocity component distribution after the 3rd NOVANE grid, Re=350 case

In Figures 86-87, the axial and transversal velocity distributions are presented at 1D distance behind the 3rd grid. In the figures, the CFD calculation and the analytically calculated velocity profiles are also presented. The analytical solution is closer to the measured one at the peak of the velocity maximum because the analytical profile is calculated with this measured maximum velocity. However, the CFD calculation can reproduce the shape of the profile better. The best match is with the laminar. The velocity profile in the middle subchannel is enlarged in the subfigure. The axial velocity profile is not so steep, as the analytical formula predicts, and the SST turbulence model gives the closest results to the measured ones. The results are well within the margin of error in the middle subchannel.
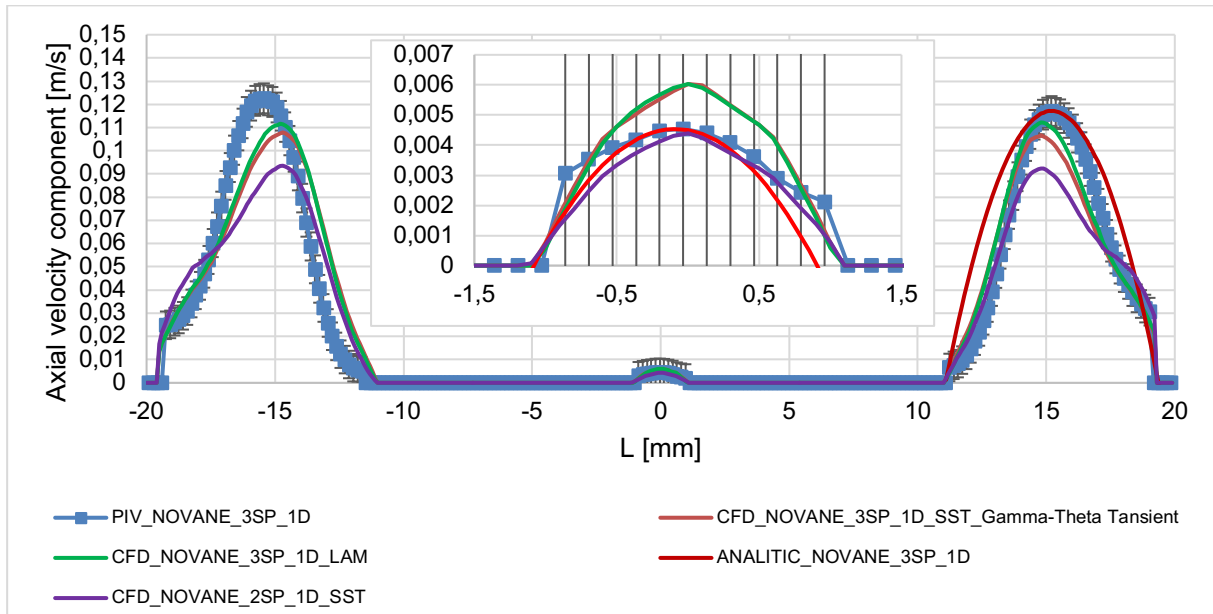
Figure 86: Line-along axial velocity distribution at 1D distance behind the 3rd NOVANE spacer, Re=350

Regarding the transversal velocity distributions, the two computation methods give similar results, which fit exceptionally well (Figure 87).

Figure 87: Line-along transversal velocity distribution at 1D distance behind the 3rd NOVANE spacer, Re=350
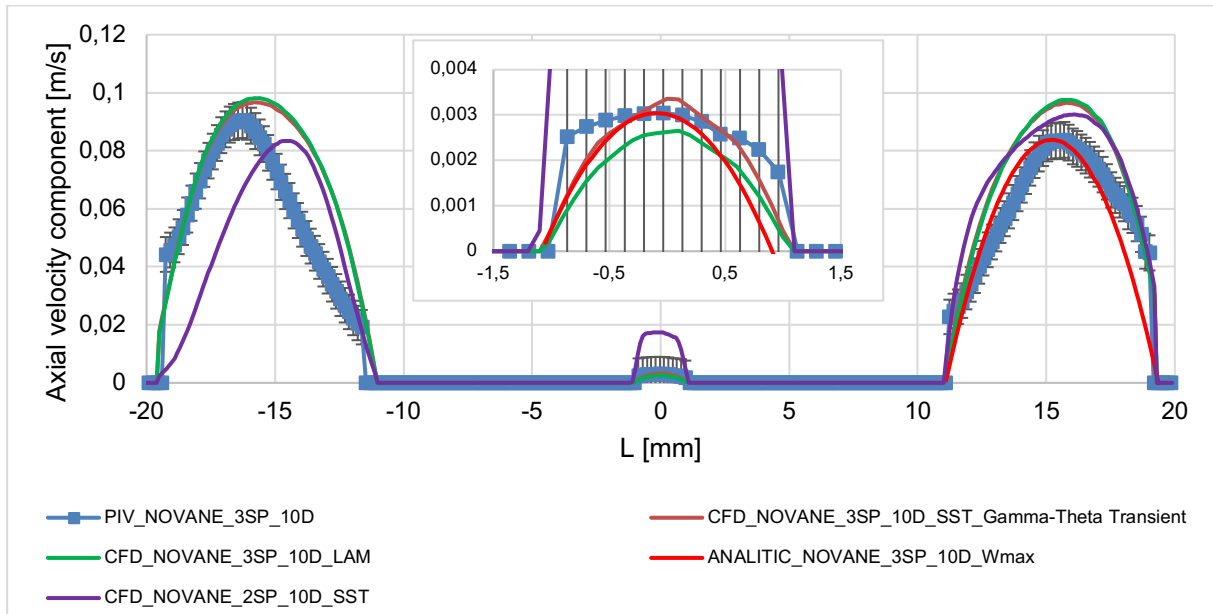
Figure 88: Line-along axial velocity distribution at 10D distance behind the 3rd NOVANE spacer, Re=350

In Figure 88, the axial velocity profile can be seen at 10D distance behind the 3rd spacer. The SST Gamma-Theta transient and the Laminar steady-state calculation produce very similar results. Regarding the transversal velocities, the calculations give values within the error margin, but the experimental results are not as convincingly consistent as the aspect of the axial velocities.

Figure 89: Line-along transversal velocity distribution at 10D distance behind the 3rd NOVANE spacer, Re=350
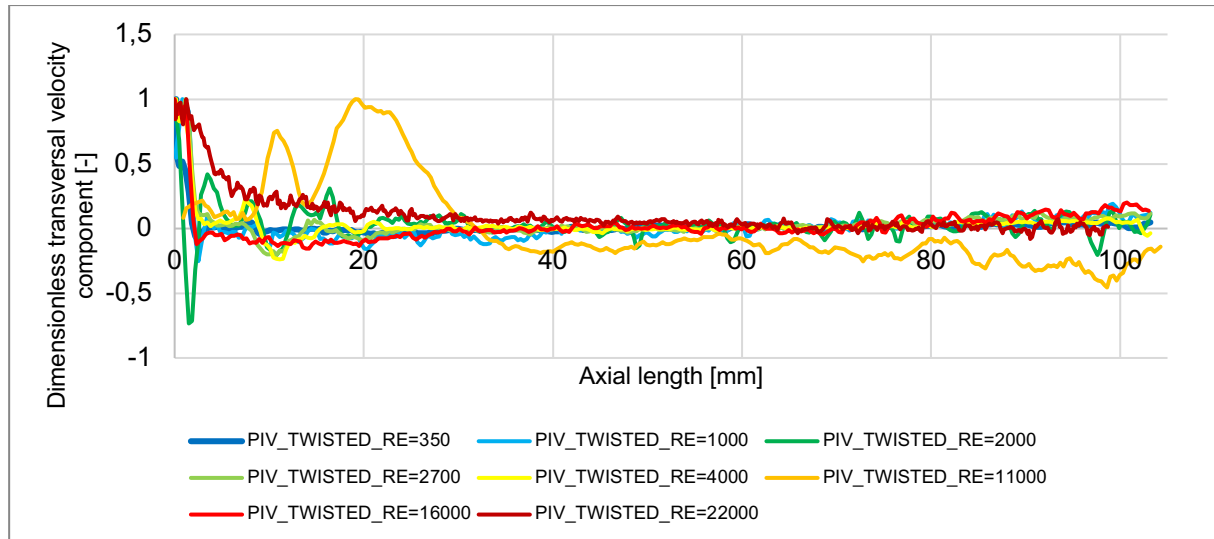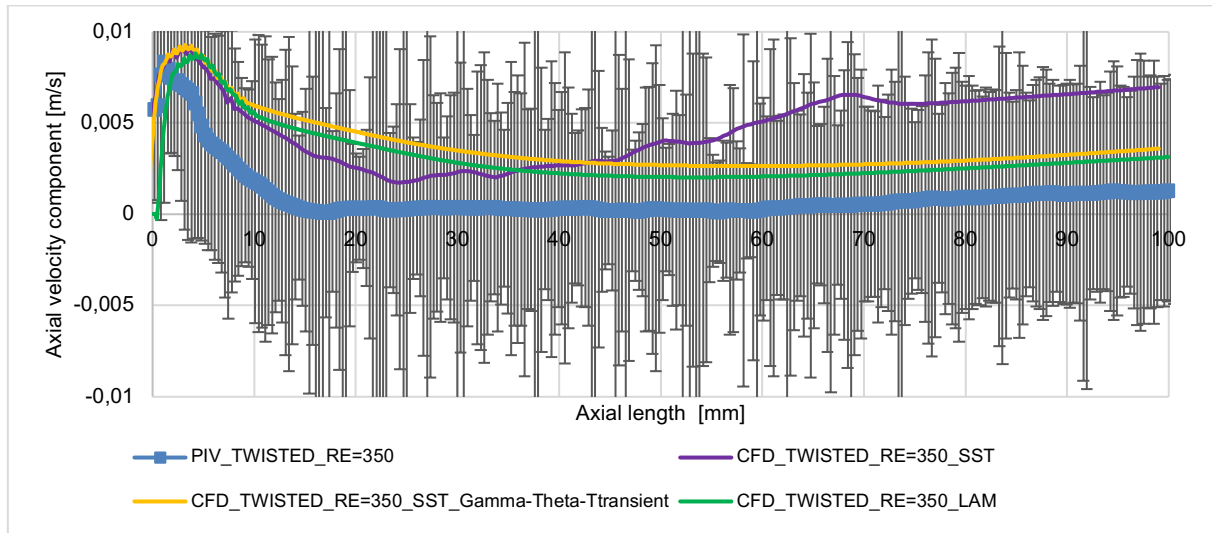
Figure 90: Axial velocity distributions in the gap between the two rods as a function of height for NOVANE type spacers after 3rd grid (monitor line position marked in Figure 10 with white arrow)

In the velocity distributions in axial direction inside the middle subchannel are presented in Figure 90. The runoffs of the velocity distributions have a congruent shape in the measurements and calculations. The transient Gamma-Theta and Laminar models gives closer results, while the SST calculation overestimates the velocity values in the middle section.

	Axial velocity component				Transversal velocity component			
	Maximum value		Averaged value		Maximum value		Averaged value	
Re-number	PIV	CFD	PIV	CFD	PIV	CFD	PIV	CFD
350	0.0047	0.0050	0.0024	0.0028	0.0010	0.0003	0.00029	0.00001
1000	0.0414	0.0319	0.0079	0.0193	0.0030	0.0014	0.00069	0.00016
2000	0.0849	0.1221	0.0332	0.0781	0.0027	0.0197	0.00050	0.00115
2700	0.0372	0.1525	0.0244	0.0985	0.0040	0.0412	0.00181	0.00184
4000	0.2114	0.2408	0.1216	0.1638	0.0097	0.0860	0.00197	0.00354
11000	0.7216	0.8541	0.6040	0.5728	0.0356	0.1943	0.00734	0.01085
16000	1.0065	1.1971	0.8726	0.8491	0.0315	0.2613	0.01024	0.01620
22000	1.5749	1.6457	1.2763	1.2156	0.0185	0.3314	0.00609	0.02252

Table 7: Maximum and line-along averaged velocity values in the different experimental cases and CFD (SST model) calculations behind 3rd NOVANE grid (inside the middle subchannel)

The comparison of the velocity values was made in every Re-number case. The main results of the velocity components, such as the maximal and line-along averaged values were calculated

on the middle line in the gap between the two rods. The calculated values are compiled in Table 7 and graphically represented in Figure 91. Since both the investigated Re numbers and the calculated values cover by several orders of magnitude, the results are presented on a log-log scale.

The maximum and the averaged axial velocity components agree well in the fully turbulent and the laminar case, but the values differ in the transitional turbulence regime. Between Re=1000 and 4000, the calculations give higher values than the measurements. The transversal velocity values are underpredicted in the lower Re cases while overpredicted in those cases where the Re number is higher than 2700.

Figure 91: Comparison of the key parameters of the PIV measurements and CFD calculations along the middle line in the middle subchannel along the Z direction

It can be concluded that the SST turbulence model is able to provide a robust and reliable solution for different Re-number problems. However, if we want to obtain specific, accurate results for certain cases, refining the tests by transient calculations, more advanced turbulent models or laminar calculations is worthwhile.

6.2.2. RESULT OF THE TWISTED VANE EXPERIMENT CASES

In this chapter, the TWISTED Vane experimental cases are compared to the CFD calculations. The transversal velocity distributions from the measurement and the different CFD calculations are compared with grayscale contours in Figure 92. According to the PIV experiment, two oppositely oriented but symmetrically positioned "angel wing shaped" transverse velocity regions are formed after the spacer in the outer subchannels. This distribution is similar to that observed for NOVANE, but slightly different in shape. These oppositely oriented regions are asymmetrical in the steady-state SST calculation (Figure 92, right side), but they are clearly displayed in the Gamma-Theta transient calculation as expected from the measurements.
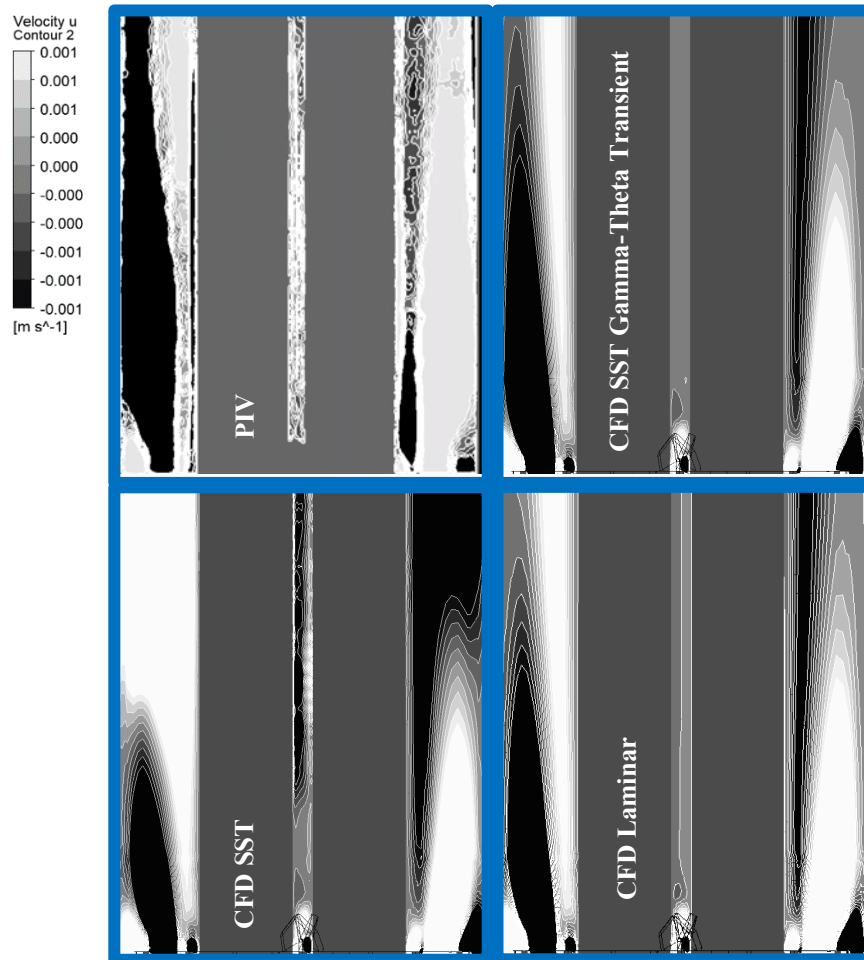
Figure 92: 2D transitional velocity component distribution after the 3rd TWISTED grid, Re=350 case
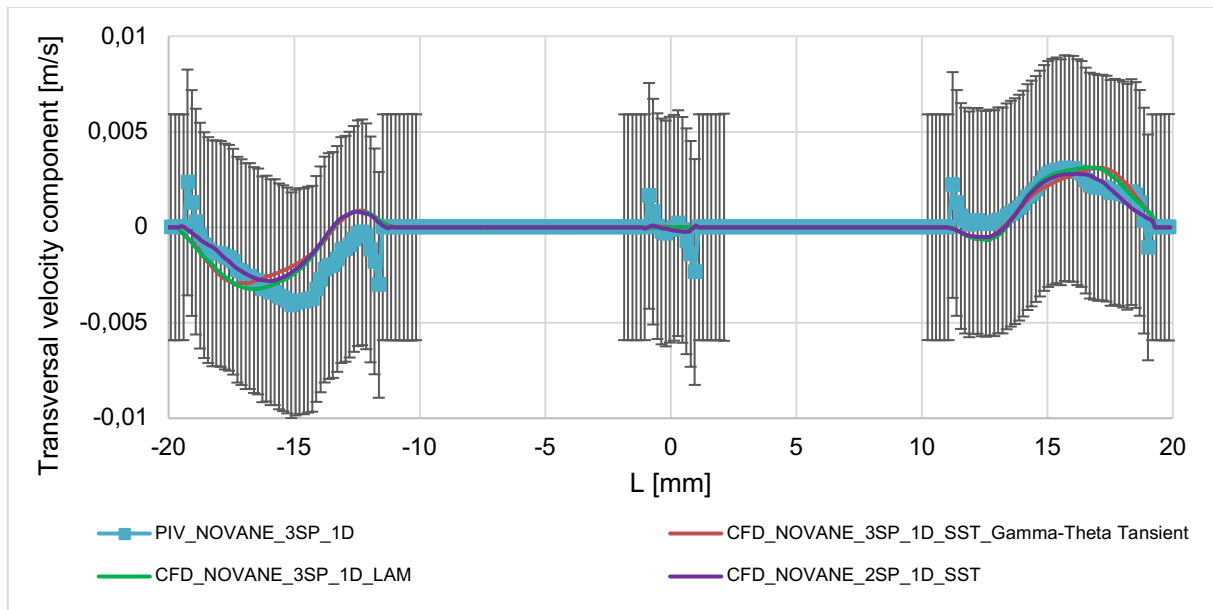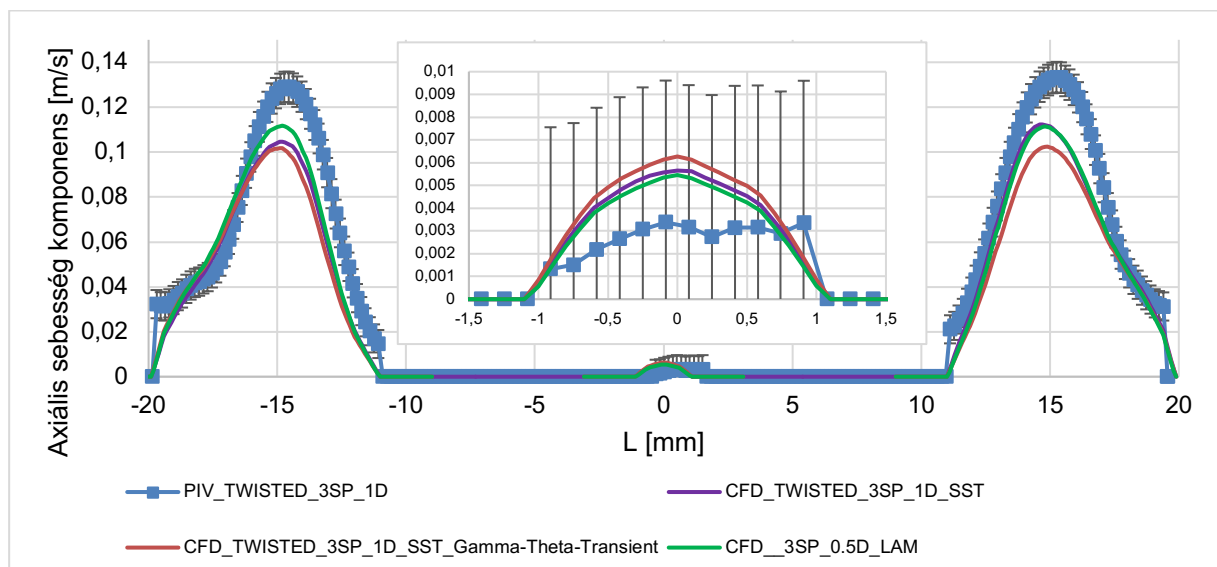

Figure 93: Line-along axial velocity distribution at 1D distance behind the 3rd TWISTED spacer, Re=350
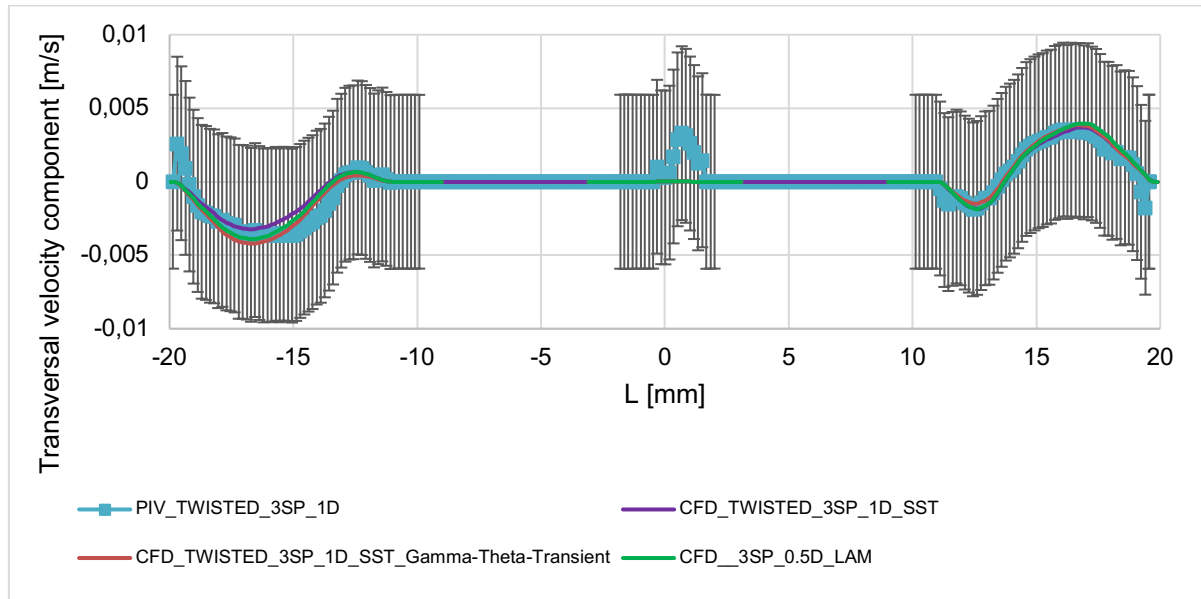
Figure 94: Line-along transversal velocity distribution at 1D distance behind the 3rd TWISTED spacer, Re=350

The axial and transversal velocity profiles along a monitor line positioned at 1D distance behind the third TWISTED grid are presented in Figure 93-94. The difference between the two turbulence model is very slight. The axial velocity is overestimated, while the transversal velocity is underestimated by the calculations in the middle subchannel. In the outer subchannels, the transversal velocity profiles show an outstandingly good match. The measurements predict a bigger axial velocity maximum than the calculations.
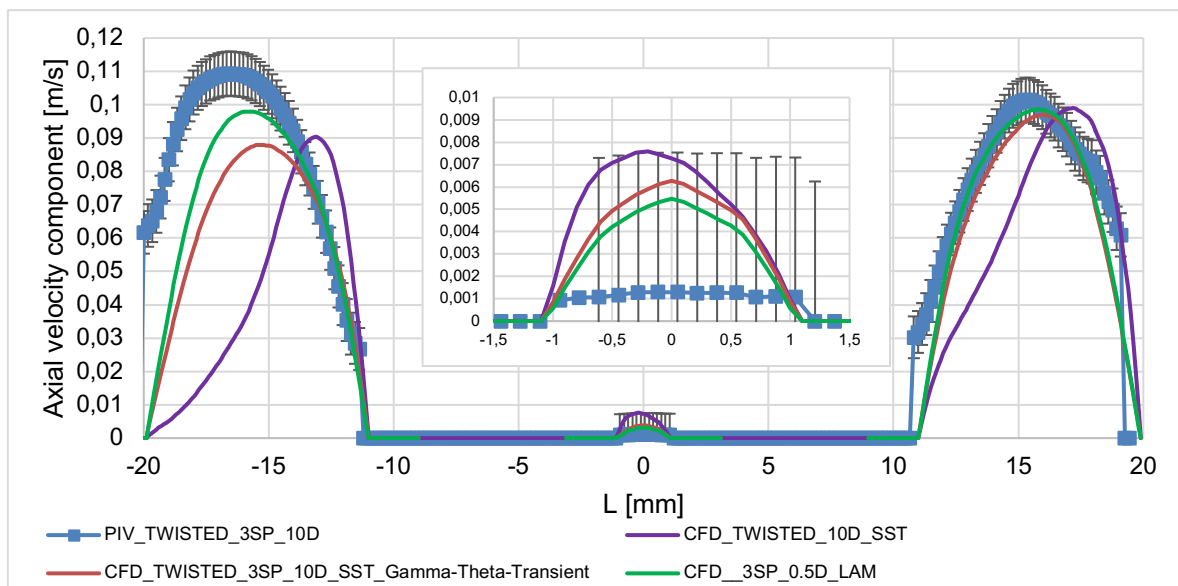
Figure 95: Line-along axial velocity distribution at 10D distance behind the 3rd TWISTED spacer, Re=350

At 10D distance (Figure 95), the steady-state calculation gives a completely different velocity distribution than what would be expected from the measurements. In contrast, the profile shape of the Gamma-Theta transient calculation approximates the measurements. The velocity values

in the inner subchannel are also overestimated in the simulations at this distance. For the transversal velocities, the Gamma-Theta transient calculation produced better approximations (Figure 96).
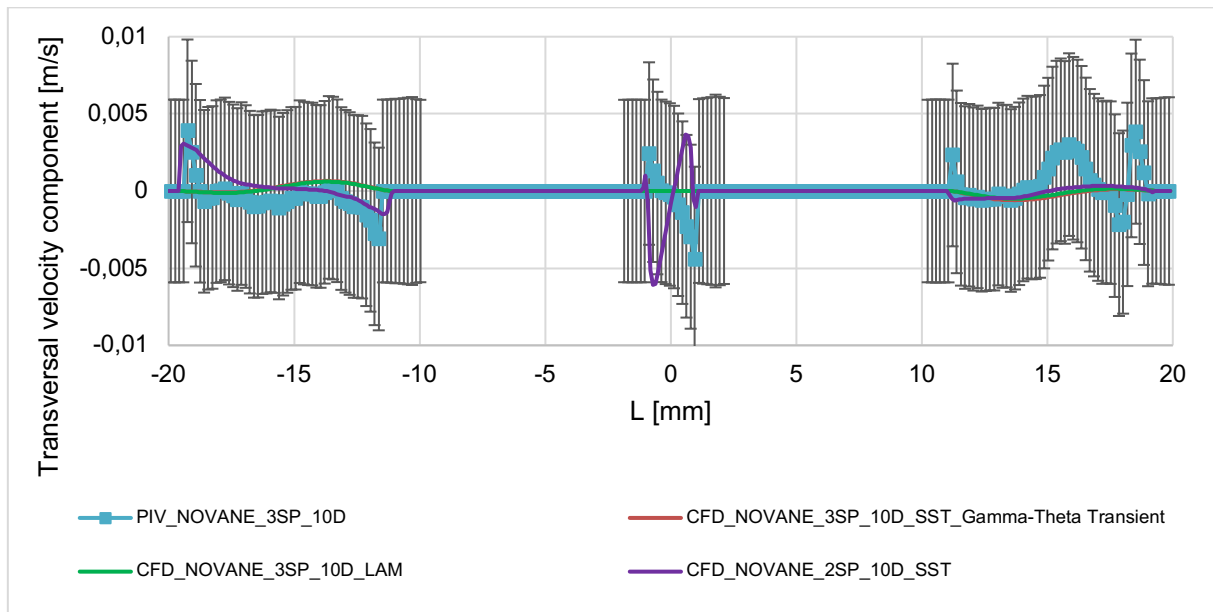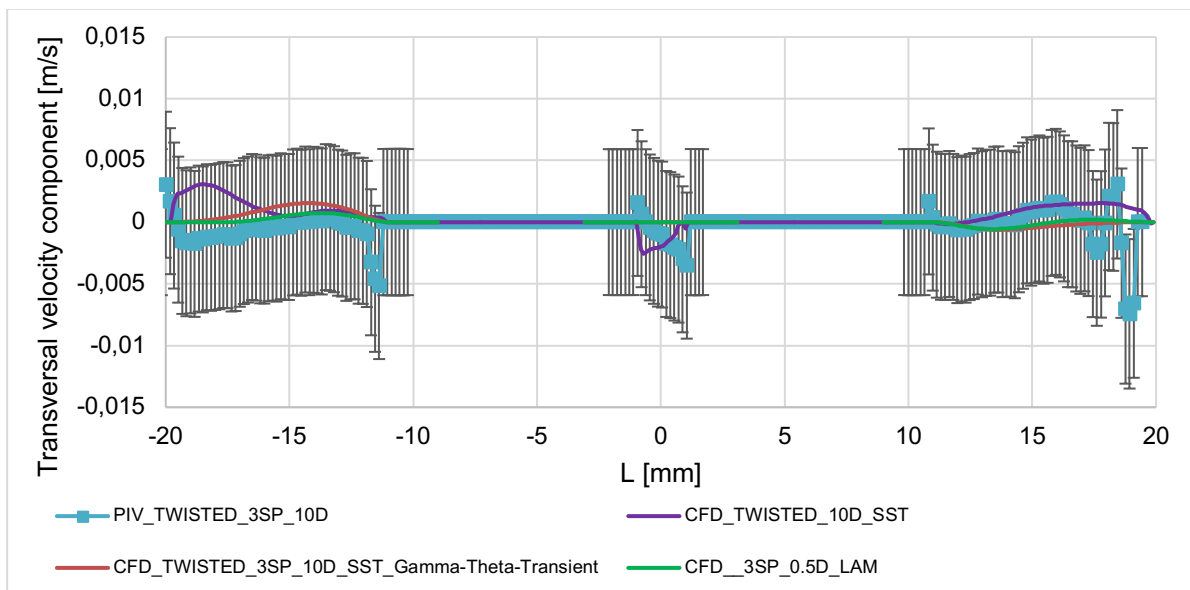

Figure 96: Line-along transversal velocity distribution at 10D distance behind the 3rd TWISTED spacer, Re=350

On Figure 97, the axial velocity distributions are presented inside the middle subchannel. The runoffs of the velocity distributions have a congruent shape in the measurements and calculations. The transient Gamma-Theta and Laminar models give closer results farther from the spacer (50-100 mm), while the agreement is better in the near spacer region (1-40mm) in the case of SST model calculation.
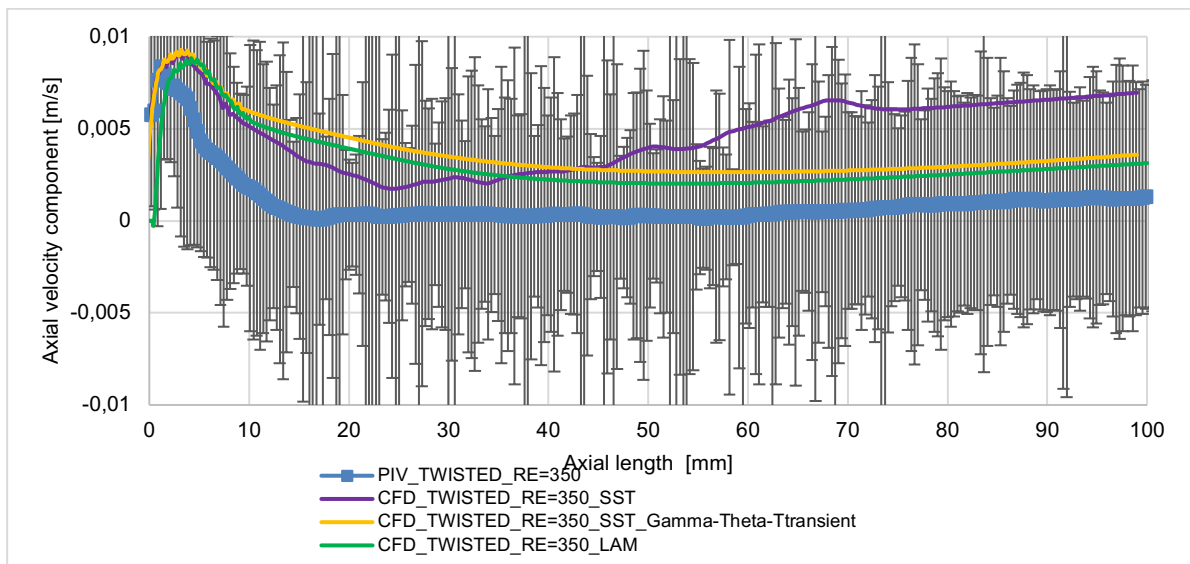
Figure 97: Axial velocity distributions in the gap between the two rods as a function of height for NOVANE type spacers after 3rd grid (monitor line position marked in Figure 10 with white arrow)

The comparison of the velocity values was made in every investigated Re number case. The main results of the velocity components, such as the maximal and line-along averaged values were calculated in the middle line in the gap between the two rods. The calculated values are compiled in Table 8 and graphically presented in Figure 98. Since the Re numbers and the calculated values vary by several orders of magnitude, the results are presented on a log-log scale.

	Axial velocity component				Transversal velocity component			
	Maximum value		Averaged value		Maximum value		Averaged value	
Re-number	PIV	CFD	PIV	CFD	PIV	CFD	PIV	CFD
350	0.0084	0.0092	0.0010	0.0048	0.0152	0.0027	0.0006	0.0014
1000	0.0518	0.0388	0.0072	0.0230	0.0106	0.0039	0.0008	0.0005
2000	0.1126	0.1061	0.0677	0.0628	0.0258	0.0105	0.0011	0.0010
2700	0.1397	0.1257	0.0778	0.0808	0.0379	0.0170	0.0023	0.0014
4000	0.2148	0.2392	0.1505	0.1989	0.0625	0.0307	0.0028	0.0033
11000	0.5493	0.6450	0.4559	0.5039	0.2038	0.0772	0.0549	0.0064
16000	1.2246	0.8513	0.8958	0.7190	0.2426	0.0941	0.0176	0.0070
22000	1.6152	1.1972	1.1838	1.1075	0.2466	0.3474	0.0514	0.0159

Table 8: Maximal and line along averaged velocity values in the different experimental cases and CFD (SST model) calculations behind 3rd TWISTED grid

In the aspect of the maximum axial velocity, the results are consistent. The line-along averaged axial velocities are smaller in the lower Re-number cases (Re=350-1000). The maximums of the transversal velocities are systematically smaller in the CFD calculations, except in the Re=22000 case. The interpretation of the averaged transversal velocities is more difficult. In the experiments, the Re=11 000 case is deviates because there are higher values than in Re=16 000 and 22 000 cases. As mentioned above, this measurement may have been incorrectly set.
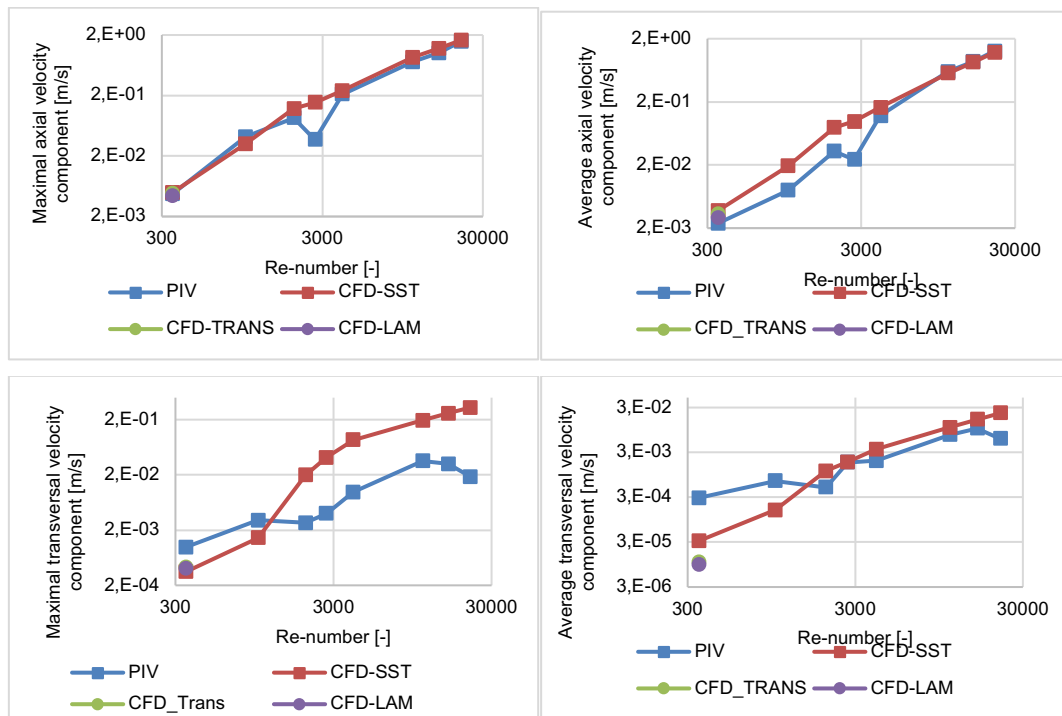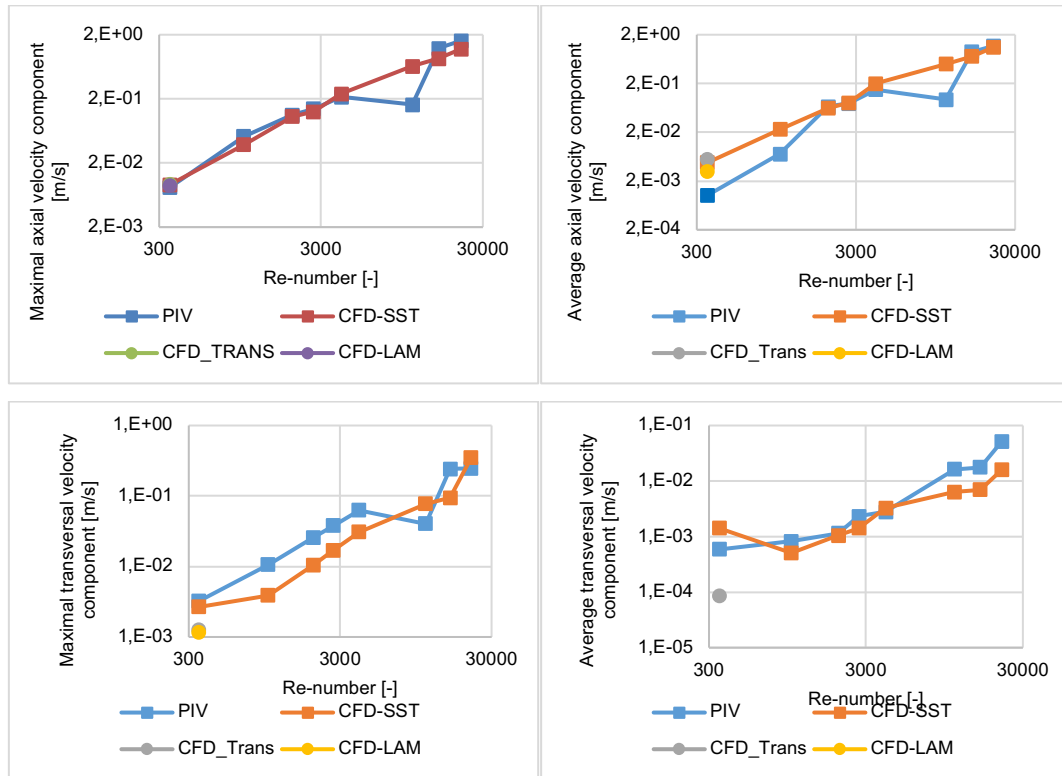
Figure 98: Comparison of the key parameters of the PIV measurements and CFD calculations along the middle line in the middle subchannel along the Z direction

6.3. Summary of the Chapter 6

In this chapter, we presented the results of our LOFA accident related measurements. Our PIV measurement system is not capable of tracking such a fast transient, but it is possible to investigate given moments of the transient in steady state mode in case of different mass flows and Reynolds numbers, to have an overview of the flow condition inside the rod bundle. We investigated 8 experimental cases in the Re-number range from 350 to 20 000 and mapped the velocity fields in the rod bundle after the NOVANE and TWISTED grids. CFD simulations were performed for the measurement cases, and error analysis was performed for the measurement points. The comparison of the measurements and calculations showed that the flow in the range Re=1000-4000 exhibits a turbulent-laminar transition character. Therefore, the CFD models are less able to describe the velocity profiles in the rod bundle correctly. This range persists only for a very short time during the LOFA accident. Lower Re-numbers are typical during long term heat dissipation. The results of measurements and CFD calculations match acceptably well at Re=350.

7. CFD CALCULATIONS FOR HEAT TRANSFER CORRELATION ESTIMATIONS

In this Chapter, we will present the complex CFD fuel assembly model and the calculation on it. The results presented here relate to a PhD work and were published in the following articles [46] [47] [48]. The turbulence model of the model was fitted based on the PIV measurements. In the first section of the chapter, the results of the calculations for nominal conditions are presented, followed by a simulation run of the LOFA simulation on the one-sixth assembly model to investigate the variation of heat transfer under different flow conditions.

7.1. GEOMETRY OF THE REFRACTORY CERAMIC FUEL ASSEMBLY FOR CFD MODELLING

There are 87 ceramic fuel assemblies in the ceramic core design of the ALLEGRO reactor. The cross section of the fuel assemblies is shown in Figure 99/a. The active length of the rods is 0.86 m, which is located in the upper part of the bundle. Four honeycomb type spacer grids will hold the rods in their positions within the active length. The individual rods are clamped with three leaf springs in every spacer (Figure 99). The spacers are 26 mm high and the axial distance between them is 240 mm. The first spacer is located 48 mm from the beginning of the active part of the fuel (Figure 101/c). The assemblies have hexagonal shrouds made of SiC. The coolant pressure is about 7 MPa and the core inlet temperature is 400 °C [49].
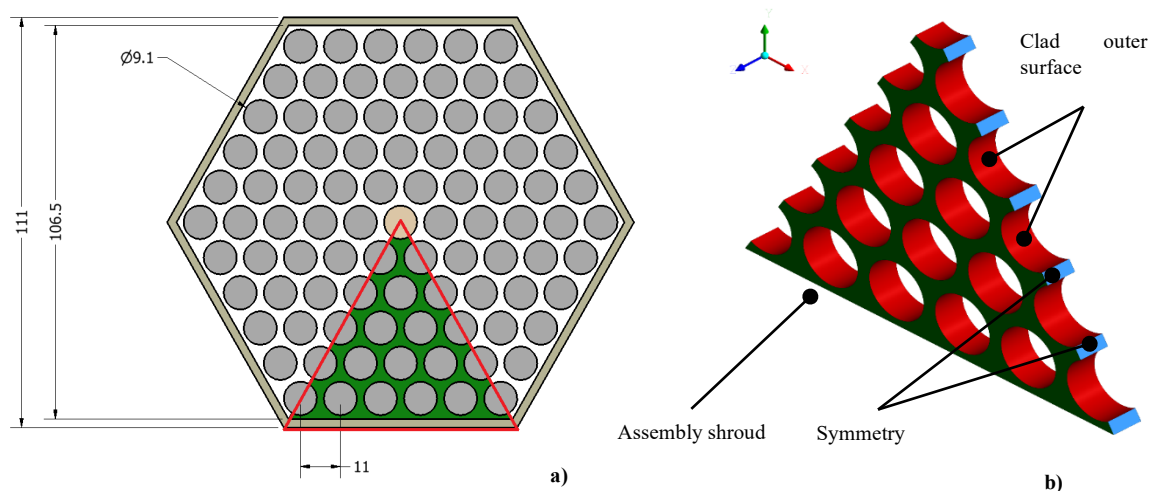
Figure 99: ALLEGRO ceramic assembly [50] and the geometry of the bare rod bundle models

7.2. MESH SENSITIVITY STUDY FOR THE ACTIVE ROD LENGTH ASSEMBLY WITH SPACERS

Before investigating the full-length assembly with spacer grids, we had to understand the flow distribution in the bare rod bundle. In the first step, a simplified bare rod bundle model created. In this CFD analysis a 60° section of the active part of the bare rod bundle was described, which is marked with orange in Figure 99/a, whereas the flow domain boundaries are marked with the red triangle. In order to generate appropriate inlet flow boundary conditions for the full length assembly model, a short 60° section simplified model was applied. The axial length of the geometry formed was 4.55 mm, which is equal to the radius of the rod. For the lateral plane surfaces symmetry boundary condition is defined. No-slip smooth wall condition is given for

the walls of the rods (Figure 99/a). In all models the upper and lower surfaces are connected with periodic box boundaries. With this method a fully developed turbulent flow can be modelled, which is independent of the Z-direction. Mass flow rate is specified according to the cross-sectional average mass flux of the assembly. The mass flow of the assembly is 0.415 kg/s. The inlet velocity profile model is adiabatic, and uses the helium material properties at constant temperature at 400 °C. The mesh sensitivity study of the investigation is not presented here but can be found in article [47].

7.2.1. GEOMETRY

In the next step model for a one-sixth segment of the fuel assembly active part has been developed (see Figure 101). Utilizing the symmetry of geometry, we have created a simplified assembly model. The cross-sectional geometry is identical to the bare rod bundle model. Modelled area can be seen in Figure 99/a. The model includes four honeycomb spacers with the distance of 246 mm between them (Figure 100). It is important to note here, that due to the pattern of the spacer spring, the lower right and left corners of the model are slightly different. In the right corner there is a leaf spring, while in the other it is missing. The CFD model geometry is longer than the 860 mm active part by 2x62 mm. This is the result of a mesh generation method, that avoids the use of interfaces. The first spacer is 110 mm far from the inlet surface. Further geometrical data can be seen in Figure 101.
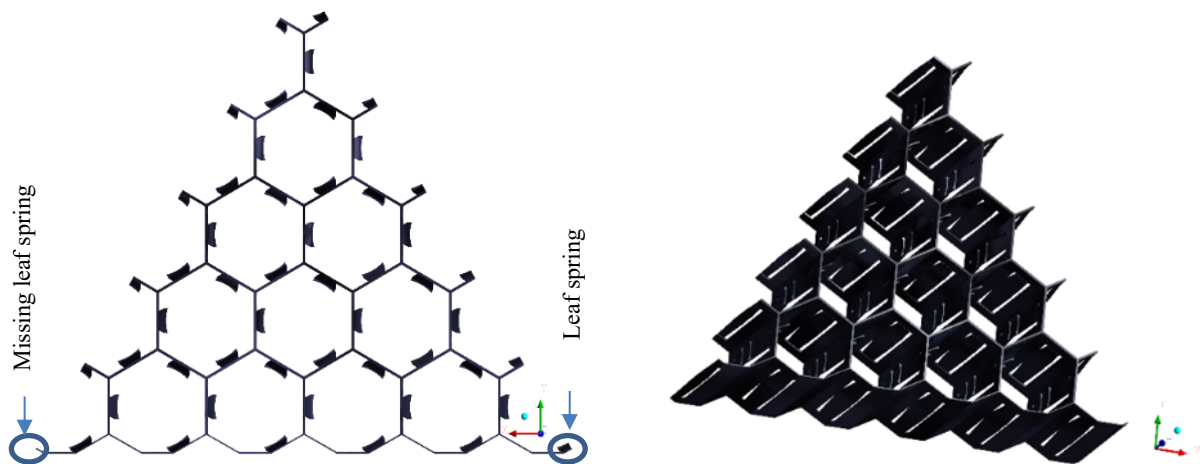
Figure 100: Geometry of the honeycomb type spacer

7.2.2. THE EFFECT OF STRUCTURAL ELEMENTS

To investigate the temperature distributions of the assembly, detailed models have been created. The models have been extended step by step to examine the effect of the structural elements and the physical process of heat radiation. The OS2 model served as basis for these investigations. The detailed parameters of the models can be seen in Table 9. Mesh resolution at the outlet of the most complete model is in Figure 102.
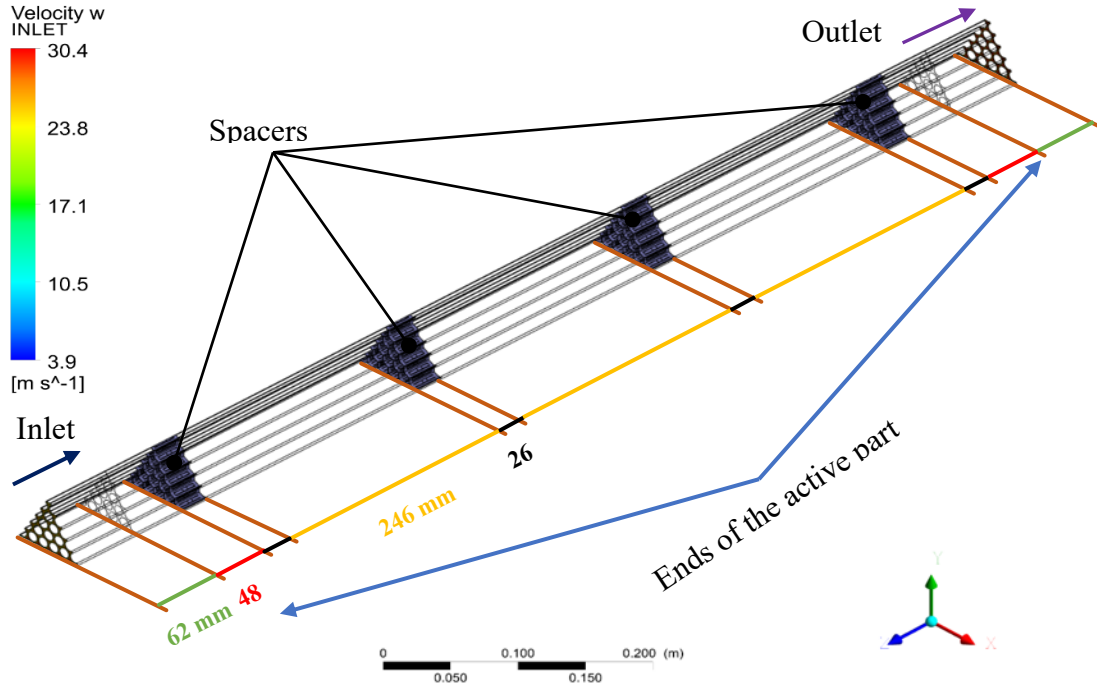
Figure 101: The structure of the active length models

6.1.1.1 Model OS2

The OS2 model (One-Sixth model with mesh density M2) describes only the fluid domain of the assembly. The mesh density has been chosen in order to reach consequent results with taking into account the heat radiation (see in [47]). The number of the element of the fluid domains in the sensitivity study were 22, 76, 117, and 182 million.

At the lower surfaces of the model inlet boundary condition was given (Figure 102) and velocity, turbulent kinetic energy and turbulent kinetic energy dissipation distributions were defined. The velocity scale in Figure 102 is referring to the inlet boundary condition axial velocity distribution. These distributions were determined with the bare rod bundle models (M4 in [47]). On the upper surfaces outlet boundary condition was defined with 0 Pa relative pressure. The reference pressure equals to the pressure of the nominal conditions (7 MPa). In this phase of the assembly development, each of the rods has the same thermal power. Rod outer surface (q"$_{CO}$) heat flux depending on the height [51] was specified with a quadratic polynomial.

$$q''_{CO} = -1.46 * 10^6 * Z_m^2 + 1.2328 * 10^6 * Z_m + 3.1595 * 10^5 \ [W/m^2] \qquad (29)$$

The temperature of the coolant at the inlet was 400 °C. The specific heat capacity of helium (c$_p$ = 5195 [J / kgK]) is considered to be practically constant between 1 and 100 bar and from room temperature to 1000K. Temperature dependent material properties of Helium were specified with polynomials. Validity range of the polynomials are: pressures from 1 to 100 bar and temperatures from room Temperature to about 1800 K [52] .

$$\varrho_{Helium} = -2.7662 * 10^{-9} * T_K^3 + 1.1934 * 10^{-5} * T_K^2 - 1.893 * 10^{-2} * T_K + 13.1 \ [kg/m^3] \qquad (30)$$

$$\mu_{Helium} = -8.4535 * 10^{-19} * T_K^4 + 5.2947 * 10^{-15} * T_K^3 - 1.527 * 10^{-11} * T_K^2 + 5.0637 * 10^{-8} * T_K - 6.4227 * 10^{-6} \ [Pa * s] \qquad (31)$$

$$\lambda_{Helium} = -7.2542 * 10^{-15} * T_K^4 + 4.5369 * 10^{-11} * T_K^3 - 1.2967 * 10^{-7} * T_K^2 + 4.0386 * 10^{-4} * T_K + 5.15242 * 10^{-6} \ [\text{W/mK}] \tag{32}$$

6.1.1.2 Model OS2_CA

The model OS2_CA (One-Sixth with Clad and Assembly shroud) includes the 1.08 mm thick SiC rod claddings (5 radial and 860 axial layer) and 1.65 mm thick SiC assembly shroud (5 radial and 860 axial layer) with the axial length of 0.86 m. The 1.07 mm thick SiC shroud of the assembly is also modelled in this case (5 radial and 860 axial layers). The shroud is connected to the fluid domain by an interface and the heat transfer is also considered. The outer surface of the shroud is adiabatic wall. The solid elements were meshed with hexahedral elements. The resolution is adjusted to the resolution of the fluid mesh. The BPG recommends that the ratio of mesh density variation along the interfaces should not be larger than 1:3 [53]. Using this principle, all model parts were described with hexagonal elements (clad, assembly shroud, gas gap and fuel). Based on experience, the resolution shown here is conservatively detailed and therefore no further mesh independence analysis was performed. As boundary condition, the surface heat flux (q"$_{CI}$) is specified on the rods' inner surface. The axial distribution of the heat flux is described with a quadratic polynomial (33).

$$q_{CI}'' = -1.9144 * 10^6 * Z_m^2 + 1.6144 * 10^6 * Z_m + 4.417 * 10^5 \ [W/m^2] \tag{33}$$

The physical process of thermal conduction in the clad and shroud is also considered. The density of the SiC was considered as constant, 2600 kg/m³. The temperature dependent material properties were given with polynomials. The polynomials based on measurements performed for temperatures varying between 20 °C and 800 °C [13].

$$\lambda_{SiC} = -3.59567 * 10^3/T_K^2 + 7.2289 * 10^{-7} * T_K^2 - 4.51 * 10^{-3} T_K + 9.952 \ [\text{W/mK}] \tag{34}$$

$$Cp_{SiC} = -2.3016 * 10^2/T_K^2 - 1.9167 * 10^{-7} * T_K^2 + 1.9774 * 10^{-4} T_K + 1.4013 \ [\text{J/g/K}] \tag{35}$$

6.1.1.3 Model OS2_CMPL

The model OS2_CMPL (One-Sixth CoMPLete) included the gas gap of the fuel rods (~5.3 million additional elements for modelling the gap with 5 radial and 860 axial layers) and the (Pu-U)C fuel elements (simplified to 0.86 m long continuous cylinders) ~4.7 million additional element (11 radial and 860 axial layer) for modelling the fissionable material. The fuel pellets and the gas gap were meshed also with hexahedral elements. The fuel pin active length is 860 mm, fuel pellet diameter is 6.64 mm and the gap between the fuel pellets and the cladding is 0.15 mm. This model contains 92.15 million elements. In this model the heat generation was taken into consideration as volumetric heat generation within the volume of the fuel pellets (36) [51].

$$q_{Vol}''' = -1.205 * 10^9 * Z_m^2 + 1.017 * 10^9 * Z_m + 2.608 * 10^8 \ [W/m^3] \tag{36}$$

The gas gap was considered as a solid heat conducting medium (the convection of the filling gas was neglected), with the temperature dependent material properties of the filling gas (helium at 10 bar pressure). The densities of the helium in the gap and the (U,Pu)C fuel are constant ($\rho_{He10bar}$=1,641 kg/m³, $\rho_{(U,Pu)C}$=10880 kg/m³) [52]. The porosity of the fuel is taken into account (20%). The thermal conductivity values are reliable in the temperature range of 500 °C <T_K<2300 °C [54].

$$\lambda_{(Pu-U)C} = -1.88 * 10^{-6} * T_K^2 + 8.71 * 10^{-3} * T_K + 12.76 \ [\text{W/mK}] \tag{37}$$

$$Cp_{(Pu-U)C} = -2.54754 * \frac{10^5}{T_K^2} + 8.1 * 10^{-7} * T_K^2 + 1.9279 * 10^{-4} T_K + 14.3951 [cal/K/mol]$$

(38)

6.1.1.4 Model OS2_CMPL,DT,MC

The model OS2_CMPL_DT,MC is the most detailed model, which takes into account the heat radiation in the gas gap and between the fuel rods outer surfaces. In the active length rod bundle model with thermal radiation in the helium coolant flow domain Discrete Transfer Model (DTM) method is used with ray numbers decreased from the default 8 to 4 [55] [56]. This reduction was necessary to gain results of the simulations with the enormously large number of elements. In the theory of this method the radiation leaving the surface element in some range of angles can be concentrated into a single ray. The ray paths are calculated and stored during the calculation. Rays are fired from the surface elements at discrete values of the polar and azimuthal angles. Each ray is then traced to calculate the interaction with volumetric and surface cells. The heat radiation in the gas gap is described with the Monte Carlo (MC) method, because with MC method the heat radiation can be modelled also in the heat conducting solid media [56]. In the Monte Carlo model, the radiation intensity is calculated from the differential angular flux of photons. The uniformity of the distribution of thermal radiation depends strongly on the size of the photon library and less on the domain discretization. I varied the size of the library from 10^4 to 10^9 with a sensitivity gradient in four steps. I found that a library size of 10^8 allows sufficiently detailed thermal radiation modelling.

Number of elements	OS2	OS2_CA	OS2_CMPL	OS2_CMPL_DT,MC
Coolant domain (hybrid) [million]	76	76	76	76
Cladding (hexahedral with 5 radial and 860 axial layer) [million]	-	5.3	5.3	5.3
Assembly shroud (hexahedral with 5 radial and 860 axial layer) [million]	-	0.85	0.85	0.85
Gas gap (hexahedral with 5 radial and 860 axial layer) [million]	-	-	5.3	5.3
Fuel (hexahedral with 11 radial and 860 axial layer) [million]	-	-	4.7	4.7
Heat radiation	-	-	-	+
SUMM [million]	76	82.15	92.15	92.15

Table 9: The properties of different meshes

In this case it is necessary to define the emissivity factor (ε) on the cladding, shroud and the fuel element surfaces. This emissivity factor for SiC is 0.8 and for (Pu-U)C is 0.42 [54]. Helium is assumed in both models as a transparent media therefore the heat radiation does not heat up the helium gas directly. Mesh resolutions and further conditions are identical with those previously described [57].
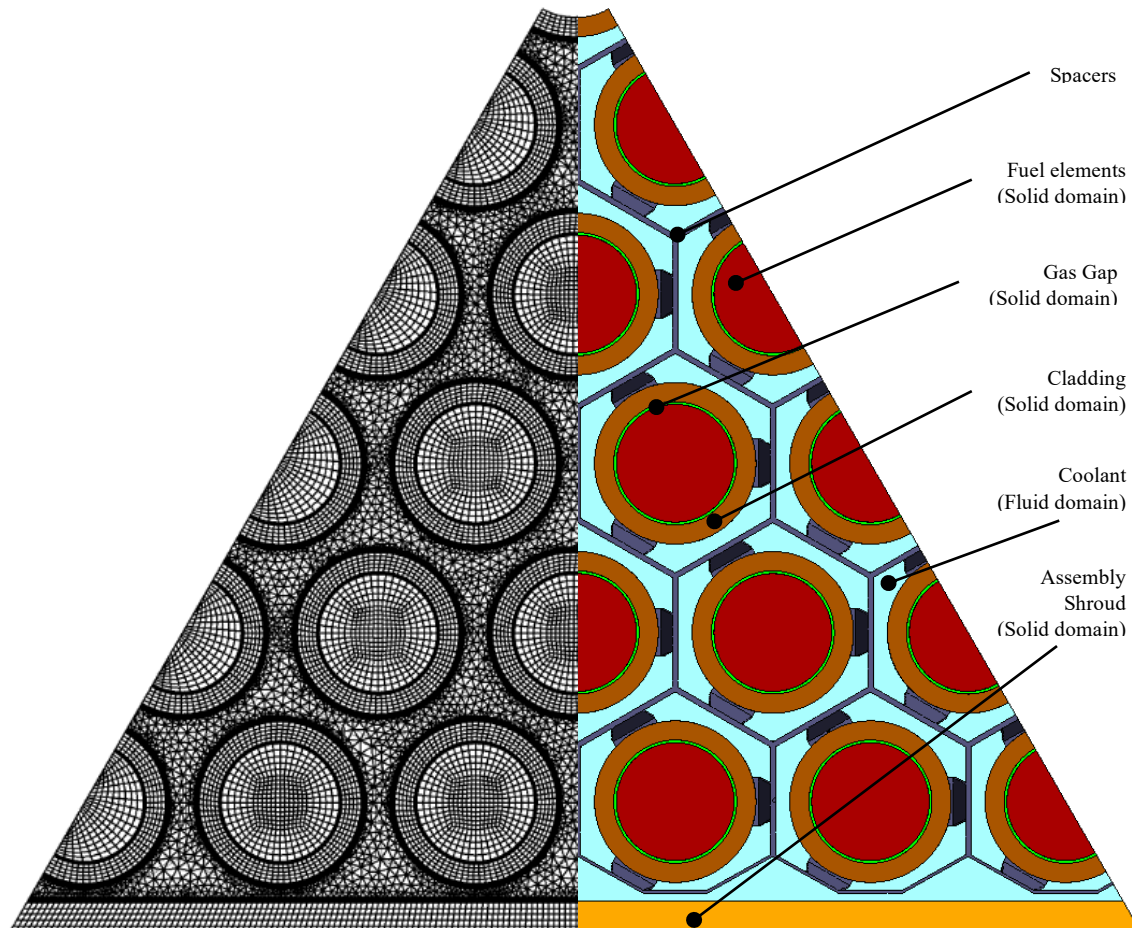
Figure 102: Mesh resolution at the outlet and the composition of the OS2_CMPL model

7.2.3. THE RESULTS OF THE MODELS
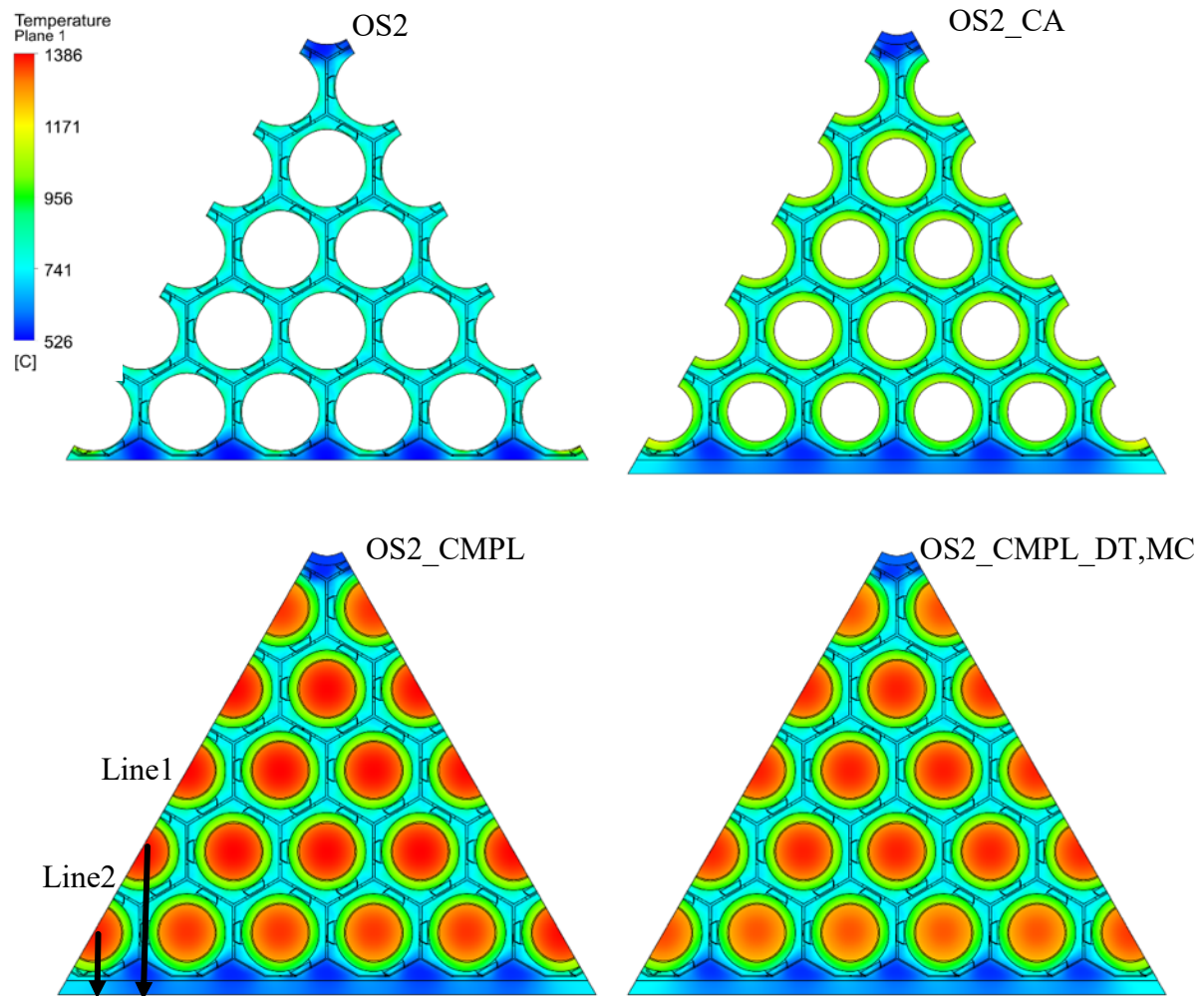
Figure 103: Cross-sectional temperature distribution at the axial position 619 mm
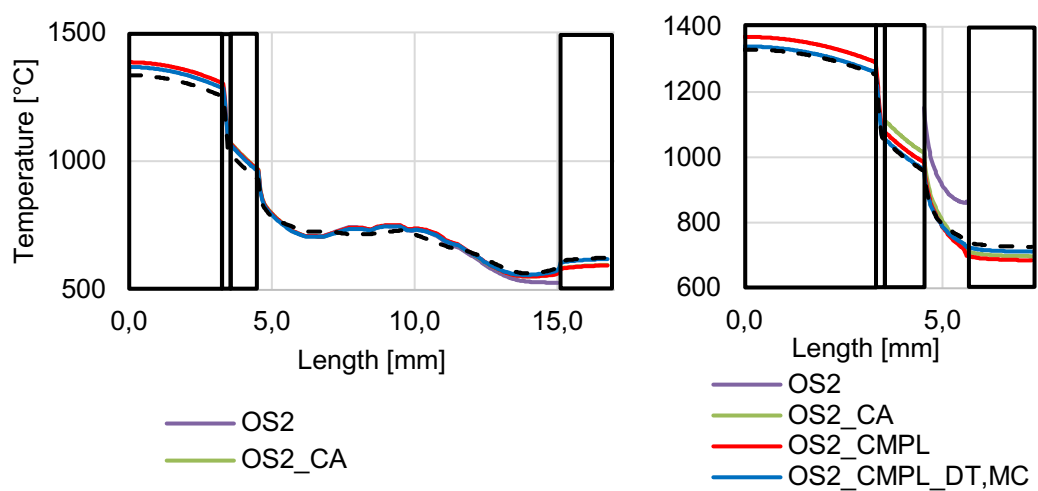
Figure 104: Temperature distributions along Line1 (left) and Line2 (right) (Line position in Figure 4.5) at the altitude of $T_{max,fuel}$

In Figures 103-104 we can see the temperature distribution at the altitude of the maximal fuel temperature. The effect of the heat conduction of the structural elements is decreasing the temperatures of the claddings. There are lower temperature regions beside the assembly shroud and the central inactive rod. The lower temperature edge subchannel region is caused by the higher mass flow rates (Figure 103). Considering the heat radiation in the fuel gap it reduces the fuel temperature. In Figure 104 it can be seen that the heat radiation transports further heat from the corner rod cladding so the maximum temperature is lower in OS2_CMPL_DT,MC (Table 10). The assembly's lower temperature shroud surface behaves as a ''heat sink'' therefore in the models with heat radiation the shroud has a higher temperature. We compared our model results with our smaller CR2_CMPL_DT,MC model, which at the same time has a finer mesh. This model describes the right corner subchannels only. The detailed description and the results of this model can be find in article [49]. The CR2_CMPL_DT,MC was taking into account the heat conduction and heat radiation in the similar way as in this current thesis. The results presented in Figure 104 show good agreement between the models of one sixth model (OS2_CMPL_DT,MC) and the smaller corner model (CR2_CMPL_DT,MC). The lower fuel temperatures of the model CR2_CMPL_DT,MC along the Line1 is caused by the smaller modelled region which cannot take into account the global effects of the inner region of the assembly. Ignoring heat radiation can be considered as a conservative estimation.

Model	Coolant [°C]	Cladding [°C]	Gas gap [°C]	Fuel [°C]
OS2	1465.2	-	-	-
OS2_CA	1135.4	1281.9	-	-
OS2_CMPL	1075.7	1171.1	1350.4	1422.2
OS2_CMPL_DT,MC	1066.6	1152.8	1323.2	1405.2

Table 10: Maximum temperatures calculated by different models
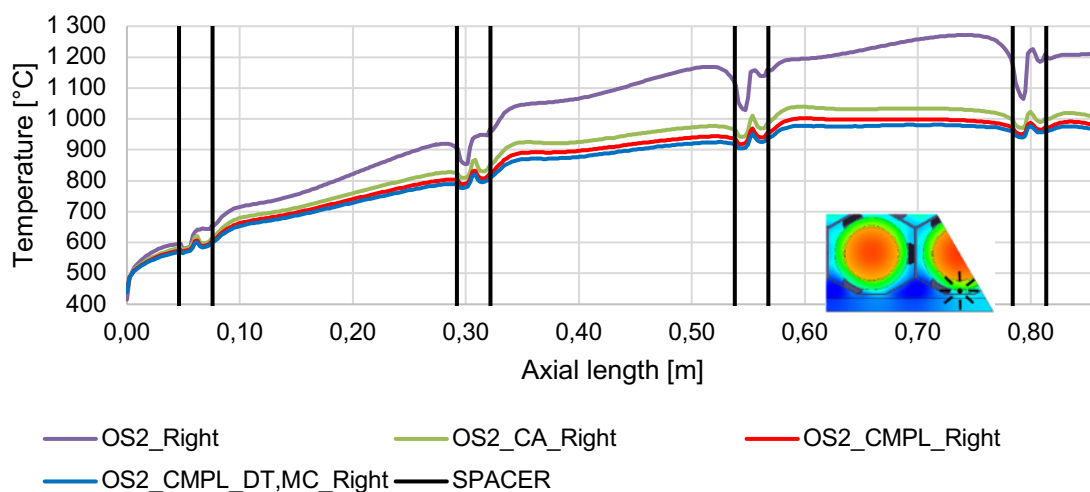
Figure 105: Fuel pin outer surface temperature distributions in the right corner along a monitor line (line position marked by black star)

In Figure 105 we can observe the significance of modelling the structural elements and the heat radiation in the conditions of a high temperature gas cooled reactor. The evaluation line is

located in the outer surface of the right-side corner clad. Without the detailed modelling of the assembly structure and heat transfer processes, the temperature values are highly overestimated (the exact values are indicated in Table 11). The OS2 model gives the highest temperature values, and the most sophisticated OS2_CMPL_DT,MC gives the lowest ones.

Maximum cladding outer temperature in the Right corner [°C]	OS2	OS2_CA	OS2_CMPL	OS2_CMPL_DT,MC
	1271.3	1039.4	1001.9	981.8

Table 11: Maximum clad outer surface temperatures in the Right corner

The ceramic assembly has a slight asymmetric temperature distribution, caused by the asymmetry of the spacers. The higher temperature values are located at the right corner (Figure 106). In the right corner of the assembly, at every spacer a leaf spring (highlighted in Figure 100) is blocking the flow, therefore the flow cross section is narrower than in the left corner subchannel. Due to the lack of the spring in the left side, the cladding surface temperatures nearby the spacers are lower.
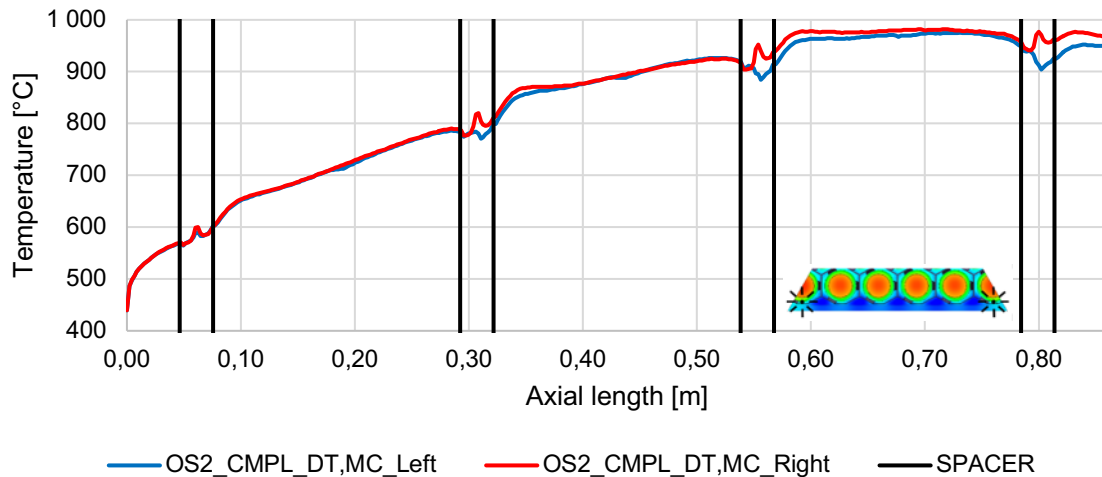
Figure 106: Temperature distribution in the Left and Right rod corner surface along a monitor line (line position marked by black star)

The highest fuel temperatures are located in the inner region of the assembly. The temperature of the uranium centreline is similar in the first half of the axial length in the different rod positions (See in Figure 107). The fuel rods in the assembly edge give the lowest values. The effect of the spacers is well observable in the temperature distributions.
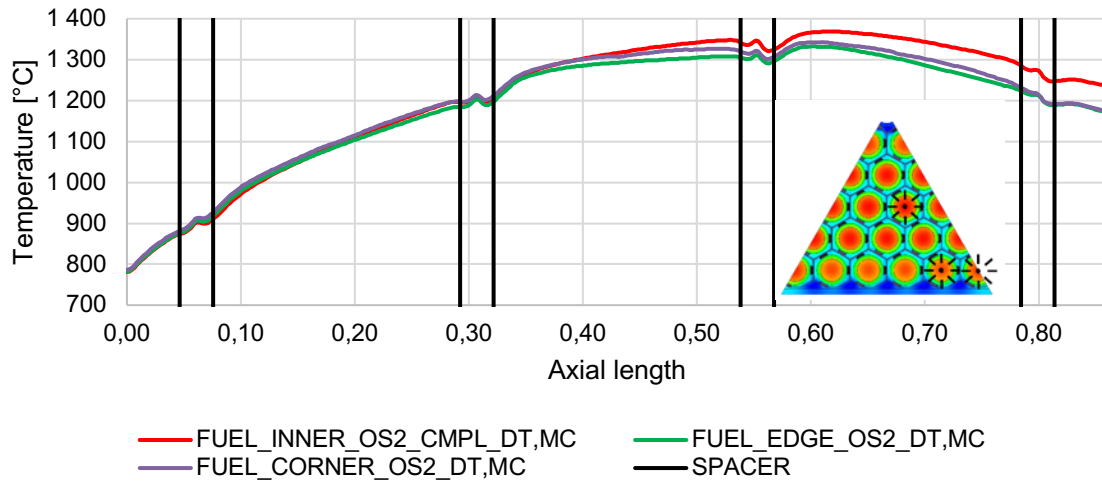
Figure 107: Comparison of the centreline temperature distributions of fuel elements in the different rod positions
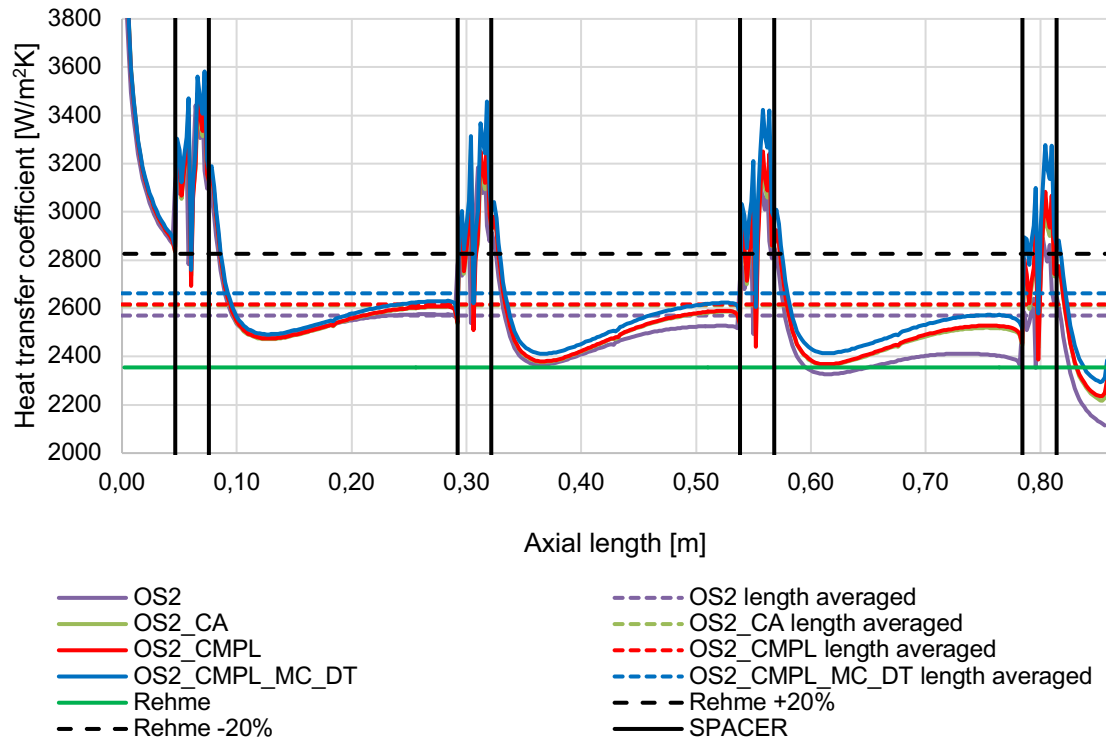
Figure 108: Heat transfer coefficient along the active rod bundle

The axial changes of the average Heat Transfer Coefficients (HTC) are calculated from the cross-sectional mass flow average temperature and heat flux values (Figure 108). Local heat transfer coefficients were calculated as follows:

$$HTC_z = \frac{\dot{q}''}{T_{wall\_z} - T_{bulk\_z}} \tag{39}$$

where:

HTC_z – local heat transfer coefficient [W/m²K],

$\dot{q}''$ – average wall heat flux [W/m²],

T_{wall_z} – wall temperature at the given altitude [K],

T_{bulk_z} – bulk temperature of the coolant at the given altitude [K].

In the heat transfer coefficients of all models, peaks can be seen at every spacer. The peaks are caused by the increased flow velocity and the intensified coolant mixing. Heat transfer coefficient distributions in case of OS2_CA and OS2_CMPL models are nearly identical. The conjugate heat transfer values are the highest in the models with thermal radiation, because of the lower clad outer surface temperatures. In Figure 108 heat transfer coefficients calculated from the CFD results are compared to the value calculated with Rehme heat transfer correlation [58].

The value of this empiric correlation based average HTC is 2355 W/m²K. The CFD calculated length averaged HTC values are significantly higher than, the ones given by the Rehme correlation. The biggest difference occurs in the case of the most complex OS2_CMPL_MC_DT model and its more than 13% (Table 12). Near the spacers the numerical values differ from the correlation result with more than 20% due to their effects presented above. The CFD calculated values are close to the values provided by the empiric correlation.

$$Nu = 0.02087 \cdot \mathrm{Re}^{0.7878} \cdot 0.855 \cdot \left(\sqrt{\frac{2\sqrt{3}}{\pi}} \cdot \frac{P}{D} \right)^{0.1688} \cdot \left(\sqrt{\frac{2\sqrt{3}}{\pi}} \cdot \frac{P}{D} + 1 \right)^{0.2122} \cdot \left(\frac{T_{out}}{T_{in}} \right)^{-0.4}$$

(40)

Where: T_{out} – the average temperature at the outlet [K]

T_{in} – the average temperature at the inlet [K]

P – Pitch distance [mm]

D – Diameter of the rod [mm]

	OS2	OS2_CA	OS2_CMPL	OS2_CMPL_MC_DT
Average HTC from CFD [W/m²K]	2 570	2 612	2 616	2 662
Difference from Rehme [%]	9.13%	10.93%	11.10%	13.04%

Table 12. The difference between the CFD and Rehme correlation calculated average heat transfer coefficient values

7.3. HEAT TRANSFER COEFFICIENT CALCULATIONS FOR DIFFERENT FLOW CONDITIONS

In this chapter, we present the heat transfer coefficients that were generated using the model outlined above. The OS2_CMPL model was used as it is less computationally demanding and the omission of the thermal radiation model has a conservative effect on the results.

12 different cases were simulated under different flow conditions. The Re numbers range from 18 000 to 330 in the cases. The simulations generally use the SST-turbulence model, but in the low Re-number ranges, laminar calculations were also performed. In Case 0-8 the inlet mass flow rate, the inlet coolant temperature and the thermal power of the assembly were decreased gradually. The last three case: DHR_Good, DHR_Bad and No_flow were selected by preliminary APROS simulations.

Figure 109 shows that the value of the HTC decreases monotonically with decreasing Re until the turbulent-laminar transition region. In the purely laminar case, the SST turbulence model estimates lower heat transfer coefficients than the laminar calculation. This means that the heat transfer in the LOFA transient CFD calculations will be underestimated if we do not take into account that the flow is transitioning to laminar.

System codes account for heat transfer using semi-empirical correlation, and it is worth using a correlation in these codes that best approximates the values presented here.

Case	Re-Number	T_inlet [°C]	Power ratio to nominal [-]	HTC [W/m²K]	
				SST	Laminar
0	18000	400	1	2639	
1	16078	378	0.893	2412	
2	14156	356	0.786	2176	
3	12234	335	0.679	1935	
4	10312	313	0.572	1694	
5	8390	292	0.466	1450	
6	6468	270	0.359	1200	
7	4546	249	0.252	944	659
8	2624	227	0.145	667	529
DHR_Good	1100	339	0.026	422	434
DHR_Bad	650	318	0.014	434	432
No_flow	330	389	0.039	410	486

Table 13. The Re-numbers, boundary conditions and average HTC values of the different CFD simulation cases
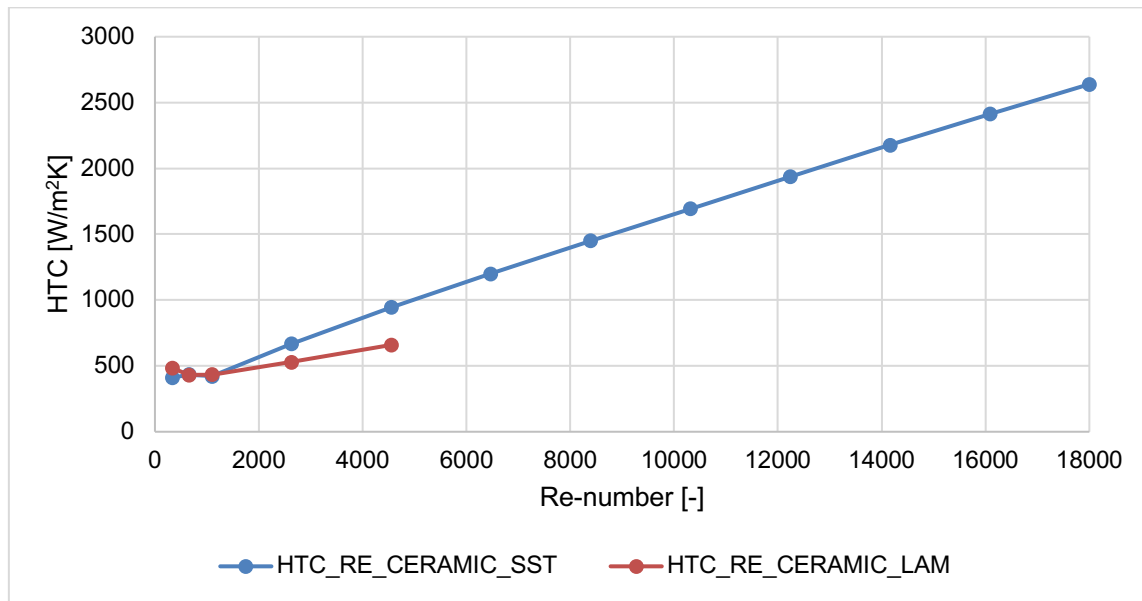
Figure 109: Average heat transfer coefficient of the ceramic assembly in the different Re-number cases

7.4. CONCLUSIONS OF CHAPTER 7

In this Chapter, my investigations were presented for the active part of the ALLEGRO ceramic fuel bundle. Bare rod bundle simulations were performed in order to create accurate inlet boundary conditions for a more detailed 60° segment model. For the one-sixth segment of the rod bundle active length, a mesh sensitivity study was made but not presented in here [11]. The active length models contained the spacer grids and considered the effects of the structural elements (heat conduction in the assembly shroud, fuel rod cladding, gas gap in the fuel elements) with increasing details. Using the CFD models the hot assembly of the core was investigated. From the results of the simulations, the flow and the thermal conditions in the corner region were evaluated in detail. Because of the high temperature values, the heat radiation was also described. Cross-sectional temperature distributions and profiles showed that the assembly has a slight asymmetry caused by the asymmetric location of the springs of the spacers. The assembly shows a strongly inhomogeneous coolant temperature distribution. The unbalanced temperature fields can be smoothed using mixing vanes on the spacers.

The fuel temperature maximum can be observed in the inner rods. More detailed models gave smaller temperature maximums. Modelling the radiative heat transfer increased the accuracy of the calculations. The effect of the heat radiation is more important in the corner region, where high temperature rod in the corner position faces the significantly colder assembly shroud. The heat radiation in the fuel gap further decreases the fuel temperature maximum. Ignoring heat radiation can be considered as a conservative estimation in the further investigations, because of the high computational needs of the heat radiation.

12 different cases were simulated under different flow conditions, with the Re number range from 18 000 to 330. The average HTC values for the ceramic fuel assembly have been calculated. The validated CFD calculations can be used to select the appropriate HTC correlation for the system codes.

8. CFD-APROS Investigation of heat transfer coefficients during LOFA

As we have seen in previous chapters, during a LOFA transient the Reynolds number inside the core can vary over the range of about 20 000 to 350. One of the key parameters affected by the large change in Re is the heat transfer coefficient (HTC) on the surface of fuel pins, especially since both laminar and turbulent flow regimes (and the transition between them) can be observed during a LOFA.

Therefore, to create accurate system TH calculations of the ALLEGRO reactor, we require our thermal hydraulic codes to be able to handle the HTC calculations in the laminar and turbulent flow regimes. Unfortunately, the homogenous solver of Apros (unlike the more widely used two-phase solver) does not contain a wide range of HTC correlations that are applicable to high temperature gases, especially at low Re numbers. It does however offer the option for the user to define their own, fully customized HTC formula for a model.

With the CFD model presented in Chapter 7, we have estimated the value of HTC and Nusselt number at different Re numbers, and used them to introduce an improved HTC calculation for our Apros model. In this chapter, we present our investigation and results.

8.1. Implementation of HTC correlations

By default, Apros uses the Dittus-Boelter correlation for HTC calculation in the following form, with a lower limitation of Nu=3.66.

$$Nu = max(0.023 * Re^{0.8} * Pr^{0.4} ; 3.66)$$ (41)

This formula was developed for turbulent flow inside cylindrical tubes [59], and although the original article doesn't specify explicitly, it is widely accepted today to be valid according to the following criteria [60]:

$$Re > 10^4 ; 0.7 < Pr < 100 ; \frac{L}{D} > 60$$ (42)

Meaning a fully developed turbulent flow. This strongly suggests that the formula is not suitable for the ALLEGRO Apros model at low Re numbers. To confirm this assumption, we ran a total of 17 CFD calculations with varying Re numbers (see Table 13), five of which were done without a turbulence model to simulate the laminar flow at low Re, while another 12 used the SST turbulence model.

The results, in comparison with the Dittus-Boelter formula can be seen on Figure 110. These show that (41) indeed underestimates Nu in the laminar regime, by a factor of two at the lowest Reynolds numbers. But perhaps more surprisingly, we also found that it significantly overestimates the Nusselt number from Re>12 000, which means that the use of this formula becomes a non-conservative estimation for most transient calculations, since it leads to an underestimation of peak cladding temperatures.
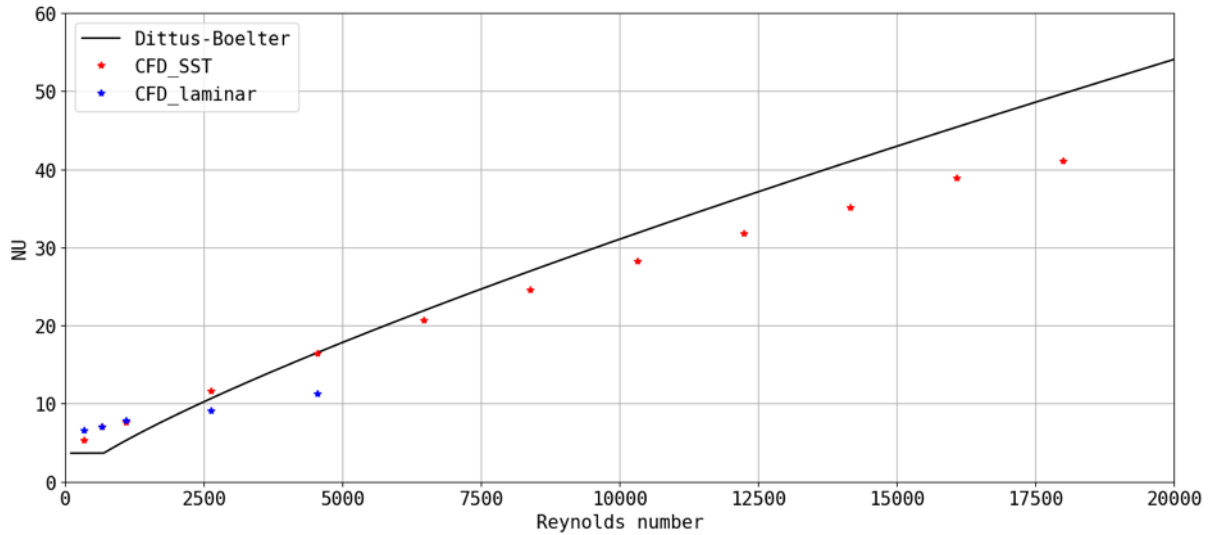
Figure 110. Nusselt numbers calculated from CFD model, compared to Dittus-Boelter formula used by Apros as default

To fix both of these issues, we decided to implement two separate formulas for the laminar and turbulent regimes. For the turbulent case, we found a formula by Gnielinski for turbulent flow in coaxial annuli to yield the best results [61]:

$$Nu_{turb} = \frac{0.125*\xi*Re*Pr}{k + 12.7*\sqrt{(\xi/8)}*(Pr^{2/3} - 1)} * \left(1 + \left(\frac{Dh}{l}\right)^{2/3}\right) * F_i \tag{43}$$

$$\xi = (1.8\,log_{10}(Re_x) - 1.5)^{-2} \tag{44}$$

$$Re_x = Re * \frac{(1+a^2)*ln(a) + (1-a^2)}{(1-a)^2*ln(a)} \tag{45}$$

$$k = 1.07 + \frac{900}{Re} - \frac{0.63}{(1 + 10Pr)} \tag{46}$$

$$F_i = 0.75 * a^{-0.17} \tag{47}$$

Where:

- ξ is the friction factor for annular ducts
- F_i is a correction factor for the case where only the inner wall is heated
- a is the ratio of inside and outside diameter: $a = d_i/d_o$
- Dh is the hydraulic equivalent diameter
- l is the characteristic axial length
- Re is the Reynolds number
- Pr is the Prandtl number

Since equations 43-47 were originally developed for coaxial tubes rather than rod bundles, we cannot explicitly determine the outer diameter to calculate $a = d_i/d_o$. (The inside diameter is naturally the diameter of the fuel pin.) Instead, we used the diameter of the equivalent annulus, as seen in [62]. (Meaning the diameter of the circle that would have an equivalent area as the subchannel plus the fuel rod.) With this, the formula for a in a hexagonal bundle becomes:

$$a = \frac{Dh}{p\sqrt{\frac{2\sqrt{3}}{\pi}}} \qquad (48)$$

Where p is the fuel rod pitch.

For laminar flow in high temperature gases, there are very few formulas developed, most sources mention the theoretical values of Nu=3.66 and 4.34, and simple formulas based on the correction of these theoretical numbers. Nevertheless, we found the following formula for hydraulically developed and thermally developing laminar flow to yield suitable results [61]:

$$Nu_1 = 3.66 + 1.2a^{-0.8} \qquad (49)$$

$$Nu_2 = 1.615\left(1 + \frac{0.14}{\sqrt{a}}\right)\sqrt[3]{Re * Pr * \frac{Dh}{l}} \qquad (50)$$

$$Nu_{lam} = \sqrt[3]{Nu_1^3 + Nu_2^3} \qquad (51)$$

Equations 49-51 were likewise developed for coaxial tubes, so the same method as described above was used for calculation of *a*.

Both the laminar and turbulent formulas are also dependent on the ratio Dh/l, a parameter which measures the relative distance from the inlet orifice, and therefore used to account for the thermal and/or hydraulic development of the flow. In an ideal scenario, we would be able to continuously change this value axially and take into account both the inlet effect and the periodic disturbance caused by the spacers. However, for the purpose of this investigation, we had to settle for a constant value for *Dh/l*. To find a constant that reflects the behaviour of the fluid over the entire axial length, we simply fitted the 43-47 and 49-51 formulas to the CFD results.

Lastly, we corrected for the variation of temperature dependent properties by using the following temperature factor for both cases [61]:

$$C_T = \left(\frac{T_B}{T_W}\right)^{0.45}$$

$$(52)$$

Where T_B is the bulk temperature and T_W is the wall surface temperature. In this case, the value of this correction factor does change with each axial node to correctly simulate the effect of the helium heating up in the core.

With this, the final form of the Nusselt number calculation method implemented in the ALLEGRO core model of Apros looks as follows:

$$Nu = \max\left(Nu_{lam} * C_T \,;\; Nu_{turb} * C_T\right) \qquad (53)$$

Figure 111. summarizes these results and shows the final formulas in comparison with the values from the CFD model. On the figure, it can be observed that the combination of our new formulas achieves a much better fit to the CFD results, while remaining slightly conservative (Since the CFD calculation also has some level of uncertainty, it might be necessary for actual safety analyses to introduce a bit more conservativism). To implement the transition to turbulent from laminar equations, we simply take the larger value of the two formulas. On Fig. 111, we

can see that the transition happens at Re=2500, very close to the theoretical value of 2300, which allows us to use this simple approach with a reasonable accuracy.
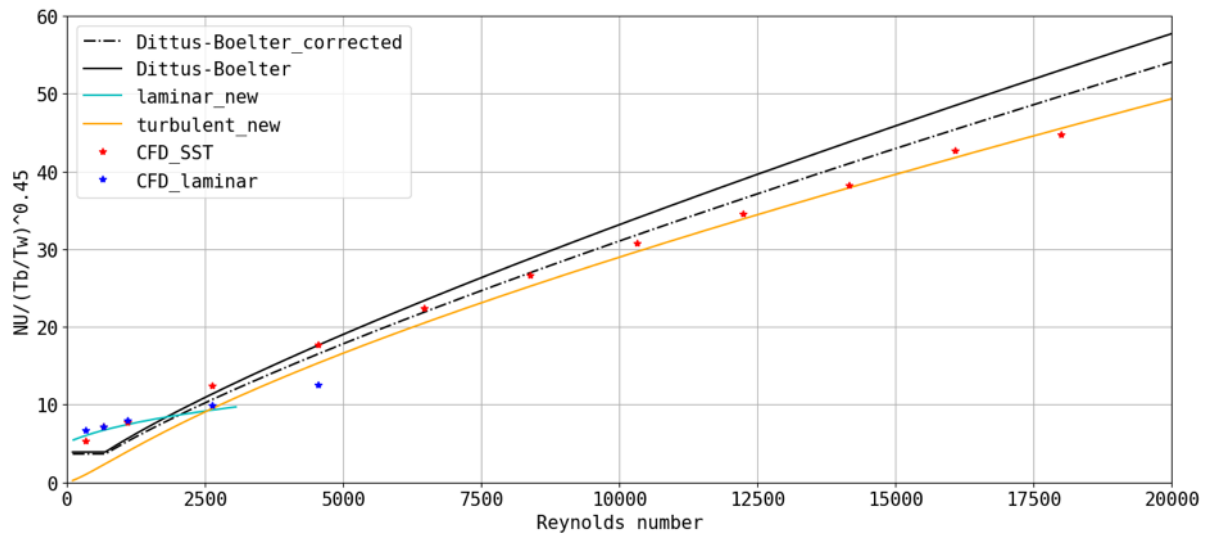

Figure 111. CFD results, compared to the original Dittus-Boelter formula, a corrected version of it, and the newly implemented 43-51. equations (Note that the Nusselt number divided by the temperature correction factor is presented on the Y-axis, so that the CFD datapoints with different temperatures could be plotted correctly in the same figure.)

Also, a very practical finding of our investigation is the effect of temperature correction on the original Dittus-Boelter formula. After we realised the importance of the correction for the newly implemented equations, we tested it on Dittus-Boelter as well, and found that approximately half of the relative error produced by the formula at high Re can be mitigated by simply applying the temperature-dependent correction described in (52). This approach (if applicable) might be useful for TH codes where the complete replacement of the HTC correlation is not possible.

It is important to note that the CFD study was completed on a model that contains the Refractory core of ALLEGRO, While the Apros model where we implemented the final correlations currently has the Driver core. Normally, this would not be a problem since all the appropriate dimensionless numbers (Re, Nu and $\frac{T_B}{T_W}$ for the temperature correction) were matched, and the boundary conditions were also set to reflect the operational conditions of the Driver core. On the other hand, as presented above, we fitted the relative distance from the inlet (Dh/l) to the CFD data, essentially treating Dh/l as a tuning parameter for the HTC model, which might introduce some uncertainty to the calculation. The relative distance is supposed to account for the development region of the flow after the inlet, and as it approaches zero, the flow can be considered fully developed. Since the spacers inflict somewhat similar constrictions to the flow as the inlet, it is very likely that the fitted value of this parameter is influenced by the geometry of the spacer grids, and therefore should be different for the model of the driver core. To estimate the extent of this potential inaccuracy, we recalculated the heat transfer correlations with 125% and 75% of the fitted Dh/l values, as presented in Figure 112. We can see that the resulting Nusselt numbers are not particularly sensitive to a ±25% percent change in Dh/l, causing only a 7.5% relative error for the laminar, and 3.8% for the turbulent formula. In fact,

with $\frac{Dh}{l} \leq 0.1$, the flow is already very close the fully developed state in every presented scenario, so any further decrease of the parameter has a negligible effect on Nu, and an increase much larger than 25% would be required for the flow development to have a meaningful effect. This also means that fitted Dh/l value can be considered a conservative estimation.
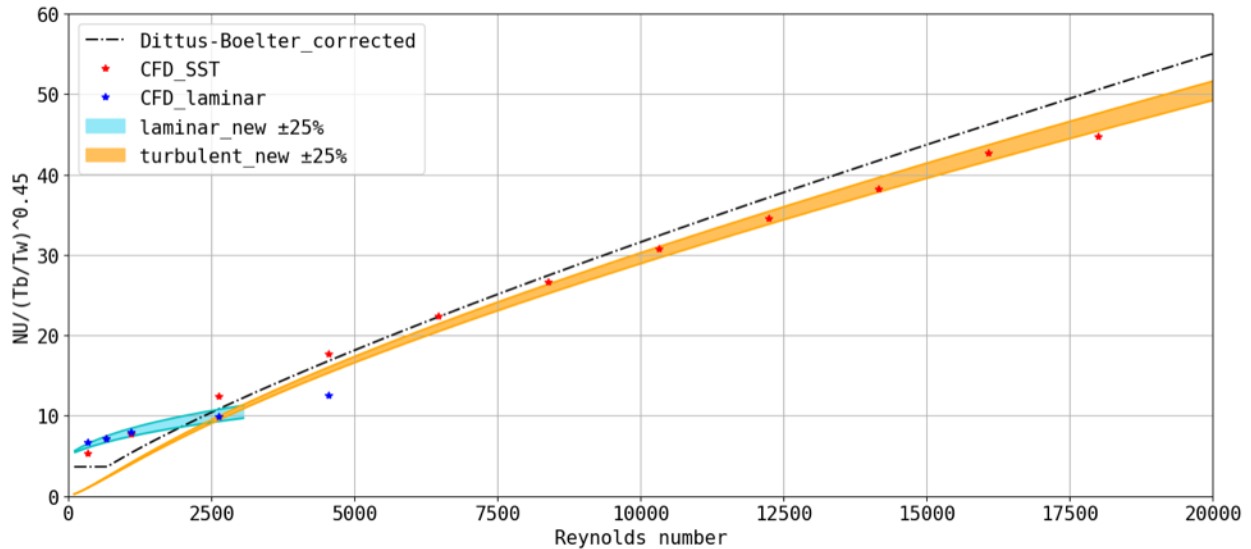
Figure 112. The newly implemented equations' sensitivity to a ±25% change of the parameter Dh/l

8.2. APROS LOFA CALCULATION FOR COMPARISON OF DIFFERENT HTC CORRELATIONS

To demonstrate the effect of the modified HTC calculation method, a LOFA (SBO) transient was calculated with the Apros model, with the following initial conditions:

parameter name	value	unit
core thermal power	100.5	%
core inlet temperature	259	°C
core outlet temperature	520.5	°C
blower outlet pressure	70.5	bar
compressor rotation speed	3800	1/min
Total primary mass flow	56.88	kg/s
Core mass flow	52.47	Kg/s
secondary circuit mass flow	125.4	kg/s
Tertiary cooler mass flow	400	kg/s

Table 14. Initial conditions for the APROS calculation

We ran the simulation for 3700 s, with the first 100 seconds being the nominal steady state, and at t=100 s, the main blowers, secondary pumps, and tertiary air coolers were stopped. The dynamic parameters governing the coast down of these devices are presented in Table 15. We also used a SCRAM delay of 1 second, and supposed a single failure, as only one DHR loop was operational. The following figures show the first 2000 s of the transient, as we found that no significant phenomena occur after that time.

parameter name	value	unit
Moment of inertia of primary blower+motor.	12.5	$Kg*m^2$
Time constant of coasting down for secondary pumps.	10	s
Time to linearly decrease the tertiary cooler mass flow boundary condition to 0.	10	s

Table 15. Dynamic parameters governing the coast down of flow machinery

First, on Figure 113, we can see the Re numbers in the average subchannel of the core, the average subchannel in the hot assembly, and the hot channel. In all subchannel types, Re starts falling very rapidly after the LOFA, and transition to laminar flow (Re<2300) happens between 130 and 140 s. (Note that the initial Re numbers are different for the three subchannel types because the gagging directs about 30% more flow towards the hot assembly than the average assembly, and the hot channel within the hot assembly has a higher average temperature, a lower density, and a slightly lower flow velocity.) Accordingly, the initial heat transfer coefficient is the lowest in the average channel of the core, higher in the hot channel, and highest in the average channel of the hot assembly (Table 16.). This relation remains true for both HTC correlations. After the transient starts, the HTC falls steeply with Re, but the new correlations switches to a much lower gradient as soon as laminar flow begins, and remains at a higher value for the rest of the simulation, creating favourable conditions for long-term heat removal from the core. HTC reaches its minimum value when the main isolation valves close in all cases, and then stabilizes after the DHR loop starts operating. After this point, the relative difference between the two HTC correlations become quite significant, with the new correlation maintaining the HTC approx. 100% higher than Dittus-Boelter (Figure 114-116.).

Subchannel type	HTC [W/m^2K] Dittus-Boelter	HTC [W/m^2K] new correlations
Average channel of the core	3290	2870
Average channel of hot assembly	4020	3460
Hot channel	3700	3205

Table 16. Heat transfer correlations in steady state before LOFA

In spite of these differences, the PCT exhibit little differences (Figure 117.). Firstly, the global maximum of PCT happens in the first few seconds after the IE, before SCRAM rod insertion. During this period, there is only a 6 °C difference between the two cases, with the new correlations leading to higher values (670 and 676 °C respectively). Moreover, even after the new HTC correlation overtakes the Dittus-Boelter after the laminar-turbulent transition, the PCT still remains lower for Dittus-Boelter case until 380 s, since it takes time to remove the excess heat stored in the fuel rod, and the absolute value of heat removal from the core is quite low in this period (hence the rising temperatures and the second peak).

These relatively small differences in temperature create no feedback effects to other parameters, meaning that the mass flowrate and pressure of the primary circuit show no significant difference between the two cases, and neither do the operational parameters of the DHR. (Note that in this investigation the HTC calculation was changed only in the core, the MHX and DHR HX was still calculated with Dittus-Boelter.)
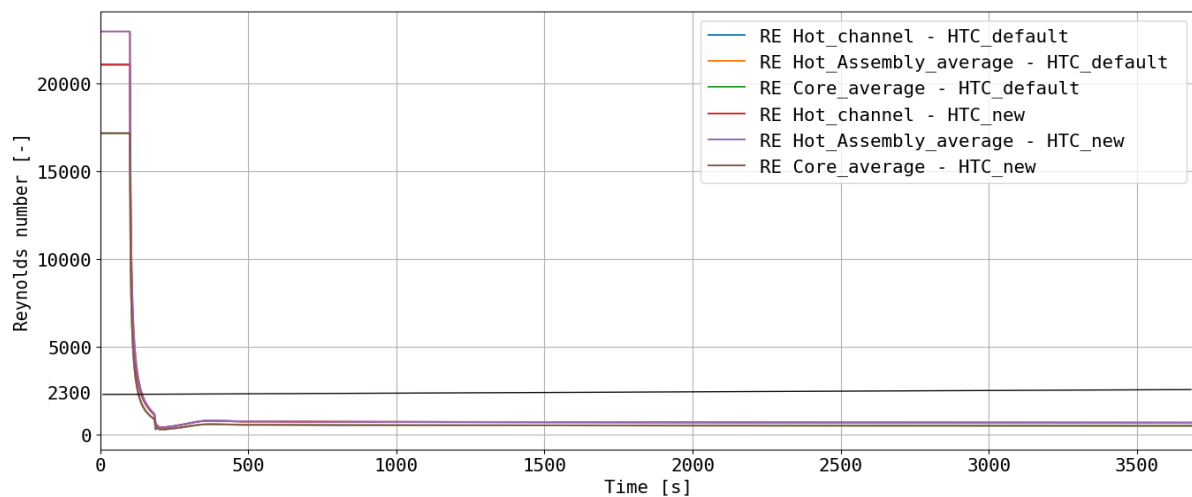
Figure 113. Reynolds numbers in 3 types of subchannels for the two investigated cases
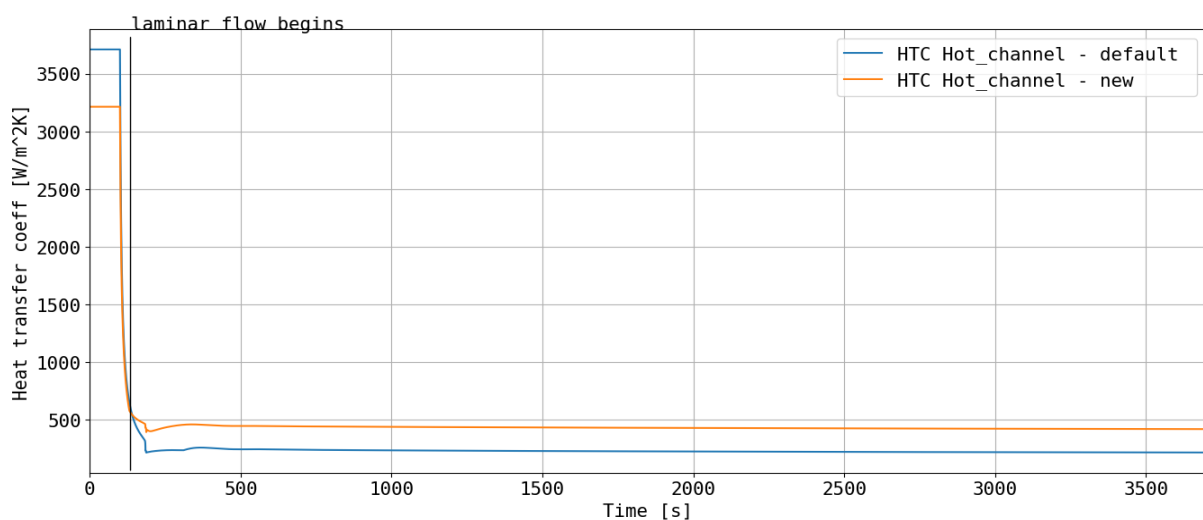
Figure 114. Heat transfer coefficient in the hot channel

Figure 115. Heat transfer coefficient in the average channel of the hot assembly

Figure 116. Heat transfer coefficient in the average channel of the core

Figure 117. Peak cladding temperature (measured in the hot channel)

Figure 118. Heat removed through the one operational DHR

Figure 119. Core inlet temperature

Figure 120. Primary circuit pressure measured above core outlet

9. SUMMARY

The PIROUETTE test facility has been installed at the Institute of Nuclear Technics of the Budapest University of Technology 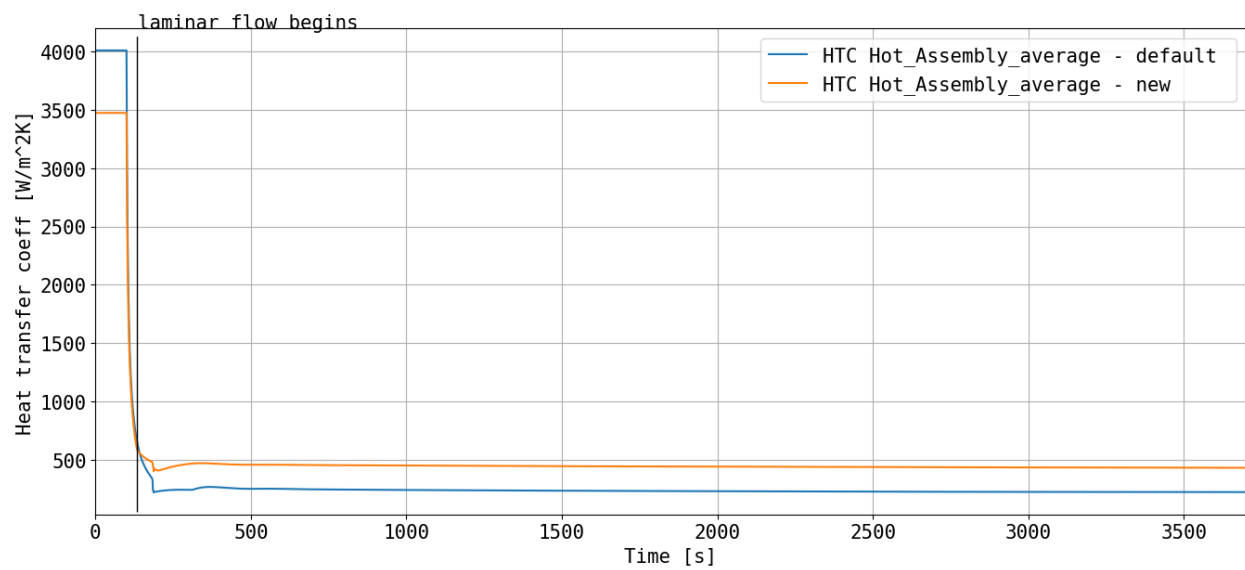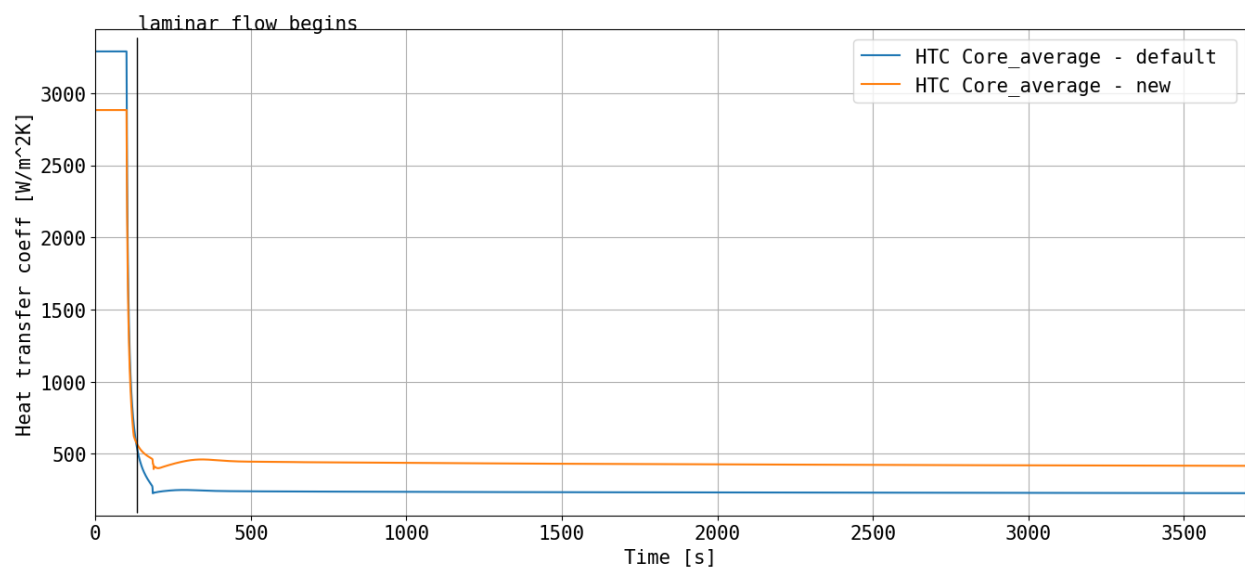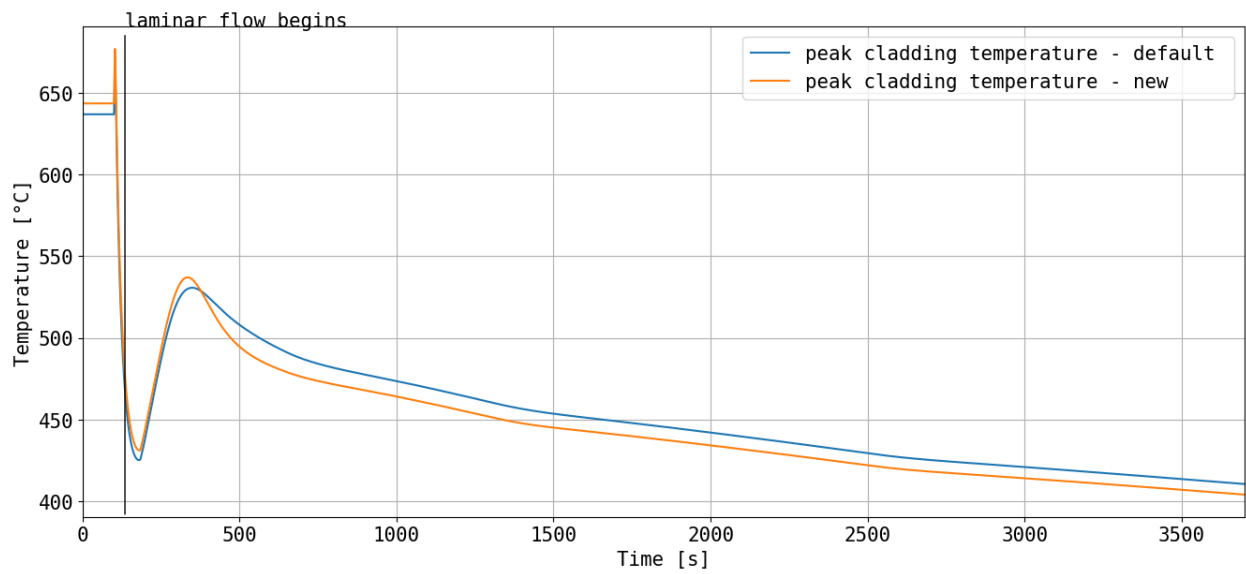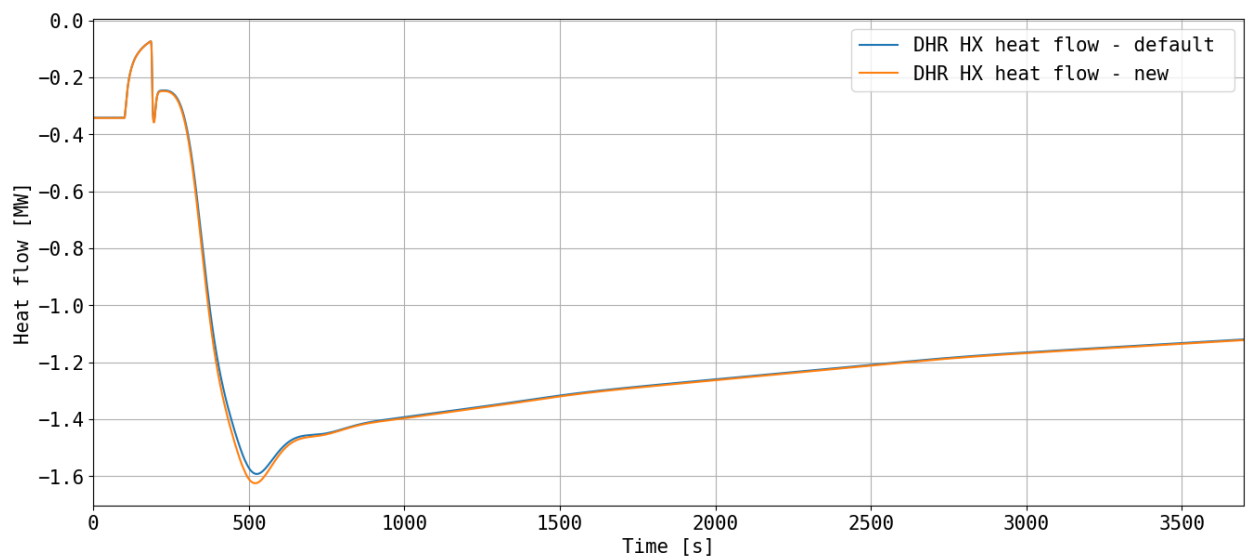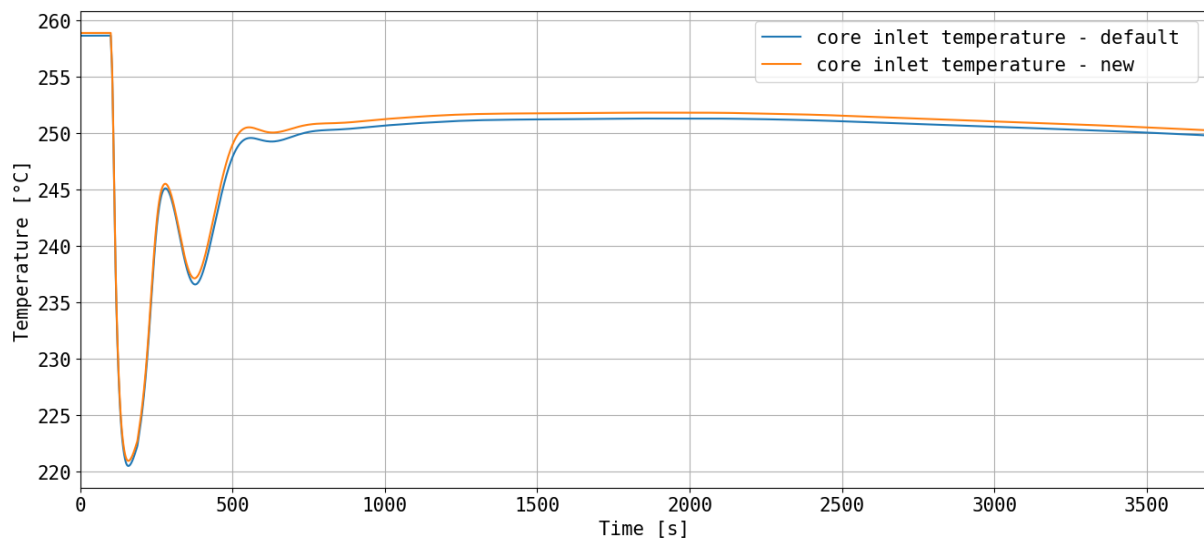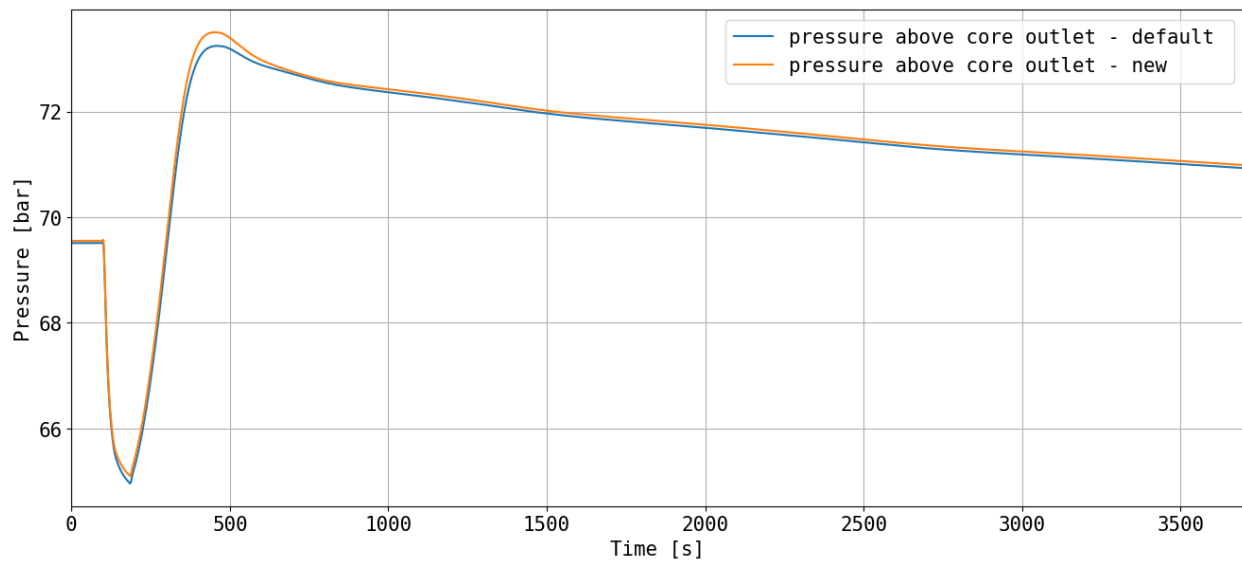and Economics. With this equipment, we had the possibility to describe a simplified 7-rod bundle model with 4 spacer grids. The spacer grids have been designed to describe as closely as possible the spacers of the GFR concept called ALLEGRO. For this purpose, a precise 3D printing methodology was used, allowing of testing different types of mixing vanes on spacer grids. In addition to the traditional spacer without vanes, the effects of split and twisted vanes were investigated.

The conditions of the gas-cooled reactor were aligned to the experimental environment by applying water as coolant medium using similarity theory considerations. The measurements were performed using PIV measurement techniques and MIR methodology, allowing the measurement of the flow field between the rods. Time-averaged flow images were successfully extracted behind the spacer grids. Distinctive features were observed in the inner subchannel sections for the different spacer grids. The highest transversal velocity maximum was observed for the TWISTED vane.

A detailed uncertainty analysis of the measurements has also been performed. A CFD model development with mesh independence analysis was conducted to numerically describe the PIROUETTE system. Simulations were performed, and the effects of turbulence models were investigated. The results of the CFD simulations were compared using 2-dimensional vector fields and monitor line velocity profiles. The measurement results showed excellent agreement with the computational simulations in many cases. In most cases, the SST turbulence model offered the best results, although there were evaluation positions and cases where other models seemed more accurate.

In the future, we would like to refine our numerical results further using a transient computation method. For a better understanding of the smaller discrepancies, a two-part benchmark exercise will be held. A description of the exercise is already available online [44].

During a LOFA event, the volumetric flow rates decrease with time. The PIROUETTE system is not suitable for the temporal resolution of such a process, but the system is capable of modelling different states associated with dedicated time instants.

8 different experimental case were investigated, where the Reynolds numbers are decreasing in the fuel assembly during the transient. It is possible to create similar flow conditions of the chosen time instants in the PIV rod bundle. The highest Reynolds number is 22600, and the lowest is 350, which represents the natural convection regime of the accident. Based on our measurements, the flow is in the laminar regime in the last experimental case.

CFD calculations have been made for the different experimental cases. The calculated velocity profiles and different velocity component values have been compared to the experiments. The CFD calculations used the special SST Gamma-Theta model for transitional turbulence and Laminar model for the lowest mass flow cases. Although in the laminar flow range, the velocity profiles of the turbulence model results deviated significantly from the measured profiles, the velocity maximums were found to be correct in magnitude. Applying CFD calculations in this way can be used for velocity estimation.

Using the results of the CFD calculations, we found that the HTC calculation method in our Apros model produces significant errors in both the laminar and transient flow regimes. Therefore, two new HTC correlations were implemented into Apros, which gave a highly improved fit to the CFD results. A LOFA transient calculation was conducted comparing the

default HTC calculation to the new improved version. We were able to observe significant differences in the values of HTC, which led to smaller differences in terms of the PCT, while the system mass flow and other operational parameters showed no significant differences.

Acknowledgements

10. REFERENCE

[1]   EU, GEN IV international forum," EU, [Online]. Available: https://www.gen-4.org/gif/. [Access Date: 15. 12. 2021.].

[2]   EU, „CORDIS EU researxh results European Gas Cooled Fast Reactor," EU, [Online]. Available: https://cordis.europa.eu/project/id/249678. [Access Date: 15 12. 2021].

[3]   J. Gadó, „The reactor ALLEGRO and the sustainable nuclear energy in Central Europe," in *EPJ Web of Conferences 78, 08001 (2014)*, 2014.

[4]   SafeG, „SafeG," EU, [Online]. Available: https://www.safeg.eu/. [Access Date: 15. 12. 2021].

[5]   F. Chen and Z. Han, „Steady-state thermal fluids analysis for the HTR-PM equilibrium core,," *International Journal of Advanced Nuclear Reactor Design and Technology,* pp. 11-17, Volume 3 (2021).

[6]   G. Mayer, „Hot duct break transient with two- and three-loop ALLEGRO models," *Nuclear Engineering and Design,* p. 110911, 370 (2020).

[7]   G. Mayer and F. Bentivoglio, „Preliminary study of the decay heat removal strategy for the gas demonstrator allegro," *Nuclear Engineering and Design,* pp. 67-76, 286 (2015).

[8]   B. Kvizda, G. Mayer, P. Vácha, J. Malesa, A. Siwiec, A. Vasile, S. Bebjak and B. Hatala, „ALLEGRO Gas-cooled Fast Reactor (GFR) demonstrator thermal hydraulic benchmark," *Nuclear Engineering and Design,* pp. 47-61, 345 (2019).

[9]   M. Berthoux and T. Cadioub, „The thermal hydraulics in a rod bundle representative of the start-up core of the ALLEGRO Gas cooled Fast Reactor—Experimental and numerical approaches," *Nuclear Engineering and Design,* pp. 3372-3386, 240 (2010).

[10]   C. Kumara, R. Wang, Y. R. Lu, C. Deck, J. Gazza and J. Qu, „Grid-to-rod fretting wear study of SiC/SiC composite accident-tolerant fuel claddings using an autoclave fretting bench test," *Wear,* 488–489 (2022) 204172.

[11]   G. I. Orosz, S. Tóth and A. Aszódi, „Detailed thermal modelling of the ALLEGRO ceramic assembly," *Nuclear Engineering and Design,* 376 (2021).

[12]   G. I. Orosz and S. Tóth, „Thermal hydraulic investigations of ALLEGRO ceramic fuel assemblies," *Annals of Nuclear Energy,* pp. 570-580, 120 (2018).

[13]   G. I. Orosz, S. Tóth and A. Aszódi, „Simulations for L-STAR experimental gas-cooled system," *Kerntechnik,* 85 (2020) 5.

[14]   N. Cinosi, S.P. Walker, M.J. Bluck and R. Issa, „CFD simulation of turbulent flow in a rod bundle with spacer grids(MATIS-H) using STAR-CCM+," *Nuclear Engineering and Design,* pp. 37-49, 279 (2014).

[15]   K. Boštjan and K. Samo, „Simulation of turbulent flow in MATIS-H rod bundle with split-type mixing," *Nuclear Engineering and Design,* pp. 112-126, 327 (2018).

[16]   T. Nguyen, N. Goth, P. Jones, S. Lee, R. Vaghetto and Y. Hassan, „PIV measurements of turbulent flows in a 61-pin wire-wrapped hexagonal fuel bundle," *International Journal of Heat and Fluid Flow,* 65 , pp. 47-59, 65 (2017).

[17]   N. Goth, P. Jones, S. Lee, T. D. Nguyen, R. Vaghetto and Y. Hassan, „Time-Resolved PIV/PTV Measurements on Interior Subchannels of a Wire-Wrapped 61-pin Hexagonal Fuel Bundle," *Transactions of the American Nuclear Society,* 11-15 June Vol. 116 (2017).

[18]   N. Goth, P. Jones, T. Nguyen, R. Vaghetto, Y. Hassan, A. Obabko, E. Merzari and F. P. Fischer, „Comparison of experimental and simulation results on interior subchannels of a 61-pin wire-wrapped hexagonal fuel bundle," *Nuclear Engineering and Design,* pp. 130-136, 338 (2018).

[19]   Y. A. Hassan and E. E. Dominguez-Ontiveros, „Flow visualization in a pebble bed reactor experiment using PIV and refractive index matching techniques," *Nuclear Engineering and Design,* pp. 3080-3085, 238 (208).

[20]   „Data sheet: Economy MHIL 903," [Online]. Available: https://www.pumps.co.za/PageFiles/5155384441.pdf. [Access Date: 15 11 2021].

[21]   Hydrus, DEIHL Metering, [Online]. Available: https://www.bellflowsystems.co.uk/files/attachments/5084/HYDRUS.pdf. [Access Date: 17 11 2021].

[22]   DIGMESA, „DIGMESA 141402-99 data sheet".

[23]   B. Weigand and V. Simon, „Laws of similarity in fluid mechanics," *WIT Transactions on State of the Art in Science and Engineerin,* 2006 (3).

[24]   G. I. Orosz and A. Aszódi , „CFD modelling of mixing vane spacer grids for ALLEGRO relevant gas cooled reactor fuel geometry," *Annals of Nuclear Energy,* 164 (2021).

[25]   Dantec Dynamics, „Seeding particles for flow visualisation, LDA and PIV, Product information," Publication No.: Pi270003, 2002.

[26]   Litron Lasers, „Lamp Pumped lasers for PIV Applications from Litron, PB0101:3,," 2010.

[27]   Dantec Dynamics, „Light guide arm system, Publication No.: pi_257_v9," 2018.

[28]   Vision Research, „Phantom: Phantom Miro LAB/LC/R Series, ZDOC-64078-MA-0021 Rev 2," 2016.

[29]   Dantec Dynamics, „Imaging Synchronization Devices, Product Information, Publication No.: pi:251_v6," 2011.

[30]   Dantec Dynamics, „DynamicStudio – User's Guide, Build no.: 6.9.0059. Publication no.: 9040U1871," 2019.

[31]   M, Raffel; C, Willert; S, Wereley; J, Kompenhans, Particle Image Velocimetry - A practical guide, Springer, Berlin, Germany, 2007.

[32]   Visualization Society of Japan, „Handbook of Particle Image Velocimetry," Morikita Publishing, 2002, p. Chapter 6: Assessment and management of measurement accuracy.

[33]   B. Yamaji, „Thermal-hydraulics of a homogeneous molten salt fast reactor concept – experimental and numerical analyses," PhD thesis, Budapest university of technology and economics, Institute of Nuclear Techniques, 2016.

[34]   19.1-1985, AANSI ASME PTC, Measurement Uncertainty, Supplement of Instrument and Apparatus, Part 1, New York: ASME, 1986.

[35]   Z. Szatmáry, Mérések kiértékelése, egyetemi jegyzet, (Evaluation of measurements, lecture textbook), Budapest: BME TTK, 2010.

[36]   W. G. Steele, R. A. Ferguson, R. P. Taylor and H. W. Coleman, Comparison of ANSI/ASME and ISO models for calculation of uncertainty, ISA Transactions 33, 1994 (339-352).

[37]   M. Shao, *Technical Issues for Narrow Angle Astrometry (STEP),* lecture note: https://www.ias.tsinghua.edu.cn/__local/A/B5/87/B94081E75AB6CF53678D0DC3BEE_5AB93B48_191E66.pdf?e=.pdf, 2021.10.18..

[38]   Visualisation Society of Japan, „Handbook of Particle Image Velocimetry," Morikita Publishing, 2002, p. Chapter 6: Assessment and management of measurement accuracy.

[39]   A. A. P. 19.1-1985, Measurement Uncertainty, Supplement of Instrument and Apparatus, Part 1, New York: ASME, 1986.

[40]   Dantec Dynamics, *Imaging Synchronization Devices, Product Information,* Publication No.: pi:251_v6 (2011).

[41]   Litron Lasers, Lamp Pumped lasers for PIV Applications from Litron, PB0101:3, 2010.

[42]   A. Westerweel, Particle Image Velocimetry, Cambridge: ISBN 978-0521-44008-0, 2011.

[43]   D. Metering, „HYDRUS ultrasonic flow metering datasheet," DIEHL Metering, [Online]. Available: https://www.diehl.com/metering/en/products-services/water-metering/water-metering-product/hydrus/63697/#tab-602188. [Access Date: 19. 10 2021.].

[44]   G. I. Orosz , M. Peiretti, B. Magyar, D. Szerbák, D. Kacz, B. Kiss, G. Zsíros and A. Aszódi , „Preliminary Thesis on the First Part of the ALLEGRO CFD Benchmark Exercise," *arXiv,* 2022.

[45]   Gusztáv Mayera, Fabrice Bentivoglio, „Preliminary study of the decay heat removal strategy for the gasdemonstrator allegro," *Nuclear Engineering and Design,* pp. 67-76, 286 (2015).

[46]   G. I. Orosz and S. Tóth, „CFD Investigation of Inner Subchannels of ALLEGRO Ceramic Fuel Assembly (In Hungarian)," *Nukleon,* May, 2016.

[47]   G. I. Orosz, S. Tóth and A. Aszódi, „Detailed thermal modelling of the ALLEGRO ceramic assembly," *Nuclear Engineering and Design,* 376, 2021.

[48]   A. Vasile, B. Kvizda, S. Bebjak, G. Mayer, and P. Vácha, „Thermal-hydraulics and Decay Heat Removal in GFR ALLEGRO," 2017.

[49]   G. I. Orosz and S. Tóth, „Thermal hydraulic investigations of ALLEGRO ceramic fuel assemblies," *Annals of Nuclear Energy,* pp. 570-580, 120 (2018).

[50]   L. Bělovský, „The ALLEGRO experimental gas-cooled fast reactor project," in *GEN IV. International Forum*, ÚJV ŘEŽ, a. s., Czech Republic, 20. March 2019..

[51]   S. Tóth, B. Kiss, E. Gyuricza, and A. Aszódi, „CFD Investigation of ALLEGRO Fuel Assemblies, The 15th International Topical Meeting on Nuclear Reactor Thermal - Hydraulics," in *NURETH-15*, Pisa, Italy, May 12-17, 2013.

[52]   H. Petersen, The Properties of Helium: Density, Specific Heats, Viscosity, and Thermal Conductivity at Pressures from 1 to 100 bar and from Room Temperature to about 1800 K, September, 1970.

[53]   OECD NEA, Best Practice Guidelines for the Use of CFD in Nuclear Reactor Safety Applications – Revision, www.oecd-nea.org: OECD NEA, February 2015.

[54]   M. Zabiego, V. Brun-Magaud, E. Castelier and M. Fle, „A Set of Data Considered for the GFR Pin Design Provided by CEA as an Input to JRC-ITU's Computations within the Frame of the GoFastR Project," CEA, Cadarache, France, 2011.

[55]   L. Yang, W. Chen, L. Luo and X. Zhao, „Calculation of Radiation Heat Transfer View Factors among Fuel Rod Bundles Based on CFD Method," *Annals of Nuclear Energy,* 71, pp. 462-466, 2014.

[56]   ANSYS Inc, ANSYS CFX Solver Theory Guide, 2010.

[57] G. I. Orosz, S. Tóth and A. Aszódi, „Simulations for L-STAR experimental gas-cooled system," *Kerntechninc,* 85, pp. 326-335, 2020.

[58] M. Schikorr, „Gas cooled fast reactor safety analysis," IAEA/EC/GRS/HAEA Workshop, Budapest, Hungary, 2012.

[59] F. W. Dittus and L. M. K. Boelter, „Heat Transfer in Automobile Radiators of the Tubular Type," *International Communications in Heat and Mass Transfer,* 12, pp. 3-22, 1985.

[60] Neil E. Todreas and Mujid S. Kazimi, NUCLEAR SYSTEMS I. Thermal Hydraulic fundamentals, Boston: Taylor & Francis, 1993.

[61] VDI-Gesellschaft Verfahrenstechnik und Chemieingenieurwesen, „Forced Convection," in *VDI Heat Atlas*, Düsseldorf, Springer, 2010, pp. 701-709.

[62] M. A. Hassan and K. Rehme, „Heat Transfer near Spacer Grids in Gas-Cooled Rod," *Nuclear Technology,* 52:3, pp. 401-414, 1981.